



# A hybrid stochastic-sectional method for the simulation of soot particle size distributions

Alexandre Bouaniche

## ► To cite this version:

Alexandre Bouaniche. A hybrid stochastic-sectional method for the simulation of soot particle size distributions. Reactive fluid environment. Normandie Université, 2019. English. NNT : 2019NORMIR23 . tel-02866741

**HAL Id: tel-02866741**

**<https://theses.hal.science/tel-02866741>**

Submitted on 12 Jun 2020

**HAL** is a multi-disciplinary open access archive for the deposit and dissemination of scientific research documents, whether they are published or not. The documents may come from teaching and research institutions in France or abroad, or from public or private research centers.

L'archive ouverte pluridisciplinaire **HAL**, est destinée au dépôt et à la diffusion de documents scientifiques de niveau recherche, publiés ou non, émanant des établissements d'enseignement et de recherche français ou étrangers, des laboratoires publics ou privés.



Normandie Université

## THÈSE

Pour obtenir le diplôme de doctorat

Spécialité **Energétique**

Préparée à l'INSA de Rouen

**A hybrid stochastic-sectional method for the simulation of  
soot particle size distributions**

présentée et soutenue par

**Alexandre BOUANICHE**

**Thèse soutenue publiquement le 27 novembre 2019  
devant le jury composé de**

S. RIGOPOULOS	Professeur, Imperial College London	Rapporteur
O. COLIN	Senior Scientist HDR, IFPEN	Rapporteur
R. FOX	Professeur, Iowa State University	Examineur
P. DESGROUX	Directrice de Recherche, Université de Lille	Examineur
A. KEMPF	Professeur, Universitat Duisburg Essen	Examineur
J. YON	Maître de Conférence, CNRS-CORIA	Examineur
L. VERVISCH	Professeur INSA de Rouen Normandie, CNRS-CORIA	Dir. de thèse
P. DOMINGO	Directrice de Recherche CNRS-CORIA	Codir. de thèse

■ Thèse dirigée par Luc VERVISCH et Pascale DOMINGO, laboratoire CORIA (UMR 6614 CNRS)





# Abstract

Soot particles (which are one kind of ultra-fine particles) can be produced and emitted in fuel rich combustion conditions. Sectors like road and air transportation, or industry are significant contributors to soot particles emissions. Soot particles are usually considered as a pollutant as their negative impact on health has been assessed. In some specific cases like nanomaterials production, they can be synthesized on purpose. In both cases, accurate understanding and prediction capability of the Particle Size Distribution (PSD) is needed, for a better combustors design.

In this thesis, a novel numerical method is proposed to predict the Particle Size Distribution (PSD) evolution. It consists in a hybrid approach featuring stochastic particles representing a Probability Density Function (PDF), and fixed sections. The objective is to solve accurately for the surface growth/oxidation term, mitigating the problem of numerical diffusion encountered in some classical sectional methods. On the other hand, the proposed method is less expensive than a full Monte Carlo method.

First, the context and motivation of the thesis are explained. Concepts and models for soot physical source terms are shortly reviewed. Then, the Population Balance Equation (PBE), which drives the evolution of the Particle Size Distribution (PSD), is presented as well as the different classes of numerical methods used for its resolution. Subsequently, the novel hybrid method is introduced. Its accuracy and efficiency are demonstrated on analytical test cases. Finally, the method is applied on a premixed ethylene sooting flame.

**Keywords:** Aerosol modelling; Sectional method; Stochastic method; Hybrid modelling; Particle Size Distribution; Population Balance Equation; Probability Density Function; Soot modelling

# Résumé

Les particules de suie (qui sont un type de particules ultrafines) peuvent être produites et émises dans des conditions de combustion riche. Les secteurs comme les transports (routier et aérien), ou l'industrie sont des contributeurs significatifs aux émissions de particules. Celles-ci sont habituellement considérées comme des polluants dans la mesure où leur impact négatif sur la santé a été mesuré. Dans certains cas spécifiques comme la production de nanomatériaux, elles peuvent être synthétisées de manière volontaire. Dans les deux cas, une compréhension précise et une capacité de prédiction de la distribution de tailles de particules (PSD en anglais) sont nécessaires, pour une meilleure conception des chambres de combustion.

Dans cette thèse, une méthode innovante est proposée pour la prédiction de l'évolution de la distribution de tailles de particules (PSD). Elle consiste en une approche hybride composée de particules stochastiques représentant une fonction de densité de probabilité (PDF en anglais) et de sections fixes. L'objectif est de résoudre de manière précise le terme source de croissance/oxydation, en traitant le problème de diffusion numérique rencontré par des méthodes sectionnelles classiques. D'autre part, la méthode proposée est moins coûteuse qu'une méthode de Monte Carlo complète.

D'abord, le contexte et les motivations de cette thèse sont expliqués. Les concepts et modèles pour les termes sources physiques de suie sont brièvement résumés. Ensuite, l'équation de bilan de population (PBE en anglais) qui pilote l'évolution de la distribution de tailles de particules (PSD), est présentée, ainsi que les différentes classes de méthodes utilisées pour sa résolution. La nouvelle méthode hybride est introduite. Sa précision et son efficacité sont démontrées sur des cas tests analytiques. Enfin, la méthode est appliquée sur une flamme prémélangée d'éthylène.

**Mots-clés:** Modélisation aérosols; Méthode sectionnelle; Méthode stochastique; Modèle hybride; Distribution de tailles de particules; Equation de bilan de population; Fonction de densité de probabilité; Modélisation des suies

## Remerciements (Acknowledgements)

Pendant ma période de travail au laboratoire CORIA j'ai bénéficié de nombreuses interactions qui ont été bénéfiques, d'un point de vue professionnel et personnel. Je tiens à remercier ici les personnes avec qui j'ai pu échanger durant ces trois années.

Tout d'abord, je remercie les membres du jury de ma soutenance de thèse pour leurs remarques et questions qui m'ont permis de présenter de manière plus précise et claire mes travaux.

Je remercie mes encadrants Luc et Pascale pour leur accompagnement. Merci de m'avoir fait confiance et orienté sur un sujet intéressant. Merci pour votre expertise scientifique et vos conseils toujours pertinents. Merci pour votre passion pour votre travail et votre disponibilité. Merci également pour votre compréhension et votre bienveillance.

Jérôme, merci pour les discussions sur la morphologie des agrégats. Merci pour tes explications et idées qui m'ont permis de prendre du recul sur différents concepts et modèles. Merci José également pour ta connaissance de la bibliographie et ton aide pendant certaines révisions d'articles.

Merci à Brigitte et Martin qui connaissent bien le monde de la recherche et m'ont expliqué en quoi consistait une thèse et pourquoi cela leur avait plu. Sans eux je ne me serais probablement pas lancé dans ce projet.

Merci à tous les collègues du CORIA. Grâce à vous j'ai eu la chance de travailler dans un environnement stimulant et agréable. Merci Frédéric et Maxime, pour votre compagnie lors des réunions de projet SOPRANO. Merci Isabelle pour ton aide et ta réactivité. Merci surtout à ceux que j'ai le plus cotoyés et qui sont aujourd'hui de grands amis, au bureau et en dehors. C'est grâce à vous que j'ai passé trois très belles années à Rouen. Kévin, merci pour ta bonne humeur et ta capacité à passer des débats les plus enflammés aux franches rigolades. Francesco merci pour ton énergie, ton ouverture d'esprit et ton sens de la dérision. Merci pour les mêmes (brésiliens ou italiens). Andréa merci pour ton écoute et ta motivation (au travail et sur la piste de danse). Merci pour les conseils musicaux et pour les beaux posters. Pierre merci pour le partage et les dégustations (pas trop tourbé quand même...). Merci pour l'accès illimité au château De Bénard. Umüt merci pour ta spontanéité et ta sincérité. Merci aussi pour ton esprit militant et informé. Loïc merci pour tes conseils culinaires et bonnes adresses parisiennes. Patri merci pour les walking tours à Bruxelles et les sorties toujours bien organisées. Merci pour ton sens de l'observation et ton empathie. Yann merci pour ta répartie toujours aiguisée. Merci Geogeo pour les discussions sérieuses (ou pas), pour les virées à LH et les parties de badminton. Merci Camille pour ton rire et l'accent (léger) du sud. Merci pour les conseils Ikea et confiture de coing. Merci aussi à Bastien, Huu-tri, Deewakar, Félix, Romain, Hakim, Nico L., Nico J., Florian, Dorian pour avoir fait du bureau un endroit aussi motivant et agréable.

Merci à mes amis et à ma famille, en particulier mes parents et mon frère qui m'ont toujours soutenu et mis dans les meilleures conditions de réussite.

Ana, obrigado pela sua alegria e coragem. Obrigado por compartilhar sua vida com a minha. Obrigado por entender minhas motivações e escolhas. E sobretudo, obrigado pelo seu apoio e seu amor.

# Contents

<b>1</b>	<b>Introduction</b>	<b>9</b>
1.1	Motivation	9
1.1.1	Impacts on health	9
1.1.2	Impacts on climate	10
1.1.3	Regulation and emissions trends in Europe	10
1.1.4	Material synthesis	13
1.2	Soot particles: Definition and description	13
1.2.1	Definition	13
1.2.2	Morphology	14
1.3	Objectives and outline	16
1.3.1	Objectives	16
1.3.2	Outline	17
<b>2</b>	<b>Models for soot formation and dynamics</b>	<b>19</b>
2.1	Gas phase chemistry	20
2.2	Nucleation	26
2.2.1	Characterization of incipient particles and experimental evidences	26
2.2.2	Theoretical models	27
2.2.3	Numerical models for nucleation	30
2.3	Agglomeration	36
2.3.1	Soot quantities	36
2.3.2	Agglomeration and Smoluchowski equation	37
2.3.3	Concepts of pure coalescence and pure aggregation	37
2.3.4	Collision diameter	38
2.3.5	Collision frequency	39
2.4	Surface growth/loss and condensation	40
2.4.1	Carbon addition surface reactions	41
2.4.2	Oxidation	42
2.4.3	Active sites	44
2.4.4	PAH Condensation	44
<b>3</b>	<b>Numerical approaches to solve the Population Balance Equation</b>	<b>46</b>
3.1	Context of polydispersed particles and definitions	47
3.2	The Population Balance Equation	49
3.2.1	Homogeneous PBE	49
3.2.2	PBE in laminar flows	50
3.3	Monodisperse assumption based models	51
3.4	Methods of Moments	54
3.4.1	Principle	54
3.4.2	QBMM	54

3.4.3	MOMIC	57
3.5	Sectional methods	58
3.5.1	Discretization schemes for agglomeration	59
3.5.2	Discretization schemes for growth	62
3.6	Monte Carlo methods	66
3.6.1	DSMC	66
3.6.2	Constant-volume or constant-number	68
3.6.3	Time-driven or event-driven	69
3.6.4	Strategies for more efficient algorithms	71
3.7	Comparative advantages and drawbacks	72
<b>4</b>	<b>A novel hybrid stochastic/sectional method: the HYPE method</b>	<b>75</b>
4.1	Problem formulation	75
4.2	Hybrid Stochastic/Fixed-Sectional method	76
4.2.1	Control parameters and statistical description	76
4.2.2	Hybrid Stochastic/Fixed-Sectional solution	78
4.3	Canonical test cases	84
4.4	Results	85
4.5	Convergence and response to resolution parameters	92
4.6	Chapter summary	97
<b>5</b>	<b>Application to a laminar premixed flame</b>	<b>98</b>
5.1	Modeling of nucleation, growth and agglomeration source terms	98
5.2	Simulation of a one-dimensional freely propagating laminar premixed flame	100
5.2.1	Flow configuration and model parameters	100
5.2.2	Results	101
5.3	Parametric analysis of aggregate shape modeling	104
5.4	Comparison between hybrid and sectional methods	107
<b>6</b>	<b>Conclusions and perspectives</b>	<b>111</b>
6.1	Conclusions	111
6.2	Perspectives	111
<b>7</b>	<b>Appendix</b>	<b>113</b>
7.1	Molecules structures	113
7.2	Additional published paper	116
7.3	Summary in french / Résumé en français	135
	<b>Bibliography</b>	<b>161</b>

# Nomenclature

## Acronyms

AFM	Atomic Force Microscopy
BC	Black Carbon. Usual name for soot particles in some areas of research like environmental science or medicine
CHRCR	Clustering of Hydrocarbons by Radical-Chain Reactions
CFD	Computational Fluid Dynamics
CQMOM	Conditional Quadrature Method of Moments
DQMOM	Direct Quadrature Method of Moments
EQMOM	Extended Quadrature Method of Moments
FEM	Finite Element Method
FVM	Finite Volume Method
HAB	Height Above Burner
HACA	Hydrogen Abstraction Carbon Addition
KDF	Kernel Density Function
LES	Large Eddy Simulation
MOMIC	Method Of Moments with Interpolative Closure
MD	Molecular Dynamics
PSD	Particle Size Distribution
PM10	Particulate Matter with diameter below 10 microns
PM2.5	Particulate Matter with diameter below 2.5 microns
PM	Particulate Matter
PAH	Polycyclic Aromatic Hydrocarbon
QBMM	Quadrature Based Methods of Moments
QMOM	Quadrature Method of Moments
RSR	Resonantly Stabilized Radicals

SPAMM Simultaneous Particle and Molecule Modeling

TEM Transmission Electron Microscopy

### Collisions and Chemistry

$N_A$  Avogadro's number

$k_B$  Boltzmann constant

$\beta(v, \bar{v})$  Collision frequency between soot particles of different volumes

$C_g$  Concentration of the reacting gaseous species  $g$

$Cu(v)$  Corrective Cunningham coefficient for a particle of size  $v$

$\mu$  Dynamic gas viscosity

$\rho$  Gas density

$\lambda$  Gas mean free path

$P$  Gas pressure

$T$  Gas temperature

$R$  Ideal gas constant

$Kn$  Knudsen number

$C_{mass}$  mass of a carbon atom

$C_{n_C}$  Notation for a soot particle (containing  $n_C$  carbon atoms) as a species in reaction equations.

$C_{soot}$  Notation for soot as a species in reaction equations.

$k_g$  Per-site (on soot particle surface) rate coefficient

$\epsilon_n$  Van der Waals enhancement factor

### Aggregate morphology

$d_p$  Diameter of a primary spherule within a soot aggregate

$d_c$  Diameter of the aggregate's circumscribed sphere. Also used as collision diameter.

$D_f$  Fractal dimension corresponding to a distribution of aggregates

$k_f$  Fractal pre-factor corresponding to a distribution of aggregates

$d_g$  Gyration diameter of the aggregate

$R_g$  Gyration radius of the aggregate

$n_p$  Number of primary spherules composing the aggregate

$R_p$  Radius of a primary spherule within a soot aggregate

$R_c$  Radius of the aggregate's circumscribed sphere

**PBE**

$\dot{A}_i$	Agglomeration source per unit of flow volume in the $i$ -th section of size
$\dot{a}$	Agglomeration source term per unit size per unit of flow volume
$F_s$	Geometric grid spacing factor
$v_i^{inf}$	Lower boundary of section $i$
$\dot{H}_o$	Nucleation source per unit of flow volume
$\dot{h}$	Nucleation source term per unit size per unit of flow volume
$M$	Number of sections (in sectional method) or number of nodes (in QBMM).
$N_{P_i}$	Number of stochastic particles in the $i$ -th section of size
$G(v)$	Particle growth/loss rate
$N_i$	Particle number density in the $i$ -th section of size
$\bar{P}(v^*; \underline{x}, t)$	Probability density function of particle size
$v_i$	Representative size inside section $i$
$N_i^R$	Residual particle number density in the $i$ -th section of size
$\dot{A}_T$	Total agglomeration source per unit of flow volume
$N_P$	Total number of stochastic particles
$v_i^{sup}$	Upper boundary of section $i$

**Soot quantities**

$\chi$	Number of sites per unit area on soot particle surface
$n(v)$	Particle number density per unit size per unit of gas volume (at size $v$ )
$Y_s$	Soot mass fraction
$\rho_{soot}$	Soot particle density
$m_k$	Statistical moment of the distribution (of order $k$ )
$s_i$	Surface area per particle in the $i$ -th section of size
$N_T$	Total number density of soot particles per unit of gas volume
$f_v(v)$	Total soot volume fraction
$S_T$	Total surface area of soot per unit of gas volume
$v$	Volume of a soot particle

# Chapter 1

## Introduction

### Contents

---

<b>1.1 Motivation</b>	<b>9</b>
1.1.1 Impacts on health	9
1.1.2 Impacts on climate	10
1.1.3 Regulation and emissions trends in Europe	10
1.1.4 Material synthesis	13
<b>1.2 Soot particles: Definition and description</b>	<b>13</b>
1.2.1 Definition	13
1.2.2 Morphology	14
<b>1.3 Objectives and outline</b>	<b>16</b>
1.3.1 Objectives	16
1.3.2 Outline	17

---

## 1.1 Motivation

Soot particles are generated from combustion in many different contexts such as fires, domestic or industrial burners, furnaces, internal combustion engines or aeronautical turbines. Generally produced from fuel rich combustion, soot particles are usually an unwanted byproduct but can also be synthesized on purpose in some applications. In this introductory section, a quick overview is given on the impacts of soot particles on the environment and industry.

### 1.1.1 Impacts on health

Soot particles can cause cardiovascular diseases, cancer or respiratory diseases ([Niranjan and Thakur, 2017](#)). In general, in medical or environmental studies, soot particles are referred to as Black Carbon (BC). They are considered as one type of particles. A more general measure of particles concentration or emissions is Particulate Matter (PM). Measured pollutants levels are usually indicated as PM2.5 or PM10 (particulate matter with diameter below 2.5 microns and below 10 microns respectively). One also refers to ultra-fine particles for particles below 100 nanometers. Estimates of the health impacts attributable to exposure to air pollution indicate that PM2.5 concentrations in 2013 were responsible for about 467 000 premature deaths originating from long-term exposure in Europe ([Guerreiro et al., 2016](#)). Groups of experts have gathered the conclusions of numerous studies to bring relevant information to decision makers and regulatory agencies. For instance, the World Health Organization issued the Review of evidence on health aspects of air pollution – REVIHAAP in which the health effects of particulate matter, including Black Carbon were assessed ([WHO](#),

2013). More recently, the ANSES (french national agency for sanitary security for food, environment and work) reviewed newer scientific contributions and assessed the impact of soot particles (and other particulate matter) from several sectors and in particular road transportation (ANSES, 2019). The main conclusions were the following:

- Within particulate matter, the strongest levels of proof of negative effect on health were gathered for soot particles, organic carbon, and ultra-fine particles (below 100 nanometers).
- The level of proof of negative effect on health of particles emitted by the road transportation sector is considered as "strong".
- The negative effect on health from coal combustion, petroleum products industry and biomass combustion was confirmed.
- For future regulation, the agency recommends to target primarily indicators on levels of soot particles, organic carbon, and ultra-fine particles in addition to indicators on bigger particles as PM<sub>2.5</sub> and PM<sub>10</sub>.

It is therefore essential to develop accurate commercial measurements and numerical models for ultra-fine particles and in particular, soot particles.

### 1.1.2 Impacts on climate

Black Carbon emissions induce a significant climate forcing. In Bond et al. (2013), a comprehensive assessment of climate forcing by all known processes relative to black-carbon-rich sources was made. Uncertainty levels are high but the main conclusions are that there is a very high probability that black carbon emissions, independent of co-emitted species, have a positive forcing and warm the climate. However, considering the co-emitted species, including some cooling agents, the net forcing of these sources may be slightly negative. A schematic overview of the processes by which Black Carbon induces climate forcing is shown in Figure 1.1. An illustration of the geographic distribution of modeled BC emissions, burden, climate forcing and temperature response is shown in Figure 1.2.

### 1.1.3 Regulation and emissions trends in Europe

European emission standards have been implemented defining the acceptable limits for exhaust emissions of new vehicles sold in the European Union and EEA member states. The latest EURO 6 standards define limits for PM levels (Particulate Matter in g/km) and PN levels (Particulate Number in Particle/km) for diesel and gasoline engines. Standards on PM have continuously become more stringent (Figure 1.3), while standards on PN have been introduced through Euro 5b for diesel engines and Euro 6b for gasoline engines, both set at  $6 \cdot 10^{11}$  [particle/km].

These standards have driven significant reduction of PM and BC emissions from road transportation in Europe as can be seen on Figure 1.4. Other sectors contribute to BC emissions, in particular the *Commercial, institutional and households* category which includes domestic biomass combustion. Also, the emissions of the non-road transport sector are not negligible. Within the aeronautical context, no standards were enforced yet on PM emissions. However, joint research programs involving industry and academic laboratories aim at getting a better understanding of soot formation in aeronautical engines. For example, the SOPRANO project, coordinated by SAFRAN Tech and funded by the European H2020 program, funded the present PhD thesis. The main objective of the project is to improve experimental and numerical approaches related to the characterization and prediction of soot emissions in Low NO<sub>x</sub> combustor environment. In particular, numerical models must be available to accurately predict the Particle Size Distribution (PSD) to enable an optimized design of future engines. Within this context, the present thesis aims at bringing an accurate numerical method for the evolution of the PSD.

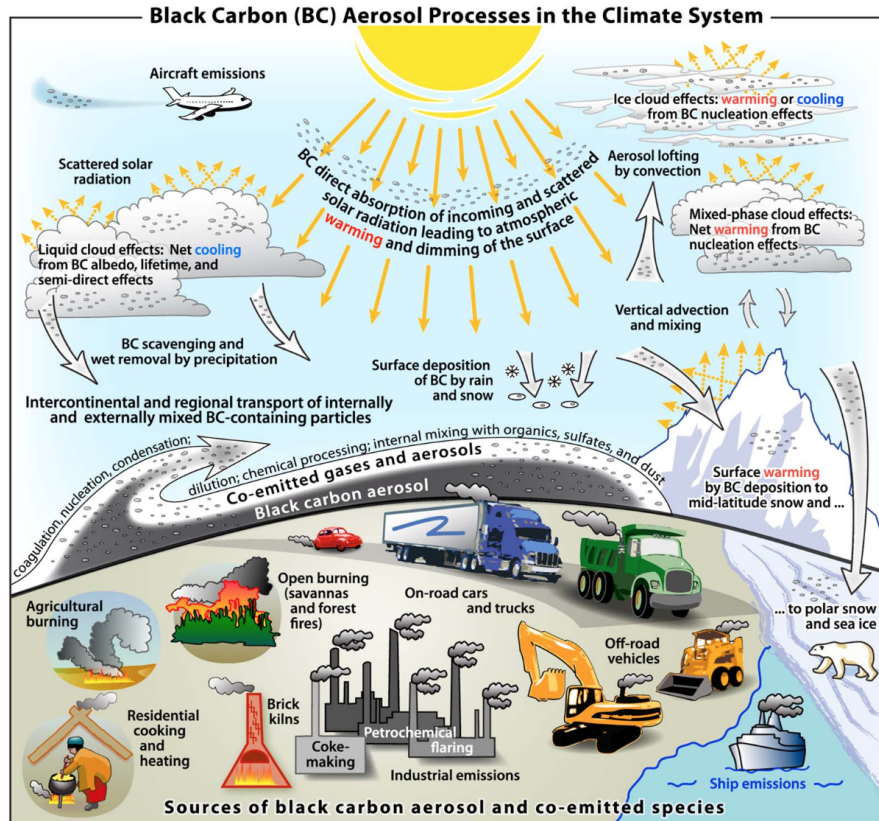


Figure 1.1: Schematic overview of the primary black-carbon emission sources and of the processes by which Black Carbon induces climate forcing. Source: Bond et al. (2013)

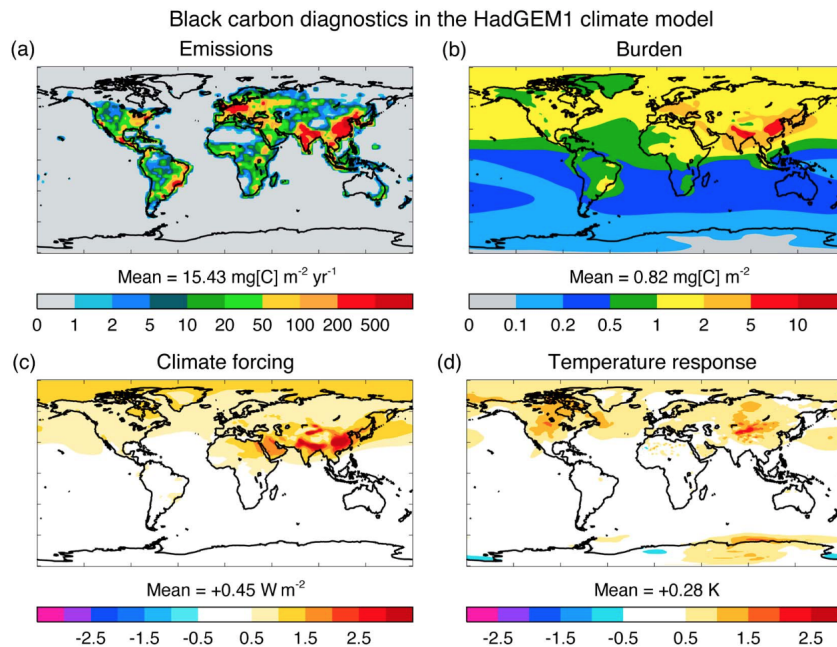


Figure 1.2: Data from the HadGEM1 climate model. Source: Bond et al. (2013). (a) Emissions of BC aerosols [ $\text{mg} \cdot \text{m}^{-2} \cdot \text{yr}^{-1}$ ], (b) burden of BC aerosols [ $\text{mg} \cdot \text{m}^{-2}$ ], (c) direct radiative forcing due to BC aerosols [ $\text{W} \cdot \text{m}^{-2}$ ], and (d) equilibrium surface temperature change [ $\text{K}$ ] in response to the BC direct radiative forcing.

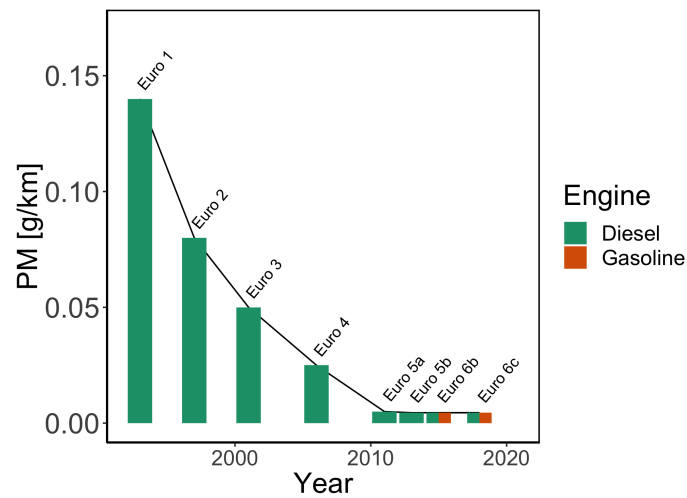


Figure 1.3: Evolution of European standards for Particulate Matter emissions.

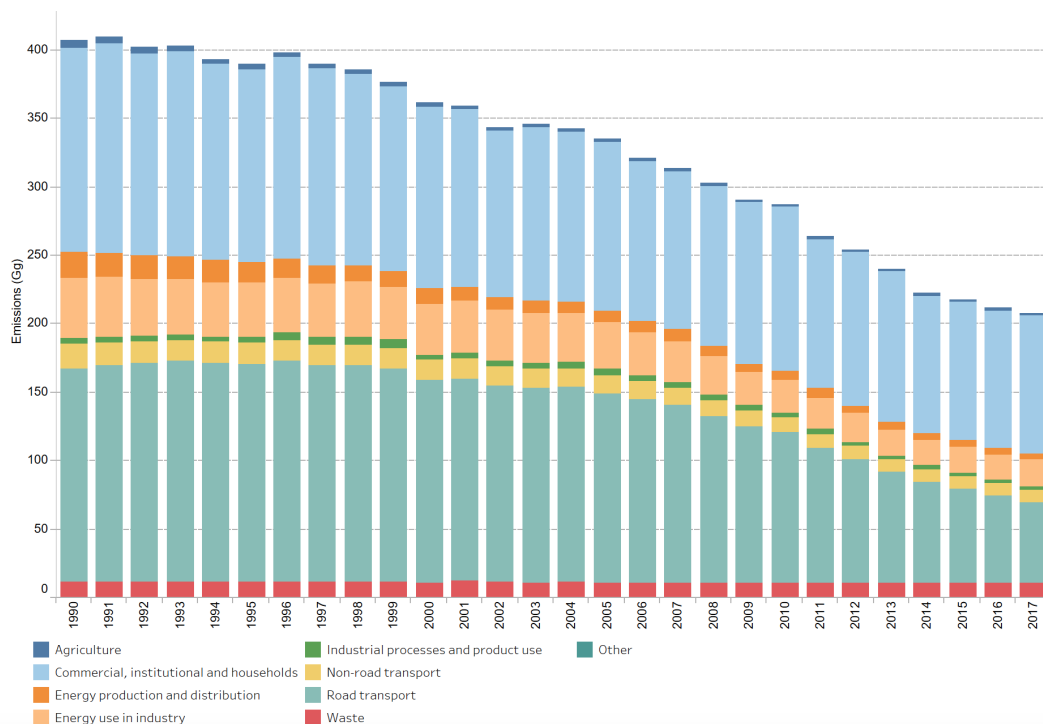


Figure 1.4: Evolution of BC emissions by sector in Europe. Source: European Environment Agency (EEA).

### 1.1.4 Material synthesis

In some applications, soot particles can be used for material synthesis. The objective is then to warrant reproducible generation of particles with well defined size, crystallinity and morphology. Soot aggregates are interesting in electroceramics (gas sensors, battery materials) because they facilitate electron transport by minimizing contact resistance (Strobel and Pratsinis, 2007). Another use of soot aggregates is in catalysts and optical fiber as they ease transport of reactive and product gases in catalyst beds (Kelesidis et al., 2017). Synthesis by combustion allows high purity materials which is not always reachable by conventional wet-phase and solid state processes. Therefore, deep knowledge on soot particle formation and on the evolution of the PSD and aggregates morphology are of interest for ensuring reproducible production of new high-value products like carbon nanotubes, nanosilver and biomagnetic nanofluids.

## 1.2 Soot particles: Definition and description

### 1.2.1 Definition

Soot particles are produced during the incomplete combustion of hydrocarbon fuels. Mainly composed of carbon atoms, they also contain a non-negligible amount of hydrogen atoms.

Terminology and definition can vary depending on the field. In atmospheric science, the term Black Carbon (BC) is used for particles exclusively formed during an incomplete combustion of hydrocarbon fuels. A combination of properties distinguishes BC from other light absorbing material, such as some organic carbon compounds (Bond et al., 2013):

- A strong visible light absorption at 550 nm.
- Refractory, meaning that BC is resistant to decomposition by heat. Its vaporization temperature is near 4000K.
- Aggregate morphology.
- Insolubility in water and common organic solvents

In combustion science, the term soot particle is not only used for aggregates but also for incipient (nascent) particles, and agglomerates. Incipient soot particles are formed by nucleation from the polycyclic aromatic hydrocarbon (PAH) species known to be precursors to soot formation (McEnally et al., 2006). Incipient particles feature elemental carbon-to-hydrogen (C/H) ratios in the range of 1.4–2.5 (Russo et al., 2015). Their size ranges between 1 and 6 nm (Wang, 2011a). These incipient particles grow through coalescence (merging with each other when colliding) and surface addition to become larger primary particles with diameters in the range of 10–50 nm (Wang, 2011a). As these particles grow, they undergo dehydrogenation and progressively solidify and aggregate rather than coalesce, forming aggregates. Aggregation as opposed to coalescence means that the primary particles (or spherules) stick together instead of merging when colliding. The agglomerates then turn into graphitic aggregates through additional surface growth. As soot matures, the C/H ratio increases (Russo et al., 2015). A schematic representation from Michelsen (2017) is reproduced here (Fig. 1.5). It represents soot formation and evolution in a flame with an illustration of the different terms used for soot particles (incipient particles, agglomerates, graphitic aggregates).

Absorption properties are also used to characterize incipient soot particles in the combustion field. Based on the ability to absorb radiations from ultraviolet (UV) to infrared (IR) (which increases with soot maturity) and soot size, two different definitions of incipient soot particles coexist in the combustion community (Betrancourt, 2017):

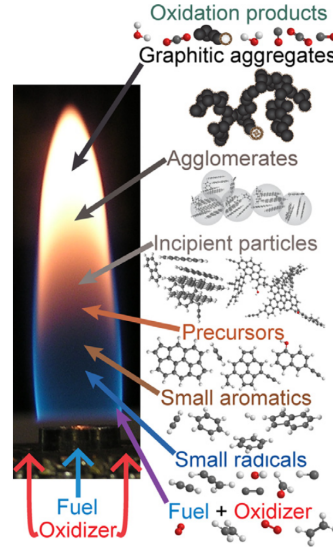


Figure 1.5: Schematic representation of soot formation and evolution in a flame. The molecular species and particles are not drawn to scale. Source: [Michelsen \(2017\)](#)

- According to the first definition, two classes of incipient soot particles exist depending on their absorption properties ([D'Anna, 2009](#); [Michelsen, 2017](#)):
  - Disordered incipient particles which are transparent to visible and IR radiations and have a mean diameter of about 3 nm.
  - Stacked incipient particles, larger than 3 nm and which absorb radiations in the visible and IR spectrum.
- According to the second definition, soot particles can absorb from UV to IR and can be as small as 1 nm. They are defined as particles able to emit black-body radiations naturally at flame temperature or induced by laser absorption (laser induced incandescence) ([Desgroux et al., 2017](#)).

### 1.2.2 Morphology

Soot particles are generally considered as either spherical (incipient particles) or as aggregates constituted of several spherical primary particles (or primary spherules). Figure 1.6 shows a representation of a fractal aggregate and corresponding characteristic dimensions which are defined hereafter.

$d_p$  is the diameter of a primary spherule with  $R_p$  the corresponding radius.  $n_p$  is the number of primary spherules composing the aggregate.  $d_c$  is the diameter of the aggregate's circumscribed sphere. It is also used as a collision diameter. Corresponding radius is noted  $R_c$ .  $d_g$  is the gyration diameter with corresponding radius  $R_g$ . It is characteristic of the mass distribution (linked to the inertial moment).

It is known that soot particles, within a certain size range, have fractal-like structure, i.e. there is a relationship between  $n_p$  and  $d_g$ . This relation is given by the fractal law:

$$n_p = k_f (d_g/d_p)^{D_f}. \quad (1.2.1)$$

$D_f$  is the fractal dimension, and  $k_f$  is the fractal pre-factor. These constants can be determined experimentally. Figure 1.7 (from [Yon et al. \(2011\)](#)) shows an example of agreement between measurements and theoretical fractal law with different values for  $D_f$  and  $k_f$  depending on the fuel.

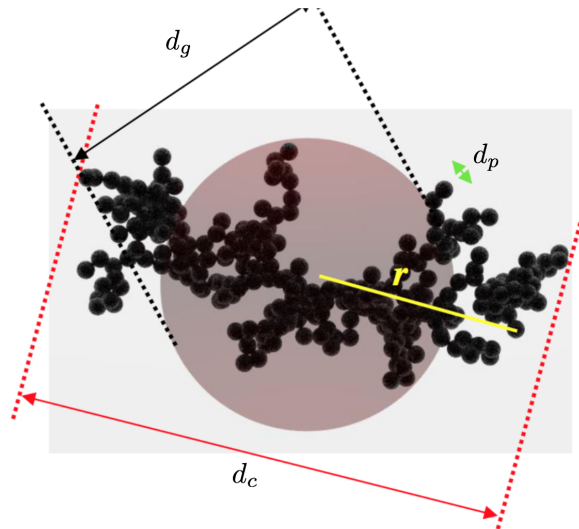


Figure 1.6: Representation of soot aggregates characteristic dimensions.

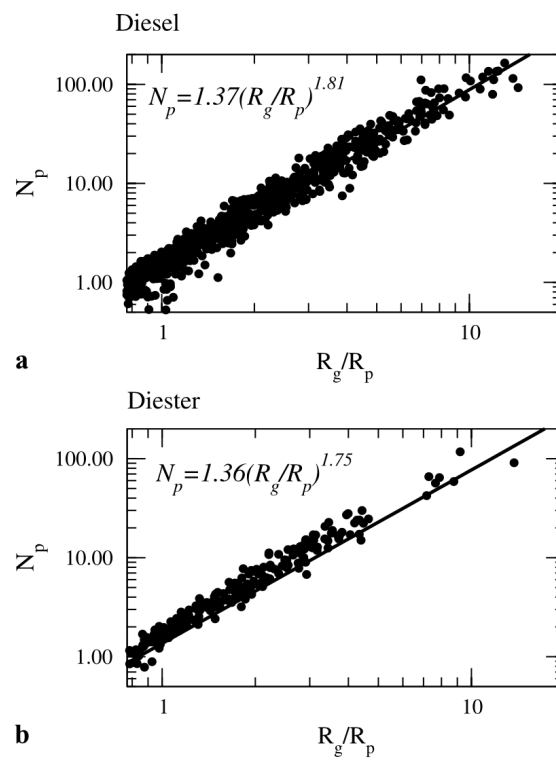


Figure 1.7: Fractal law for (a) diesel and (b) diester soot. Points: Measurements. Line: fitted fractal law. Source: [Yon et al. \(2011\)](#)

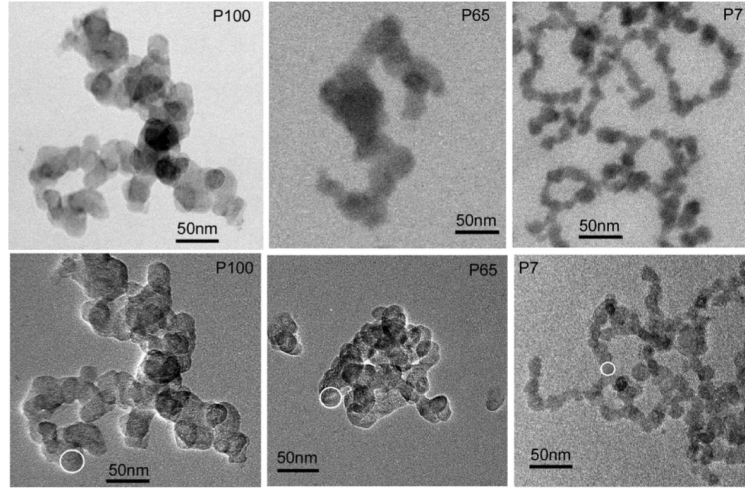


Figure 1.8: BF-STEM mode (upper row) and TEM mode images (lower row) of soot agglomerates from different engine thrust levels. Encircled in the lower row images are examples of primary spherules. Source: [Liati et al. \(2014\)](#)

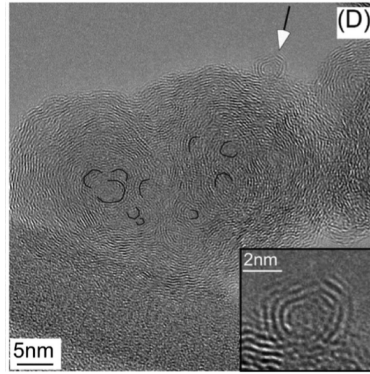


Figure 1.9: HRTEM images of primary multicore soot particles (from the P100 samples) surrounded by relatively well-ordered, deformed graphene lamellae. Source: [Liati et al. \(2014\)](#)

Soot morphology depends on many parameters and can be difficult to predict. It may vary with the fuel but also with operating conditions. For example, in [Liati et al. \(2014\)](#), comparison was made of transmission electron microscopy (TEM) images of samples of soot particles from the same gas turbine (a CFM 56-7B26/3 turbofan engine) at different engine thrust levels. 100%, 65% and 7% engine thrust respectively noted P100, P65 and P7 were sampled. These thrust levels roughly correspond to takeoff, cruising, and taxiing, respectively. Images of representative aggregates for each engine thrust level are shown in Figure 1.8. As observed by the authors, the samples exhibit a diminishing size of the primary soot particles from the higher to the lower thrust. Also, the primary spherules in the 7% engine thrust level are significantly smaller as compared to the 65% and the 100% thrust samples. The primary spherules composing an aggregate from the P100 sample can be observed in Figure 1.9.

## 1.3 Objectives and outline

### 1.3.1 Objectives

The simulation of sooting flames is challenging at several levels.

- First, complex chemistry and physical phenomena as nucleation are involved in soot formation. It is difficult to produce quantitative and generic models and the most accurate ones feature heavy kinetical schemes.
- Second, once the physical source terms are estimated, the evolution of the Particle Size Distribution (PSD) through nucleation, agglomeration and surface growth/loss must be tracked. This is done through the resolution of the Population Balance Equation (PBE). Several techniques have been derived for this purpose. They can be classified into the following main classes: monodisperse assumption-based, Method of Moments (MOM), sectional methods and Monte Carlo methods. Each class presents specific advantages and drawbacks and choice between them may vary depending on the application.
- Finally, radiation and chemistry-turbulence interaction may play an important role in sooting flame applications.

In this thesis, we will focus on the second point. The main objective is to **develop an accurate and efficient method for the resolution of the Population Balance Equation**. Radiation and chemistry-turbulence interaction are beyond the scope of the present work. General background and recent advances in the understanding of soot physics and chemistry (first point) will be presented. However, the innovative part of the present work lies in the development and validation of a novel numerical method.

The proposed method, called HYPE (for HYbrid Population balance Equation) features a hybrid formulation with stochastic particles defining a Probability Density Function, and a fixed-sectional discretization for agglomeration source terms calculation. The goals of this method are:

- To solve accurately for the Particle Size Distribution. Specific attention will be given to the growth/loss source term.
- To maintain a relatively moderate computational cost as compared to other highly accurate numerical methods.

Figure 1.10 illustrates the main steps involved in the simulation of a sooting flame and the role of the proposed numerical method (HYPE).

### 1.3.2 Outline

This thesis is organized as follows:

- **Chapter 2: Models for soot formation and dynamics**  
Some background on soot chemistry and physics is provided. In particular, the phenomena of PAH growth, soot nucleation, agglomeration and surface growth/oxidation are described. Several widely used models are presented as well as some more recent breakthroughs.
- **Chapter 3: Numerical approaches to solve the Population Balance Equation**  
The main classes of numerical methods for the resolution of the Population Balance Equation are presented. The concept of numerical diffusion is explained. Advantages and drawbacks of each class of methods are listed. The positioning and strategy of the HYPE method are introduced.
- **Chapter 4: A novel hybrid stochastic/sectional method: the HYPE method**  
Detailed theoretical formulation of the HYPE method is carried on. Practical algorithm is presented. Analytical test cases are performed. Accuracy and computational cost are measured and compared to reference sectional methods.

- **Chapter 5: Application to a laminar premixed flame**

A laminar premixed ethylene flame is simulated using the HYPE method for soot modelling. Results are compared to a reference sectional method. Aggregate shape modelling is discussed and a parametric study is carried out.

- **Chapter 6: Conclusion and perspectives**

- **Appendix**

Some chemical species cited in this thesis are represented (structure and formula) in the appendix. Also, [Bouaniche et al. \(2019a\)](#) was included in the appendix because it is not directly linked to the topic of this thesis (in contrast, [Bouaniche et al. \(2019b\)](#) was used to write chapter 4). Finally, a summary of this thesis in french has been added in the appendix.

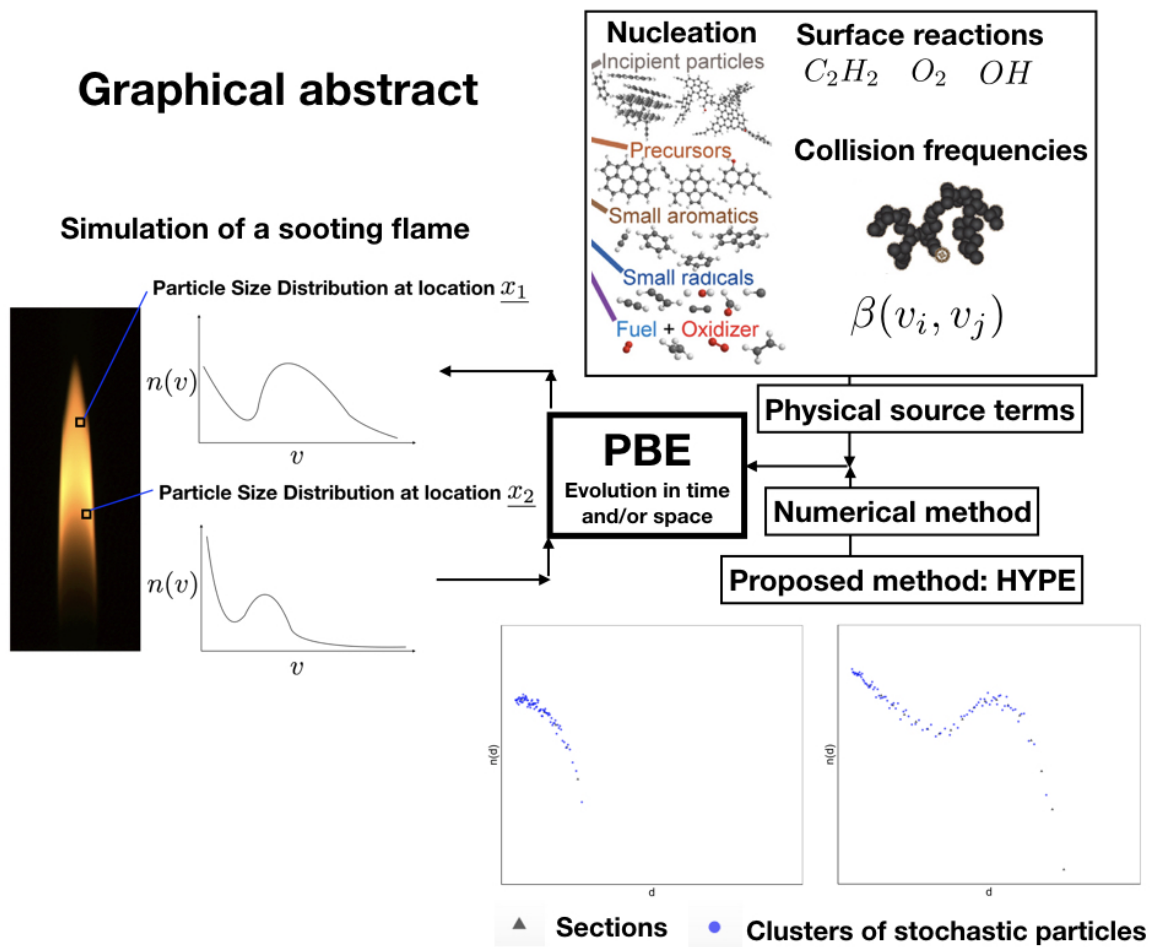


Figure 1.10: Graphical abstract

## Chapter 2

# Models for soot formation and dynamics

### Contents

---

<b>2.1</b>	<b>Gas phase chemistry</b>	<b>20</b>
<b>2.2</b>	<b>Nucleation</b>	<b>26</b>
2.2.1	Characterization of incipient particles and experimental evidences	26
2.2.2	Theoretical models	27
2.2.3	Numerical models for nucleation	30
2.2.3.1	Acetylene based models	30
2.2.3.2	Stacked neutral PAH dimers	32
2.2.3.3	Analogy to gas phase reactions: Lumping techniques and nucleation involving PAH radicals	33
2.2.3.4	Reversible nucleation	35
<b>2.3</b>	<b>Agglomeration</b>	<b>36</b>
2.3.1	Soot quantities	36
2.3.2	Agglomeration and Smoluchowski equation	37
2.3.3	Concepts of pure coalescence and pure aggregation	37
2.3.4	Collision diameter	38
2.3.5	Collision frequency	39
<b>2.4</b>	<b>Surface growth/loss and condensation</b>	<b>40</b>
2.4.1	Carbon addition surface reactions	41
2.4.1.1	HACA mechanism	41
2.4.1.2	Resonantly Stabilized Radicals addition	41
2.4.2	Oxidation	42
2.4.3	Active sites	44
2.4.4	PAH Condensation	44

---

In this chapter, Some background on soot chemistry and physics is provided. Many uncertainties remain on soot formation processes. However, these processes can be broken into different steps: Gas phase chemistry, nucleation, agglomeration, surface growth/loss through surface reactions and PAH condensation. Some of the most accepted theories and models will be presented for each step in this chapter.

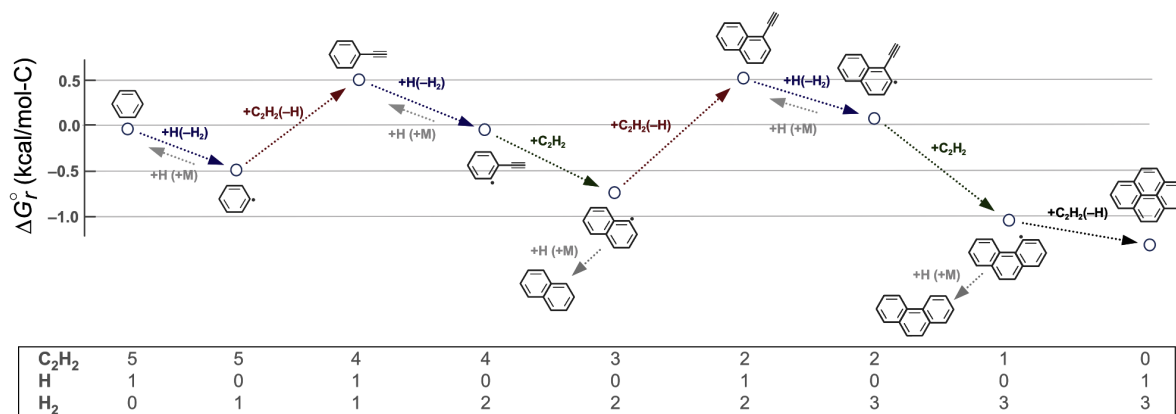


Figure 2.1: A version of the Hydrogen Abstraction Carbon Addition (HACA) reaction mechanism. The standard Gibbs function per carbon atom is plotted relative to an initial system with benzene:acetylene:H atom = 1:5:1 at 1800 K. Source: Wang (2011b)

## 2.1 Gas phase chemistry

The nucleation processes are still widely uncertain and subject to intense research. However, it is widely accepted that PAH (Polycyclic Aromatic Hydrocarbon) species are the main precursors for the formation of incipient soot particles. It is therefore crucial to predict correctly at least some PAH species for most nucleation models. Kinetic mechanisms must be able to reproduce accurately fuel oxidation and the evolution of the main species as well as PAH formation. Different PAH formation and growth pathways have been proposed.

One of the most popular pathways is the Hydrogen-Abstraction-Carbon-Addition (HACA) mechanism which was introduced in Frenklach and Wang (1991). It is based on the postulate that factors important to both flame chemistry and soot formation are:

- Acetylene ( $C_2H_2$ ), because it is the most abundant hydrocarbon intermediate. It plays the role of molecular building block.
- The H atom, because it is the driving force behind chain branching and flame propagation. It plays the role of "catalyst".
- High temperature because it facilitates fast kinetics. However, high temperature also limits the molecular mass growth through fragmentation of PAH molecules.

A schematic representation of the HACA mechanism (from Wang (2011b)) is shown in Figure 2.1. The fact that soot precursors must survive from fragmentation at high temperatures advocates for the participation of Stein's stabilomers (Stein and Fahr, 1985) in soot formation. The presence of these stabilomers in sooting flames has been experimentally confirmed. The pericondensed PAHs, consisting of six-membered benzenoid rings are probably the most important for soot formation (even though more recent experimental results may indicate a significant importance of five-membered rings) and indices of acetylenic PAH growth process have been observed (Dobbins et al., 1995, 1998). Examples of pericondensed PAHs include naphthalene, phenanthrene, pyrene, and coronene.

It can be noted on Figure 2.1 that the Gibbs free energy does not evolve monotonically as benzene grows towards naphthalene, phenanthrene and pyrene. This means that these reactions are highly reversible and kinetically controlled. This high reversibility results in a high dependence on flame temperature and a high sensitivity of PAH formation to a multitude of chemical reactions including the first aromatic ring formation. Other pathways for PAH growth have been proposed since the

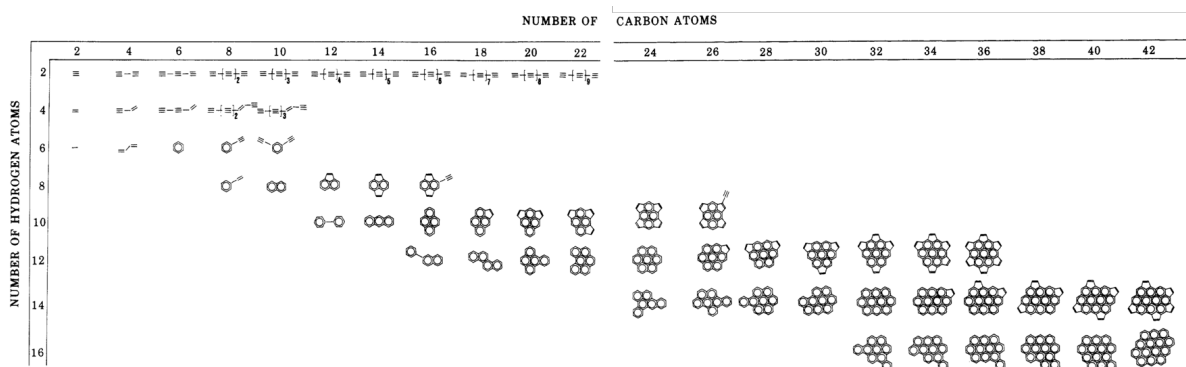


Figure 2.2: Structures of the most stable isomers in the most stable classes of  $C_{2n}H_{2m}$  molecules (“stabilomers”). Source: [Stein and Fahr \(1985\)](#)

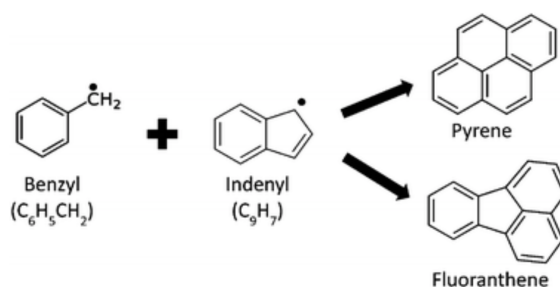


Figure 2.3: Pyrene and fluoranthene formation through the combination of benzyl and indenyl radicals. From [Sinha et al. \(2017\)](#)

introduction of the HACA mechanism. In particular, mechanisms involving Resonantly Stabilized Radicals (RSR) like propargyl ( $C_3H_3^\bullet$ ), benzyl ( $C_7H_7^\bullet$ ), and cyclopentadienyl ( $C_5H_5^\bullet$ ) have been presented. Propargyl recombination to form benzene has been supported by several works ([Miller and Melius, 1992](#); [Miller and Klippenstein, 2001](#)). The formation of four-ring aromatics, pyrene and fluoranthene, through the combination of benzyl and indenyl radicals was studied in [Sinha et al. \(2017\)](#) (Fig. 2.3). Other types of mechanisms like phenyl addition/cyclization (PAC) or methyl addition/cyclization (MAC) have been proposed ([Shukla and Koshi, 2011](#)) (Figs. 2.4 and 2.5).

More recently, high-resolution atomic force microscopy (AFM) was used for direct imaging of the building blocks forming the particles in the early stages of soot formation in a laminar premixed ethylene/air flame ([Schulz et al., 2019](#)). The main conclusions of this work were that:

- There is a large variety of aromatic compounds participating in the formation of the initial soot particles.
- Not only six-membered benzenoid rings but also penta-rings were frequently observed in the

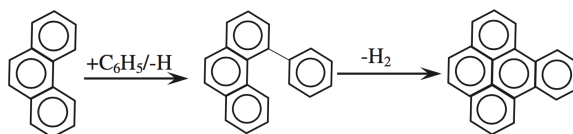
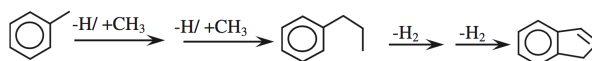
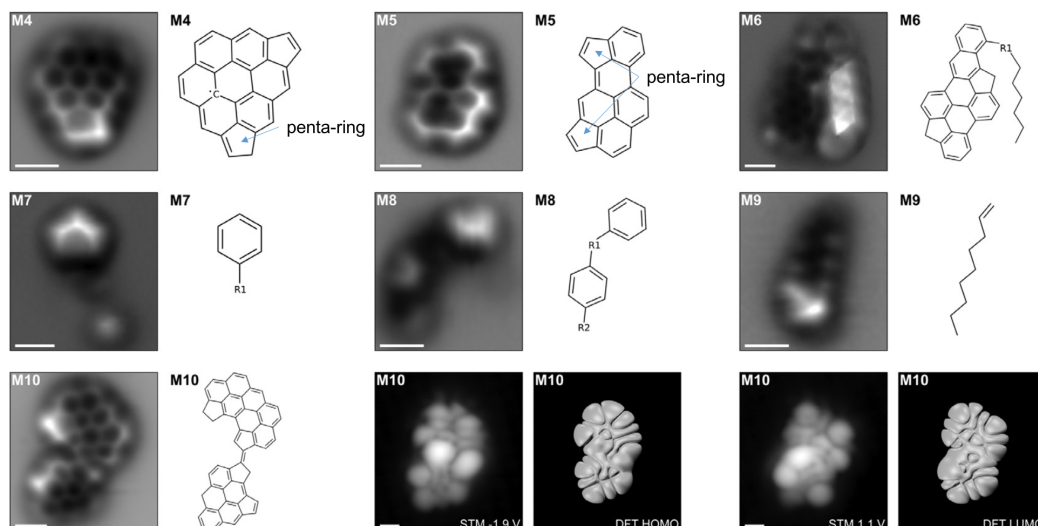


Figure 2.4: PAC mechanism from [Shukla and Koshi \(2011\)](#)

Figure 2.5: MAC mechanism from [Shukla and Koshi \(2011\)](#)Figure 2.6: AFM images and chemical structure of some representative molecules, as well as molecular orbital densities measured by scanning tunneling microscopy (STM) and corresponding density functional theory (DFT) simulations. “R” labels denote unidentified parts of the molecules. Scale bars are 5 Angstroms. Adapted from: [Schulz et al. \(2019\)](#)

imaged aromatic molecules.

- Several molecules contained non-aromatic side-groups such as cycloaliphatic moieties, methyl groups and alkyl chains.
- There are indications for the presence of unpaired  $\pi$ -electrons within the aromatic building blocks.

Other experimental contributions like [Johansson et al. \(2015\)](#) indicate the existence of a variety of PAH species that extends beyond the traditional Stein stabilomers classification in sooting flames. These evidences may drive research towards new pathways for PAH growth and lead to better prediction of PAH concentrations and soot nucleation. A non-exhaustive list of some kinetic schemes among the most used for PAH growth is given in Table 2.1. Currently, available kinetic schemes for PAH growth can give reasonable results depending on the application and species reported but consistent accuracy on a wide variety of flames and species is still difficult to obtain. [Pejpichestakul et al. \(2019\)](#) conducted a wide review of available data on rich laminar premixed flames of hydrocarbon fuels. The CRECK (Politecnico di Milano kinetic modeling group) kinetic mechanism of PAH and soot formation was tested and compared to experimental data from 60 flames from the literature, for more than 20 different fuels, in a wide range of equivalence ratios ( $\phi = 1.00$  to  $\phi = 3.06$ ) and pressures ( $P = 0.03$  atm to  $P = 1.00$  atm). Some comparisons were also made with mechanisms from other groups: the Blanquart mechanism from [Blanquart et al. \(2009\)](#) and the KAUST KM2 mechanism from [Wang et al. \(2013\)](#) (also cited in Table 2.1). Their main conclusions are the following:

Group(s)/Mech. name	Reference(s)
ABF	Wang and Frenklach (1997), Appel et al. (2000)
Stanford / Caltech	Blanquart et al. (2009), Narayanaswamy et al. (2010)
KAUST	Wang et al. (2013), Park et al. (2017)
Sandia / BTU	Moshhammer et al. (2017)
USTC	Yang et al. (2015), Yuan et al. (2015)
DLR	Slavinskaya and Frank (2009), Slavinskaya et al. (2012)
PC2A	Bakali et al. (2012), Desgroux et al. (2017)
MIT	Richter et al. (2005), Ergut et al. (2006)
LLNL	Marinov et al. (1998)
CRECKM	Sagge et al. (2013), Pelucchi et al. (2014)

Table 2.1: A non-exhaustive list of some kinetic schemes among the most used for PAH growth.

- Most major species ( $CO_2$ ,  $H_2$ ,  $H_2O$ ,  $CH_4$ ) are well predicted for the whole range of flames. (Fig. 2.7).
- Other important species like  $C_2H_4$  and  $C_2H_2$  show some significant error levels depending on the pressure and fuel type. (Even though the sum of  $C_2H_4$  and  $C_2H_2$  is consistently well predicted). (Fig. 2.7).
- Large under-predictions of  $C_4H_2$  are observed in atmospheric flames. (Fig. 2.8).
- The overall prediction of PAHs in atmospheric flames is satisfactory. However, most of the low-pressure benzene flames show an overestimation of phenylacetylene ( $C_6H_5C_2H$ ) and underestimation of naphthalene ( $C_{10}H_8$ ). (Fig. 2.9).
- The effect of soot formation on PAH consumption is significant. Therefore, soot models must systematically be included in kinetic modeling efforts aiming at reproducing PAH growth in sooting flames. (Fig. 2.10).
- Similar levels of error were observed for the two other tested mechanisms (Blanquart from Blanquart et al. (2009) and KAUST KM2 from Wang et al. (2013)).

PAH growth modeling is difficult for several reasons:

- Rate constants are challenging because of the difficulties of applying ab-initio techniques to PAH molecules which are large.
- The large number of different species and isomers makes lumping necessary at some level.
- Aromatics formation is highly kinetically controlled. Therefore, a precise knowledge about the underlying mechanism and kinetics at almost every step of the reaction sequence is needed (Wang, 2011a).
- The need to take soot into account for PAH growth modeling because of PAH consumption makes the coupling even more intricate. Also, there is no consensus yet on soot nucleation modeling.

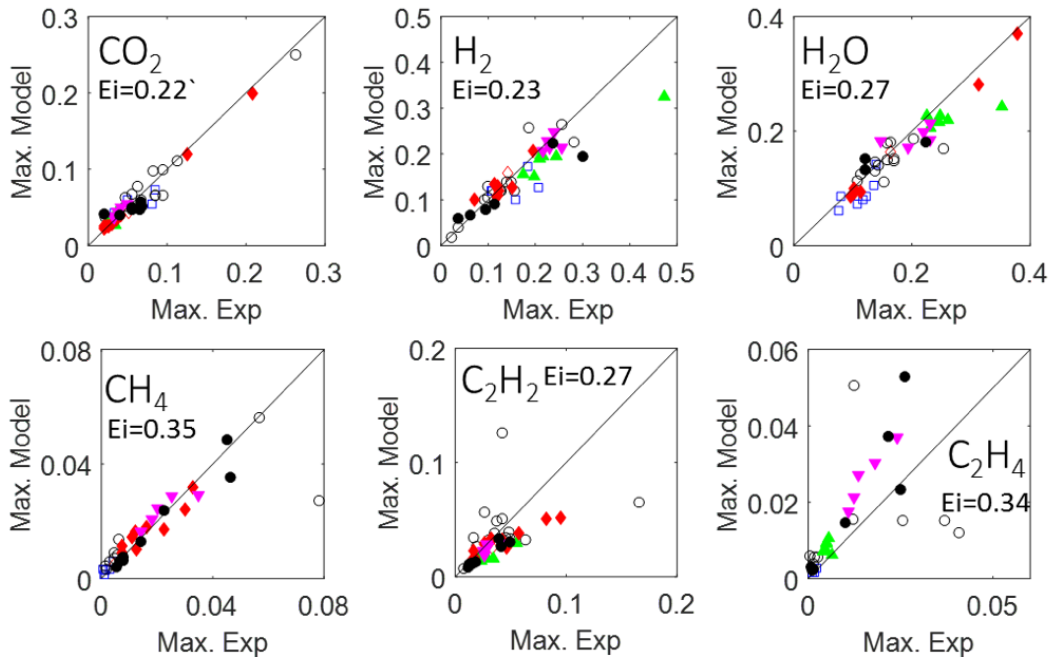


Figure 2.7: Scatter plots of the maximum calculated and measured concentration of major species. Each marker represents main fuels,  $\Delta$ : CH<sub>4</sub>,  $\square$ : C<sub>2</sub>H<sub>2</sub>,  $\diamond$ : C<sub>2</sub>H<sub>4</sub>,  $\nabla$ : C<sub>2</sub>H<sub>6</sub>, and  $\circ$ : C<sub>3</sub>+. Void symbol: low-pressure flames. Filled symbol: atmospheric flames. Source: [Pejpichestakul et al. \(2019\)](#)

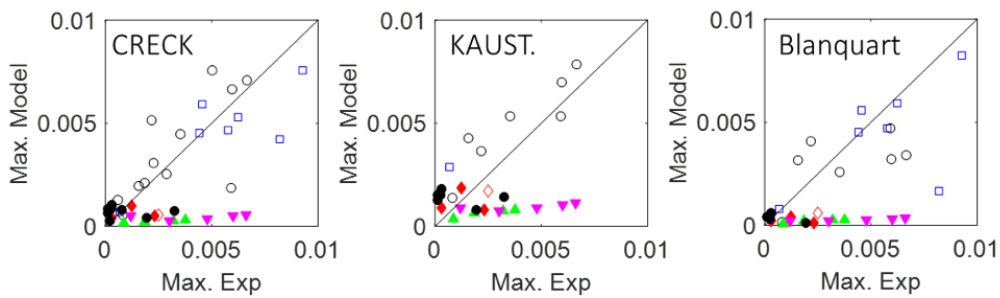


Figure 2.8: Scatter plots of the maximum calculated and measured concentration of C<sub>4</sub>H<sub>2</sub> using CRECK, KAUST and Blanquart models. Symbols as in Fig. 2.7. Source: [Pejpichestakul et al. \(2019\)](#)

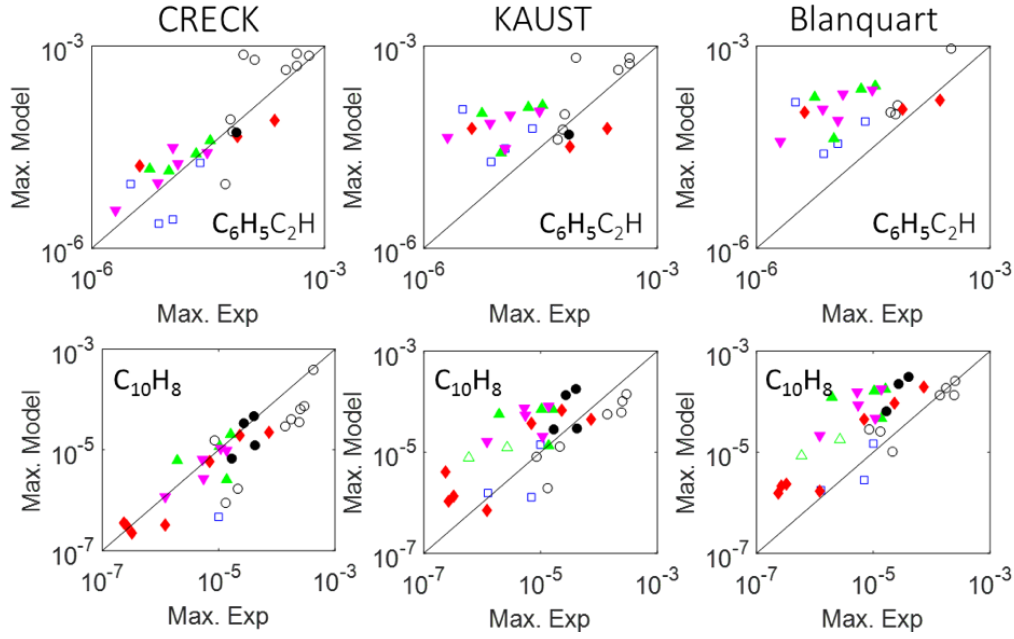


Figure 2.9: Scatter plots of the maximum calculated and measured concentration of phenylacetylene and naphthalene using CRECK, KAUST and Blanquart models. Symbols as in Fig. 2.7. Source: [Pejpichestakul et al. \(2019\)](#)

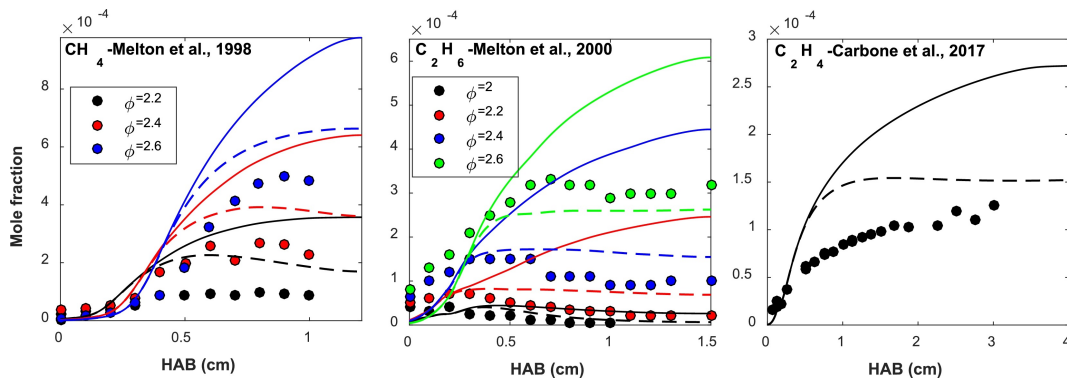


Figure 2.10: Comparison between experimental (symbols) and predicted benzene profiles. Model predictions with (dashed lines) and without soot kinetic model (solid lines). Left panel:  $CH_4$  flames (flames from [Melton et al. \(1998\)](#)). Middle panel:  $C_2H_6$  flames (Flames from [Melton et al. \(2000\)](#)). Right panel:  $C_2H_4$  flame (Flame from [Carbone et al. \(2017\)](#)). Source: [Pejpichestakul et al. \(2019\)](#)

## 2.2 Nucleation

### 2.2.1 Characterization of incipient particles and experimental evidences

In this subsection, an attempt is made to gather and summarize some of the current knowledge on incipient particles based on experimental observations.

Incipient soot particles are freshly nucleated particles (from PAH precursors). They have been detected in the size range of 1 to 6 nm (Wang, 2011a; Oktem et al., 2005; Commodo et al., 2015b). According to Michelsen (2017), incipient particles can be classified in at least two types which may be referred to as: *Disordered incipient particles* and *Stacked incipient particles*.

*Disordered incipient particles:*

- Absorb in the UV but are transparent at visible and IR wavelengths (D’Anna et al., 2005; Sgro et al., 2003).
- Fluoresce predominantly in the UV (Bruno et al., 2007).
- Have diameters smaller than 3 nm (Commodo et al., 2015b; Bruno et al., 2007).
- Are formed under relatively fuel-lean conditions (Commodo et al., 2015b; Sirignano et al., 2012)
- Seem to be constituted of randomly ordered aromatic structures combined with some aliphatic content (Sirignano et al., 2012; Commodo et al., 2015a).

*Stacked incipient particles:*

- Absorb in the visible and IR regions (Sirignano et al., 2012; Minutolo et al., 1996).
- Fluoresce in the visible (Bruno et al., 2007; Sirignano et al., 2012).
- Have diameters larger than 3 nm (Wang, 2011a; Abid et al., 2008; Grotheer et al., 2009)
- Are formed under fuel-rich conditions (Commodo et al., 2015b; Grotheer et al., 2009; Sirignano et al., 2012).
- Seem to be composed of nucleated stacked (Chen and Dobbins, 2000) PAH structures held together by van der Waals forces (Sirignano et al., 2012).
- Appear spherical (Russo et al., 2015; Abid et al., 2008) and liquid-like (Wang, 2011a; Kholghy et al., 2013) when observed through Transmission Electron Microscopy (TEM) and Atomic-Force Microscopy (AFM).

Alternatively, incipient particles can also be defined in a different way (Desgroux et al., 2017): Soot particles are able to absorb 1064 nm radiation and to radiate spectrally continuous blackbody-type radiation. Incipient soot particles can be as small as 1.5 to 4 nm.

Independently of the differing definitions or categories of incipient soot particles, information on their composition and on their precursors is crucial for the understanding and modeling of the nucleation process. Incipient particles have elemental carbon to hydrogen ratios (C/H) ranging from 1.4 to 2.5 (Russo et al., 2015; Blevins et al., 2002; Ciajolo et al., 1998). It is usually considered that they have significantly more aromatic than aliphatic character (Russo et al., 2015; Cain et al., 2014; Mckinnon et al., 1996). However, they have significant abundances of aliphatic and oxygenated groups (Cain et al., 2014; Mckinnon et al., 1996). Recently, aliphatically bridged multi-core PAH have been detected in sooting flames (Adamson et al., 2018) (Fig. 2.11). Also, as stated in the

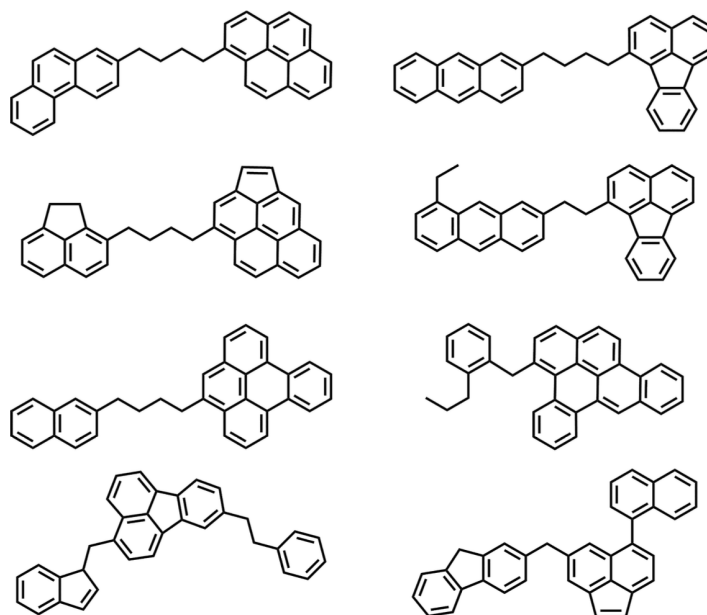


Figure 2.11: Conceivable  $C_{34}H_{26}$  isomers that are consistent with the findings of the tandem mass spectra. The structures consist of dual and triple core aromatics that are bridged through aliphatic chains. Source: [Adamson et al. \(2018\)](#)

previous section, penta-rings were observed in sooting flames ([Schulz et al., 2019](#)) and may be abundant in incipient soot particles.

A wide range of species may be involved in soot particle nucleation. The precursors may not be the most thermodynamically stable isomers as was previously thought (Stein’s stabilomers ([Stein and Fahr, 1985](#))). The presence of Resonantly Stabilized Radicals in an atmospheric-pressure laminar premixed ethylene-oxygen flame was observed in [Johansson et al. \(2018\)](#) (Fig. 2.12). RSR’s may be an important contributor to soot nucleation. Also, dimers, constituted of two stacked PAH monomers, may play an important role in soot nucleation even though they are not thermodynamically stable at flame temperature. In [Mercier et al. \(2019\)](#), experimental evidence supporting the existence of PAH dimers in the proximity of the soot nucleation region of a methane laminar diffusion flame was reported (Fig. 2.13).

## 2.2.2 Theoretical models

Experimental diagnostics bring important insights on the species that participate to soot nucleation. Theoretical models must be consistent with experimental observations and, at the same time, enable to propose numerical models to quantitatively predict nucleation. The main theoretical models for nucleation can be summarized in three conceptual pathways ([Wang, 2011a](#)) (Fig. 2.14):

- Fullerene-like Nucleation (Path A): Growth of “two-dimensional” PAHs into curved, fullerene-like structures ([Homann, 1998](#)).
- Physical Nucleation (Path B): Physical coalescence of moderate-sized PAHs into stacked clusters ([Herdman and Miller, 2008](#); [Schuetz and Frenklach, 2002](#)).
- Chemical Nucleation (Path C): Reaction or chemical coalescence of PAHs into crosslinked three-dimensional structures ([Violi et al., 2004](#); [Richter and Howard, 2000](#)).

Even though the three paths probably all contribute to soot nucleation in flames, their relative importance or feasibility at different temperatures remains to be clarified. Molecular Dynamics

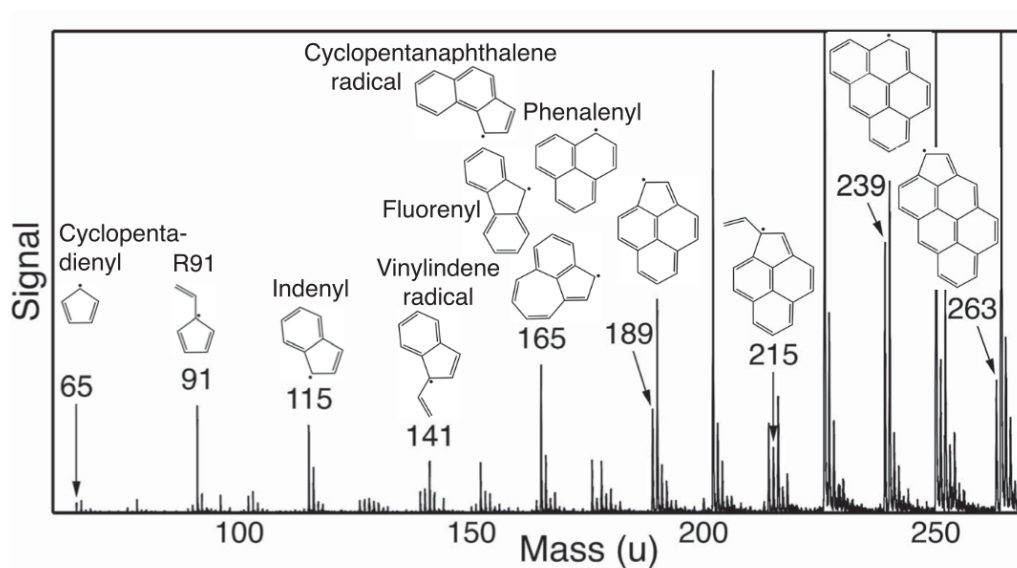


Figure 2.12: Schematic overview of the clustering of hydrocarbons by radical-chain reactions (CHRCR) mechanism. Source: [Johansson et al. \(2018\)](#)

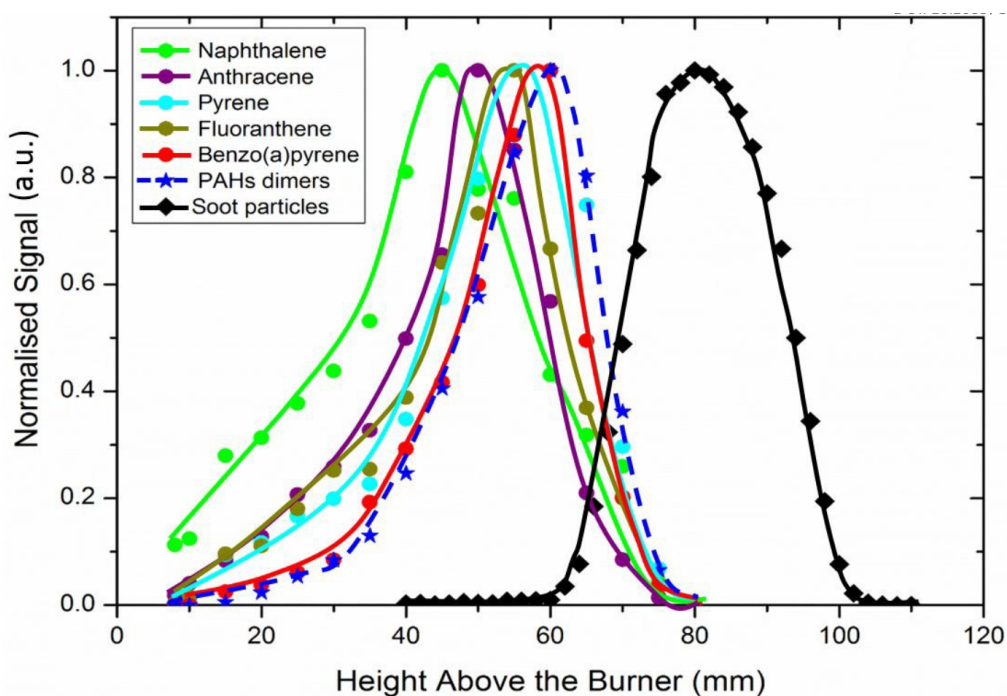


Figure 2.13: Specific profiles of PAHs and dimers subtracted from the LIF intensities determined from the simulated spectra obtained along the centerline of the flame. The dimers profile is an average profile of the dimers profile of pyrene, benzo(a)pyrene and perylene. The soot profile has been obtained with laser induced incandescence (LII). Source: [Mercier et al. \(2019\)](#)

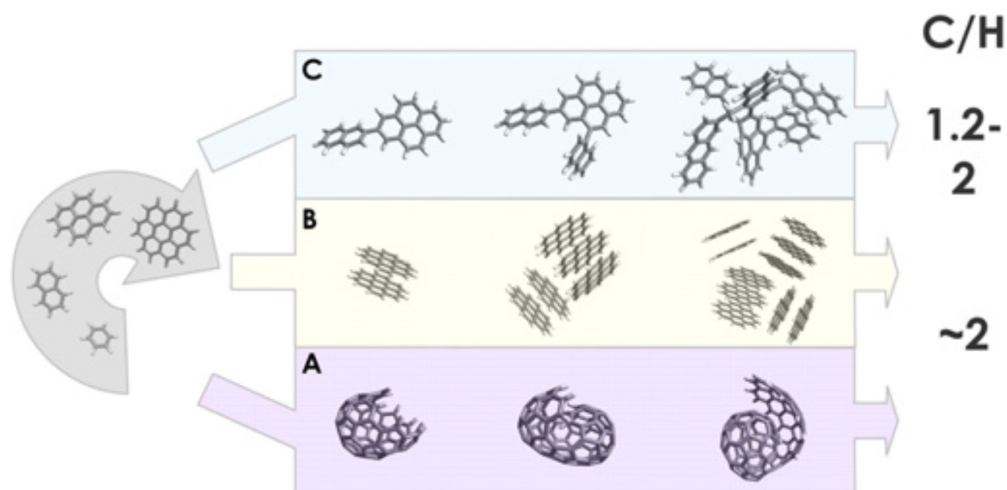


Figure 2.14: Conceptual mechanisms of soot particle nucleation. Source: Wang (2011a)

(MD) simulations can be useful to determine under which conditions and for which compositions one path has more chances to be dominant. MD is a computer simulation method for studying the physical movements of atoms and molecules. Interactions between particles/molecules and their potential energies are calculated using inter-atomic potentials or molecular mechanics force fields. In Mao et al. (2017) an efficient simulation method (ReaxFF MD) is used to investigate soot nucleation and growth from PAHs of different masses at varied temperatures. The authors conclude that three distinctive regimes can be identified for soot formation as a function of temperature and PAH mass (Fig. 2.15):

- Physical nucleation regime: At low temperatures (around 400 K), PAHs of all sizes experience physical nucleation and form incipient particles constituted of stacked clusters with different orientations.
- No nucleation regime: As temperature increases, PAH dimers and trimers are formed but do not grow into incipient soot particles. Large PAH monomers have higher probability to grow into incipient soot particles than small PAHs due to stronger physical interactions.
- Chemical nucleation regime: At 2500 K, PAHs grow to incipient soot particles by the chemical mechanism. PAH monomers are submitted to ring opening with the abstraction of H,  $C_2H_2$  and polyacetylenic chain radicals. For large PAHs like coronene, ovalene and circumcoronene, polyacetylenic chain radicals help to connect them to form soot particles in stacked structures with ‘carbon bridges’ on the edge. Moreover, the dissociated radicals connect with each other and nucleate to form fullerene-like soot particles for all types of PAHs.

This kind of study may help to develop more accurate soot nucleation models by considering temperature and PAH mass together with physical and chemical effects. However, further work is needed to confirm these regimes experimentally. Indeed, several experiments seem to indicate the presence of nucleation from small PAHs at temperatures lower than 2400K and higher than 800K (which would be the “no nucleation regime”) (Sirignano et al., 2017).

In Johansson et al. (2018) a chemical path to soot nucleation, viable at flame temperature was proposed. The idea is that hydrocarbon complexes could be bound covalently and form clusters. These bounds would be promoted by abundant radicals reacting with the hydrocarbon species. The proposed mechanism regenerates radicals and is likely to eject free H atoms as it proceeds. This mechanism, called Clustering of Hydrocarbons by Radical-Chain Reactions (CHRCR) may be a key

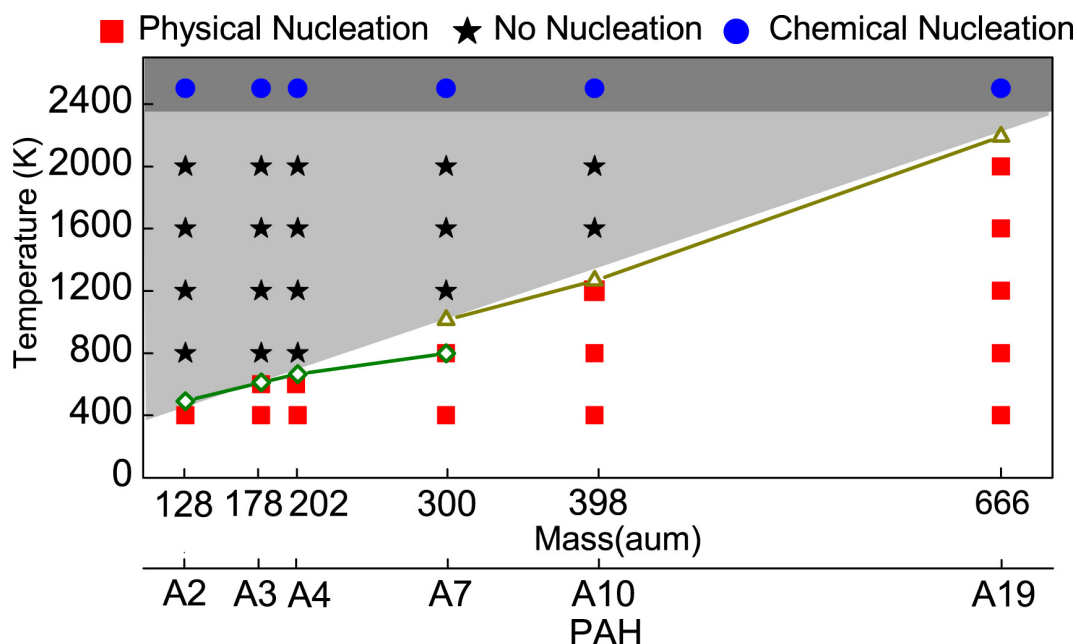


Figure 2.15: Nucleation mechanisms of PAHs in homogeneous systems. The closed red squares, black stars and blue circles represent physical nucleation, no nucleation and chemical nucleation, respectively. The open olive diamonds and tan triangles are from the previous studies on the PAH boiling/sublimation temperatures (White, 1986) and equilibrium temperatures for PAH dimerization (Wang, 2011a), respectively. Soot nucleation mechanisms can be roughly divided into three regions according to PAH masses and temperatures, (i) physical nucleation (white), (ii) no nucleation (light grey) and (iii) chemical nucleation (dark grey). Source: Mao et al. (2017)

theoretical breakthrough as it may explain the aliphatic and aromatic content observed spectroscopically in carbonaceous particles. It also could overcome the issue of insufficient abundances of viable PAHs and of dimers instability at flame temperature as it features clustering of a wide range of hydrocarbon sizes and structures. Figure 2.16 provides an overview of the CHRCR mechanism in three stages:

- (A) The CHRCR mechanism is initiated and propagated by resonantly stabilized radicals sequentially generated through radical-chain reactions involving acetylene or vinyl.
- (B) To form an incipient particle, these RSRs can cluster a wide range of hydrocarbons, including radicals, stable PAHs, and unsaturated aliphatic species, through radical chain reactions fueled by loss and gain of extended conjugation.
- (C) Cyclopentadienyl-type groups are deposited on cluster surfaces and further propagate growth via the CHRCR mechanism.

Even though there is no consensus yet on soot nucleation mechanisms, numerical models have evolved in an attempt to take into account these advances on the theoretical and experimental knowledge.

## 2.2.3 Numerical models for nucleation

### 2.2.3.1 Acetylene based models

In some simplified numerical models, nucleation does not rely on any PAH. Probably one of the most used of these simplified models is the one of Leung et al. (1991). In this model, nucleation

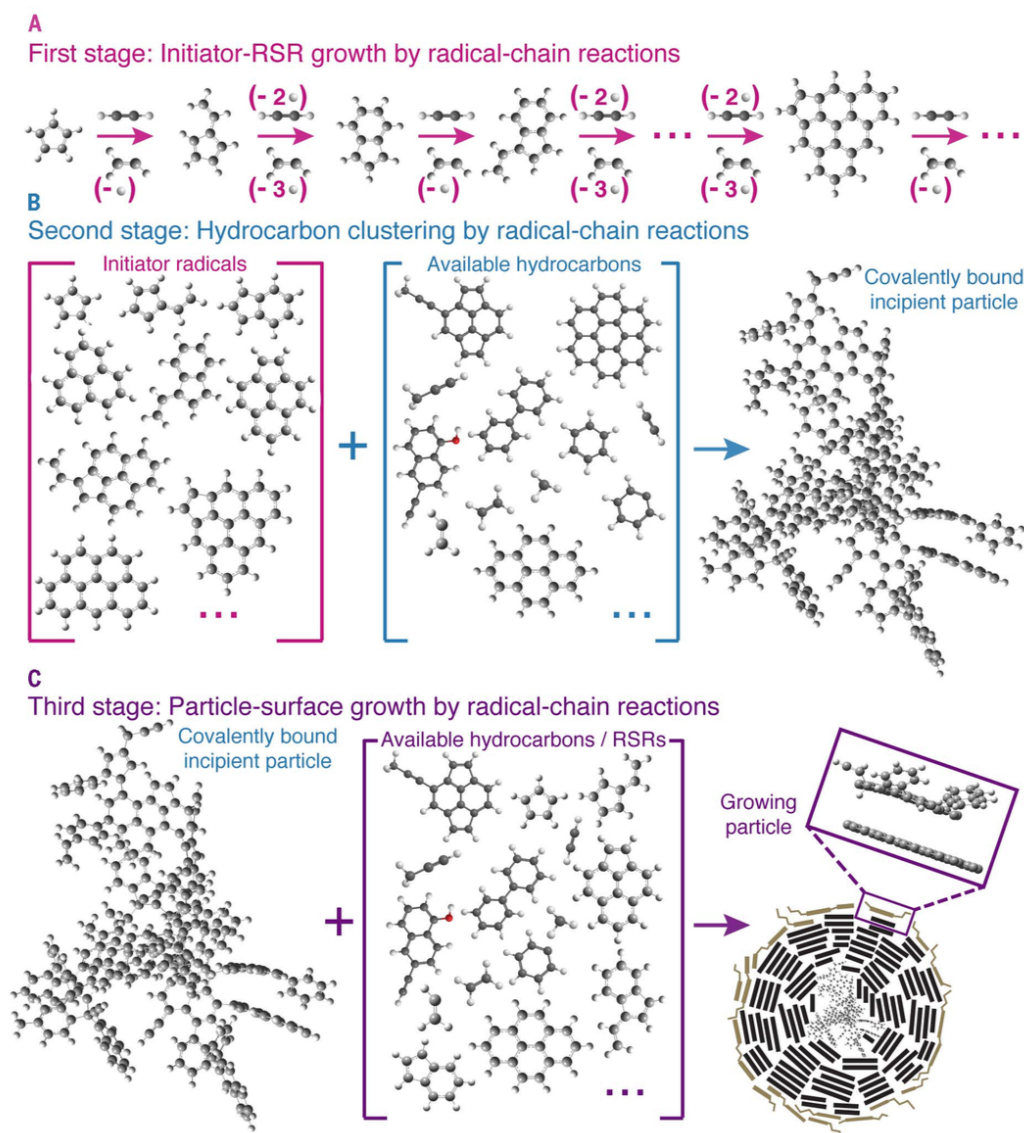


Figure 2.16: Schematic overview of the clustering of hydrocarbons by radical-chain reactions (CHRCR) mechanism. Source: [Johansson et al. \(2018\)](#)

takes place through an irreversible reaction from  $C_2H_2$ :



This has the advantage to enable the use of a light gas phase kinetic mechanism as the PAH growth pathways are bypassed. Also  $C_2H_2$  is usually more abundant and easier to predict than PAH species. Because this model is computationally efficient, it is still used in some cases nowadays for simulations of complex combustion configurations like diesel engines (Bolla et al., 2014). Also, when important computational effort is focused on turbulent combustion modeling,  $C_2H_2$  based nucleation can be used. For example, in Schiener and Lindstedt (2019), a transported probability density function is used and nucleation is modelled as first order in the acetylene concentration via:



With  $A_4$  corresponding to pyrene considered as incipient soot particle.

### 2.2.3.2 Stacked neutral PAH dimers

Even though Acetylene based nucleation is sometimes used, it is now admitted that PAH species play an important role in soot nucleation. Taking this into account, many numerical models for nucleation rely on PAH growth or dimerization. A first category of PAH based nucleation models features stacked neutral dimers. PAH dimers are formed through the collision of neutral PAH molecules held together by van der Waals forces. These dimers, or more generally PAH clusters, are considered as incipient soot particles. In Frenklach and Wang (1991) PAH species grow through the HACA mechanism. They can then collide with each other forming dimers. The dimers are assumed to be solid phase e.g. incipient soot particles (and therefore, bigger PAH clusters as trimers, tetramers are also considered to be incipient soot particles). They can then grow further either through surface reaction or through collision with PAH monomers or clusters. This model for nucleation can be summarized in the following equations:



Representing PAH growth in the gas phase.  $A_l$  represents an aromatic species containing  $l$  rings. Nucleation takes place through:



with  $i \in l, l+1, \dots, \infty$ . Depending on the variants of this models, dimerization can involve different PAH species, dimerization of one specific PAH species (typically pyrene) or dimerization of a lumped PAH species. In Frenklach and Wang (1991) all the  $A_i$ 's can collide with each other and form dimers.

Nucleation reaction is treated as irreversible in Frenklach and Wang (1991). The sticking coefficient  $\gamma$  (also called collision factor) defines the probability for two colliding PAHs to stick together and form a dimer/incipient particle. In Frenklach and Wang (1991)  $\gamma = 1$  meaning that all collisions between PAHs form dimers. At the stage of nucleation, incipient particles are small and the collision dynamics is assumed to be in the free-molecular regime. A size-independent enhancement factor of 2.2, based on the results of Harris and Kennedy (1988) is used in calculations of collision frequencies  $\beta_{A_i}$ . The details of the calculation of collision frequencies are given in sub-section 2.3.5. A nucleation source term  $\dot{H}$  can then be defined, for example considering only collisions between pyrene molecules as in Appel et al. (2000). Pyrene  $C_{16}H_{10}$  is also commonly designed as  $A_4$  (because it is a 4 rings PAH):

$$\dot{H} = \frac{1}{2} \beta_{A_4} N_{A_4} N_{A_4} \quad (2.2.5)$$

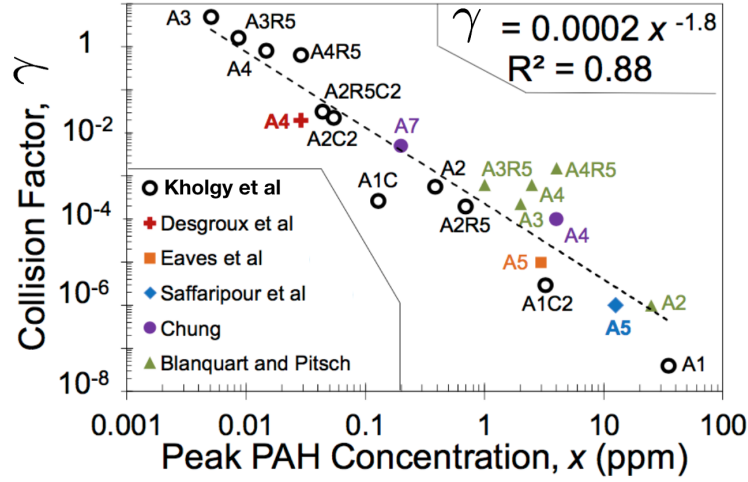


Figure 2.17: Collision factors used for modeling soot nucleation with irreversible nucleation model (IN) vs. peak PAH concentration in different premixed flames. In this figure, *Kholgy et al* refers to [Kholghy et al. \(2018\)](#), *Desgroux et al* refers to [Desgroux et al. \(2017\)](#), *Eaves et al* refers to [Eaves et al. \(2015\)](#), *Saffaripour et al* refers to [Saffaripour et al. \(2014\)](#), *Chung* refers to [Chung \(2011\)](#), *Blanquart and Pitsch* refers to [Blanquart and Pitsch \(2009a\)](#). Adapted from [Kholghy et al. \(2018\)](#)

$N_{A_4}$  being the number of  $A_4$  molecules per  $cm^3$ .  $\dot{H}$  is then a nucleation term expressed in  $[part.cm^{-3}.s^{-1}]$ .

$N_{A_4}$  can be deduced from the molar concentration  $[A_4]$ :

$$N_{A_4} = [A_4].N_A \quad (2.2.6)$$

With  $N_A = 6.024.10^{23} [mol^{-1}]$  the Avogadro number. Similar numerical models where incipient soot particles are dimers or are formed by collision of dimers are still commonly used ([Desgroux et al., 2017](#); [Rodrigues et al., 2018](#); [Blanquart and Pitsch, 2009a](#)).

### 2.2.3.3 Analogy to gas phase reactions: Lumping techniques and nucleation involving PAH radicals

The choice of which PAH molecule should be used for nucleation is not clear. First, the relative importance of small PAHs and big PAHs in nucleation is still subject to controversy. Also, the value of  $\gamma$  is difficult to determine and seems to be adjusted to evolve with the peak PAH concentration in the flames studied ([Kholghy et al., 2018](#)) (see Fig. 2.17). Some models consider dimerization of a single PAH species like pyrene ([Bhatt and Lindstedt, 2009](#); [Dworkin et al., 2011](#)) or an ensemble of PAH species ([Slavinskaya and Frank, 2009](#); [Kholghy et al., 2016](#)). Lumping techniques for PAHs above a certain size have been developed ([Richter et al., 2005](#)). In these PAH models lumped PAH molecules and lumped PAH radicals are used to distinguish dimerization of molecules and dimerization involving radicals. Also, discretization for the H/C-ratio of PAHs was introduced for example in [Saggese et al. \(2015\)](#) (Fig. 2.18).

With the use of lumped PAHs and radicals, nucleation models propose a "chemical" nucleation model as a complement or an alternative to the "physical" nucleation that would result of collisions between neutral molecules or dimers. It is to be noted that the nucleation source term can be expressed in the form of an Arrhenius law (even for the "physical" nucleation). In this case, nucleation is expressed as a chemical reaction with a rate constant  $k$  which is calculated through:

$$k = AT^m e^{\frac{-E_a}{RT}} \quad (2.2.7)$$

BIN <sub>i</sub>	n <sub>c</sub>	Median mass [amu]	Diameter [nm]	H/C		
				A	B	C
PAHs						
i = 1	20	250	0.81	0.8	0.5	0.3
2	40	500	1.02	0.8	0.5	0.3
3	80	1000	1.28	0.75	0.45	0.3
4	160	2000	1.62	0.7	0.4	0.3
Particles						
i = 5	320	4 × 10 <sup>3</sup>	2.04	0.65	0.35	0.2
6	640	8 × 10 <sup>3</sup>	2.57	0.6	0.35	0.15
7	1250	1.55 × 10 <sup>4</sup>	3.21	0.55	0.3	0.1
8	2500	3 × 10 <sup>4</sup>	4.04	0.5	0.25	0.1
9	5000	6 × 10 <sup>4</sup>	5.09	0.45	0.2	0.1
10	1 × 10 <sup>4</sup>	1.2 × 10 <sup>5</sup>	6.40	0.4	0.15	0.1
11	2 × 10 <sup>4</sup>	2.45 × 10 <sup>5</sup>	8.05	0.35	0.1	
12	4 × 10 <sup>4</sup>	4.9 × 10 <sup>5</sup>	10.14	0.35	0.1	
BIN <sub>i</sub>	n <sub>c</sub>	Median mass [amu]	Collision diameter [nm]	H/C		
				N <sub>p</sub>	A	B
Aggregates						
i = 13	8 × 10 <sup>4</sup>	9.7 × 10 <sup>5</sup>	13.27	2	0.3	0.1
14	1.6 × 10 <sup>5</sup>	1.95 × 10 <sup>6</sup>	19.50	4	0.3	0.1
15	3.2 × 10 <sup>5</sup>	3.9 × 10 <sup>6</sup>	28.63	8	0.25	0.1
16	6.4 × 10 <sup>5</sup>	7.8 × 10 <sup>6</sup>	41.98	16	0.2	0.05
17	1.25 × 10 <sup>6</sup>	1.51 × 10 <sup>7</sup>	60.89	32	0.2	0.05
18	2.5 × 10 <sup>6</sup>	3.02 × 10 <sup>7</sup>	89.49	64	0.2	0.05
19	5 × 10 <sup>6</sup>	6.02 × 10 <sup>7</sup>	131.53	128	0.2	0.05
20	1 × 10 <sup>7</sup>	1.21 × 10 <sup>8</sup>	193.32	256	0.2	0.05

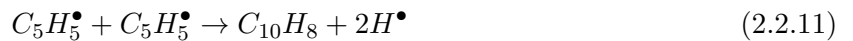
Figure 2.18: Classes of lumped pseudo-species defined as BINs (PAHs, particles, and aggregates) and their properties: median mass, equivalent spherical diameter and H/C ratio for particles; collision diameter and number of primary particles for each aggregate ( $N_p$ ). Source: [Saggese et al. \(2015\)](#)

In general, the units of the rate constant  $k$  in an Arrhenius law depend on the global order of the reaction. If the reaction is first order it has the units  $[s^{-1}]$ . For order two, the rate constant has units  $[mol^{-1}.cm^3.s^{-1}]$  (if concentration is expressed in  $[mol.cm^{-3}]$ ) and for third order reactions it has units  $mol^{-2}.cm^6.s^{-1}$ .  $T$  is the temperature in [K].  $A$  is the pre-exponential factor. Its units also depend on the order of reaction.  $AT^m$  is homogeneous with  $k$  and with a collision frequency.  $m$  is an exponent addressing dependence on temperature (in addition to the  $e^{-\frac{E_a}{RT}}$  term).  $E_a$  is the activation energy for the reaction in  $[J.mol^{-1}]$ , and  $R$  the universal gas constant in  $[J.mol^{-1}K^{-1}]$ .

Using the formalism of Arrhenius law, it is possible to define nucleation reactions by analogy to gas phase reactions. For example, in [Saggese et al. \(2015\)](#) (as shown in Fig. 2.18), heavy PAHs and particle sizes are discretized into 20 classes of pseudo-species with their masses doubled from one class to the next. Each class is represented by lumped pseudo-species called  $BIN_i$ . The transition between gas phase PAHs and soot particles is assumed to be between  $BIN_4$  and  $BIN_5$ . This nucleation step can happen either through, radical-radical reactions (Eq. 2.2.8), radical-molecule reactions (Eq. 2.2.9) or molecule-molecule reactions (Eq. 2.2.10):



With  $(i, n < 5)$ . *products* designs bins of PAHs or soot particles with according stoichiometric coefficients. The kinetic constants of theses reactions are calculated by analogy with reference gaseous reactions. The reference values are then adjusted to take into account the specificity of soot particles and PAH's reactivity depending on criteria like H/C ratio and collision diameter. The three reference reactions used to adjust the Arrhenius constants of Eq. 2.2.8, 2.2.9, 2.2.10 are respectively reactions EQ. 2.2.11, 2.2.12, 2.2.13:



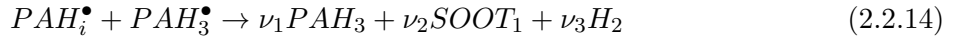
which is the reference for the recombination of two resonantly stabilized radicals.



for radical-molecule nucleation. Finally, molecule-molecule collisions leading to van der Waals interactions correspond to the reference reaction:



Similarly, in Eberle et al. (2017a), lumped pseudo-species are called  $PAH_i$  for the gas phase and  $SOOT_i$  for soot particles. Transition from the gas phase to the solid phase is considered to happen from  $PAH_3$  to  $SOOT_1$ . In this model, PAH molecule (neutral) dimerization was considered to be negligibly slow as compared to reactions involving PAH radicals  $PAH_i^\bullet$ . Therefore, the nucleation reactions are either radical-radical (EQ. 2.2.14) or radical-molecule reactions (EQ. 2.2.15).



With  $\nu_i$  the corresponding stoichiometric coefficients.

### 2.2.3.4 Reversible nucleation

Models taking into account reversibility for soot nucleation and PAH condensation processes have been proposed, for example in Eaves et al. (2015); Veshkini et al. (2016). In these models, reverse rates are introduced and parameters like *gamma* (sticking coefficient also called collision efficiency) are not needed anymore. The reversible nucleation equation is then the following:



In Veshkini et al. (2016) the forward rate of this dimerization reaction is determined by the rate of physical collision of the precursors PAH molecules in the free-molecular regime, similar to the nucleation model based on non-reversible dimerization. The forward rate of dimerization and the forward rate coefficient ( $k_{FWD}$ ) for a dimer composed of  $PAH_j$  and  $PAH_k$  are calculated according to Eqs. 2.2.17 and 2.2.18 respectively:

$$\left( \frac{\partial N_{DIM}}{\partial t} \right)_{FWD} = k_{FWD} [PAH_j] [PAH_k] \quad (2.2.17)$$

With  $N_{DIM}$  the number of dimers per unit of gas volume.

$$k_{FWD} = \frac{2.2}{\rho} \sqrt{\frac{8\pi (N_{C,PAH_j} + N_{C,PAH_k}) k_B T}{C_{mass} N_{C,PAH_j} N_{C,PAH_k}}} (d_{PAH_j} + d_{PAH_k})^2 N_A^2 \quad (2.2.18)$$

where  $k_B$  is the Boltzmann constant,  $C_{mass}$  is the mass of a carbon atom,  $N_{C,PAH_j}$  is the number of carbon atoms in the incipient  $PAH_j$  species,  $d_{PAH_j}$  is the diameter of the incipient  $PAH_j$  species,  $N_A$  is Avogadro's number, and  $[PAH]$  denotes the molar concentration of the incipient PAH species.

Then the reverse rate coefficient  $k_{REV}$  needs to be calculated. It is done through the relationship between the dimerization equilibrium constant  $K_D$  and rate coefficients:

$$\frac{k_{FWD}}{k_{REV}} = K_D (RT)^{\Delta n} \quad (2.2.19)$$

Assuming the dimer is a gaseous species leads to  $\Delta n$  equal to 1.  $K_D$  can be expressed as a function of the Gibbs free energy of dimerization  $\Delta G_D^\circ$

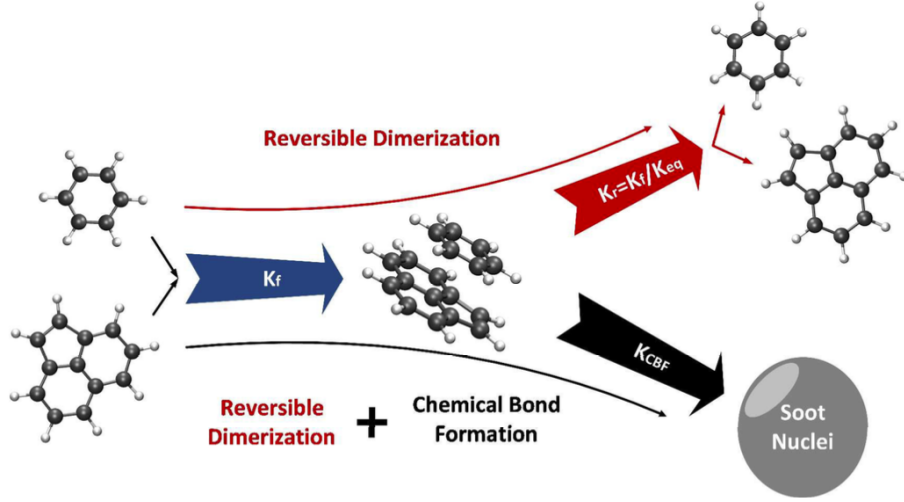


Figure 2.19: Illustration of the reversible nucleation and PAH chemical bond formation (RNCBF) model. Source: [Kholghy et al. \(2018\)](#)

$$K_D = \exp\left(-\frac{\Delta G_D^\circ}{RT}\right) \quad (2.2.20)$$

Then,  $\Delta G_D^\circ$  is estimated utilizing statistical mechanical principles to estimate the change in entropy and enthalpy linked to the dimerization reaction. For further details see [Veshkini et al. \(2016\)](#).

Finally, the reverse source term can be calculated:

$$\left(\frac{\partial N_{DIM}}{\partial t}\right)_{REV} = \frac{k_{FWD}}{RTK_D} [Dim] \quad (2.2.21)$$

Where  $[Dim]$  is the concentration of the dimers.

In [Kholghy et al. \(2018\)](#), it is proposed to use the reversible model of [Eaves et al. \(2015\)](#) and to add a step from dimers to soot particles through chemical bond formation (Fig. 2.19). Other recent contributions feature reversible nucleation and nucleation involving PAH radicals ([Eberle et al., 2017a](#)). Another nucleation submodel, based on a dampening factor was proposed in [Aubagnac-Karkar et al. \(2018\)](#).

## 2.3 Agglomeration

### 2.3.1 Soot quantities

Here some quantities of interest for soot particles are defined. In this thesis,  $N_T$  will be used for the total (meaning all particle sizes) number density of soot particles per unit of gas volume in  $[part.cm^{-3}]$ . (Here *part* is used for denoting particles in units definition. *part* is homogeneous to a number e.g. homogeneous to  $[-]$ ). If we describe soot particles as spheres and with a constant particle density  $\rho_{soot} = 1.8 g.cm^{-3}$ , then a mono-variate description can be used. Each soot particle can be characterized by its volume  $v [cm^3]$  (particle mass or diameter can also be chosen as characteristic size variable). In order to describe the distribution of particles over the range of particle size  $v$ , a number density function  $n(v)$  is defined.  $n(v)$  is the number of particles of characteristic size  $v$  per unit of flow volume and per unit of characteristic size  $[part.cm^{-6}]$ . Finally,  $f_v$  is the soot

volume fraction  $[-]$ . It quantifies the fraction of volume of the studied system which is constituted of soot.  $N_T$  can be calculated from  $n(v)$  integrating over the whole particle size range:

$$N_T = \int_0^\infty n(v)dv \quad (2.3.1)$$

Similarly,  $f_v$  relates to the size distribution through the integration of  $n(v)v$  over the whole particle size range:

$$f_v = \int_0^\infty n(v)v dv \quad (2.3.2)$$

### 2.3.2 Agglomeration and Smoluchowski equation

Agglomeration can be defined by the collision of two soot particles of volumes  $v$  and  $\bar{v}$  to form a new particle of volume  $v + \bar{v}$ . One collision event results in the death of one particle at the level of  $N_T$ . It has no impact of  $f_v$ . It changes the distribution  $n(v)$  towards bigger particles. This change induced by agglomeration on the number density function  $n(v)$  is expressed by the agglomeration source term  $\dot{a}(v)$ . This term can be calculated through the continuous counterpart of Smoluchowski equation (Smoluchowski, 1917):

$$\dot{a}(v) = \frac{1}{2} \int_0^v \beta(v - \bar{v}, \bar{v}) n(v - \bar{v}) n(\bar{v}) d\bar{v} - n(v) \int_0^\infty \beta(v, \bar{v}) n(\bar{v}) d\bar{v} \quad (2.3.3)$$

Where  $\beta(v, \bar{v})$  is the collision frequency between particles of volume  $v$  and  $\bar{v}$ . The calculation of  $\beta(v, \bar{v})$  is described in 2.3.5.

### 2.3.3 Concepts of pure coalescence and pure aggregation

We refer to the terminology of Eberle et al. (2017c) and Fredrick et al. (2010) for the different concepts used to describe agglomeration processes in soot formation:

- Pure aggregation (Fig. 2.20 (a)).
- Pure coalescence (Fig. 2.20 (b)).
- Partial coalescence (Fig. 2.20 (c)).

In the *pure aggregation* regime, two colliding particles stick together without merging. They are linked by a contact point. After the collision of several particles, aggregates are formed (Fig. 2.20 (a)). In a *pure coalescence* regime, the two colliding particles merge totally to form a new bigger spherical particle (Fig. 2.20 (b)). In reality, soot particles agglomeration is somewhere between these two asymptotic regimes. An intermediate regime is defined as *partial coalescence* (Fig. 2.20 (c)). When an aggregate or spherical particle collides with another particle, the changes induced on its geometrical variables vary depending on the collision model. In the case of pure aggregation between spherules of the same size,  $n_p$  increases while  $d_p$  stays constant. On the other hand, in the case of pure coalescence,  $n_p$  stays constant (equal to one) and  $d_p$  increases. In Eberle et al. (2017c) an aggregation factor  $\chi_{agg}$  is defined to quantify how close to pure aggregation or pure coalescence the model is. The range of particle size is discretized into  $M$  sections. In each section, a representative aggregate geometry is considered with a fixed set of geometric characteristics in each section  $i$ :  $v_i$ ,  $d_{p,i}$ ,  $n_{p,i}$ . The discretization is defined by a constant factor  $F_s = v_{i+1}/v_i$ . Then  $\chi_{agg} = n_{p,i+1}/n_{p,i}$  and  $\chi_{agg} \in [1, F_s]$ . If  $\chi_{agg} = 1$  pure coalescence is modeled and if  $\chi_{agg} = F_s$  pure aggregation is modeled. Depending on the flame studied  $\chi_{agg}$  needs to be carefully validated. In Eberle et al. (2017c)  $\chi_{agg} = 1.5$  is used as this value is found to lead to very good predictions

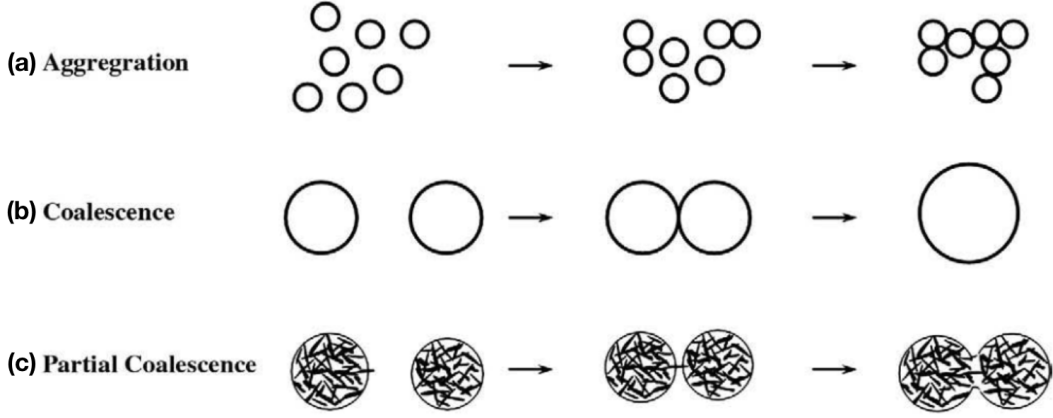


Figure 2.20: Schematic representation of agglomeration conceptual descriptions. Source: [Fredrick et al. \(2010\)](#)

of soot morphology in a series of laminar diffusion flames. Additionally, a critical diameter  $d_{crit}$  is considered, below which pure coalescence is modeled. In [Eberle et al. \(2017c\)](#) the value of  $d_{crit} = 14$  nm is chosen, in line with the literature values in the range of 10 nm to 40 nm ([Saggese et al., 2015](#); [Kazakov and Frenklach, 1998](#); [Bhatt and Lindstedt, 2009](#); [Smooke et al., 2005](#)). Once a value of  $\chi_{agg}$  is chosen, all the  $n_{p,i}$  are known  $\forall i$ .  $d_{p,i}$  can be deduced using:

$$d_{p,i} = \left( \frac{6v_i}{\pi n_{p,i}} \right)^{\frac{1}{3}} \quad (2.3.4)$$

and the aggregate geometry is defined as a function of  $v_i$ .

### 2.3.4 Collision diameter

In order to calculate the collision frequency  $\beta(v, \bar{v})$  between two particles, the collision diameter  $d_c$  corresponding to an aggregate of volume  $v$  must be estimated. When soot particles are considered as spheres,  $d_c$  is equal to the equivalent sphere diameter  $d_c = d_{ev} = (6v/\pi)^{1/3}$ . When soot particles are considered as fractal aggregates, it is usually assumed ([Eberle et al., 2017c](#)) that the collision diameter  $d_c(v)$  is the diameter of the aggregate's circumscribed sphere. Then  $d_c$  can be estimated using the relation of [Koeylue et al. \(1995\)](#):

$$d_c = \sqrt{\frac{D_f + 2}{D_f}} d_g \quad (2.3.5)$$

and  $d_g$  can be deduced from the fractal law (Eq. 1.2.1).

$$d_g = d_p \cdot \left( \frac{n_p}{k_f} \right)^{\frac{1}{D_f}} \quad (2.3.6)$$

$D_f$  and  $k_f$  are usually assumed constant for a given type of flame. The estimation of  $d_p$  and  $n_p$  depends on the model used. In ([Eberle et al., 2017c](#)) as described in subsection 2.3.3  $d_{p,i}$  and  $n_{p,i}$  are directly known for each section discretizing the range of  $v$ . Alternatively, in some multi-variate models, multiple variables are directly solved for. In particular, Monte Carlo methods are convenient for solving several independent variables and not only  $v$  as the space of particle size does not need to be discretized. For example, in [Patterson \(2007\)](#) particle mass and surface area are considered

as independent variables. In [Park and Rogak \(2004\)](#) the authors propose a discretized (sectional) method where the number density of particles (aggregates) and the number density of primary spherules are solved for separately in each section.  $n_{p,i}$  can then be deduced and subsequently  $d_{p,i}$  is deduced from  $v$  and  $n_{p,i}$  through Eq. (2.3.4).

### 2.3.5 Collision frequency

Once the expression of  $d_c(v)$  is known, the collision frequency  $\beta(v, \bar{v})$  between a particle of size  $v$  and a particle of size  $\bar{v}$  can be calculated.  $\beta(v, \bar{v})$  depends on the value of the Knudsen number of the considered particles. The Knudsen number  $Kn$  is defined for a particle of size  $v$  as follows:

$$Kn = \frac{2\lambda}{d_c(v)} \quad (2.3.7)$$

Where  $\lambda$  is the gas mean free path.  $\lambda$  is calculated through:

$$\lambda = \frac{RT}{\pi\sqrt{2}d_{gas}^2N_AP} \quad (2.3.8)$$

where  $R$  is the ideal gas constant and  $d_{gas}$  the diameter of a gas particle, considered constant and equal to 0.2 nm as in [Rodrigues \(2018\)](#).

Once  $Kn$  is determined, three collisional regimes can be identified as classified by [Kazakov and Frenklach \(1998\)](#):

- *Free molecular regime* for  $Kn > 10$ . This regime corresponds to a relatively low pressure and/or relatively small particles.
- *Continuum regime* for  $Kn < 0.1$ . This regime corresponds to relatively high pressure and/or relatively large particles.
- *Intermediate regime* for  $0.1 < Kn < 10$ .

In the free molecular regime  $\beta(v, \bar{v})$  is expressed as:

$$\beta_{v,\bar{v}} = \beta_{v,\bar{v}}^{fm} = \epsilon_n \sqrt{\frac{\pi k_B T}{2m_{v,\bar{v}}}} (d_c(v) + d_c(\bar{v}))^2 \quad (2.3.9)$$

Where  $\epsilon_n$  is the Van der Waals enhancement factor taken equal to 2.2 ([Blanquart and Pitsch, 2009b](#)) and  $m_{v,\bar{v}}$  is the reduced mass as in [Blanquart and Pitsch \(2009b\)](#) expressed as:

$$m_{v,\bar{v}} = \rho_{soot} \frac{v\bar{v}}{v + \bar{v}} \quad (2.3.10)$$

In the continuum regime  $\beta(v, \bar{v})$  is expressed as:

$$\beta(v, \bar{v}) = \beta(v, \bar{v})^c = \frac{2k_B T}{3\mu} (d_c(v) + d_c(\bar{v})) \left( \frac{Cu(v)}{d_c(v)} + \frac{Cu(\bar{v})}{d_c(\bar{v})} \right) \quad (2.3.11)$$

where  $\mu$  is the dynamic gas viscosity:

$$\mu = \frac{C_1 T^{\frac{3}{2}}}{T + C_2} \quad (2.3.12)$$

$Cu(v)$  is the corrective Cunningham coefficient for a particle of size  $v$ :

$$Cu(v) = 1 + 1.257Kn(v) \quad (2.3.13)$$

with  $C_1 = 1.4558 \cdot 10^{-6} [kg.m^{-1}.s^{-1}.K^{-\frac{1}{2}}]$  and  $C_2 = 110.4[K]$

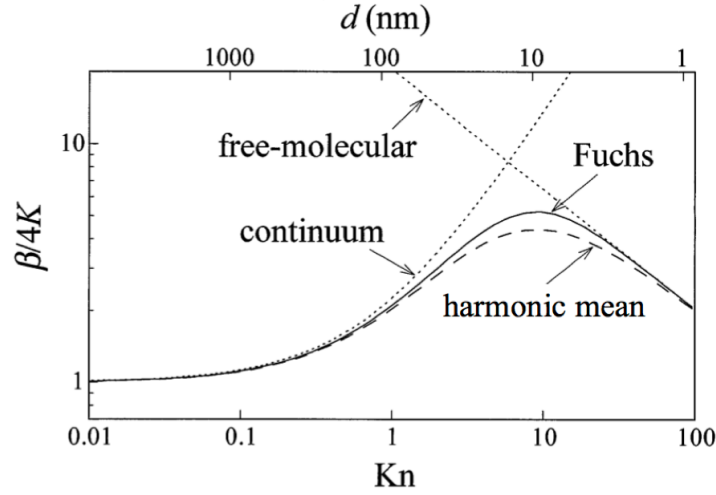


Figure 2.21: Collision frequency  $\beta(v, \bar{v})$  as a function of  $Kn$  calculated with different analytical expressions at a pressure of 10 bar and a temperature of 1800 K. In the plotted quantity  $\beta/4K$ ,  $K = 2k_B T/3\mu$ . Source: [Kazakov and Frenklach \(1998\)](#)

In the intermediate regime  $\beta(v, \bar{v})$  is calculated through the harmonic mean of  $\beta(v, \bar{v})^{fm}$  and  $\beta(v, \bar{v})^c$ :

$$\beta(v, \bar{v}) = \beta(v, \bar{v})^{int} = \frac{\beta(v, \bar{v})^{fm} \beta(v, \bar{v})^c}{\beta(v, \bar{v})^{fm} + \beta(v, \bar{v})^c} \quad (2.3.14)$$

Alternatively, The collision frequency in the intermediate regime  $\beta(v, \bar{v})^{int}$  can be expressed by the semi-empirical formula of [Fuchs \(1964\)](#). Fig. 2.21 illustrates the variation of  $\beta(v, \bar{v})$  with  $Kn$  for the different expressions of  $\beta(v, \bar{v})$ .

## 2.4 Surface growth/loss and condensation

Soot particles interact with gaseous species through three main processes:

- Carbon addition surface reactions:  $C_2H_2$  molecules or Resonantly Stabilized Radicals react at the surface of a soot particle and increase its number of carbon atoms (and size). This process is believed to be similar to the processes of PAH growth (HACA mechanism, RSRs recombination).
- Particle oxidation: Oxidant species react at the surface of a soot particle and decrease its number of carbon atoms (and size).
- PAH condensation: A gaseous PAH molecule collides with a solid soot particle which increases its number of carbon atoms (and size). This process is similar to agglomeration except it features a gas molecule - solid particle collision instead of a collision between two solid particles.

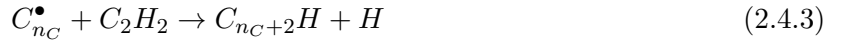
Formally, all these processes only increase or decrease particle size but have no impact on particle number (unless particle "death" by oxidation is considered). Therefore  $N_T$  and  $n_p$  are not influenced by surface growth/loss and condensation while  $f_v$  and  $d_p$  increase with carbon addition and PAH condensation and decrease with oxidation.

## 2.4.1 Carbon addition surface reactions

Some of the main models proposed for carbon addition surface reactions are described below.

### 2.4.1.1 HACA mechanism

The HACA mechanism was already introduced in section 2.1 as it is used for PAH growth reactions. In their study, [Frenklach and Wang \(1991\)](#) proposed to use the HACA mechanism for soot surface growth by similarity to gaseous PAH surface growth. The reactions of the HACA mechanism corresponding to surface growth are the following:



with  $C_{n_C}H$  representing a soot particle with  $n_C$  carbon atoms and  $C_{n_C}^\bullet$  the corresponding radical. Reaction 2.4.1 represents the hydrogen atom abstraction from  $C_{n_C}H$  which results in the appearance of  $C_{n_C}^\bullet$ . Reaction 2.4.2 is the associated deactivation reaction. Just like in the case of gaseous PAH growth, the key species for soot surface growth in the HACA mechanism is acetylene ( $C_2H_2$ ). Acetylene reacts with a radical  $C_{n_C}^\bullet$  at soot surface through reaction 2.4.3 which increases particle's size. In [Wang et al. \(1996\)](#) two reactions were added:



Where reaction 2.4.4 is another surface activation reaction by  $OH$  instead of  $H$  and reaction 2.4.5 is similar to 2.4.3 except the radical site on the soot particle surface is preserved after the reaction. The HACA soot oxidation reactions are presented in section 2.4.2. Modified versions of the HACA mechanism have been proposed, for example the Hydrogen-Abstraction/Carbon-Addition Ring-Closure (HACA-RC) mechanism from [Mauss et al. \(1994\)](#).

### 2.4.1.2 Resonantly Stabilized Radicals addition

As explained in section 2.1, different pathways have been proposed as an alternative to the HACA mechanism for PAH growth. These can be used for soot surface growth as well. In particular, growth mechanisms involving RSRs have been proposed. For example, in [Saggese et al. \(2015\)](#), small resonantly stabilized radicals contribute to soot growth through addition reactions (in addition to the HACA Mechanism). These RSRs (denoted  $RR^\bullet$  in the following equations) can react with lumped bins  $BIN_i$  corresponding to lumped PAHs or soot particles via:



again, as for nucleation, kinetic constants are calculated by analogy to gaseous reactions and then adjusted to account for soot particle size, morphology and H/C ratio. The reference reactions for surface growth involve propargyl radicals  $C_3H_3^\bullet$ :





## 2.4.2 Oxidation

The oxidation reactions of the HACA mechanism proposed in [Frenklach and Wang \(1991\)](#) are the following:



Where the products can be explicitly described as in [Mauss et al. \(1994\)](#):



Usual models consider oxidation rates to be proportional to soot surface. Also, as stated earlier, most models consider that oxidation decreases  $d_p$  and  $f_v$  but has no impact on  $n_p$  and  $N_T$ . Reality may be more complex. In [Yon et al. \(2018\)](#), *in-situ* characterization of soot particles oxidation was carried out by coupling three different techniques (Small Angle X-ray Scattering, Static Light Scattering and Laser Induced Incandescence). In order to isolate the oxidation phenomenon, soot was generated upstream by a miniCAST generator and injected into a non-sooting flame. The main conclusions of this work were the following:

- As expected,  $D_{p,geo}$  (which is  $d_p$  distribution's modal or peak value) decreases through oxidation. (Fig. 2.22 top-left).
- Oxidation results in an increase of the geometric standard deviation of the primary sphere diameter. (Fig. 2.22 bottom-left)
  - The previous observation could be explained by a transition from a volume (diffusion) to a surface (reaction) oxidation process.
  - This transition could be explained by a transition from an oxidation process by  $O_2$  at smaller heights above burner (HAB) to an oxidation process by  $OH$  at higher HAB which is consistent with these species concentration variations in flat flame burners. Mature soot graphitization could be a cause of the decrease of  $O_2$  volume oxidation for higher HAB.
- At lower HAB  $n_p$  increases (Fig. 2.22 top-right) and  $N_T$  decreases (Fig. 2.22 bottom-right) because of aggregation.
- At higher HAB  $n_p$  decreases (Fig. 2.22 top-right) and  $N_T$  increases (Fig. 2.22 bottom-right) indicating that a fragmentation process is dominating over aggregation. This fragmentation process would be caused by oxidation.

Soot oxidation is a complex phenomenon which may involve surface and volume oxidation, fragmentation and variable oxidation rates depending on soot maturity and graphitization. Taking all these aspects into account in numerical simulations may bring improvements in the accuracy of the models. However, due to the complexity of all processes involved in soot formation, growth and oxidation, some simplifications are often made and most current numerical models don't consider

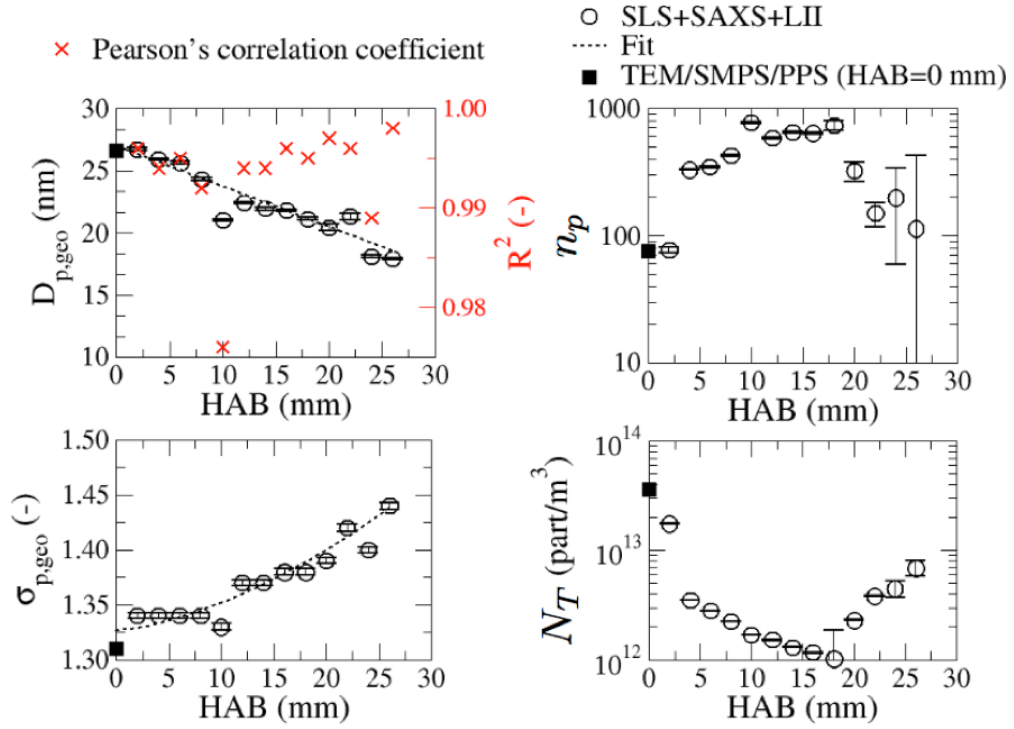


Figure 2.22: Result of the SLS/SAXS/LII data inversion. Reported values at Height Above Burner (HAB) = 0 mm correspond to the values determined on fresh soot by non-optical methods (TEM/SMPS/PPS-TEOM). On the top-left plot the modal diameter of primary particles is represented. On the bottom-left plot the geometric standard deviation of the primary sphere diameter is represented. Source: [Yon et al. \(2018\)](#)

soot fragmentation and only consider surface oxidation (and not volume oxidation) (Desgroux et al., 2017; Rodrigues et al., 2018; Eberle et al., 2017a). This is also the case of the present work. When making the assumption that soot growth and oxidation reactions happen at the surface of soot particles, the concentration in active sites and radical sites at soot surface needs to be calculated to determine growth and oxidation source terms. This calculation is described hereafter.

### 2.4.3 Active sites

In Frenklach and Wang (1991) the rate expression for the reactions of the HACA mechanism was assumed to take the following form

$$\dot{x}_g = k_{g,s} C_g \alpha \chi s_i N_i \quad (2.4.14)$$

where  $k_{g,s}$  is the per-site rate coefficient,  $C_g$  is the concentration of the reacting gaseous species  $g$  such as  $C_2H_2$  in reaction 2.4.3,  $\alpha$  is the fraction of surface sites available for a given reaction,  $\chi$  is the number density of surface sites (i.e., number of sites per unit area),  $s_i$  is the surface area per particle of size  $i$ , and  $N_i$  is the number density of particles of size  $i$ . The exact definition of  $N_i$  depends on the statistical model adopted for the Particle Size Distribution. More details on statistical descriptions of Particle Size Distributions will be given in chapter 3. For example, in a sectional model,  $N_i$  is the particle number density in the  $i$ -th section of size.  $\chi_{C_{n_C}H}$  The number density of  $C_{n_C}H$  sites per soot surface area is assumed to be constant equal to  $2.3 \cdot 10^{15} \text{ sites.cm}^{-2}$ .  $\chi_{C_{n_C}^\bullet}$  The number density of radical sites  $C_{n_C}^\bullet$  per soot surface area can then be determined assuming steady state for  $\chi_{C_{n_C}^\bullet}$ .  $s_i$  is generally calculated depending on particle size (for example particle volume  $v_i$ ) and on the description of aggregates morphology (sphere, fractal law...).

Many recent works rely on this approach or very similar variants (Desgroux et al., 2017; Rodrigues et al., 2018). The  $\alpha$  parameter is still subject to uncertainty and may vary from one study to the other. In Appel et al. (2000) a dependence on temperature and soot particle size is introduced for the  $\alpha$  parameter. This dependence of  $\alpha$  on particle size expresses the fact that mature particles have a lower proportion of active sites per unit of surface.

In other works like Blanquart and Pitsch (2009b) multi-variate models are used to solve for soot particle surface and number of hydrogenated (or active) sites as independent variables in addition to particle volume. In this case, the assumed constants  $\chi_{C_{n_C}H}$  and  $\alpha$  are not needed. In another alternative model, Singh et al. (2006) introduced an equation for the number of active sites per surface area. This relaxation equation features a starting surface reactivity of  $\chi_0 = 2.3 \cdot 10^{19} \text{ m}^{-2}$  in the nucleation zone and decreases with residence time towards an asymptotic value of  $\chi^\infty = 4.6 \cdot 10^{18} \text{ m}^{-2}$ .

### 2.4.4 PAH Condensation

Condensation is the process involving a collision between a gaseous PAH species and a solid soot particle. Conceptually, it is considered that condensation increases particle volume without agglomerating new primary spherules. In other words,  $n_p$  and  $N_T$  stay constant while  $d_p$  and  $f_v$  increase through condensation.

The total rate of molecules of a PAH species  $PAH_g$  condensing on soot particles of all sizes can be expressed as:

$$\dot{H}_{cond_T} = N_{PAH_g} \int_0^\infty \beta(v_{PAH_g}, v) n(v) dv \quad (2.4.15)$$

with  $N_{PAH_g} = [PAH_g] N_A$  and  $\beta(v_{PAH_g}, v)$  calculated as in section 2.3.5. More details on statistical descriptions of Particle Size Distributions will be given in chapter 3 but let us consider the example of a sectional method with a discretization of particle volume  $v$  into  $M$  intervals  $I_{v_i}$

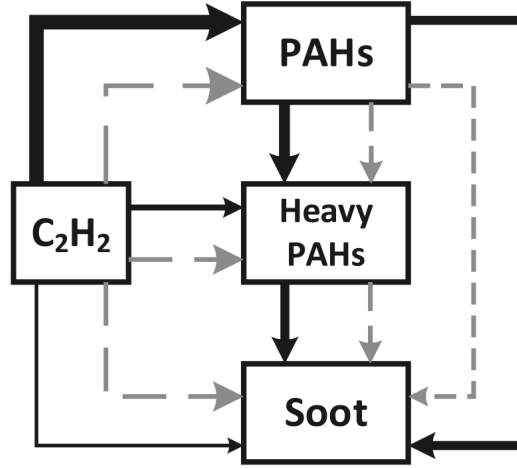


Figure 2.23: Relative contributions of HACA mechanism and PAH condensation reactions to the growth of soot particles at low (dashed lines) and atmospheric pressure (solid lines). The thickness of the arrows represents the importance of the different paths. Source: [Pejpichestakul et al. \(2019\)](#)

also called sections. Each section has a representative volume  $v_i$ . Then the rate of molecules of  $PAH_g$  condensing on soot particles contained in  $I_{v_i}$  can be expressed as

$$\dot{H}_{cond_i} = \beta(v_{PAH_g}, v_i) N_{PAH_g} N_i \quad (2.4.16)$$

with  $N_i = \int_{I_{v_i}} n(v) dv$  and  $v_{PAH_g}$  the volume of one  $PAH_g$  molecule. Note that the assumption that  $\beta(v_{PAH_g}, v) = \beta(v_{PAH_g}, v_i)$  is constant over  $I_{v_i}$  has been made. Then an equivalent growth source term  $G_{cond}(v_{PAH_g}, v_i)$  for the soot particles contained in  $I_{v_i}$  due to condensation of species  $PAH_g$  can be expressed as:

$$G_{cond}(v_{PAH_g}, v_i) = \frac{m_{PAH_g} \dot{H}_{cond_i}}{\rho_{soot} N_i} \quad (2.4.17)$$

with  $m_{PAH_g}$  the mass of one  $PAH_g$  molecule.  $G_{cond}(v_{PAH_g}, v_i)$  expresses a rate of volume increase per soot particle contained in  $I_{v_i}$ . Therefore, condensation can be treated as a growth source term in the same way as surface growth reactions like acetylene addition. Note that the assumption of constant density  $\rho_{soot}$  for soot particles has been made.

The condensation process is usually considered irreversible ([Desgroux et al., 2017](#); [Rodrigues et al., 2018](#)) but can also be modeled as reversible ([Veshkini et al., 2016](#); [Aubagnac-Karkar et al., 2018](#)).

The relative importance of condensation and acetylene addition depends on the models used and on the flame conditions, in particular pressure. In ([Pejpichestakul et al., 2019](#)) a series of premixed flames were simulated and the relative contribution of both phenomena was looked at. Their results can be seen in Fig. 2.23. In their simulations Acetylene is primarily involved in the HACA mechanism with PAH growth. Mainly in very rich flames at high pressure, condensation of benzene and heavy PAHs are important. However, at lower pressure acetylene addition dominates over PAH condensation which heavily depends on pressure ([Mebel et al., 2017](#)). This is in agreement with previous experimental observations (in diffusion flames) ([Guo et al., 2013](#)).

## Chapter 3

# Numerical approaches to solve the Population Balance Equation

### Contents

---

<b>3.1</b>	<b>Context of polydispersed particles and definitions</b>	<b>47</b>
<b>3.2</b>	<b>The Population Balance Equation</b>	<b>49</b>
3.2.1	Homogeneous PBE	49
3.2.2	PBE in laminar flows	50
<b>3.3</b>	<b>Monodisperse assumption based models</b>	<b>51</b>
<b>3.4</b>	<b>Methods of Moments</b>	<b>54</b>
3.4.1	Principle	54
3.4.2	QBMM	54
3.4.2.1	QMOM	54
3.4.2.2	DQMOM	55
3.4.2.3	EQMOM	56
3.4.2.4	CQMOM	57
3.4.3	MOMIC	57
<b>3.5</b>	<b>Sectional methods</b>	<b>58</b>
3.5.1	Discretization schemes for agglomeration	59
3.5.1.1	Pointwise approximation methods	59
3.5.1.2	Finite Element/Volume Methods (FEM/FVM)	60
3.5.1.3	The SPAMM approach	61
3.5.2	Discretization schemes for growth	62
3.5.2.1	First order upwind finite difference	62
3.5.2.2	High resolution schemes	62
3.5.2.3	High resolution scheme from Park and Rogak (2004)	64
3.5.2.4	Moving and adaptive grid methods	66
<b>3.6</b>	<b>Monte Carlo methods</b>	<b>66</b>
3.6.1	DSMC	66
3.6.2	Constant-volume or constant-number	68
3.6.3	Time-driven or event-driven	69
3.6.4	Strategies for more efficient algorithms	71
<b>3.7</b>	<b>Comparative advantages and drawbacks</b>	<b>72</b>

---

In this chapter, the concepts of polydispersed particles and Population Balance Equation are first explained. Then, the main classes of numerical methods for its resolution are presented. Advantages and drawbacks of each class of methods are listed. The positioning and strategy of the HYPE method are introduced.

### 3.1 Context of polydispersed particles and definitions

As stated in the introductory chapter, there is great interest in describing and predicting soot Particle Size Distribution. Soot PSDs feature large ranges of particle size even very locally in physical space. They can therefore be referred to as polydispersed particles. This wider term refers to any population of particles, droplets or bubbles, characterized by one variable (usually linked to their size like volume, mass, diameter...) which features a range of values. The concept of polydispersed particles is at the opposite of a monodisperse phase featuring only one size (at one point in space and time). The resolution of the evolution of polydispersed particles distributions is of interest in several fields like soot formation but also nanomaterial synthesis, crystallisation and precipitation, cloud formation...

One could think, as a straightforward approach, to simulate individually one computational particle for each real particle and to follow the evolution of particles properties like size and to solve for the motion in physical space in a Lagrangian way. However, this approach is only feasible in very specific applications with small populations of particles. Indeed in most applications the number of particles is very high (up to  $10^{10}$  -  $10^{11}$  soot particles per  $cm^3$  in a rich premixed flame for example). Simulation of individual particles is then computationally intractable. Some statistical treatment of the polydispersed particles is required. These can be described by several properties, especially when complex geometries are modeled. For now, we will consider a mono-variate model describing each particle by its volume  $v$ . Then, a statistical description of the distribution can be done via particle number density  $n$ .  $n$  describes how many particles of a given volume  $v$  are present at a given location  $\underline{x}$  in physical space (and at a given time  $t$ ). Formally, if we integrate  $n(v, \underline{x}, t)$  over a particle size interval  $I_{v_i}$  and over a volume of gas  $V$  in physical space we get the number of particles contained in  $V$  of size  $v \in I_{v_i}$ . If  $n(v, \underline{x}, t)$  is integrated only over  $I_{v_i}$ , the number of particles of size  $v \in I_{v_i}$  per unit of gas volume at location  $\underline{x}$  and time  $t$  is obtained:

$$N_i(\underline{x}, t) = \int_{I_{v_i}} n(v, \underline{x}, t) dv \quad (3.1.1)$$

with  $N_i$  in  $[part.m^{-3}]$  and  $n(v, \underline{x}, t)$  in  $[part.m^{-6}]$ . Moments of the distribution can be defined integrating over  $v$ . For example, the zeroth moment of the distribution  $m_0$ , also called  $N_T$  in this thesis, denotes the total number of particles per unit of gas volume:

$$m_0(\underline{x}, t) = N_T(\underline{x}, t) = \int_0^\infty n(v, \underline{x}, t) dv \quad (3.1.2)$$

with  $N_T(\underline{x}, t)$  in  $[part.m^{-3}]$  The first moment  $m_1$ , also called  $f_v$  in this thesis, denotes the total volume of particulate matter per unit of gas volume (more precisely per unit of the system volume composed of the containing gas and particulate matter):

$$m_1(\underline{x}, t) = f_v(\underline{x}, t) = \int_0^\infty vn(v, \underline{x}, t) dv \quad (3.1.3)$$

with  $f_v(\underline{x}, t)$  in  $[-]$ . In this thesis, the term Particle Size Distribution (PSD) will refer to  $n$  (unless stated otherwise. In some test cases, PSD refers to  $n(v)v$ ). If one fixes location in physical space (and time), then number density only depends on particle volume. Figures 3.1 and 3.2 illustrate the concepts explained above.

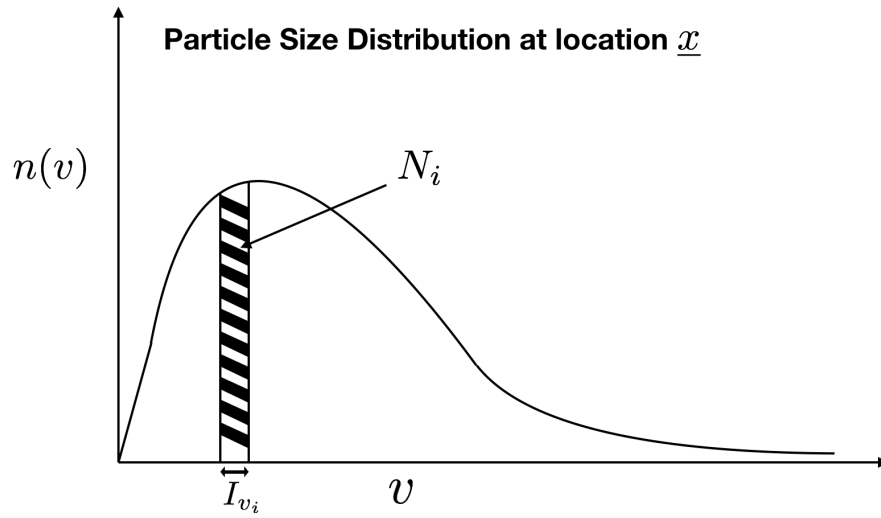


Figure 3.1: Schematic representation of number density  $n(v)$  (at a given location  $\underline{x}$ ).

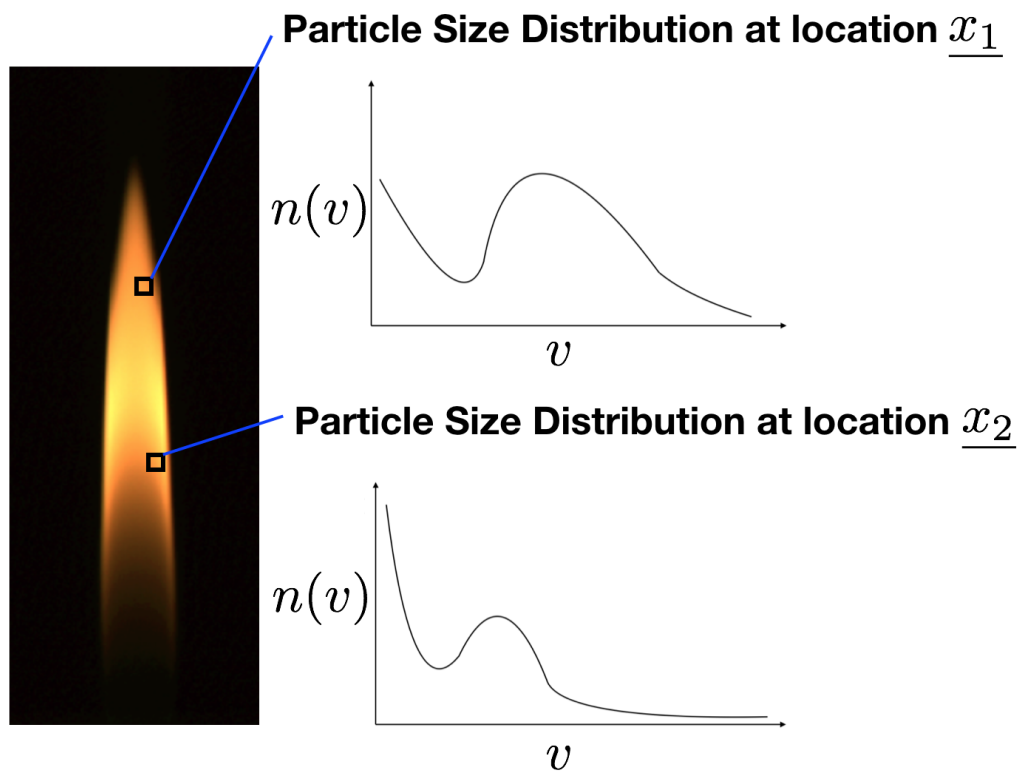


Figure 3.2: Schematic representation of number density  $n(v)$  at two different locations  $\underline{x}_1$  and  $\underline{x}_2$  in a diffusion flame.

## 3.2 The Population Balance Equation

### 3.2.1 Homogeneous PBE

The objective of the Population Balance Equation is to solve for the evolution of  $n(v, \underline{x}, t)$ . Let us begin with the example of a spatially homogeneous, stirred reactor where particles are only submitted to growth and not to nucleation, agglomeration or transport in physical space. Then, the Population Balance Equation (PBE) can be written as a continuity equation in the space of particle size (volume  $v$ ):

$$\frac{\partial n(v, t)}{\partial t} + \frac{\partial (G(v, t)n(v, t))}{\partial v} = 0 \quad (3.2.1)$$

with  $G(v, t)$  the particle growth rate. Eq (3.2.1) accounts for convection in the space of particle size (particle growth). Dependence on  $\underline{x}$  does not appear here because we are considering the case of a spatially homogeneous, stirred reactor. Of course,  $G(v, t)$  can be negative and then correspond to a loss rate. In the case of soot particles,  $G(v, t)$  can be calculated as described in section 2.4. It depends on particle volume  $v$  and on gas phase composition (implicitly shown by the dependence on time  $t$ ).

Depending on applications, a term for particle formation can be necessary. In the case of soot particles, this is the nucleation term  $\dot{h}(v, t)$ . For soot particles,  $\dot{h}(v, t)$  is non-zero only at very small sizes, (often modeled as  $> 0$  only at the smallest size considered solid).  $\dot{h}(v, t)$  can be calculated as described in section 2.2. The PBE with growth and nucleation in a spatially homogeneous, stirred reactor becomes:

$$\frac{\partial n(v, t)}{\partial t} + \frac{\partial (G(v, t)n(v, t))}{\partial v} = \dot{h}(v, t) \quad (3.2.2)$$

To account for particle collisions, an agglomeration source term  $\dot{a}(v, t)$  must be added to the PBE:

$$\frac{\partial n(v, t)}{\partial t} + \frac{\partial (G(v, t)n(v, t))}{\partial v} = \dot{h}(v, t) + \dot{a}(v, t) \quad (3.2.3)$$

with  $\dot{a}(v, t)$  following the continuous counterpart of Smoluchowski equation (Smoluchowski, 1917) (as already explained in section 2.3.2):

$$\dot{a}(v, t) = \frac{1}{2} \int_0^v \beta(v - \bar{v}, \bar{v}) n(v - \bar{v}, t) n(\bar{v}, t) d\bar{v} - n(v, t) \int_0^\infty \beta(v, \bar{v}) n(\bar{v}, t) d\bar{v} \quad (3.2.4)$$

The calculation of  $\beta(v, \bar{v})$  is described in 2.3.5. Equation (3.2.3), which represents the case of a homogeneous system, is an integro-partial differential equation which makes its direct numerical resolution difficult (as opposed to a set of Ordinary Differential Equations for example). Moreover, nucleation and growth rates require coupling with gas phase source terms and their response can be stiff. Except some specific canonical cases, analytical solutions are not achievable. Up to now, no universal numerical method has emerged as best suited for all applications. Many numerical methods have been proposed for the solution of the homogeneous PBE with nucleation, growth and agglomeration (Eq. 3.2.3), each with its advantages and drawbacks. Comprehensive reviews on this topic are available, for example in Ramkrishna (2000). In the following sections, a short, non-exhaustive review will be made on these methods in order to better clarify the objectives of the new presented method. It is important to note that this chapter focuses on the homogeneous PBE (with no transport in physical space) as it is a prerequisite to understand the challenges of numerical solution of the PBE. A quick description of the PBE for laminar flows is given hereafter. For the extension to turbulent flows, one is referred to dedicated reviews like Rigopoulos (2010) as this is an even more intricate problem than the case of homogeneous PBE.

### 3.2.2 PBE in laminar flows

Transport in physical space is now introduced into the PBE for the case of a laminar flow. A first distinction to be made is between inertial and non-inertial particles. The Stokes number  $St$  can be used to characterize the effect of inertia on particles suspended in a fluid flow.  $St$  can be defined as:

$$St = \frac{\tau_P}{\tau_F} \quad (3.2.5)$$

with  $\tau_P$  the relaxation time of the particle (related to the decay of particle velocity due to drag force) and  $\tau_F$  a flow characteristic time. If  $St \ll 1$  particles will follow the fluid streamlines. In this case, particles are called *non-inertial*. If  $St \gg 1$  the effect of inertia on particles trajectories is important and they will deviate from fluid streamlines. In this case, particles are called *inertial*. For inertial particles, the drag forces imposed on the particles will depend on their size. Therefore, particles of different sizes will exhibit different velocities in physical space. Number densities depending on particle velocities must then be introduced. For more details on the PBE for inertial particles, one is referred to [Rigopoulos \(2010\)](#). In the case of soot particles in flames, the Stoke number is low and the assumption of non-inertial particles is generally made. If particle size is described by one variable  $v$  as previously then the PBE (in a laminar flow) is:

$$\begin{aligned} \frac{\partial n(v, \underline{x}, t)}{\partial t} + \frac{\partial (G(v, \underline{x}, t)n(v, \underline{x}, t))}{\partial v} + \nabla \cdot (\mathbf{u}n(v, \underline{x}, t)) = \\ + \nabla \cdot (D_s \nabla n(v, \underline{x}, t)) + \nabla \cdot \left( C_{th} \nu \frac{\nabla T}{T} n(v, \underline{x}, t) \right) + \\ \dot{h}(v, \underline{x}, t) + \dot{a}(v, \underline{x}, t) \end{aligned} \quad (3.2.6)$$

where:

- $\mathbf{u}_T = -\left(C_{th} \nu \frac{\nabla T}{T}\right)$  is the thermophoretic velocity,
- The approximation  $C_{th} = 0.556$  is used as in [Bisetti et al. \(2012\)](#)
- $\nu$  is gas kinematic viscosity,
- $D_s$  is the particle diffusion coefficient

In the case of sooting flames, the thermophoretic velocity may not be negligible. It is generally included in the velocity term such that:

$$\begin{aligned} \frac{\partial n(v, \underline{x}, t)}{\partial t} + \frac{\partial (G(v, \underline{x}, t)n(v, \underline{x}, t))}{\partial v} + \nabla \cdot ((\mathbf{u} + \mathbf{u}_T)n(v, \underline{x}, t)) = \\ \nabla \cdot (D_s \nabla n(v, \underline{x}, t)) + \dot{h}(v, \underline{x}, t) + \dot{a}(v, \underline{x}, t) \end{aligned} \quad (3.2.7)$$

The Schmidt number  $Sc$  is defined as the ratio of momentum diffusivity (kinematic viscosity)  $\nu$  and mass diffusivity (diffusion coefficient)  $D_s$ .

$$Sc = \frac{\nu}{D_s} \quad (3.2.8)$$

In the case of sooting flames,  $Sc$  is very high and molecular diffusion can be neglected as in [Bisetti et al. \(2012\)](#). The PBE for a laminar sooting flames is then:

$$\begin{aligned} \frac{\partial n(v, \underline{x}, t)}{\partial t} + \frac{\partial (G(v, \underline{x}, t)n(v, \underline{x}, t))}{\partial v} + \nabla \cdot ((\mathbf{u} + \mathbf{u}_T)n(v, \underline{x}, t)) = \\ \dot{h}(v, \underline{x}, t) + \dot{a}(v, \underline{x}, t) \end{aligned} \quad (3.2.9)$$

In the following sections, some of the existing methods for solving the homogeneous PBE with nucleation, growth and agglomeration (Eq. 3.2.3) are presented. Finally, an attempt to compare the respective advantages and drawbacks of each method will be made, which will motivate the introduction of the novel hybrid method. For brevity, notations of the dependence on external coordinates  $\bar{x}$  and  $t$  will be dropped in the rest of this chapter and only dependence on internal coordinate  $v$  will be explicitly written.

### 3.3 Monodisperse assumption based models

In some simplified models, polydispersed particles are modeled as monodisperse. This means that at one given physical location  $\underline{x}$  and time  $t$  there is a unique particle size and not a distribution. This rather drastic assumption has been widely used to lower the associated computational cost and ease the coupling of soot models with LES computations on complex geometries. These methods are generally based on empirical or semi-empirical correlations and they generally feature two equations (for the homogeneous PBE). Therefore, they are often referred to as two-equation models. Examples of this kind of method are [Tesner et al. \(1971\)](#); [Kennedy et al. \(1990\)](#); [Leung et al. \(1991\)](#). The model of [Leung et al. \(1991\)](#) has been used up to now in some LES simulations for its low computational cost ([Gallen et al., 2019](#); [Felden et al., 2018](#)). In this model, equations for  $N_T$  and for soot mass fraction  $Y_s$  are solved. In the homogeneous case (without transport in physical space) the equations are the following:

$$\frac{\partial Y_s}{\partial t} = \frac{M_S}{\rho} (\dot{r}_1 + \dot{r}_2 + \dot{r}_3) \quad (3.3.1)$$

$$\frac{\partial N_T}{\partial t} = \frac{2N_A}{C_{min}} \dot{r}_1 + \dot{r}_4 \quad (3.3.2)$$

with  $\dot{r}_1$ ,  $\dot{r}_2$ ,  $\dot{r}_3$ ,  $\dot{r}_4$  the rates of, respectively, the nucleation, surface growth, oxidation and agglomeration reactions. It is to be noted that  $f_v$  can be deduced from  $Y_s$  through:

$$f_v = \frac{\rho}{\rho_s} Y_s \quad (3.3.3)$$

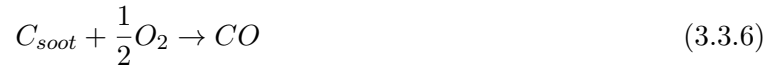
Reaction (1) for nucleation corresponds to:



Reaction (2) for surface growth is:



Reaction (3) for oxidation is:



And reaction (4) for agglomeration is:



The rates for the above reactions are calculated as follows:

$$\dot{r}_1 = k_1(T)[C_2H_2] \quad (3.3.8)$$

$$\dot{r}_2 = k_2(T)[C_2H_2]S_T^{1/2} \quad (3.3.9)$$

$$\dot{r}_3 = -k_3(T)S_T[O_2] \quad (3.3.10)$$

$$\dot{r}_4 = -2C_a \left( \frac{6M_s}{\pi\rho_{soot}} \right)^{1/6} \left( \frac{6k_BT}{\rho_{soot}} \right)^{1/2} N_T^{11/6} \left( \frac{\rho Y_s}{M_s} \right)^{1/6} \quad (3.3.11)$$

where  $\rho$  is the gas density in  $kg.m^{-3}$ ,  $C_{min} = 100$  is the number of carbon atoms in incipient particles and  $C_a = 9$  is a constant for the agglomeration source term.  $[X]$  designs the molar concentration of species  $X$ .  $M_s = 12.011 \text{ kg.kmol}^{-1}$  is carbon molar mass.  $S_T$  is the total surface area of soot per unit of gas volume in  $[m^{-1}]$  depending on the estimated mean particle size. Finally, the two-equation model can be written:

$$\frac{\partial Y_s}{\partial t} = \frac{M_s}{\rho} \left( k_1(T)[C_2H_2] + k_2(T)[C_2H_2]S_T^{1/2} - k_3(T)S_T[O_2] \right) \quad (3.3.12)$$

$$\frac{\partial N_T}{\partial t} = \frac{2N_A k_1(T)}{C_{min}} [C_2H_2] - 2C_a \left( \frac{6M_s}{\pi\rho_{soot}} \right)^{1/6} \left( \frac{6k_BT}{\rho_{soot}} \right)^{1/2} N_T^{11/6} \left( \frac{\rho Y_s}{M_s} \right)^{1/6} \quad (3.3.13)$$

Thus,  $N_T$  evolves according to nucleation and agglomeration while  $Y_s$  evolves through nucleation, surface growth and oxidation. However, as particles are considered monodisperse, the variability of collision frequencies  $\beta(v, \bar{v})$  is not taken into account as well as the variability of available reactive surface on soot particles of different sizes. Therefore, the parameters for this method must be adjusted to each specific case and it is not easily generalizable for different types of flames. Moreover, no distribution can be obtained.

More recently, a three-equation model aimed at soot modeling in LES of gas turbines was proposed in [Franzelli et al. \(2019\)](#). Equations for  $N_T$ ,  $Y_s$  and  $S_T$  are solved. The objective of the additional equation for  $S_T$  is to better account for soot fractality and for the increased available surface of fractal aggregates over spherical particles. However, this model also relies on the monodisperse assumption and the three equations only solve for integral values. Nevertheless, a post-processing method for PSD reconstruction based on the solved integral quantities is proposed. It relies on a priori assumptions on the PSD shape.

The equations for the three integral quantities are the following:

$$\frac{\partial Y_s}{\partial t} = \dot{\omega}_{Y_s} \quad (3.3.14)$$

$$\frac{\partial N_T}{\partial t} = \dot{\omega}_{N_T} \quad (3.3.15)$$

$$\frac{\partial S_T}{\partial t} = \dot{\omega}_{S_T} \quad (3.3.16)$$

with the source terms expressed as:

$$\frac{\dot{\omega}_{Y_s}}{\rho_{soot}} = \underbrace{v_{dim}\beta(v_{dim}, v_{dim})N_{dim}^2}_{\text{nucleation}} + \underbrace{v_{dim}\beta(v_{dim}, v)N_{dim}N_T}_{\text{condensation}} + \underbrace{v_{C_2}\lambda k_{sg}S_T}_{\text{surface growth}} - \underbrace{c_{C_2}\lambda k_{ox}S_T}_{\text{surface oxidation}} \quad (3.3.17)$$

$$\dot{\omega}_{N_T} = \underbrace{\frac{\beta(v_{dim}, v_{dim})N_{dim}^2}{2}}_{\text{nucleation}} - \underbrace{(1 - \mathcal{H}(v - v_{C_2}))\lambda k_{ox}S_T}_{\text{surface oxidation}} - \underbrace{\frac{\beta(v, v)N_T^2}{2}}_{\text{agglomeration}} \quad (3.3.18)$$

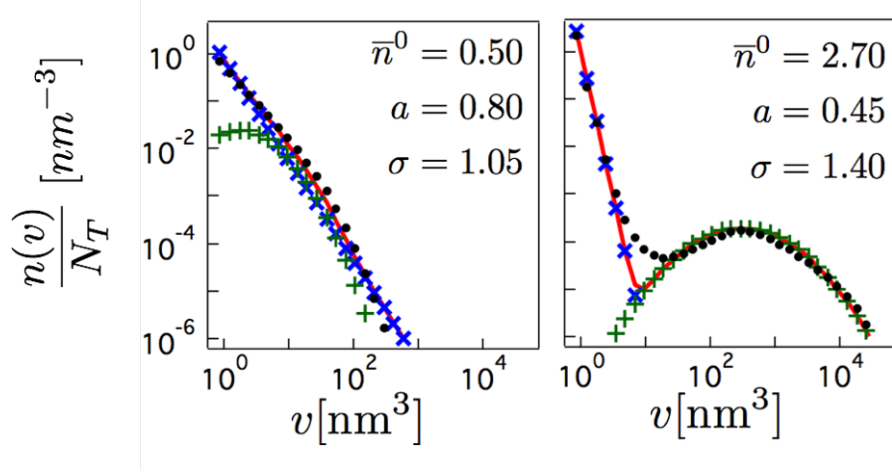


Figure 3.3: Reconstruction (red continuous line) of the normalized PSD as the sum of a Pareto (blue cross) and a log-normal (green plus) distribution. Results correspond to two axial positions:  $x = 3$  mm (left),  $x = 9$  mm (right). The reference PSD obtained from a sectional method is presented as black circles. Source: [Franzelli et al. \(2019\)](#)

$$\begin{aligned} \dot{\omega}_{ST} = & \underbrace{(18\pi)^{1/3}(v_{dim})^{2/3}\beta(v_{dim}, v_{dim})N_{dim}^2}_{\text{nucleation}} + \underbrace{\delta s_{v_{dim}}^{frac}\beta(v_{dim}, v)N_{dim}N_s}_{\text{condensation}} + \\ & \underbrace{\delta s_{v_{C_2}}^{frac}\lambda k_{sg}sN_T}_{\text{surface growth}} - \underbrace{\delta s_{v_{C_2}}^{spher}\lambda k_{ox}sN_T}_{\text{surface oxidation}} \end{aligned} \quad (3.3.19)$$

where  $s$  and  $v$  are the (unique) values for the solved surface and volume of a representative soot particle.  $\mathcal{H}(v)$  is the Heaviside function,  $v_{C_2}$  is the volume of two carbon atoms and  $v_{dim}$  is the volume of a PAH dimer. Spherical dimers are assumed for nucleation.  $N_{dim}$  represents dimers number density.  $\delta s_{\delta v}^{frac}$  denotes the particle surface variation induced by a particle volume variation  $\delta v$  following a fractal behavior, while  $\delta s_{\delta v}^{spher}$  denotes the particle surface variation induced by a particle volume variation  $\delta v$  following a spherical behavior.  $k_{sg}$  and  $k_{ox}$  are surface growth and surface oxidation reactions constants respectively.  $\lambda = 1/s_{C_2}$  is the number of active sites per unit surface with  $s_{C_2}$  the surface of two carbon atoms.

Based on the solved integral quantities and deduced  $v$  and  $s$ , a reconstruction of the PSD can be calculated assuming an a priori shape. Again, the PSD is not solved for in this method but assuming that the PSD is a sum of a Pareto distribution and a log-Normal distribution, a post-processing can be done on the solved values to get an approximated PSD. The Pareto and log-Normal distributions are defined by three parameters which evolve with  $v$ . The evolution of these parameters according to  $v$  has been fitted and generalization to a wide range of flames is not obvious. Nevertheless, when correctly calibrated, this method can give satisfactory results. For illustration, an example of PSD reconstruction at two axial positions in a burner-stabilized stagnation laminar premixed  $C_2H_4/Ar/O_2$  flame is shown in Figure . The PSD reconstruction is compared to a reference solution from a sectional method.

It is important to notice at this point, that  $N_T$  and  $f_v$  are the  $0^{th}$  and  $1^{st}$  order moments of a polydispersed distribution in general. In the so-called two-equation models or three-equation models, the source terms for the  $0^{th}$  and  $1^{st}$  order moments (sometimes  $Y_s$  is solved for but  $f_v$  can be directly deduced from  $Y_s$ ) are derived using the monodisperse assumption. In contrast, in methods of moments, the source terms are closed without this assumption thanks to other techniques. More details on the methods of moments are given in the next section.

## 3.4 Methods of Moments

### 3.4.1 Principle

Aside from the PSD, a population of polydispersed particles can be described by integral values like the moments of the distribution. The statistical moment  $m_k$  is defined as:

$$m_k = \int_0^\infty v^k n(v) dv \quad (3.4.1)$$

As stated earlier, the moments that have easiest physical representation are the zeroth and the first moment which correspond respectively to  $N_T$  and  $f_v$ . In the method of moments the equation for  $n(v)$  (PBE) is transformed into an equation for the moments of the distribution. The moments are directly solved for. Still in the context of a homogeneous PBE, a general form of the equations to be solved is:

$$\frac{\partial m_k}{\partial t} = \dot{m}_k \quad (3.4.2)$$

where  $\dot{m}_k$  denotes the source terms for the moments corresponding to the nucleation, agglomeration and surface growth/loss processes. The advantage of equation 3.4.2 over equation 3.2.3 (PBE solving for  $n(v)$ ) is that it does not depend on the internal coordinate  $v$ , it only depends on external coordinates  $\underline{x}$  and  $t$ . This makes coupling with a Computational Fluid Dynamics (CFD) code easier. However, the PSD is not directly calculated in the method of moments (only the moments are solved for). In theory, knowing all the moments ( $k = 0, \dots, \infty$ ) would be equivalent to knowing the PSD. But in practice, only a few moments are transported (to maintain a low computational cost). In some applications, the knowledge of some moments is a valuable information and can be sufficient but techniques must be implemented to reconstruct the PSD from them if information on the distribution is needed.

Another difficulty is the calculation of the source terms  $\dot{m}_k$ . Even if one is not interested in the PSD and only wants to know some moments, the source terms often require information on the PSD to be calculated. In this case they are unclosed. Therefore, closure approaches are necessary. The strategies for closing the source terms  $\dot{m}_k$  can be separated into two main categories:

- A number density  $n^*(v)$  is reconstructed from the known set of solved moments  $m_{\underline{k}} = [m_0, \dots, m_{k-1}]$ . Then  $n^*(v)$  is used to calculate the set of source terms  $\dot{m}_{\underline{k}} = [\dot{m}_0, \dots, \dot{m}_{k-1}]$ . Finally, these source terms are used to advance equation 3.4.2 and  $n^*(v)$  can be reconstructed again. Methods like the Quadrature Method of Moments (QMOM) (McGraw, 1997) follow this strategy.
- Unknown moments are estimated directly from the set of solved moments. No reconstruction of the distribution is needed. For example, the Method of Moments with Interpolative Closure (MOMIC) (Frenklach and Harris, 1987) and the Taylor-series Expansion Method of Moments (TEMOM) (Yu et al., 2008) follow this strategy.

### 3.4.2 QBMM

Quadrature Based Methods of Moments (QBMM) include QMOM and other approaches of the same 'family' like DQMOM, EQMOM and CQMOM. These methods are shortly described hereafter.

#### 3.4.2.1 QMOM

In the Quadrature Method of Moments (QMOM) the moments are approximated by a  $M$ -point Gaussian quadrature rule. In general, the Gaussian quadrature rule is a method, also used outside

this specific application, for approximating the integral of a function  $f(x)$ . Usually, a weighted sum of the function value at specific points of the integration domain (called nodes or abscissas) is used:

$$\int_a^b w(x)f(x) \simeq \sum_{i=1}^M w_i f(x_i) \quad (3.4.3)$$

where  $w : (a, b) \rightarrow \mathbb{R}^+$  is a weight function which ensures  $f$  integrability. The  $w_i$  coefficients are the quadrature weights and the  $x_i$  values are the quadrature abscissas. It can be shown that the expression of the integral by a  $M$ -point Gaussian quadrature is exact if  $f(x)$  is a polynomial of order less or equal to  $2M - 1$ .

In the case of the method of moments, the integral which must be approximated is  $m_k = \int_0^\infty v^k n(v) dv$ . In practice, the use of the  $M$ -point quadrature in is then equivalent to:

$$m_k = \int_0^\infty v^k n(v) dv = \sum_{i=1}^M w_i v_i^k, \quad k \in \{0, \dots, 2M - 1\} \quad (3.4.4)$$

If the moments of order  $k = 0, \dots, 2M - 1$  are known, the  $M$  abscissas  $v_i$  and the  $M$  weights  $w_i$  can be calculated solving a set of  $2M$  equations (with  $2M$  unknown parameters):

$$\begin{aligned} m_0 &= \sum_{i=1}^M w_i \\ m_1 &= \sum_{i=1}^M w_i v_i \\ &\dots \\ m_{2M-1} &= \sum_{i=1}^M w_i v_i^{2M-1} \end{aligned} \quad (3.4.5)$$

Once this system of equations is solved, the PSD can be reconstructed:

$$n^*(v) = \sum_{i=1}^M w_i \delta(v - v_i) \quad (3.4.6)$$

Then,  $n^*(v)$  can be used to calculate the source terms  $\dot{m}_k$  and close equation 3.4.2.

The resolution of equation 3.4.5 involves the use of specific algorithms at each iteration. A widely used algorithm for this task is the product-difference algorithm formulated in [Gordon \(1968\)](#).

The QMOM has been shown to be accurate ([Marchisio et al., 2003](#)) for problems which are well described by a mono-variate formulation of the PBE and where the source terms  $\dot{m}_k$  do not depend strongly on  $n(v)$ . Indeed, the two main drawbacks of the method are ([Marchisio and Fox, 2005](#)):

- As moments are solved for instead of  $n(v)$ , it is difficult to account for strong dependency of the source terms on the internal coordinates ( $v$  if we stick to the mono-variate case described by particle volume).
- If a multi-variate formulation is needed, the use of QMOM becomes complex as the application of product-difference algorithm (or similar algorithms) becomes intractable.

### 3.4.2.2 DQMOM

As explained above, the QMOM relies on the ability to efficiently invert the moments to get the quadrature weights and abscissas (solving equation 3.4.5). As an alternative, Direct Quadrature Method of Moments was proposed in [Marchisio and Fox \(2005\)](#). The idea is to solve directly for

the quadrature parameters (weights and abscissas), while in QMOM the strategy was to solve for the moments, deduce the quadrature parameters from the known set of moments and close the moments source terms with the quadrature parameters. Like  $n^*(v)$  in the QMOM,  $n(v)$  is directly modeled as a summation of (potentially multi-dimensional) Dirac delta functions in DQMOM. In the mono-variate case:

$$n(v) = \sum_{i=1}^M w_i \delta(v - v_i) \quad (3.4.7)$$

Introducing equation. (3.4.7) directly into the PBE (Eq. 3.2.3), equations for the evolution of the weights and abscissas can be derived. In the case of a homogeneous PBE formulation:

$$\begin{aligned} \frac{\partial w_i}{\partial t} &= \dot{w}_i \\ \frac{\partial v_i}{\partial t} &= \dot{v}_i \end{aligned} \quad (3.4.8)$$

where  $\dot{w}_i$  and  $\dot{v}_i$  for  $i = \{1, \dots, M\}$  are closed thanks to the assumption on the PSD shape.

In the homogeneous mono-variate case, the QMOM and DQMOM solutions are equivalent (Marchisio and Fox, 2005). The improvement of DQMOM over QMOM appears for multivariate PBE formulations. In cases where it is important to solve for more than one internal coordinates (for example particle volume and surface) the multivariate PBE may be necessary. The extension of DQMOM to multivariate cases is straightforward and the additional computational cost scales as the number of internal coordinates whereas QMOM is no longer computationally tractable in this case Marchisio and Fox (2005).

### 3.4.2.3 EQMOM

In Extended Quadrature Method of Moments, Kernel Density Functions are used instead of Dirac delta functions to approximate  $n(v)$ . In general, Kernel Density Functions (KDF) are known distribution functions like Gaussian, gamma, log-normal which are used to estimate the probability density function of a random variable. Here the KDFs  $\delta_\sigma(v, v_i)$  are used to estimate  $n(v)$ . The reconstructed distribution  $n^*(v)$  is a weighted sum of  $N_{kdf}$  continuous KDFs positioned at  $\tilde{v}_i$ :

$$n^*(\tilde{v}) = \sum_{i=1}^{N_{kdf}} w_i \delta_\sigma(\tilde{v}, \tilde{v}_i) \quad (3.4.9)$$

where  $\sigma$  is a parameter of the chosen KDF and  $\tilde{v}$  is a new coordinate introduced to match the physical boundaries of the problem studied with the limits of the chosen KDF. For example, if we consider a minimum nucleating volume for soot particles  $v_o$ , and if gamma distributions, supporting  $[0, \infty[$  are used as KDFs then  $\tilde{v}$  is defined as:

$$\tilde{v} = v - v_o, \quad \tilde{v} \in [0, \infty[ \quad (3.4.10)$$

The choice of the shape of the KDFs used to describe  $n(v)$  depends on the application. Previous studies involving EQMOM for soot PSD description featured gamma and/or log-normal distributions (Wick et al., 2017; Salenbauch et al., 2015). In the original EQMOM  $\sigma$  is assumed to be the same for all the nodes. The weights, abscissas and  $\sigma$  can be solved iteratively from the moments. However, the solution is non-unique as several values can exist for  $\sigma$  (Salenbauch, 2018). Then a second gaussian quadrature is applied on each KDF with  $N_{sgq,i}$  nodes on each KDF as in Yuan et al. (2012). The advantage of EQMOM over QMOM is that the KDFs have known shapes. Two transported moments per KDF are necessary, but then, no additional transported moment is needed for the nodes of the second quadrature and  $N_{sgq,i}$  can be chosen arbitrarily. Greater accuracy for

the calculation of the source terms can be achieved by increasing the number of quadrature nodes  $N_{sgq,i}$  independent of the number of transported moments. Taking into account the second Gaussian quadrature, the reconstructed distribution is expressed as:

$$n^*(v) = \sum_{i=1}^{N_{kdf}} \sum_{j=1}^{N_{sgq,i}} w_i w_{i,sgq,i,j} \delta(\tilde{v} - \tilde{v}_{sgq,i,j}) \quad (3.4.11)$$

Alternatively, a split-based EQMOM can be applied. The principle, introduced in [Megaridis and Dobbins \(1990\)](#) is to define the distribution by the sum of  $N_s$  overlapping sub-distributions  $n_s(v)$ :

$$n(v) = \sum_{s=1}^{N_s} n_s(v) \quad (3.4.12)$$

The sub-distributions are also modeled with known KDFs. However, different values for  $\sigma_s$  for each KDF are possible:

$$n^*(\tilde{v}) = \sum_{s=1}^{N_s} \delta_{\sigma_s}(\tilde{v}; \tilde{v}_s) w_s \quad (3.4.13)$$

As compared to original EQMOM, more transported moments per KDF are necessary. For each sub-distribution, three moments are transported, to deduce three unknowns:  $\tilde{v}_s$ ,  $w_s$  and  $\sigma_s$ . The inversion step is numerically robust. In original EQMOM ([Yuan et al., 2012](#)) only two moments are transported per KDF to deduce  $\tilde{v}_s$ ,  $w_i$  and  $\sigma$  (which is identical for all KDF). The  $N_{sgq,i}$  weights and nodes of the KDFs require no additional transported moment.

### 3.4.2.4 CQMOM

The Conditional Quadrature Method of Moments proposed in [Yuan and Fox \(2011\)](#) relies on another quadrature-based formulation of the distribution. In contrast with QMOM and EQMOM which were designed for mono-variate problems, CQMOM can be efficiently applied on multivariate problems (like DQMOM). The principle of CQMOM is to split a joint multivariate distribution into a product of conditional density functions. As the focus of this thesis is not on multivariate formulations this method is not described in details here.

## 3.4.3 MOMIC

The Method Of Moments with Interpolative Closure (MOMIC) belongs to the second category of Methods of Moments as presented at the beginning of the section. Indeed, the source terms are formulated in terms of moments and are not calculated based on a reconstructed distribution. The additional unknown moments needed to close the source terms are directly determined from the transported ones. For illustration, we can look into the expression of the source terms for the evolution of the moments ( $\dot{m}_k$  in Eq. 3.4.2) in the case of a spatially homogeneous gas phase with polydispersed particles submitted to agglomeration only (with no growth/loss or nucleation). Here, a discretized representation of the distribution is used and it is assumed that  $v_i = i \cdot v_1$  and particle bulk density (generalization of  $\rho_{soot}$  for the type of particle considered) is constant as in [Frenklach \(2002\)](#). The variation of number density  $N_i$  at size  $v_i$  then evolves as:

$$\frac{dN_i}{dt} = \frac{1}{2} \sum_{j=1}^{i-1} \beta(v_j, v_{i-j}) N_j N_{i-j} - \sum_{j=1}^{\infty} \beta(v_i, v_j) N_i N_j \quad (3.4.14)$$

The corresponding source terms for the moments are:

$$\begin{aligned}
 \frac{dm_0}{dt} &= -\frac{1}{2} \sum_{i=1}^{\infty} \sum_{j=1}^{\infty} \beta(v_i, v_j) N_i N_j, \\
 \frac{dm_1}{dt} &= 0, \\
 \frac{dm_2}{dt} &= \sum_{i=1}^{\infty} \sum_{j=1}^{\infty} ij \beta(v_i, v_j) N_i N_j, \\
 &\dots \\
 \frac{dm_r}{dt} &= \frac{1}{2} \sum_{k=1}^{r-1} \binom{r}{k} \left( \sum_{i=1}^{\infty} \sum_{j=1}^{\infty} m_i^k m_j^{r-k} \beta(v_i, v_j) N_i N_j \right)
 \end{aligned} \tag{3.4.15}$$

In this form, the equations are unclosed as only a set of moments is transported. Moreover,  $N_i$ ,  $N_j$  are not known and  $\beta(v_i, v_j)$  depends on particle volume. Instead of trying to estimate  $N_i$  and  $N_j$ , equation 3.4.15 is derived to express  $dm_r/dt$  as a function of fractional-order moments. As shown in Frenklach (2002), for the continuum regime,  $dm_r/dt$  can be expressed as:

$$\begin{aligned}
 \frac{dm_r}{dt} &= \frac{1}{2} K_c \sum_{k=1}^{r-1} \binom{r}{k} [2\mu_k \mu_{r-k} + \mu_{k+1/3} \mu_{r-k-1/3} + \mu_{k-1/3} \mu_{r-k+1/3} + \\
 &K'_c (\mu_{k-1/3} \mu_{r-k} + \mu_k \mu_{r-k-1/3} + \mu_{k+1/3} \mu_{r-k-2/3} \mu_{k-2/3} \mu_{r-k+1/3})] m_0^2
 \end{aligned} \tag{3.4.16}$$

where  $K_c = 2k_B T / 3\mu$  with  $\mu$  the dynamic gas viscosity,  $K'_c = 2.514\lambda(\pi\rho_{soot}/6)^{1/3}$  and  $\mu_r = m_r/m_0$  is the reduced moment of order  $r$ . Only integer-order moments are solved for. Therefore, fractional-order moments need to be determined to close equation 3.4.16. In MOMIC, this is done through Lagrange interpolation of the fractional-order moments based on known integer-order moments. Once the fractional-order moment have been determined by interpolation, the source terms are closed and the evolution of integer-order moments can be advanced. The results of a test case from Frenklach and Harris (1987) are shown in Figure 3.4.

As compared to quadrature-based methods of moments, MOMIC presents the advantage of closing the source terms without inversion of the moments (to get weights and abscissas representing a reconstructed distribution) and without assumption on PSD shape. However, a disadvantage is the non-uniqueness of PSD reconstruction from its moments.

## 3.5 Sectional methods

Sectional methods rely on the discretization of the space of the internal coordinate (here, particle volume  $v$ ). These methods aim at direct solving of  $n(v)$  over this discretized space. Sectional methods are flexible and do not require a priori assumptions on the PSD shape. However, the discretization of the PBE can be challenging. Equation 3.2.3 is integro-differential and hyperbolic. The simultaneous resolution of agglomeration source terms and nucleation-growth source terms is intricate. Moreover, the range of the domain to be discretized is very wide for a limited number of cells. In practice, for soot modeling, particle diameter varies roughly from 1 nm to 100 nm which corresponds to a factor  $10^6$  in volume. At the same time, for computational cost issues, when coupling soot modeling to an inhomogeneous CFD calculation, the number of cells/sections is often limited to approximately 30 (Eberle et al., 2017a; Rodrigues et al., 2018). In the following, an overview of the sectional methods is given. First, the discretization of the agglomeration source term is described. Then, methods for the discretization of the growth/loss term are studied.

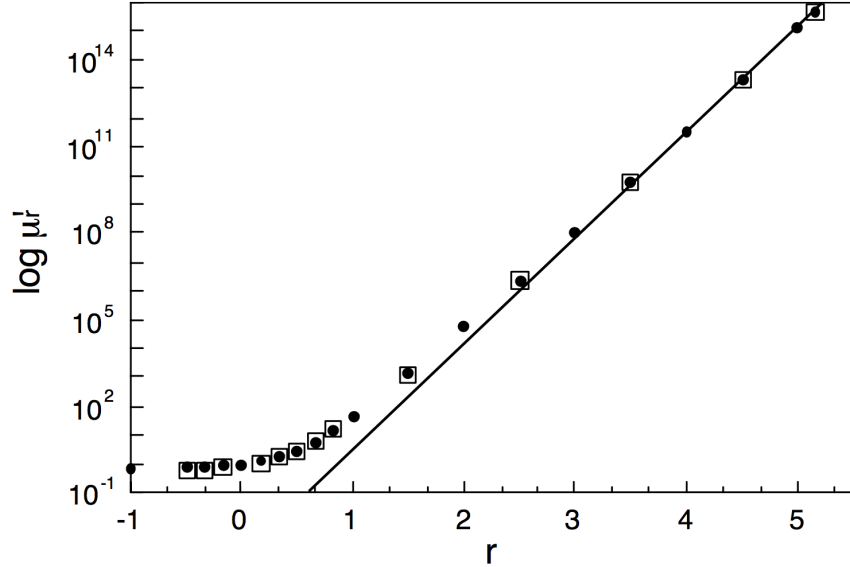


Figure 3.4: Normalized moments vs. moment order. Solid dots represent results of numerical simulations with a reference population balance model (see the 'soot' case of [Frenklach and Harris \(1987\)](#)); and open squares denote the corresponding results of moment interpolation. The solid line exemplifies a linear relationship in these coordinates. Source: [Frenklach \(2002\)](#)

### 3.5.1 Discretization schemes for agglomeration

The integral source term  $\dot{a}$  of equation 3.2.3 (expressed in equation 3.2.4) needs to be discretized so that the PBE can be transformed into a set of Ordinary Differential Equations and subsequently solved. Many different methods have been proposed. Their common characteristic is that the space of particle volume  $v$  (or another internal coordinate) is discretized into an integer number  $M$  of intervals  $I_{v_i}$  called sections or bins. They can be classified into two main categories (following the terminology of [Liu and Rigopoulos \(2019\)](#)).

- *Pointwise approximation methods*: In these methods, the distribution is concentrated at discrete points  $v_i$  (one per section) in the space of  $v$ . Each of these points is assigned a number density value  $N_i$ . The coefficients in the discretized source terms are derived to conserve one or two moments of the distribution  $n(v)$ .
- *Finite Element/Volume methods (FEM/FVM)*: In these methods, a continuous function (often simply a constant, sometimes more complex functions) is used to model  $n(v)$  within each interval. Integration over continuous intervals can then be carried out. In these methods, conservation of the first moment is not obvious on a general non-uniform grid. Some FEM/FVM aim at higher accuracy while others were derived aiming at conservation of one or two moments.

#### 3.5.1.1 Pointwise approximation methods

In the first implementations of this type of method, the grid (in the space of  $v$ ) had to follow a geometric progression such that  $v_{i+1}/v_i = 2$  ([Bleck, 1970](#); [Hounslow et al., 1988](#)). This assumption simplifies the form of the source terms but is quite restrictive. Later on, the method of [Hounslow et al. \(1988\)](#) was extended to grids such that  $v_{i+1}/v_i = 2^{1/q}$  where  $q$  is an integer. An even more flexible approach was proposed in [Kumar and Ramkrishna \(1996a,b\)](#) where any two chosen moments are conserved with no constraint on the grid. In this approach, called the pivot technique, the particles contained in a section are supposed to be concentrated at representative sizes  $v_i$ . As

the grid has a general form, the sum of two colliding pivots may not match with another existing pivot. Then, the principle of the method is to assign the colliding particles to two adjacent sections so that mass and number (in the case of the zeroth and first moment) are conserved through the agglomeration event. The pivot technique has been widely used (Park and Rogak, 2004; Schiener and Lindstedt, 2019) for its flexibility and ease of implementation and because it enables to conserve two moments. For the conservation of the zeroth and first moment, the homogeneous PBE with agglomeration only is:

$$\left. \frac{dN_i}{dt} \right|_{aggl} = \sum_{\substack{k \leq j \leq i \\ v_{i-1} \leq v_j + v_k \leq v_{i+1}}} \left( 1 - \frac{\delta_{j,k}}{2} \right) \eta \beta_{j,k} N_j N_k - N_i \sum_{k=0}^{M-1} \beta_{i,k} N_k \quad (3.5.1)$$

with:

$$\eta = \begin{cases} \frac{v_{i+1} - (v_j + v_k)}{v_{i+1} - v_i} & \text{if } v_i \leq v_j + v_k \leq v_{i+1} \\ \frac{v_{i-1} - (v_j + v_k)}{v_{i-1} - v_i} & \text{if } v_{i-1} \leq v_j + v_k \leq v_i \end{cases} \quad (3.5.2)$$

Where  $\delta_{j,k} = 1$  if  $j = k$  and  $\delta_{j,k} = 0$  if  $j \neq k$  (Kronecker delta). The notation  $\beta_{j,k} = \beta(v_j, v_k)$  is used for brevity. Accuracy of the method has been assessed against analytical solutions in Kumar and Ramkrishna (1996a). However, the fact that colliding particles are assigned on only two adjacent sections (and therefore at two representative sizes, also called pivots) introduces a discretization error as shown in Liu and Rigopoulos (2019).

### 3.5.1.2 Finite Element/Volume Methods (FEM/FVM)

In the class of Finite Element/Volume Methods (FEM/FVM), a continuous function is used to model the distribution  $n(v)$  within each section. Different types of functions have been assumed: cubic splines (Gelbard and Seinfeld, 1978), constant functions (Gelbard and Seinfeld, 1980), collocation and Galerkin methods (Nicmanis and Hounslow, 1996; Roussos et al., 2005), collocation with linear trial functions (Rigopoulos and Jones, 2003). In Netzell et al. (2007) soot volume fraction density  $q(v) = n(v) \cdot v$  is directly solved for instead of  $n(v)$ . A piecewise linear description of  $q(v)$  was originally developed in this work. However, subsequent implementations of this approach featured constant functions for  $q(v)$  in each section (Rodrigues, 2018; Aubagnac-Karkar, 2014). Finite volume methods have also been applied to the PBE (Filbet and Laurencot, 2004; Qamar and Warnecke, 2007; Liu and Rigopoulos, 2019).

In the FEM approach, once a function is chosen to represent  $n(v)$  within the section, the source term for agglomeration  $\dot{a}$  given in equation 3.2.4 must be integrated over each section. Different strategies exist to ease this integration step. Generally, the assumption is made that  $\beta(v, \bar{v}) = \beta(v_i, v_j) = \beta_{i,j}$  is constant within sections i.e. for any pair of particles of volume  $\{v, \bar{v}\}$  with  $v \in I_{v_i}$  and  $\bar{v} \in I_{v_j}$ . Moreover, some assumptions on the grid (in the space of  $v$ ) can simplify the calculation of these integral terms.

For example, in (Aubagnac-Karkar, 2014) it is supposed that the width of the sections (or intervals) grows (or stays constant) with  $v$  (which is usually the case of fixed-sectional grids). Then, the terms representing the positive and negative terms of  $dN_i/dt$  due to agglomeration can be expressed more easily. For two colliding sections  $i$  and  $j$ , the middle  $v_l^c$  of the 'receiving' interval  $[v_i^{inf} + v_j^{inf}; v_i^{sup} + v_j^{sup}]$  is contained in section  $I_{v_l}$ . Thanks to the assumption on the grid, one can conclude that the particles agglomerated from sections  $I_{v_i}$  and  $I_{v_j}$  belong to at most three sections  $I_{v_{l-1}}$ ,  $I_{v_l}$  and  $I_{v_{l+1}}$ . Moreover, assuming constant  $q(v)$  within each section enables to express  $n(v)$  within each section  $I_{v_i}$  as:

$$n_i(v) = \frac{q_i}{v} \quad \forall v \in [v_i^{inf}, v_i^{sup}] \quad (3.5.3)$$

Defining  $Q_i$  the soot volume fraction in section  $I_{vi}$ :

$$Q_i = \int_{I_{vi}} q(v) dv = \int_{I_{vi}} q_i dv = q_i(v_i^{sup} - v_i^{inf}) \quad (3.5.4)$$

$\dot{Q}_{agglo,i}$  the variation of  $Q_i$  due to agglomeration can then be calculated through:

$$\dot{Q}_{agglo,i} = \left( \sum_{j,k} \dot{N}_{agglo}^{j,k \rightarrow i} - \sum_{j=0}^{M-1} \dot{N}_{ij}^{out} \right) \frac{v_i^{sup} - v_i^{inf}}{\ln \left( \frac{v_i^{sup}}{v_i^{inf}} \right)} \quad (3.5.5)$$

where  $\dot{N}_{ij}^{out}$  corresponds to the negative term for section  $i$  of particles from this section colliding with particles from section  $j$  and  $\dot{N}_{agglo}^{j,k \rightarrow i}$  corresponds to the positive source term of colliding particles from sections  $j$  and  $k$  giving birth to particles in section  $i$ . These terms are expressed as:

$$\dot{N}_{ij}^{out} = \int \int_{I_{vi}, I_{vj}} \beta_{i,j} n_i(v_i) n_j(v_j) dv_i dv_j \quad (3.5.6)$$

$$\dot{N}_{agglo}^{j,k \rightarrow i} = G_{agglo}(j, k, i) \dot{N}_{jk}^{out} \quad (3.5.7)$$

where  $G_{agglo}(j, k, i)$  is a coefficient expressing the proportion of colliding particles from sections  $j$  and  $k$  'transferred' to section  $i$  through agglomeration. The details of the calculation of  $G_{agglo}(j, k, i)$  are not given here for brevity but can be found in (Aubagnac-Karkar, 2014). These coefficients  $G_{agglo}(j, k, i)$  can be compared conceptually to the  $\eta$  coefficients in equation 3.5.1.

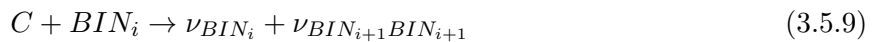
One can observe that in both classes of sectional methods (pointwise approximation and FEM/FVM), the discretization of the internal coordinate into  $M$  sections results in a double sum (equations 3.5.1 and 3.5.5) in which a size dependant value for  $\beta$  is calculated. For computational cost considerations, we will refer to this step as a  $M \times M$  calculation.

### 3.5.1.3 The SPAMM approach

The simultaneous particle and molecule modeling (SPAMM) approach also relies on the discretization of the space of particle size for the resolution of the PBE. Once the grid is fixed and when additional assumptions are made like constant  $\beta_{i,j}$  and constant  $n_i$  within sections, transfer coefficients between sections like  $G_{agglo}(j, k, i)$  from equation 3.5.7 or  $\eta$  from equation 3.5.1 can be calculated in advance. These don't depend on the time evolution of  $n(v)$ , only on the chosen grid. Therefore, so-called 'stoichiometric' coefficients can be derived, so that the agglomeration process is modeled as a chemical reaction and each section (or bin) is modeled as a chemical species. This approach was introduced in Pope and Howard (1997) and is still commonly used currently (Eberle et al., 2017a; Saggese et al., 2015). Collisions involving particles from intervals  $I_{vi}$  and  $I_{vj}$  are represented as a reaction between species  $BIN_i$  and  $BIN_j$ :



where  $BIN_i$  can represent a section containing solid particles, gaseous PAHs, or PAH radicals. A dependence of particle composition on particle size (as for example a decreasing H/C ratio with increasing size of soot particles) can be accounted for by release of gas phase species (species  $A$  in this case). Surface growth/loss can also be formulated in terms of a chemical reaction:



where  $C$  denotes a reacting gas species as  $C_2H_2$  for example. Of course, the stoichiometric coefficients are different for each 'reaction'.

The SPAMM approach (also sometimes called kinetic approach) has the advantage of easy and direct coupling with chemistry solvers. However, if the grid is changed, the stoichiometric

coefficients must be changed accordingly. Moreover, constraints on the grid are usually necessary as for example  $v_{i+1}/v_i \geq 2$  in [Eberle et al. \(2017a\)](#). Furthermore, the SPAMM approach excludes the use of separate time steps for gas phase chemistry and for the PBE, which may have different characteristic times.

### 3.5.2 Discretization schemes for growth

Different discretization methods were presented for the resolution of agglomeration source terms. Let us now examine the PBE with growth only:

$$\frac{\partial n(v, t)}{\partial t} + \frac{\partial (G(v, t)n(v, t))}{\partial v} = 0 \quad (3.5.10)$$

Similarly to transport in physical space, finite difference methods or finite volume methods can be applied. When the discretization grid is fixed, one refers to fixed-sectional methods as opposed to moving sectional methods or adaptive grid methods when the grid is moving. Before getting into the details of existing approaches for the resolution of the general case (where  $G(v)$  depends on  $v$  and the grid can be of any form) let us study the special case of constant growth  $G$  and uniform grid. This will illustrate some of the main challenges faced when discretizing equation 3.5.10.

#### 3.5.2.1 First order upwind finite difference

If  $G$  does not depend on  $v$ , then equation 3.5.10 can be reduced to:

$$\frac{\partial n(v, t)}{\partial t} + G \frac{\partial n(v, t)}{\partial v} = 0 \quad (3.5.11)$$

Let us denote here for brevity  $n_i^m = n(v_i, t^m)$  the discretized number density at volume  $v_i$  and at time  $t_m$ .  $t_{m+1} = t_m + \Delta t$  denotes the subsequent time instant and  $v_{i+1} = v_i + \Delta v$  denotes the next representative size in the grid. A simple way to discretize equation 3.5.11 is to use a first-order upwind finite difference method such that:

$$n_i^{m+1} = n_i^m - G \frac{\Delta t}{\Delta v} (n_i^m - n_{i-1}^m) \quad (3.5.12)$$

This method presents the advantage of being stable and robust. However, it exhibits significant numerical diffusion. This can be illustrated with a simple numerical test. Such a test case was run in [Ma et al. \(2002\)](#) where an initial distribution is submitted to constant growth. The analytical solution is simply the translation of the initial distribution towards bigger size. The result for the first order upwind scheme can be seen in Figure 3.5. One can observe that this scheme gives a smeared solution because of numerical diffusion. At this point, it is important to notice that several recent simulations featuring sectional methods coupled to LES for soot modeling rely on upwind schemes (for solving particle growth) due to the stability and robustness of the method ([Rodrigues et al., 2018](#); [Aubagnac-Karkar et al., 2015](#); [Eberle et al., 2017a](#)). A major objective of this thesis is to present existing alternatives to this scheme in the context of the PBE and to propose a novel hybrid method. The latter will be presented in the next chapter. For now, existing alternatives are presented. In order to tackle the issue of numerical diffusion, higher order schemes have been proposed. Some of them are presented hereafter.

#### 3.5.2.2 High resolution schemes

Still in [Ma et al. \(2002\)](#), the authors propose a high-resolution method based on the ones that have been developed for solving hyperbolic partial differential equations in the context of transport in physical space ([LeVeque, 1992](#); [LeVeque, 1997](#)). First, they show that some commonly used second-order schemes result in spurious oscillations. To demonstrate this, they test the Lax-Wendroff

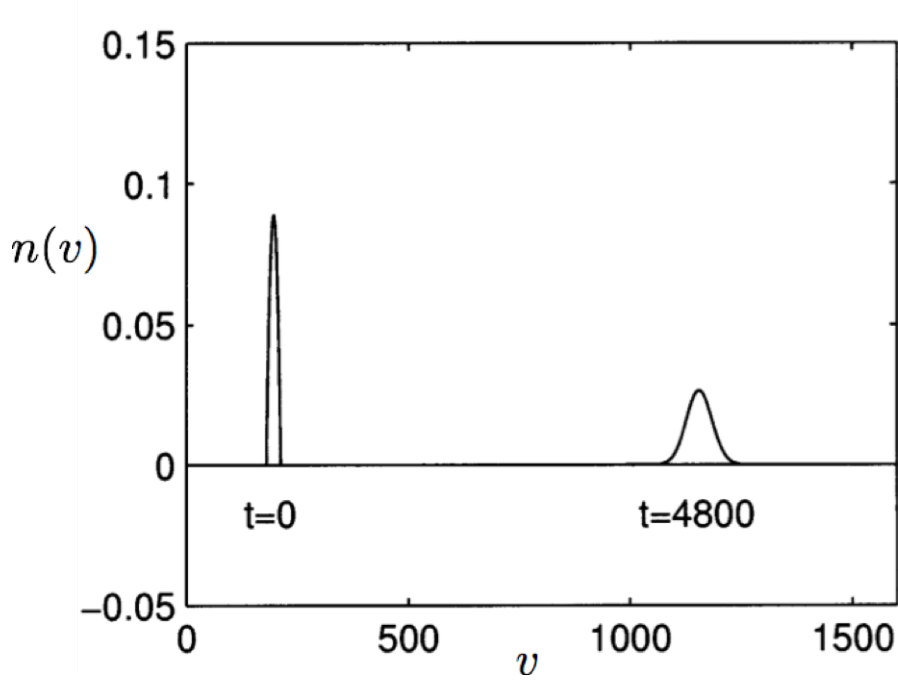


Figure 3.5: Numerical resolution of equation 3.5.11 using the first order upwind discretization. Adapted from Ma et al. (2002)

discretization scheme. It is designed to eliminate numerical diffusion and gives second-order accuracy. This scheme can be expressed (for equation 3.5.11) as follows:

$$n_i^{m+1} = n_i^m - \frac{\Delta t G}{2\Delta v} (n_{i+1}^m - n_{i-1}^m) + \frac{\Delta t^2 G^2}{2\Delta v^2} (n_{i+1}^m - 2n_i^m + n_{i-1}^m) \quad (3.5.13)$$

While this method does not give numerical diffusion, it can add spurious oscillations in some cases. The authors of Ma et al. (2002) applied the same test case of pure growth to an initial distribution with the Lax-Wendroff scheme. The results are presented on Figure 3.6. One can observe the oscillations that would result in nonphysical negative values for  $n(v)$ .

To better understand the causes for these spurious oscillations, the Lax-Wendroff scheme can be rewritten as:

$$n_i^{m+1} = n_i^m - \frac{\Delta t G}{\Delta v} (n_i^m - n_{i-1}^m) - \frac{\Delta t G}{2\Delta v} \left(1 - \frac{\Delta t G}{\Delta v}\right) [(n_{i+1}^m - n_i^m) - (n_i^m - n_{i-1}^m)] \quad (3.5.14)$$

which shows that the Lax-Wendroff method is a sum of the first-order upwind method and an anti-diffusion term. The observed oscillations are caused by a too large amplitude of the anti-diffusion term close to discontinuities of the distribution. Therefore the use of limiter functions  $\phi_i$  is proposed in Ma et al. (2002) to control the amplitude of the anti-diffusion term and tackle the spurious oscillations. The limiters depend on local gradients. Several different limiter functions exist, the one proposed in Ma et al. (2002) is:

$$\phi_i = \frac{|\theta_i| + \theta_i}{1 + \theta_i} \quad (3.5.15)$$

where  $\theta_i$  is the ratio of the local gradients:

$$\theta_i = \frac{n_i^m - n_{i-1}^m}{n_{i+1}^m - n_i^m} \quad (3.5.16)$$

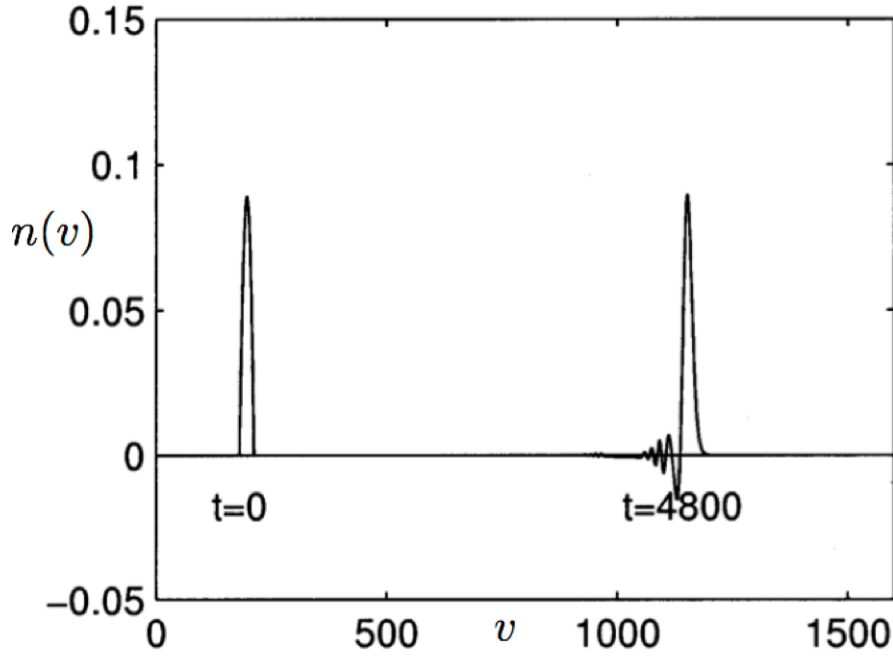


Figure 3.6: Numerical resolution of equation 3.5.11 using the Lax-Wendroff discretization. Adapted from Ma et al. (2002)

Finally, equation 3.5.11 can be solved through the high-resolution scheme with limiter:

$$n_i^{m+1} = n_i^m - \frac{\Delta t G}{\Delta v} (n_i^m - n_{i-1}^m) - \frac{\Delta t G}{2\Delta v} \left(1 - \frac{\Delta t G}{\Delta v}\right) [(n_{i+1}^m - n_i^m)\phi_i - (n_i^m - n_{i-1}^m)\phi_{i+1}] \quad (3.5.17)$$

The same test case as run with the first order upwind and the Lax-Wendroff schemes is run with the high-resolution scheme with limiter in Ma et al. (2002). The results are shown in Figure 3.7.

One can observe that the solution does not present oscillations. The scheme still gives a small amount of spurious diffusion but significantly less than the first order upwind scheme.

Several other high-resolution schemes have been proposed including finite volume schemes. A comparison between some of these high-resolution schemes in the context of the PBE was realized in Qamar et al. (2006). In this thesis, the high-resolution scheme of Park and Rogak (2004) was chosen as a reference fixed-sectional scheme. This scheme is similar to the one of Ma et al. (2002) as it features a limiter function complementing a three-point centered scheme. This choice was made as this scheme was specifically derived for coarse geometrically spaced grids, which are well suited for the resolution of soot agglomeration (for a moderate computational cost). It has recently been used by other authors for soot modeling (Schiener and Lindstedt, 2019). The details of this scheme are given hereafter.

### 3.5.2.3 High resolution scheme from Park and Rogak (2004)

The objective of this scheme is to solve for the growth source term of the PBE with no oscillations and with the least numerical diffusion possible. It was specifically derived and tested on geometric grids where  $F_s = v_{i+1}/v_i$  is the grid spacing factor. A three-point centered scheme is used together with limiters to get a good trade-off between accuracy and stability. Here we come back to a more general case where  $G(v)$  depends on particle size and the grid is not uniform (but is geometric such that  $F_s$  is constant). The variation of  $N_i$  is expressed instead of  $n_i$  as the particles are assumed to be concentrated at representative sizes of 'pivots' like in the method of Kumar and Ramkrishna

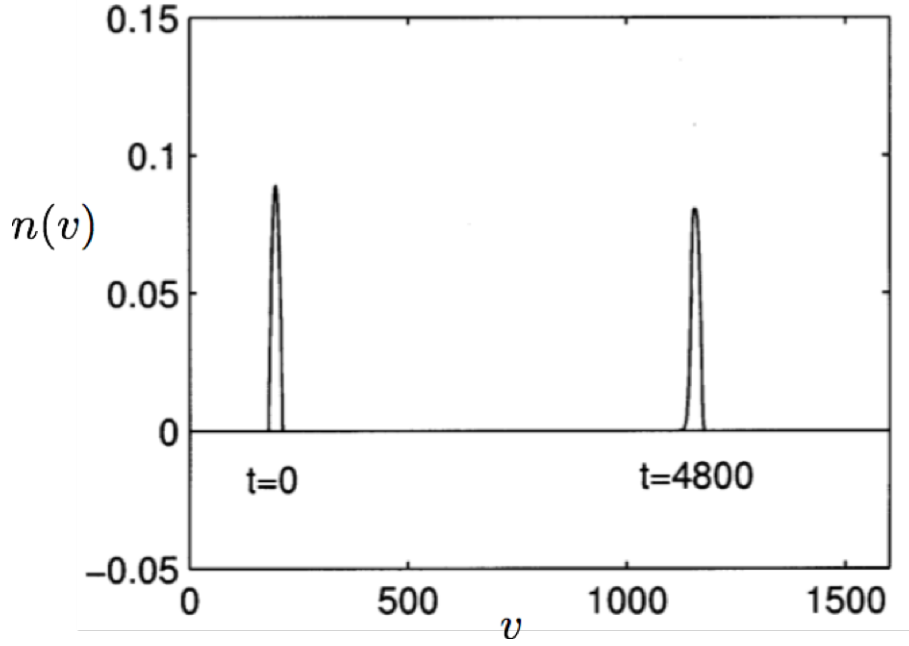


Figure 3.7: Numerical resolution of equation 3.5.11 using the high-resolution scheme with limiter. Adapted from Ma et al. (2002)

(1996a).  $G_i = G(v_i)$  is used in this discretized expression. The evolution of  $N_i$  due to growth only is then expressed as:

$$\left. \frac{dN_i}{dt} \right|_{\text{growth}} = \frac{A_{i-1}G_{i-1}N_{i-1}}{v_{i-1}} + \frac{B_iG_iN_i}{v_i} + \frac{C_{i+1}G_{i+1}N_{i+1}}{v_{i+1}} \quad (3.5.18)$$

where  $A_i$ ,  $B_i$  and  $C_i$  are coefficients derived to conserve the zeroth and first moment, reduce numerical diffusion and mitigate spurious oscillations. Detailed explanations on how these coefficients were derived can be found in Park and Rogak (2004). They depend on the local slope of the distribution such that:

$$B_i = \begin{cases} -\frac{F_s}{F_s-1} \operatorname{erf} \left( \frac{1}{4} \frac{d \ln(N_i)}{d \ln(v_i)} \right) & \text{if } \frac{d \ln(N_i)}{d \ln(v_i)} \leq 0 \\ -\frac{1}{F_s-1} \operatorname{erf} \left( \frac{1}{4} \frac{d \ln(N_i)}{d \ln(v_i)} \right) & \text{if } \frac{d \ln(N_i)}{d \ln(v_i)} > 0 \end{cases} \quad (3.5.19)$$

where  $d \ln(N_i)/d \ln(v_i)$  is calculated using the second-order central scheme. Once  $B_i$  is calculated,  $A_i$  and  $C_i$  can be deduced:

$$A_i = \frac{F_s - B_i(F_s - 1)}{F_s^2 - 1} \quad (3.5.20)$$

$$C_i = -(A_i + B_i) \quad (3.5.21)$$

For comparison, a first order upwind scheme for any grid shape is also given in Park and Rogak (2004):

$$\left. \frac{dN_i}{dt} \right|_{\text{growth}} = \frac{G_{i-1}N_{i-1}}{v_i - v_{i-1}} - \frac{G_iN_i}{v_{i+1} - v_i} \quad (3.5.22)$$

In the following, the schemes defined by equations 3.5.18 and 3.5.22 will be called the 3-point and 2-point sectional methods respectively. Equation 3.5.18 is taken as being representative of high resolution schemes while Equation 3.5.22 is representative of first order upwind schemes. During

this thesis, these methods have been implemented and run on analytical test cases. Results obtained with these two reference methods are compared with the novel hybrid method in chapter 4.

### 3.5.2.4 Moving and adaptive grid methods

As an alternative to fixed sectional methods with high resolution schemes, moving sectional methods have been proposed. In [Kumar and Ramkrishna \(1997\)](#) the authors introduced the method of characteristics where the section's boundaries move at the rate of  $G(v)$ . The growth source term is solved in a Lagrangian manner (in the space of  $v$ ). This technique totally remedies the problem of numerical diffusion as growth/loss is not solved by transfer between sections anymore. However, special treatments are needed like continuous introduction of new sections at the smallest size to account for nucleation and split/merges of sections when they become too big or too small. Moreover, the generalization of such methods to a general spatially inhomogeneous problem can be challenging.

Different from the method of characteristics, adaptive grid methods have been developed. In these methods, the grid is adapted to the distribution for better resolution but the growth source term still results in fluxes between sections. Therefore, adaptive grid methods are often coupled with high resolution schemes. In [Qamar et al. \(2007\)](#), a finite volume scheme is combined with an adaptive mesh technique to solve for the PBE. This technique had first been developed for hyperbolic conservation laws in [Tang and Tang \(2003\)](#). It consists in an iterative procedure where the mesh is first redistributed by moving the spatial grid points. Then, the corresponding numerical solution at the new grid points is obtained by solving a linear advection equation.

A different adaptive grid approach was proposed in [Sewerin and Rigopoulos \(2017\)](#) where the mesh and the solution are redistributed according to the shape of the distribution at previous time instant directly. In contrast with many moving or adaptive grid approaches, no additional system of equations needs to be solved for the transport of the solution and mesh nodes in the space of  $v$ . This explicit coordinate transformation aims at facilitating the extension to spatially inhomogeneous cases. Moreover, a numerical scheme for accommodating localized source terms and preventing grid distortion (which could be problematic with some other moving grid approaches) was proposed, based on node density distribution. Figure 3.8 compares the results of a fully upwinded orthogonal collocation finite element method (OCFEM) ([Rigopoulos and Jones, 2003](#)) and a high resolution Finite Volume Method ([Koren and Vreugdenhil, 1993](#)), both with and without the explicit adaptive grid method (EAGM) proposed in [Sewerin and Rigopoulos \(2017\)](#). The test case is the time evolution of a step-shaped profile only submitted to growth. One can observe that coupled high resolution FVM and EAGM give the best results for the same number of grid cells. In general, coupled high resolution schemes with adaptive grids constitute generic and accurate methods for solving the PBE.

## 3.6 Monte Carlo methods

### 3.6.1 DSMC

Another class of methods that has been widely used for PBE resolution is the class of Monte Carlo methods. The simplest and most widely used Monte Carlo method is the Direct Simulation Monte Carlo (DSMC) method which was originally used in the field of molecular gas dynamics [Bird \(1976\)](#). The principle is the following: instead of directly discretizing the space of internal coordinates (in our case  $v$ ), the population of real physical particles is represented by a (smaller) population of computational (also called stochastic) particles. The real system is represented by a smaller sample. This sampling can be viewed as an indirect discretization where each stochastic particle corresponds to a number of real particles. Then, each stochastic particle evolves individually being submitted to source terms modeling the physics of the problem and events like nucleation or agglomeration will

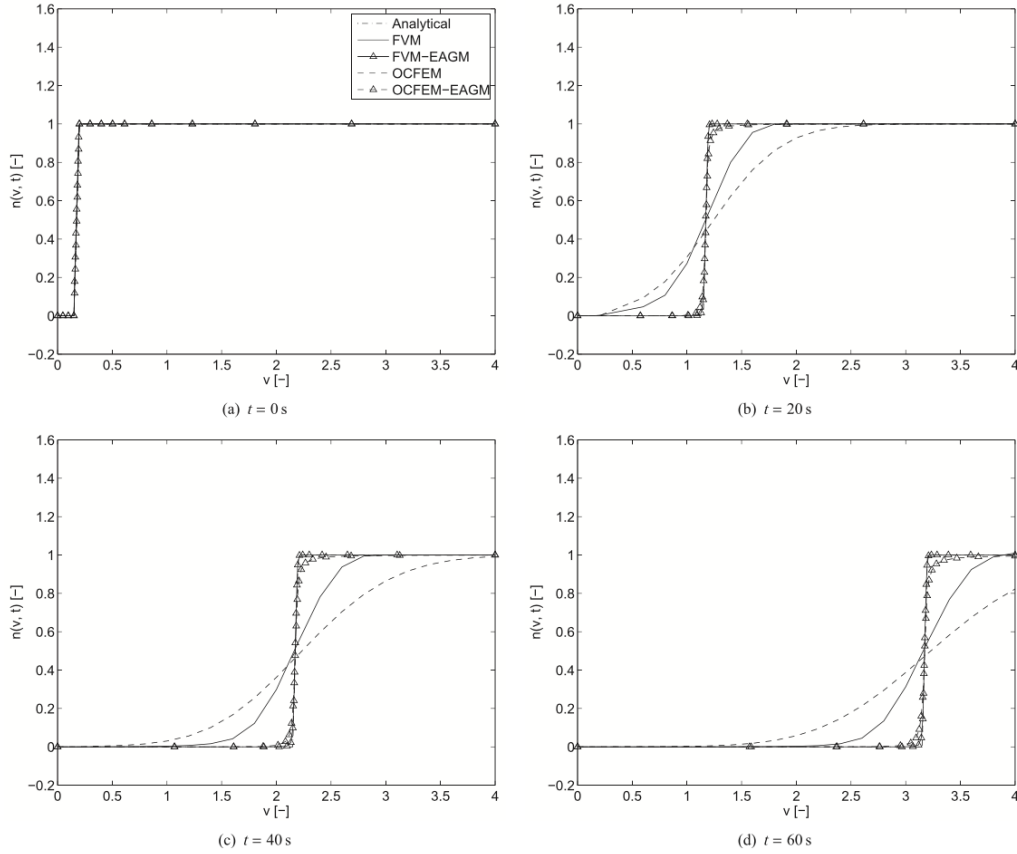


Figure 3.8: Comparison of the analytical solution for the time evolution of a step-shaped profile with different numerical methods. FVM denotes the high resolution Finite Volume Method from [Koren and Vreugdenhil \(1993\)](#) (first applied to the PBE in [Qamar et al. \(2006\)](#)) with fixed sections. OCFEM stands for a fully upwinded orthogonal collocation finite element method by [Rigopoulos and Jones \(2003\)](#). EAGM denotes the explicit adaptive grid method proposed in [Sewerin and Rigopoulos \(2017\)](#). The numerical solutions were obtained using 20 finite volume cells/finite elements. The markers, indicate the cell face/node locations in physical particle property space. Source: [Sewerin and Rigopoulos \(2017\)](#)

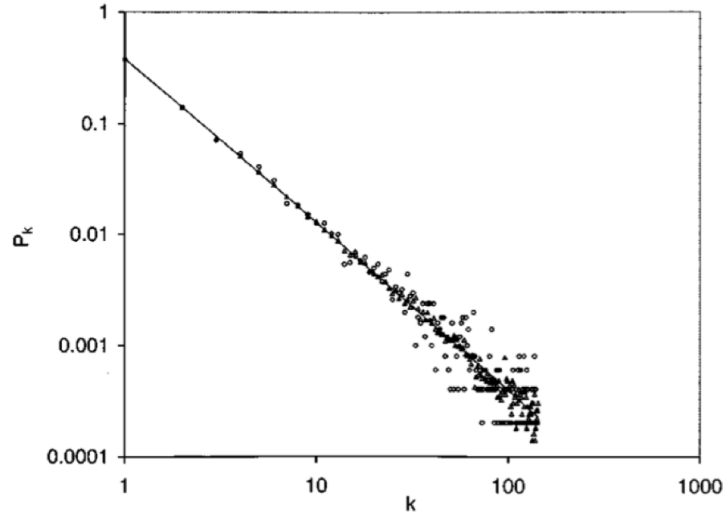


Figure 3.9: Probability  $P_k$  of obtaining an aggregate containing  $k$  primary spherules as a function of particle size. Solid line: analytical solution. Triangles: DSMC with  $N_P = 10^5$ . Circles: DSMC with  $N_P = 10^4$ . Adapted from: [Kruis et al. \(2000\)](#)

be directly, individually represented, for example with the introduction of a new stochastic particle in the simulation or with one stochastic particle merging with another. Known collision frequencies are transformed into event probabilities (events represented individually).

One advantage of DSMC is that growth source terms can be solved in a straightforward manner, with great accuracy for size-dependant growth as it is applied individually on each stochastic particle, and with no numerical diffusion as the space of particle size is not discretized. Another advantage, that also comes from the fact that the space of internal coordinates is not discretized, is that models can easily be extended to multi-variate formulations ([van Peborgh-Gooch and Hounslow, 1996](#); [Kruis et al., 2000](#)).

On the other hand, an inherent drawback of the method is that 'rare' particles (namely the part of the distribution that has lowest number density or probability) will be modeled by few stochastic particles and their evolution will be more prone to error. This is illustrated in Figure 3.9 from [Kruis et al. \(2000\)](#) where the DSMC method is accurate at higher values of the distributions but shows some statistical noise at the tails of the distributions. In order to tackle this issue, a very high number of stochastic particles is sometimes necessary which can result in a high computational cost.

Another issue arises in cases where the number of physical particles represented evolves rapidly. Typically nucleation or agglomeration can lead to a fast increase or decrease of the number of physical particles and, consequently, of stochastic particles. A rapid increase of stochastic particles may lead to intractable computational cost while a rapid decrease of stochastic particles may increase the statistical error by using a too small sample for calculating events probabilities. In order to tackle this issue and maintain an optimal level of resolution, two strategies have been used: constant-volume Monte Carlo and constant-number Monte Carlo, which are explained in the next subsection.

### 3.6.2 Constant-volume or constant-number

The concepts of constant-volume and constant-number Monte Carlo are illustrated in figure 3.10 for particles submitted to agglomeration. In constant-volume Monte Carlo, a constant fluid volume is tracked. Therefore, in presence of agglomeration, the number of physical particles represented in the volume decreases in time and so does the number of stochastic particles. In the constant-number Monte Carlo, the control fluid volume is continuously adjusted to maintain the same number of

physical particles inside the control volume and therefore, the same number of stochastic particles. In both cases, agglomeration results in the same decrease of the number of particles per unit of gas volume  $N_T$ .

In the constant-volume Monte Carlo method, if a simulation with agglomeration was run indefinitely, the number of stochastic particles  $N_P$  would decrease until there is only one left. Before this happens, accuracy decreases as  $N_P$  decreases. To solve this issue, a procedure was introduced in Liffman (1992) and later used, for example in Kruis et al. (2000), where when  $N_P$  reaches half of its initial number it is multiplied by two as well as corresponding volume. At this point the simulation goes back to its initial number of stochastic particles with a doubled volume. The properties of each 'old' particle are copied to the 'new' particles in the added volume in order to conserve the statistical properties. Therefore, one can observe that at the end this adjustment is conceptually similar to a constant-number Monte Carlo except it is done in a stepwise manner instead of a continuous manner for the constant-number Monte Carlo.

In the case of constant-number Monte Carlo (Smith and Matsoukas, 1998; Lin et al., 2002), the level of resolution/accuracy does not vary but two questions arise: First, when a stochastic particle is depleted by an agglomeration event, it must be replaced by a new particle to maintain  $N_P$  constant. Therefore, a particle is selected at random and copied. Second,  $N_T$  must be tracked. Indeed, in constant-volume Monte Carlo, the knowledge of  $N_T$  is straightforward because the ratio  $N_T/N_P$  stays constant until the adjustment (mentioned above) is carried out, and when multiplying  $N_P$  by two, the ratio  $N_T/N_P$  is instantly divided by two. However, in constant-number Monte Carlo, there is no such direct relationship. In Lin et al. (2002) the authors propose strategies to follow the evolution of  $N_T$  in the context of constant-number Monte Carlo (these won't be detailed here for brevity).

### 3.6.3 Time-driven or event-driven

DSMC techniques can also be distinguished depending on the way time-steps are calculated. In time-driven Monte Carlo (Liffman, 1992; Eibeck and Wagner, 2000), the time step is explicitly determined and several events can take place during this time step. In contrast, in event-driven Monte Carlo (Shah et al., 1977; Kruis et al., 2000; Goodson and Kraft, 2002), only one event can occur in each time step and the duration of each time step must be calculated at each iteration depending on the events probabilities.

In event-driven Monte Carlo, important steps are the calculation of the time step  $\Delta t$  and the selection of the next event. In constant-number event driven Monte Carlo like Lin et al. (2002), the time increment follows:

$$\Delta t = \frac{N_T}{N_P} \frac{1}{\sum_i R_i} \quad (3.6.1)$$

where  $\sum_i R_i$  is the sum of all source terms per unit of fluid volume [ $m^{-3}s^{-1}$ ] corresponding to all physical processes taking place in the problem studied. In the case of event-driven step-wise constant-volume Monte Carlo like Kruis et al. (2000),  $\Delta t$  follows:

$$\Delta t = \left(\frac{1}{2}\right)^q \frac{N_T(t=0)}{N_P(t=0)} \frac{1}{\sum_i R_i} \quad (3.6.2)$$

where  $q$  is the number of times control volume and number of stochastic particles were doubled following the procedure explained above from Liffman (1992).

Now let us have a look at the expression of the agglomeration rate  $R_{ag}$ . For the single event of agglomeration between two particles of volumes  $v_i$  and  $v_j$  in the control volume  $V$ , the rate is determined as:

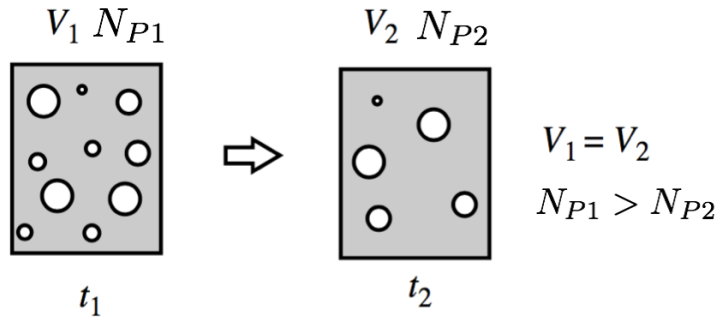
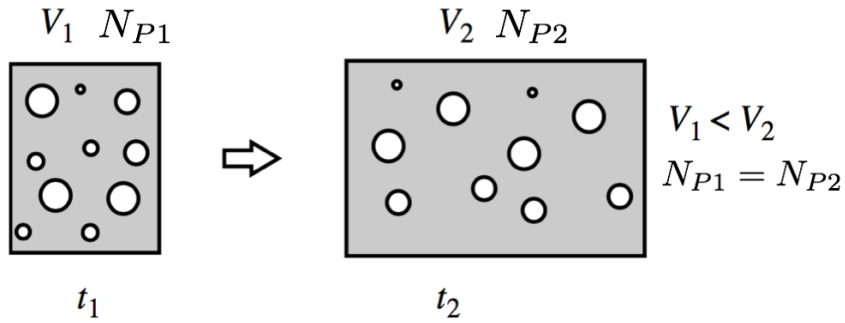
Constant- $V$ Constant- $N$ 

Figure 3.10: Schematic representation of constant-volume and constant-number sampling in Monte Carlo simulation of agglomeration. At each instant  $t_m$  the simulation tracks  $N_{Pm}$  stochastic particles in volume  $V_m$ . The total number of real particle per unit of volume (total number density)  $N_T$  decreases with agglomeration process.  $N_T$  values at a given time are the same in the two methods (one with less particles in the same volume and the other with the same number of particles in a bigger volume). Adapted from: [Lin et al. \(2002\)](#)

$$R_{ag} = \frac{1}{2V^2} \sum_i^{N_P} \sum_{j \neq i}^{N_P} \beta(v_i, v_j) \quad (3.6.3)$$

In a standard implementation, the calculation of the total agglomeration rate and therefore, the calculation of the time increment implies a double sum on all stochastic particles with the calculation of the size-dependant  $\beta(v_i, v_j)$ . This double sum is very expensive and some alternative techniques have been proposed to lower the computational cost (see next subsection).

Once  $\Delta t$  has been calculated, decision is made of which kind of process will occur (nucleation or agglomeration or surface growth...). This decision is made by a random pick between these processes with a probability  $P_i$  proportional to their rates:

$$P_i = \frac{R_i}{\sum_l R_l} \quad (3.6.4)$$

Then the specific particle or particle pair which will go through the process must be chosen. A commonly used method is the acceptance/rejection method (Garcia et al., 1987) even though other techniques have been proposed (Kruis et al., 2000). In the case of agglomeration with the acceptance/rejection method, a pair of particles,  $(i, j)$  is selected at random and is accepted for the event to occur with probability:

$$P_{i,j} = \frac{\beta(v_i, v_j)}{\sum_i^{N_P} \sum_{j \neq i}^{N_P} \beta(v_i, v_j)} \quad (3.6.5)$$

Let us denote  $rnd$  a randomly generated number from a uniform distribution in  $[0, 1]$ . Then, the particle pair is accepted if  $rnd \leq P_{i,j}$ . Else, the pair is rejected. The process of acceptance/rejection is repeated until acceptance occurs. Alternatively, the acceptance ratio can be artificially increased by substituting equation 3.6.5 for:

$$P_{i,j} = \frac{\beta(v_i, v_j)}{MAX_{i,j}\{\beta(v_i, v_j)\}} \quad (3.6.6)$$

$MAX_{i,j}\{\}$  denoting for the maximum value over  $i$  and  $j$ .

In time-driven Monte Carlo like Liffman (1992),  $\Delta t$  is fixed and every stochastic particle goes through a random test to see if it participates in a process during this time step or not. For example, stochastic particle  $i$  will be involved in an agglomeration event if:

$$rnd < 1 - \exp\left(-\frac{\Delta t}{2t_{aggl,i}}\right) \quad (3.6.7)$$

with

$$t_{aggl,i} = \frac{V}{\sum_j \beta(v_i, v_j)} \quad (3.6.8)$$

### 3.6.4 Strategies for more efficient algorithms

Comparisons between different Monte Carlo techniques were carried out, for example in Maisels et al. (2004); Zhao et al. (2007). Some of the main conclusions of Zhao et al. (2007) were that :

- The levels of error of the compared methods (time-driven and event-driven, constant-volume and constant-number) are similar.
- The error is primarily controlled by the number of stochastic particles  $N_P$

		Absence of numerical diffusion linked to the growth source term	Accounting for complex polydispersity without a priori assumed shape	Easy extension to multivariate models	Easy coupling with a CFD solver	Low CPU cost
Monodisperse assumption		++	--	+	++	++
MOM		++	+	+	+	+
Fixed sectional	First order upwind	--	++	+	+	+
	High resolution schemes	+	++	+	+	+
Moving/adaptive sectional		+	++	+	+	+
Monte Carlo		++	++	++	+	--
Hybrid sectional/stochastic (HYPE)		++	++	+	+	+

Figure 3.11: Qualitative comparison of the advantages and drawbacks of each class of method for the resolution of the PBE.

- Event-driven methods may be more computationally efficient but are more difficult to couple to a larger simulation (e.g. CFD) that performs explicit integration in time.

As the order of magnitude of  $N_P$  is at least  $10^3$  in the studies cited above, the main challenges for elaborating more efficient Monte Carlo algorithms have been:

- To avoid the double sum of size dependant kernels on  $N_P$  stochastic particles (equation 3.6.3).
- To better account for the 'tails' (lower values of  $n(v)$ ) of the distribution without increasing  $N_P$ .

Concerning the first point of the above list, majorant kernels were first proposed in [Eibeck and Wagner \(2000\)](#) and further developed in [Goodson and Kraft \(2002\)](#); [Patterson et al. \(2006\)](#). They rely on the use of inequalities where majorant values for the kernel are used to simplify the calculation of agglomeration rates. Thanks to majorant kernels the cost of equation 3.6.3 scales as  $\mathcal{O}(N_P)$  or  $\mathcal{O}(N_P \log N_P)$  instead of  $\mathcal{O}(N_P^2)$  ([Patterson, 2007](#)).

Moreover, in order to avoid the cost of this double sum again at the step of particle pair selection, the binary tree technique has been proposed [Patterson \(2007\)](#).

Concerning the second point, differentially weighted Monte Carlo methods have been proposed to increase accuracy and reduce statistical noise ([Zhao et al., 2009](#); [Patterson et al., 2011](#)). Similarly, the mass flow algorithm (MFA) ([Babovsky, 1999](#)) and the multi Monte Carlo method (MMC) ([Haibo et al., 2005](#)) rely on the concept of weighting stochastic particles.

### 3.7 Comparative advantages and drawbacks

Now that the main classes of methods for the resolution of the PBE in a homogeneous gas phase have been presented, an attempt is made to summarize the advantages and drawbacks of each class of method. For this purpose, a comparative table is presented in Figure 3.11. Of course, one could argue that the relative evaluations are not accurate. Moreover, a diversity of different methods exists within each class so that such comparison cannot be exhaustive. Nevertheless, this effort of qualitative comparison seems worthwhile for two reasons. First, the non-expert reader may be interested in having an overview of the relative strengths of each class of method and have a first clue of what kind of method to choose based on the application and objectives. Second, this comparative table will be useful to better introduce the positioning and added value of the novel hybrid method (HYPE: HYbrid Population balance Equation) developed in this thesis. Detailed description of this method will be given in the next chapter but its comparative strengths and weaknesses are already introduced here so that the reader can better understand the adopted strategy and objectives.

Let us explain each evaluated category:

- As explained in section 3.5.2, the discretization of the space of  $v$ , necessary in sectional methods, induces spurious numerical diffusion. Even though first order upwind schemes introduce significant numerical diffusion, they are still widely used in LES simulations (Rodrigues et al., 2018; Eberle et al., 2017a) because they accurately account for polydispersity and are robust and easy to couple with CFD. High resolution schemes were proposed to mitigate numerical diffusion. However, in the context of soot modelling, the range of values of  $v$  is very large and only a few cells are used for discretization. Therefore, even these high resolution schemes exhibit some numerical diffusion. This will be demonstrated in the next chapter through the resolution of analytical test cases with Park and Rogak (2004) as a reference high resolution scheme. Adaptive grid methods go further in numerical diffusion reduction but they are still sensitive to grid resolution for the growth source term calculation. On the other hand, the space of internal coordinates is not discretized for Monodisperse assumption-based models, Methods of Moments and Monte Carlo methods. Therefore, these do not exhibit numerical diffusion in the space of  $v$ . In the novel method developed in this thesis (HYPE for HYbrid Population balance Equation), the space of  $v$  is discretized for agglomeration solving but not for growth. A formalism featuring stochastic particles is used such that the HYPE method is not subject to numerical diffusion. This will also be demonstrated in the next chapter.
- By definition, monodisperse assumption-based models are not designed to account for complex polydispersity. They usually give a single average particle size. Sometimes, a PSD is reconstructed but it is based on a priori assumed shape like log-normal or pareto functions. In methods of moments, the PSD is not solved for directly. Some PSD reconstruction is possible but this is usually done with a limited number of nodes (for example in the context of QMOM). Therefore, polydispersity is accounted for but not as precisely as with sectional or Monte Carlo methods. In the HYPE method, polydispersity is fully accounted for by a set of stochastic particles.
- The use of multivariate models (with multiple internal coordinates like particle volume  $v$ , particle surface  $s$  and primary spherule diameter  $d_p$ ) can be useful for complex modeling of aggregate's shape. In Monte Carlo methods extension to multivariate models is straightforward and complex interaction between particles can be modeled as well as the historical evolution of single stochastic particles. In monodisperse assumption-based models and in some classes of MOM the simultaneous resolution of several internal coordinates is affordable. In contrast, in sectional methods, as the space of each internal coordinate must be discretized, the CPU cost grows very quickly with the number of internal variables solved for. In the case of the HYPE method, internal coordinates are discretized for agglomeration solving, therefore, the same problem exists.
- In most industrial applications, the homogeneous gas phase PBE is not sufficient. Methods must be extended to inhomogeneous (sometimes turbulent) cases. Ease of coupling with CFD solvers can be a criteria of choice. The easiest methods to couple with CFD are the monodisperse assumption based models as they usually resume to a 2-equation or 3-equation model. Methods of Moments and fixed sectional methods also have been widely coupled to CFD calculations. Special treatment is necessary in the case of adaptive grid sectional methods (Sewerin and Rigopoulos, 2017). Coupling of Monte Carlo methods to CFD has also been successfully realized even though it is not straightforward (Zhao and Zheng, 2013; Pesmazoglou et al., 2016). Extension of the HYPE method to inhomogeneous systems could be realized along these lines.
- Finally, the CPU cost inherent to each class of methods is also naturally a criteria of choice, depending on the final application. Here, we will focus on the cost linked to the calculation of agglomeration source terms, as it is often the most expensive operation in PSD prediction. As one could expect, monodisperse assumption-based models are the fastest as a single equation

with no sum of size-dependant kernels is necessary for the resolution of agglomeration (for example Eq 3.3.11). In methods of moments like QMOM, a reconstruction of the PSD based on a limited number of nodes (of the order of 3-5) is used for agglomeration calculation so that the associated CPU cost is low. In sectional methods, the cost associated to agglomeration source terms usually scales as  $\mathcal{O}(M^2)$  (with  $M$  the number of sections of the order of 30). This quadratic relation can be understood by the presence of double sums of size-dependant kernels (Eq. 3.5.1 or 3.5.5). Special techniques have been developed to reduce the cost for sectional methods to  $\mathcal{O}(M \log M)$  Hackbusch (2006). In the case of Monte Carlo approaches, the original DSMC results in a cost that scales as  $\mathcal{O}(N_P^2)$  with  $N_P$  the number of stochastic particles (of the order of  $10^3$ - $10^5$ ). This is also explained by the double sum of size-dependant kernels on all stochastic particle pairs (Eq. 3.6.3). Even though techniques have been developed to reduce the associated CPU cost to  $\mathcal{O}(N_P)$  or  $\mathcal{O}(N_P \log N_P)$  as explained in section 3.6.4, the cost of Monte Carlo techniques stays high as compared to other methods. The originality of the HYPE method is to combine a stochastic description with a sectional one for agglomeration such that agglomeration source terms are solved through equation 3.5.1 instead of equation 3.6.3 as would be the case for a Monte Carlo method. The stochastic particles are then dynamically reallocated following a process described in the next chapter. This enables to drastically reduce the cost of the HYPE method as compared to a Monte Carlo method. At the same time, the HYPE method features no numerical diffusion as growth is solved on individual stochastic particles.

Now that the motivation and strategy for the novel hybrid method have been explained, the latter is described in details hereafter.

## Chapter 4

# A novel hybrid stochastic/sectional method: the HYPE method

### Contents

<b>4.1 Problem formulation</b>	<b>75</b>
<b>4.2 Hybrid Stochastic/Fixed-Sectional method</b>	<b>76</b>
4.2.1 Control parameters and statistical description	76
4.2.2 Hybrid Stochastic/Fixed-Sectional solution	78
4.2.2.1 Surface growth/loss	80
4.2.2.2 Nucleation and agglomeration	80
4.2.2.3 Agglomeration source	81
4.2.2.4 Time steps	83
<b>4.3 Canonical test cases</b>	<b>84</b>
<b>4.4 Results</b>	<b>85</b>
<b>4.5 Convergence and response to resolution parameters</b>	<b>92</b>
<b>4.6 Chapter summary</b>	<b>97</b>

In this chapter, detailed theoretical formulation of the HYPE method is carried out. Then, practical algorithm is presented. Analytical test cases are performed. Finally, accuracy and computational cost are measured and compared to reference sectional methods.

## 4.1 Problem formulation

The method is described here as in [Bouaniche et al. \(2019b\)](#). As seen earlier, the Particle Size Distribution  $n(v; \underline{x}, t)$ , number of particles of characteristic size  $v$  (in terms of volume or mass,  $v$  is a continuous independent variable), per unit of flow volume and per unit of characteristic size of an aerosol submitted to simultaneous nucleation, surface variation and agglomeration, is governed by a Population Balance Equation (PBE) ([Ramkrishna, 2000](#); [Solsvik and Jakobsen, 2015](#)):

$$\begin{aligned} & \frac{\partial n(v; \underline{x}, t)}{\partial t} + \mathbf{u} \cdot \nabla n(v; \underline{x}, t) + \frac{\partial}{\partial v} [G(v)n(v; \underline{x}, t)] = \dot{h}(v_o; \underline{x}, t) \\ & + \frac{1}{2} \int_0^v \beta(v - \bar{v}, \bar{v}) n(v - \bar{v}; \underline{x}, t) n(\bar{v}; \underline{x}, t) d\bar{v} - n(v; \underline{x}, t) \int_0^\infty \beta(v, \bar{v}) n(\bar{v}; \underline{x}, t) d\bar{v}, \end{aligned} \quad (4.1.1)$$

where usual notations are adopted.  $G(v) > 0$  is the surface growth rate or  $G(v) < 0$  the surface loss rate.  $\dot{h}(v_o) > 0$  is the nucleation rate or  $\dot{h}(v_o) < 0$  the disappearance rate, seen at size  $v_o$ . The integral source term on the RHS accounts for agglomeration following the continuous counterpart

of Smoluchowski equation (Smoluchowski, 1917), with  $\beta(v, \bar{v})$  the collision kernel for two particles of volume  $v$  and  $\bar{v}$ . The PSD evolution is thus driven by an integro-partial-differential equation of the hyperbolic type.

The surface variation rate  $G(v)$  stands as a convective term in the particle size space. Resolution of  $G(v)$  is challenging, similarly to the non-linear flow convective term in physical space (Ferziger and Perić, 1996), which motivates the present study.

Further quantities related to the PSD are introduced.  $N_i(\underline{x}, t)$  is defined as the number of particles of characteristic size  $v_i$  per unit of flow volume

$$N_i(\underline{x}, t) = \int_{I_{v_i}} n(v; \underline{x}, t) dv, \quad (4.1.2)$$

where the interval  $I_{v_i} \equiv [v_i^{inf}, v_i^{sup}]$  defines the  $i$ -th fixed-section of size. The total number density per unit of flow volume is the sum over all sizes or over the  $M$  sections considered

$$N_T(\underline{x}, t) = \int_{v_o}^{\infty} n(v; \underline{x}, t) dv = \sum_{i=0}^{M-1} N_i(\underline{x}, t). \quad (4.1.3)$$

Similarly, the nucleation source per unit of flow volume is

$$\dot{H}_o(\underline{x}, t) = \int_{I_{v_o}} \dot{h}(v; \underline{x}, t) dv. \quad (4.1.4)$$

The Smoluchowski agglomeration sources/sink (Eq. (4.1.1)),

$$\begin{aligned} & \dot{a}(v; \underline{x}, t) \\ &= \frac{1}{2} \int_0^v \beta(v - \bar{v}, \bar{v}) n(v - \bar{v}; \underline{x}, t) n(\bar{v}; \underline{x}, t) d\bar{v} - n(v; \underline{x}, t) \int_0^{\infty} \beta(v, \bar{v}) n(\bar{v}; \underline{x}, t) d\bar{v}, \end{aligned} \quad (4.1.5)$$

leads to the definition of the agglomeration source for the  $i$ -th section

$$\dot{A}_i(\underline{x}, t) = \int_{I_{v_i}} \dot{a}(v; \underline{x}, t) dv, \quad (4.1.6)$$

and  $A_T$  is the total sink due to agglomeration over all particles, thus the sum of  $A_i(\underline{x}, t)$  over all sections

$$\dot{A}_T(\underline{x}, t) = \int_{v_o}^{\infty} \dot{a}(v; \underline{x}, t) dv = \sum_{i=0}^{M-1} \dot{A}_i(\underline{x}, t). \quad (4.1.7)$$

All these quantities allow for combining the PBE with the evolution of the probability density function of the characteristic particle size.

## 4.2 Hybrid Stochastic/Fixed-Sectional method

### 4.2.1 Control parameters and statistical description

To benefit from a description in which surface growth or loss is cast into the form of a linear term, instead of directly solving for the population balance equation, it is proposed to consider both  $N_T(\underline{x}, t)$ , the total number of particles per unit volume, and  $\bar{P}(v^*; \underline{x}, t)$ , the probability density function (PDF) of the particles characteristic size, where  $v^* \in [v_o, \infty]$  denotes the sample space variable associated to  $v$ , seen as a random variable.

The relation between  $n(v; \underline{x}, t)$ , the particle number density per unit size,  $N_i(\underline{x}, t)$ , the number density of particles whose size is in the section  $I_{v_i}$  ( $v \in I_{v_i}$ ) at the flow position ' $\underline{x}$ ' at time 't' (Eq. (4.1.2)), and  $\bar{P}(v^*; \underline{x}, t)$ , the PDF of the particles sizes reads:

$$\int_{I_{v_i}} n(v^*; \underline{x}, t) dv^* = N_i(\underline{x}, t) = N_T(\underline{x}, t) \int_{I_{v_i}} \bar{P}(v^*; \underline{x}, t) dv^* , \quad (4.2.1)$$

where

$$\int_{I_{v_i}} \bar{P}(v^*; \underline{x}, t) dv^* \quad (4.2.2)$$

is the probability to find particles of sizes  $v \in I_{v_i}$ . Because (4.2.1) should be valid whatever  $I_{v_i}$ ,

$$n(v^*; \underline{x}, t) = N_T(\underline{x}, t) \bar{P}(v^*; \underline{x}, t) . \quad (4.2.3)$$

The function

$$\delta(v - v^*) = \lim_{dv \rightarrow 0} 1/dv \text{ if } v \in [v^* - dv/2, v^* + dv/2] \quad (4.2.4)$$

$$= 0 \text{ otherwise ,} \quad (4.2.5)$$

is introduced and  $\bar{P}(v^*; \underline{x}, t) = \overline{\delta(v(\underline{x}, t) - v^*)}$ , where  $\bar{\cdot}$  denotes a statistical average (Lundgren, 1967; Dopazo, 1979; Kollmann, 1990; Dopazo et al., 1997).

The nucleation term in the PBE (Eq. (4.1.1)) may be written  $\dot{h}(v_o; \underline{x}, t) = \dot{H}_o(\underline{x}, t) \delta(v_o - v^*)$ , with  $\dot{H}_o(\underline{x}, t)$  defined by (4.1.4) in the limit where the size of the interval  $I_o$  goes to zero. Similarly, the agglomeration term may be written  $\dot{a}(v^*; \underline{x}, t) = \dot{A}_i(\underline{x}, t) \delta(v_i - v^*)$ , with  $\dot{A}_i(\underline{x}, t)$  defined by (4.1.6) in the limit where  $I_{v_i}$  goes to zero. Then the PBE formally becomes

$$\begin{aligned} \frac{\partial n(v^*; \underline{x}, t)}{\partial t} + \mathbf{u} \cdot \nabla n(v^*; \underline{x}, t) &+ \frac{\partial}{\partial v^*} [G(v^*) n(v^*; \underline{x}, t)] \\ &= \dot{H}_o(\underline{x}, t) \delta(v_o - v^*) + \dot{A}_i(\underline{x}, t) \delta(v_i - v^*) . \end{aligned} \quad (4.2.6)$$

The total number density  $N_T$  evolves according to

$$\frac{\partial N_T(\underline{x}, t)}{\partial t} + \mathbf{u}(\underline{x}, t) \cdot \nabla N_T(\underline{x}, t) = \dot{H}(\underline{x}, t) + \dot{A}_T(\underline{x}, t) , \quad (4.2.7)$$

with  $\dot{A}_T(\underline{x}, t)$  given by (4.1.7). From (4.2.3) the PDF evolves as

$$\frac{\partial \bar{P}(v^*; \underline{x}, t)}{\partial t} = \left[ \frac{1}{n(v^*; \underline{x}, t)} \frac{\partial n(v^*; \underline{x}, t)}{\partial t} - \frac{1}{N_T(\underline{x}, t)} \frac{\partial N_T(\underline{x}, t)}{\partial t} \right] \bar{P}(v^*; \underline{x}, t) . \quad (4.2.8)$$

Introducing (4.2.6) and (4.2.7) in this relation, the PDF evolution equation is obtained

$$\begin{aligned} \frac{\partial \bar{P}(v^*; \underline{x}, t)}{\partial t} + \mathbf{u}(\underline{x}, t) \cdot \nabla \bar{P}(v^*; \underline{x}, t) &= - \overbrace{\frac{\partial}{\partial v^*} [G(v^*) \bar{P}(v^*; \underline{x}, t)]}^{(i)} \\ &+ \underbrace{\frac{\dot{H}_o(\underline{x}, t)}{N_T(\underline{x}, t)} (\delta(v_o - v^*) - \bar{P}(v^*; \underline{x}, t))}_{(ii)} \\ &+ \underbrace{\frac{1}{N_T(\underline{x}, t)} (\dot{A}_i(\underline{x}, t) \delta(v_i - v^*) - \dot{A}_T(\underline{x}, t) \bar{P}(v^*; \underline{x}, t))}_{(iii)} . \end{aligned} \quad (4.2.9)$$

In this balance equation, as in the PBE, the change of particles sizes at the rate  $G(v_i)$  is a convective term in size space (term (i)). The term (ii) on the RHS is nucleation, which is decomposed into two parts preserving the normalisation of the PDF. The first, proportional to  $\delta(v_o - v^*)$ , increases the probability to find the smallest particles at the nucleation rate  $\dot{H}_o(\underline{x}, t)/N_T(\underline{x}, t)$ , while the second decreases, at the same rate, the probability for all sizes. A similar formulation is found for agglomeration (term (iii)), with the probability evolving at the positive or negative rate  $\dot{A}_i(\underline{x}, t)/N_T(\underline{x}, t)$ , associated to a correction proportional to  $-\dot{A}_T(\underline{x}, t)/N_T(\underline{x}, t) > 0$ , so that the PDF normalisation is preserved. Indeed, when two particles of characteristic sizes  $v_i$  and  $v_j$  agglomerate, the probability of their respective initial size decreases ( $\dot{A}_i(\underline{x}, t) < 0$  and  $\dot{A}_j(\underline{x}, t) < 0$ ), to increase the probability of their new size  $v_k$  ( $\dot{A}_k(\underline{x}, t) > 0$ ). However, because the total number of physical particles decreases in this process, the probability of all sizes benefit from an increase proportional to  $-A_T$ , the overall particle sink.

The solutions of the equations (4.2.7) and (4.2.9) provide all the necessary information to simulate the nucleation and the growth of an ensemble of particles transported in a flow. The particle size distribution  $N_i(\underline{x}, t)$  can then be recovered from (4.2.1).

Because the focus is on the numerical solving of terms controlling the PSD shape, a perfectly stirred/homogeneous reactor is considered ( $\mathbf{u} = 0$ ). However, the addition of the convective flow velocity is discussed in the last chapter of this thesis (perspectives).

### 4.2.2 Hybrid Stochastic/Fixed-Sectional solution

The probability density function  $\bar{P}(v^*; t)$  can be discretized over a set of  $N_P$  stochastic particles,<sup>1</sup> each carrying information on the particle size, *i.e.*  $v = v^k$  for  $k = 1, \dots, N_P$  and  $\bar{P}(v^*; t) = (1/N_P) \sum_{k=1}^{N_P} \delta(v^k(t) - v^*)$ . The total number of stochastic particles  $N_P$  is fixed.

The  $v$ -space is also discretized in  $M$  fixed sections, to define a mesh providing a distribution of  $\Delta v_i = v_i^{sup} - v_i^{inf}$ , for  $i = 0, \dots, M - 1$ . Uniform, geometric and exponential sectional grids will be tested thereafter. The characteristic size  $v^k$  of a stochastic particle can take any value between the considered size bounds  $[v_o, v_M]$ , independently of the fixed sectional mesh.

Within this set of  $N_P$  particles, an integer number  $n_{P_i}(t)$  of stochastic particles features sizes so that  $v^k \in I_{v_i} \equiv [v_i^{inf}, v_i^{sup}]$ . This number of stochastic particles relates to the PDF and to  $N_i(t)$ , the number densities of the physical particles (Eq. (4.2.1)), according to:

$$\int_{I_{v_i}} \bar{P}(v^*; t) dv^* = \frac{n_{P_i}(t)}{N_P} = \frac{N_i(t)}{N_T(t)}. \quad (4.2.10)$$

To simulate the PDF time evolution through  $v^k(t)$ , the stochastic particles time evolution, a fractional-step method is followed. Starting at time  $t^n$ , surface growth/loss is first applied to advance the solution to time  $t^{n+\frac{1}{2}}$ . This is applied in a deterministic way to every  $k$ -th particle, as a simple linear process proportional to  $G(v^k(t))$ , which is the major advantage of the proposed approach. Then from the time  $t^{n+\frac{1}{2}}$ , the solution is advanced to  $t^{n+1}$  by applying nucleation and agglomeration effects, which are simulated by moving the stochastic particles between the defined sections. The number of stochastic particles randomly selected to be removed from a section and dispatched over the others, are calculated according to the nucleation and agglomeration rates controlling the PDF evolution (Eq. (4.2.9)). At every instant  $t^n$ ,  $\delta t$  is determined so that stability is secured, different amplitudes of  $\delta t$  may be required in practice to advance from  $t^n$  to  $t^{n+\frac{1}{2}}$  (growth/loss) and from  $t^{n+\frac{1}{2}}$  to  $t^{n+1}$  (nucleation and agglomeration).

<sup>1</sup>Physical space is omitted in this subsection for brevity.

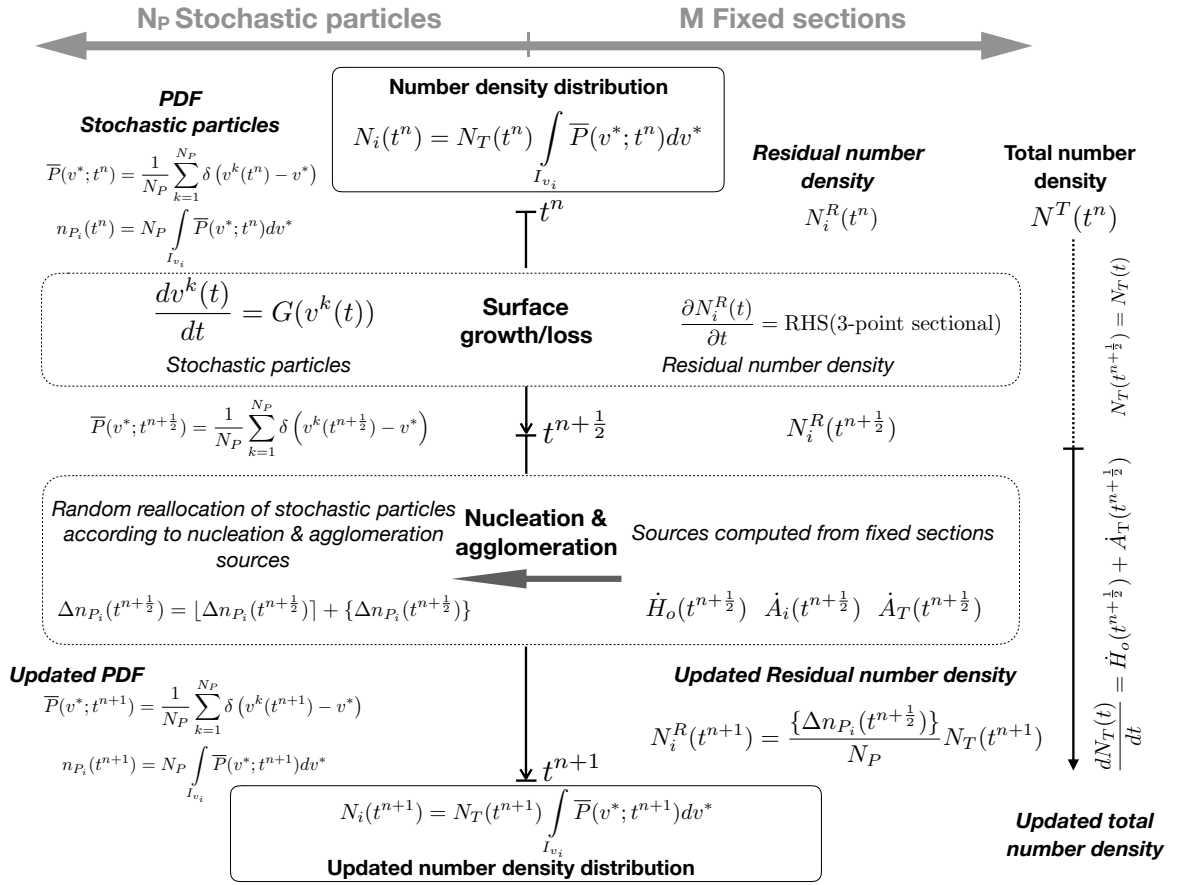


Figure 4.1: Flowchart of the hybrid stochastic/fixed-sectional method.

### 4.2.2.1 Surface growth/loss

During surface growth or loss, the size of the  $k$ -th stochastic particle evolves according to:

$$\frac{dv^k(t)}{dt} = G(v^k(t)), \quad k = 1, \dots, N_P. \quad (4.2.11)$$

Each stochastic particle then carries information on an updated size  $v^k(t^{n+\frac{1}{2}})$ . The total number density stays constant during growth ( $dN_T(t)/dt = 0$ ). Once Eq. (4.2.11) is solved for each particle, an updated distribution of the stochastic particles is available and the PDF  $\bar{P}(v^*; t^{n+\frac{1}{2}})$  is known along with  $n_{P_i}(t^{n+\frac{1}{2}})$  the number of stochastic particles in every section.

### 4.2.2.2 Nucleation and agglomeration

Nucleation and agglomeration are subsequently applied, which impacts on the number density  $N_T(t)$  and on the PDF through the change of  $n_{P_i}(t^{n+\frac{1}{2}})$  for each interval  $I_{v_i}$ . Starting from  $N_T(t^n) = N_T(t^{n+\frac{1}{2}})$ , the number density evolves from  $t^{n+\frac{1}{2}}$  to  $t^{n+1}$  with

$$\frac{dN_T(t)}{dt} = \dot{H}_o(t) + \dot{A}_T(t). \quad (4.2.12)$$

Once  $N_T(\underline{x}, t^{n+1})$  is known solving (4.2.12), the PDF equation (4.2.9) is advanced in time with nucleation and agglomeration:

$$\begin{aligned} \bar{P}(v^*; t^{n+1}) &= \alpha_{H_o} \delta(v_o - v^*) + \alpha_{A_i} \delta(v_i - v^*) \\ &+ (1 - \alpha_{H_o} - \alpha_{A_T}) \bar{P}(v^*; t^{n+\frac{1}{2}}), \end{aligned} \quad (4.2.13)$$

with  $\alpha_{H_o}$  the relative increase of  $\bar{P}(v_o; t^{n+\frac{1}{2}})$  by nucleation (and decrease of  $\bar{P}(v^*; t^{n+\frac{1}{2}})$  for  $v^* \neq v_o$ ),  $\alpha_{A_i}$  the relative increase/decrease due to agglomeration and  $\alpha_{A_T}$  the total agglomeration sink defined by Eq. (4.2.9):

$$\alpha_{H_o} = \frac{\dot{H}_o(t^{n+\frac{1}{2}})}{N_T(t^{n+1})} \cdot \delta t, \quad (4.2.14)$$

$$\alpha_{A_i} = \frac{\dot{A}_i(t^{n+\frac{1}{2}})}{N_T(t^{n+1})} \cdot \delta t, \quad (4.2.15)$$

$$\alpha_{A_T} = \frac{\dot{A}_T(t^{n+\frac{1}{2}})}{N_T(t^{n+1})} \cdot \delta t. \quad (4.2.16)$$

According to Eq. (4.2.10), integrating over  $I_{v_i}$  and multiplying by  $N_P$  the PDF evolution given by the relation (4.2.13) leads to the evolution of the number of stochastic particles per section. This discretized time evolution is organised as:

$$n_{P_i}(t^{n+1}) = n_{P_i}(t^{n+\frac{1}{2}}) + \Delta n_{P_i}(t^{n+\frac{1}{2}}), \quad (4.2.17)$$

with increments  $\Delta n_{P_i}(t^{n+\frac{1}{2}})$  in the form of real numbers, which will need to be transformed subsequently into integer numbers of particles in the Monte Carlo algorithm. From (4.2.13),

$$\begin{aligned} \Delta n_{P_o}(t^{n+\frac{1}{2}}) &= (\alpha_{H_o} + \alpha_{A_o}) N_P - (\alpha_{H_o} + \alpha_{A_T}) n_{P_o}(t^{n+\frac{1}{2}}) \\ &+ \alpha_{R_o} N_P, \end{aligned} \quad (4.2.18)$$

$$\begin{aligned} \Delta n_{P_i}(t^{n+\frac{1}{2}}) &= \alpha_{A_i} N_P - (\alpha_{H_o} + \alpha_{A_T}) n_{P_i}(t^{n+\frac{1}{2}}) \\ &+ \alpha_{R_i} N_P \text{ for } i \neq o. \end{aligned} \quad (4.2.19)$$

The terms proportional to  $\alpha_{R_i}$  are the accumulation of the round-off error, which goes to zero for  $N_P \rightarrow \infty$ . Cumulated over the iterations, this will impact on particles when  $\alpha_{R_i} \geq 1/N_P$ . At every iteration,  $\Delta n_{P_i}(t^{n+\frac{1}{2}})$  is thus decomposed into its integer and fractional (or decimal) parts. The fractional part  $\{\Delta n_{P_i}(t^{n+\frac{1}{2}})\}$  is defined from the nearest integer  $\lfloor \Delta n_{P_i}(t^{n+\frac{1}{2}}) \rfloor$ ,

$$\{\Delta n_{P_i}(t^{n+\frac{1}{2}})\} = \Delta n_{P_i}(t^{n+\frac{1}{2}}) - \lfloor \Delta n_{P_i}(t^{n+\frac{1}{2}}) \rfloor. \quad (4.2.20)$$

The integer part  $\lfloor \Delta n_{P_i}(t^{n+\frac{1}{2}}) \rfloor$  sets the variation of the number of stochastic particles within a section during the reallocation step corresponding to nucleation and agglomeration. The following Monte Carlo algorithm is applied:

- If  $\lfloor \Delta n_{P_i}(t^{n+\frac{1}{2}}) \rfloor$  is negative, a random number  $-\lfloor \Delta n_{P_i}(t^{n+\frac{1}{2}}) \rfloor$  of stochastic particles is picked among the  $n_{P_i}(t^{n+\frac{1}{2}})$  present in  $I_{v_i}$ .
- All the picked particles from all  $I_{v_i}$  intervals ( $i = 0, \dots, M-1$ ) constitute an ensemble  $\mathcal{P}(t^{n+\frac{1}{2}})$  of particles whose characteristic size needs to change.
- If  $\lfloor \Delta n_{P_i}(t^{n+\frac{1}{2}}) \rfloor$  is positive,  $\lfloor \Delta n_{P_i}(t^{n+\frac{1}{2}}) \rfloor$  particles are taken from  $\mathcal{P}(t^{n+\frac{1}{2}})$  and allocated to  $I_{v_i}$  at the representative size  $v_i^*(t^{n+\frac{1}{2}})$ , defined to conserve mass, as discussed in the next subsection.

The larger the total number of stochastic particles  $N_P$ , the smaller the relative contribution of the decimal part  $\{\Delta n_{P_i}(t^{n+\frac{1}{2}})\}$  to  $\Delta n_{P_i}(t^{n+\frac{1}{2}})$ . This residual decimal part defines  $N_i^R(t^n)$ , a residual number density of physical particles in the section  $v_i$ , which is computed at time  $t^n$  following (4.2.10)

$$N_i^R(t^n) = \frac{\{\Delta n_{P_i}(t^{n-\frac{1}{2}})\}}{N_P} N_T(t^n), \quad (4.2.21)$$

where  $\Delta n_{P_i}(t^{n-\frac{1}{2}})$  denotes  $\Delta n_{P_i}$  of the previous iteration in time. The growth/loss of the physical particles represented by this number density residual  $N_i^R(t^n)$  is not included in the stochastic particles and needs a separate solving, between  $t^n$  and  $t^{n+\frac{1}{2}}$  (*i.e.*, simultaneously with growth/loss for the stochastic particles Eq. (4.2.11)) This is done with a sectional method based on the 3-point discretization for particle growth/loss (Park and Rogak, 2004) (Eq. 3.5.18). Then,  $N_i^R(t^{n+\frac{1}{2}})$  is known and  $\alpha_{R_i}$  is obtained from

$$\alpha_{R_i} = \frac{N_i^R(t^{n+\frac{1}{2}})}{N_T(t^{n+1})}, \quad (4.2.22)$$

and applied to Eqs. (4.2.18) and (4.2.19) to compute  $\Delta n_{P_i}(t^{n+\frac{1}{2}})$ . For sufficiently large values of  $N_P$ , typically  $10^5$  as shown thereafter, the residual number density of particles is expected to be negligible and will not perturb much the accuracy of the method. Then,  $\alpha_R(v_i)$  can be set to zero in the relations (4.2.18) and (4.2.19). However as shown below, accounting for the contribution of the residual part allows for reducing  $N_P$  (such as  $10^3$  or less) and therefore the CPU time.

Optionally, a trigger can also be set so that when the number of stochastic particles present in a given section becomes too small, the surface growth/loss is then fully solved through the evolution of  $N_i^R(t)$ . In practice, a trigger of 5 particles per section is used and has been found to be sufficient to avoid any noise on the tails of distributions.

Figure 4.1 displays a flowchart summarising the method.

### 4.2.2.3 Agglomeration source

The method proposed in Kumar and Ramkrishna (1996a) is retained for computing the agglomeration source  $\dot{A}_i(t)$  of Eq. (4.2.15). For any colliding particles of volume  $v$  in section  $i$  and  $\bar{v}$  in section

Table 4.1: Growth parameters

Case	1(a)	1(b)
Initial	1 for $0.2 \leq v$ ; 0 else	$\delta(1)$
Growth kernel	0.05	$v$
Agglo. kernel	0	0
Number of sections	20	40
Grid type	unif. $\Delta v = 0.2$	geo. $F_s = 2$
Size range	0 – 4	$0.7 - 7.3 \cdot 10^{11}$

$j$ , the collision kernel  $\beta(v, \bar{v})$  is assumed fixed to  $\beta(v_i, v_j) = \beta_{i,j}$ . Particles formed by agglomeration are distributed in the sections in a manner that conserves the zeroth and first moments of the PSD, namely number and mass. This method avoids the evaluation of the double integrals of the collision kernel and is therefore computationally efficient (see [Kumar and Ramkrishna \(1996a\)](#) for more details). The agglomeration source used in (4.2.15) reads

$$\begin{aligned} \dot{A}_i(t) = & \sum_{\substack{j,k \\ v_{i-1} \leq v_j + v_k \leq v_{i+1}}}^{k \leq j \leq i} \left(1 - \frac{\delta_{j,k}}{2}\right) \eta \beta_{j,k} N_j(t) N_k(t) \\ & - N_i(t) \sum_{k=0}^{M-1} \beta_{i,k} N_k(t), \end{aligned} \quad (4.2.23)$$

with

$$\eta = \begin{cases} \frac{v_{i+1}^* - (v_j^* + v_k^*)}{v_{i+1}^* - v_i^*} & \text{if } v_i^* \leq v_j^* + v_k^* \leq v_{i+1}^*, \\ \frac{v_{i-1}^* - (v_j^* + v_k^*)}{v_{i-1}^* - v_i^*} & \text{if } v_{i-1}^* \leq v_j^* + v_k^* \leq v_i^*, \end{cases} \quad (4.2.24)$$

In the hybrid stochastic/fixed-sectional approach, the characteristic volume  $v_i^*$  must be representative of the average mass contained in the  $i$ -th section.  $v_i^*$  is calculated dynamically, depending on the volumes of the stochastic particles contained in both the section and the residual terms resulting from the round-off,

$$v_i^*(t^{n+\frac{1}{2}}) = \frac{(N_T(t^n)/N_P) \sum_{k=1}^{n_{P_i}(t)} v_i^k(t^{n+\frac{1}{2}}) + N_i^R(t^{n+\frac{1}{2}}) v_i^*(t^n)}{(N_T(t^n)/N_P) n_{P_i}(t^{n+\frac{1}{2}}) + N_i^R(t^{n+\frac{1}{2}})}, \quad (4.2.25)$$

where  $v_i^k = v^k$  if  $v^k \in I_{v_i}$  and  $v_i^k = 0$  otherwise,  $n_{P_i}(t^{n+\frac{1}{2}})$  is the number of stochastic particles in the  $i$ -th section (Eq. (4.2.10)) and  $N_i^R(t^{n+\frac{1}{2}})$  is the residual number density of the particles in the section after applying surface gross or loss.  $v_i^*$  needs to be updated again after reallocation of the particles due to agglomeration, to provide  $v_i^*(t^{n+1})$  from (4.2.25) with  $N_T(t^{n+1})$ ,  $v_i^k(t^{n+1})$ ,  $N_i^R(t^{n+1})$ ,  $v_i^*(t^{n+\frac{1}{2}})$ ,  $n_{P_i}(t^{n+1})$ .

Once  $v_i^*$  has been determined, the particles reassigned to the  $i$ -th section are distributed in this section following a two-step process:

- First, the  $\lfloor \Delta n_{P_i}(t^{n+\frac{1}{2}}) \rfloor$  particles are allocated randomly within the section at sizes  $v^k(t^{n+\frac{3}{4}})$ , which are samples of a random variable  $v$  following a target piecewise linear distribution defined by the probability density function,

$$p(v \mid v_i^{inf}, v_i^{sup}, w_i, w_{i+1}) = 2 \frac{w_i(v_i^{sup} - v) + w_{i+1}(v - v_i^{inf})}{(w_i + w_{i+1}) \Delta v_i^2}. \quad (4.2.26)$$

Table 4.2: Agglomeration parameters

Case	2(a)	2(b)
Initial	$e^{-v}$	$e^{-v}$
Agglo. kernel	1	$v_i + v_j$
Number of sections	40	40
Grid type: Exponential, $\alpha$	1.17	1.25
Size range	$6.7 \cdot 10^{-2} - 209$	$6.7 \cdot 10^{-2} - 2006$

In this distribution, the weights,  $w_i$ , are calculated from the variations of the number densities at  $v_i^*$ ,

$$\begin{aligned}
 w_i &= \Delta n_i(t^{n+\frac{1}{2}}) + \frac{\Delta n_i(t^{n+\frac{1}{2}}) - \Delta n_{i-1}(t^{n+\frac{1}{2}})}{v_i^* - v_{i-1}^*} (v_i^{inf} - v_{i-1}^*), \\
 w_{i+1} &= \Delta n_{i+1}(t^{n+\frac{1}{2}}) + \frac{\Delta n_{i+1}(t^{n+\frac{1}{2}}) - \Delta n_i(t^{n+\frac{1}{2}})}{v_{i+1}^* - v_i^*} (v_i^{sup} - v_i^*),
 \end{aligned}$$

with  $\Delta n_i(t) = \Delta n_{P_i}(t) N_T(t) / (N_P \Delta v_i)$  (Eq. (4.2.10)). Such random piecewise linear distribution secures a continuous distribution of the stochastic particles. However, it does not guarantee strict volume/mass conservation by itself.

- Mass conservation is achieved in a second step by calculating a corrective factor  $K_i$

$$K_i = \frac{v_i^*(t^{n+\frac{1}{2}})}{(1/n_{P_i}(t^{n+\frac{3}{4}})) \sum_{k=1}^{n_{P_i}(t^{n+1})} v_i^k(t^{n+\frac{3}{4}})}, \quad (4.2.27)$$

then,

$$v_i^k(t^{n+1}) = K_i v_i^k(t^{n+\frac{3}{4}}), \quad (4.2.28)$$

and mass is conserved through the reallocation process.

Nucleation size is set as the lower boundary of the smallest size section  $v_o$ . As the numerical steps corresponding to nucleation/agglomeration and growth are sequential in the present model, it is necessary to account for a dispersion of effective nucleation sizes due to particle growth during the nucleation/agglomeration time step. For  $\lfloor \Delta n_{P_o}(t^{n+\frac{1}{2}}) \rfloor > 0$ , the  $\lfloor \Delta n_{P_o}(t^{n+\frac{1}{2}}) \rfloor$  particles are therefore allocated randomly following a target uniform distribution between  $v_o$  and  $v_o + G(v_o)\delta t$ .

#### 4.2.2.4 Time steps

As stated earlier, a fractional-step method is followed. The notation  $\delta t$  used above was schematic to explain the algorithm structure. The characteristic time step size of the first growth/loss sub-step (Fig. 4.1) is calculated following a usual Courant Friedrichs Lewy (CFL) condition (Ferziger and Perić, 1996), based on the velocity  $G(v)$  and sections discretization

$$\delta t_G = C \min [\Delta v_0 / |G(v_0)|, \dots, \Delta v_{M-1} / |G(v_{M-1})|] . \quad (4.2.29)$$

Calculations have been performed with  $C = 0.01$ , to fully secure stability for both stochastic and sectional parts.

The characteristic time step size of the nucleation-agglomeration sub-step of the algorithm is determined to limit the relative change of the distribution

$$\delta t_A = (\gamma + \sigma) \frac{N_T}{\left| \dot{H}_o + \dot{A}_T \right| + \sum_{i=0}^{M-1} \left| \dot{A}_i \right|}, \quad (4.2.30)$$

Table 4.3: Growth/Loss &amp; agglomeration parameters

Case	3(a)	3(b)	3(c)	3(d)	3(e)
Initial	$e^{-v}$	$e^{-v}$	$e^{-v}$	$e^{-v}$	$e^{-v}$
Growth kernel	$v$	$v$	$v$	$v$	$-v$
Agglo. kernel	0.1	1	10	1	1
Number of sections	40	40	40	80	40
Geometric grid, $F_s$	2	2	2	$\sqrt{2}$	2
Size range	$6.7 \cdot 10^{-4} - 7.3 \cdot 10^8$		$8.3 \cdot 10^{-4} - 9.1 \cdot 10^8$		$6.7 \cdot 10^{-11} - 73$

with  $\sigma = 0.02$  in the simulations presented thereafter. If particle nucleation dominates, as in the beginning of a calculation with a negligible initial distribution mostly present in the smallest section with also very few exchange of particles between sections, larger time steps may be allowed to let  $N_T$  increase faster until the exchange of particles between sections becomes significant, then  $\gamma = 1$  is used in (4.2.30). This specific ‘nucleation dominated’ regime is considered reached at a given time in a simulation if

$$\left| \dot{H}_o(t) + \dot{A}_T(t) \right| > 100 \cdot \sum_{i=0}^{M-1} \left| \dot{A}_i(t) \right|, \quad (4.2.31)$$

$$N_0(t)/N_T(t) > 0.99. \quad (4.2.32)$$

Otherwise,  $\gamma = 0$  is imposed in (4.2.30) to solve for the more general regimes of PSD evolution. For the test cases considered in this work,  $\delta t_G \leq \delta t_A$  and one or several surface growth/loss sub-iterations can be applied between two agglomeration/nucleation sub-iterations.  $\delta t_G$  is then further adjusted so that  $\delta t_A$  is one of its multiple, still verifying the stability condition.

### 4.3 Canonical test cases

Four main representative cases for which analytical solutions exist are considered. Sectional methods, based on two discretization of the growth term, and the hybrid stochastic/sectional approach discussed above are applied to simulate these canonical problems.

The number of sections set to discretize the normalised problems is fixed to 20, 40 or 80 depending on the case, for various size ranges (see the details in Tables 4.1 to 4.4). Following the literature, three types of grid discretization are used: uniform, geometric and exponential. Defining  $v_i^{inf}$  the inferior boundary of section  $i$ , the uniform grid reads

$$v_i^{inf} = v_0^{inf} + i\Delta v, \quad (4.3.1)$$

the geometric grid is constructed as in [Park and Rogak \(2004\)](#) following

$$v_i^{inf} = v_0^{inf} F_s^i, \quad (4.3.2)$$

and the exponential grid as in [Rigopoulos and Jones \(2003\)](#)<sup>2</sup>

$$v_i^{inf} = v_0^{inf} + v_0^{inf} \frac{1 - \alpha^i}{1 - \alpha}. \quad (4.3.3)$$

The values of  $F_s$  and  $\alpha$  are given in Tables 4.1 to 4.4.

The first main case features only growth and is broken into two sub-cases 1(a) and 1(b). Following [Sewerin and Rigopoulos \(2017\)](#), case 1(a) of Table 4.1 considers the advection of a unit step distribution, whose exact solution is a pure advection of the step function at the constant normalised speed  $G = 0.05$ .

<sup>2</sup>Exponent  $i$  is used instead of  $i - 1$  of [Rigopoulos and Jones \(2003\)](#) as  $i$  begins at 0 in the present case.

Table 4.4: Nucleation &amp; growth parameters

Case	4
Initial	$10^{-5} \delta(v_o)$
Growth kernel	$v$
Number of sections	40
Geometric grid, $F_s$	2
Size range	$0.7 - 7.3 \cdot 10^{11}$

Case 1(b) in Table 4.1 is from [Park and Rogak \(2004\)](#) and represents the pure growth of a set of mono-disperse particles. The initial particle size distribution is a delta function, which is translated in size space at a speed proportional to the particle volume  $G(v) = v$ . Cases 1(a) and 1(b) are quite stringent, since numerical diffusion can transform the expected delta function into a poly-disperse distribution.

The second case in Table 4.2 is pure agglomeration. Case 2(a) is with a fixed agglomeration frequency, as proposed in [Rigopoulos and Jones \(2003\)](#). From an initial exponential distribution  $\exp(-v)$ , the analytical solution of the time evolution of the PSD was discussed in [Scott \(1968\)](#),

$$n(v; t) = \frac{4}{(t+2)^2} \exp\left(-\frac{2v}{t+2}\right). \quad (4.3.4)$$

Case 2(b) is with a non-uniform collision frequency. Here, the Golovin sum kernel  $\beta(v_i, v_j) = (v_i + v_j)$  is retained to mimic the expected increase with volume of the collision frequency between two particles of characteristic sizes  $v_i$  and  $v_j$ . Starting from the same initial exponential distribution, the analytical solution of the PSD reads ([Scott, 1968](#); [Rigopoulos and Jones, 2003](#))

$$n(v; t) = \left(\frac{1-\theta}{\theta^{1/2}}\right) \cdot \frac{\exp(-v(\theta+1))}{v} \cdot I_1\left[2v\theta^{1/2}\right], \quad (4.3.5)$$

where  $\theta = 1 - \exp(-t)$  and  $I_1$  denotes the first order Bessel-I function.

In a third series of cases, agglomeration with either surface growth or loss is considered (Table 4.3). Starting from an initial exponential distribution, the time evolution follows ([Ramabhadran et al., 1976](#)):

$$n(v; t) = \frac{4}{(2 + \beta_0 t)^2} \exp\left(-\frac{2v \exp(-t)}{2 + \beta_0 t} - t\right). \quad (4.3.6)$$

The value of the size-independent collision kernel  $\beta_o$  is varied by two orders of magnitude ( $\beta_o = 0.1$  case 3(a),  $\beta_o = 1$  case 3(b), 3(d) and 3(e),  $\beta_o = 10$  case 3(c), Table 4.3). In case 3(d), in the comparison between the hybrid method and the fixed-sectional one, the latter benefits from twice the number of sections. In case 3(e), surface loss is applied instead of surface growth with  $G(v) = -v$ . The initial distribution and collision kernel are the same as in case 3(b).

Case 4 is the evolution of an initial exponential distribution submitted to nucleation and growth (Table 4.4), evolving into a uniform distribution for large times. The normalised nucleation kernel  $\dot{H}(v_o, t)$  is fixed to unity in this last test case.

## 4.4 Results

Analytical solutions are compared with simulation results. Simulations were run for all cases of Tables 4.1 to 4.4 with the hybrid stochastic/fixed-sectional approach and with the standard fixed-sectional method. Convection in size space was solved using either a 2-point or a 3-point algorithm ([Park and Rogak, 2004](#)) (see equations 3.5.22 and 3.5.18 respectively). Only test case 1(a) was not run with the 3-point algorithm, which is not designed to solve for growth on a uniform grid.

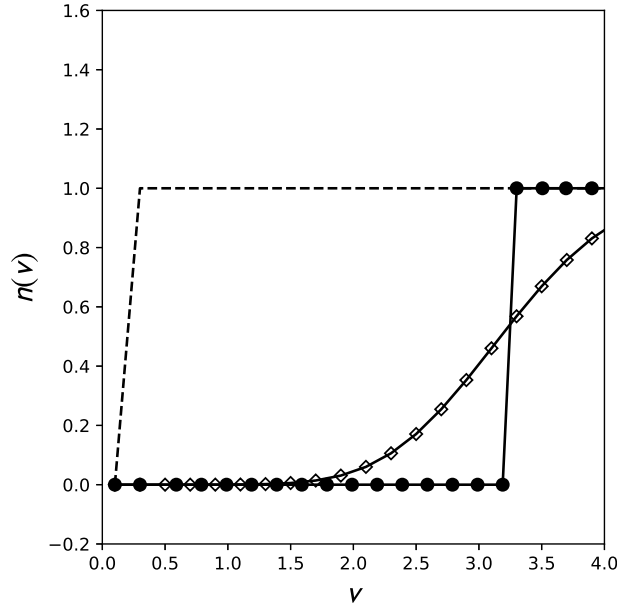


Figure 4.2: Particle Size Distribution  $n(v; t)$ . Growth: case 1(a) of Table 4.1. Dashed line: initial distribution (jump is between centred sections values). Normalised time  $t = 60$ . Line with empty diamonds: 2-point sectional method. Line with full circles: hybrid method,  $N_P = 10^3$  (values are shown at  $v_i^*$  (Eq. (4.2.25))).

In case 1(a), the hybrid method perfectly reproduces the analytical solution (Fig. 4.2), with the pure convection of the step function. As expected, applying growth directly on the stochastic particles enables to convect the distribution in size space with no numerical diffusion. Similar results were obtained by Sewerin and Rigopoulos (2017) using explicit adaptive grid method (EAGM), while in Fig. 4.2, the 2-point fixed sectional approach yields results close to those of fully upwinded orthogonal collocation finite element method (OCFEM), see Fig. 7 of Rigopoulos and Jones (2003).

Case 1(b) of Table 4.1 features an initial monodisperse distribution submitted to growth only, with a particle surface growth rate proportional to the particle volume. The expected solution is thus a translation of the distribution in size space. Figure 4.3 shows that the fixed-sectional methods (line with diamonds and circles) would need much more advanced numerics to capture this extreme case. However, the hybrid method operating here without any residual, returns the exact solution. In specific aerosol flow zones, where nucleation and pure growth can dominate the physics, the spurious spreading of the distributions observed with sectional methods could strongly impair the calibration of the physical models.

The pure agglomeration case 2(a) of Table 4.2, with a fixed agglomeration frequency, is simulated with the hybrid approach for  $N_P = 10^3$ ,  $10^4$  and  $10^5$ . The initial distribution and the solutions at two successive times are shown in Fig. 4.4. To assess the impact of the residual number density (Eq. (4.2.21)), Figs 4.4a, 4.4b and 4.4c are obtained forcing  $\alpha_R = 0$  (Eq. (4.2.22)). As  $N_P$  is decreased from  $10^5$  to  $10^3$ , the effect of the round-off then becomes visible. The introduction of the procedure discussed above to deal with the residual part, allows for alleviating this effect to better match the solution (Fig. 4.4d). The case 2(b) of Table 4.2 with the Golovin agglomeration kernel (Eq. (4.3.5)) is also perfectly reproduced (Fig. 4.5).

The cases 3(a), (b) and (c), with both surface growth and agglomeration of the particles, are shown in Fig. 4.6. Here comparisons are made between the exact solution given by the relation (4.3.6), the solution with the hybrid method and the solutions with the fixed-sectional method using the classical 2-point and 3-point discretization for growth (Park and Rogak, 2004). Three collision parameters are applied ( $\beta_o = 0.1, 1.0$  and  $10$ ) and results are given in both linear and log

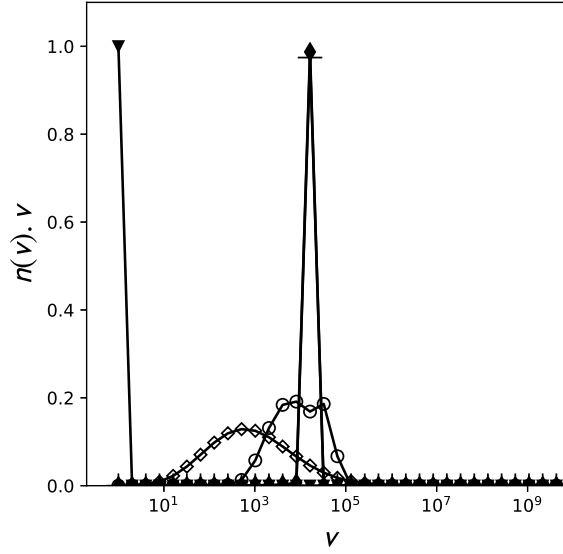


Figure 4.3: Size Distribution  $n(v;t) \cdot v$ . Growth: case 1(b) of Table 4.1. Triangle: Initial distribution. Plus symbol: Analytical solution. Line with empty diamonds: sectional 2-point method. Line with circles: sectional park 3-point method (Park and Rogak, 2004). Full diamond symbols: hybrid method without residual term,  $\alpha_R = 0$ ,  $N_P = 10^3$ .

scale for the amplitude of the PSD. As expected, the sectional 3-point method is more accurate than its 2-point counterpart (Fig. 4.6). The hybrid stochastic/fixed-sectional method returns the best results, with a better prediction of the peak value and less spurious diffusion of the distribution. The comparison between log-scale and linear plots also illustrates the risk in concluding from log-plots only, specifically for physical problems with high sensitivity to small fluctuations of size around a targeted peak level. Even in case 3(d),  $\beta_o = 1$  with a much finer grid for the sectional method, which results in a number of sections multiplied by two ( $M = 80$ ), still keeping ( $M = 40$ ) for the hybrid method, the latter achieves a similar level of accuracy as compared with the three-point fixed-sectional method and performs better than the two-point one (Fig. 4.7). The case 3(e) with surface loss (Fig. 4.8) combined with agglomeration shows that the sectional 3-point method overestimates the peak value of the distribution with a too narrow size distribution, as a result of the effect of the flux-limiting in case of negative velocity. On the opposite, the hybrid method follows with much better accuracy the analytical solution.

In case 4 of Table 4.4, simultaneous growth and constant nucleation are applied as in Park and Rogak (2004). A negligible initial distribution, orders of magnitude smaller than the expected converged solution, is introduced to initialize the stochastic particles. Both fixed-sectional and hybrid methods are applied and results are seen in Fig. 4.9. The hybrid method reproduces the steep moving front induced by simultaneous growth and nucleation, with results closer to the analytical number density than those of the 3-point fixed-sectional method over the whole range of particles sizes. The 3-point fixed-sectional method overestimates the number density for  $v \in [2, 10^3]$ . Then, from sizes around  $2 \cdot 10^3$  up to the theoretically moving front, the number density is largely underestimated by the 3-point fixed-sectional method. The 2-point method is highly diffusive as compared with the 3-point and hybrid approaches.

In addition to the visualisation of the PSD distributions, to verify that no additional error accumulates with the hybrid method compared with the sectional ones, three measures of the error against  $n(v;t)$ , the exact solutions of the canonical test cases given by (4.3.4), (4.3.5) and (4.3.6), have been computed.  $\epsilon_{M_q}$ , with  $q = 1$  or  $2$ , is the departure in % between the  $q$ -th moment of the

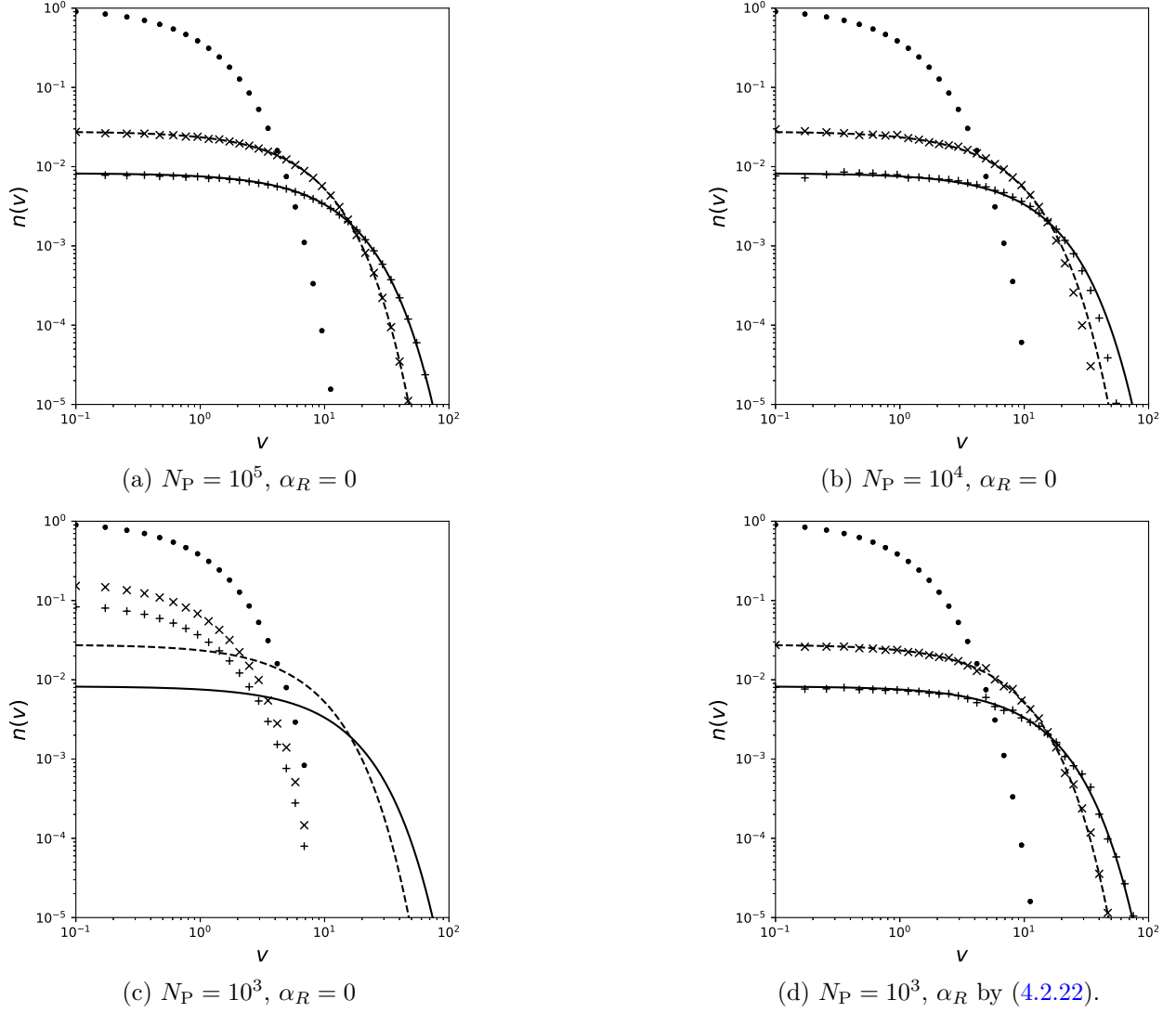


Figure 4.4: Particle Size Distribution  $n(v; t)$ . Size independent agglomeration: case 2(a) of Table 4.2 (Eq. (4.3.4)). Points: initial distribution.  $t = 10$ , dashed line: analytical solution, crosses: hybrid method.  $t = 20$ , solid line: analytical solution, plus: hybrid method. (a)-(c): without residual term,  $\alpha_R = 0$ . (d): with residual term (Eq. (4.2.22)).

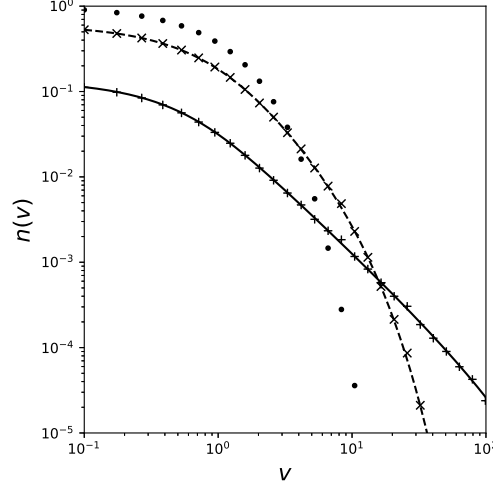


Figure 4.5: Particle Size Distribution  $n(v; t)$ . Size dependant agglomeration: case 2(b) of Table 4.2 (Eq. (4.3.4)). Points: initial distribution.  $t = 0.5$ , dashed line: analytical solution, crosses: Hybrid method.  $t = 2$ , solid line: analytical solution, plus: hybrid method,  $N_P = 10^4$ .

analytical solution

$$M_q(t) = \int_{v_o}^{v_M} n(v; t) v^q dv, \quad (4.4.1)$$

against either the moment of the hybrid method

$$M_q^{Hyb}(t) = \sum_{i=0}^{M-1} \left( \frac{N_T(t)}{N_P} \sum_{k=1}^{n_{P_i}(t)} \left( v_i^k(t) \right)^q + N_i^R(t) (v_i^*(t))^q \right) \quad (4.4.2)$$

with  $v_i^*(t)$  from (4.2.25), or the moment of the fixed-sectional method

$$M_q^{Sec}(t) = \sum_{i=0}^{M-1} N_i(t) v_i^q. \quad (4.4.3)$$

As expected, the fixed-sectional methods are accurate on the integral first moment of the distribution (Table 4.5). The hybrid stochastic/fixed-sectional approach returns values of  $\epsilon_{M_1}$  which are also of the order of a few percent. The error on the second moment,  $\epsilon_{M_2}$ , reveals the accumulation of a much larger level of error with the sectional methods as soon as surface growth or loss is acting on the PSD (Table 4.5), confirming the better description of PSD shape with the hybrid approach.

The third measure is based on the Earth Mover's Distance (EMD) (Rubner et al., 1998), or Wasserstein metric, computed using the package 'emdist' of the cran project (Urbanek, 2012). EMD is a statistical metric that represents the distance between two probability distributions. It does not require the same discretization of the compared distributions. EMD has previously been used for Particle Size Distributions and compared with other distance measures (Hu et al., 2018). The EMD is normalised by the standard deviation of the exact distribution. The hybrid method reports for  $\epsilon_{EMD}$  similar trends than with the fixed-sectional methods (Table 4.5), with better estimation in case 3 (agglomeration and growth) and case 4 (nucleation and growth), as expected from the above discussion.

With fixed-sectional methods, the error on the PSD usually increases as  $\mathcal{R}_\tau$ , the ratio between the characteristic growth and agglomeration times, decreases (Park and Rogak, 2004), *i.e.*, when growth tends to dominate over agglomeration. Going from case 3(c) to 3(b) and 3(a), the collision frequency  $\beta_0$  decreases while keeping the surface growth rate constant (Table 4.3), which is

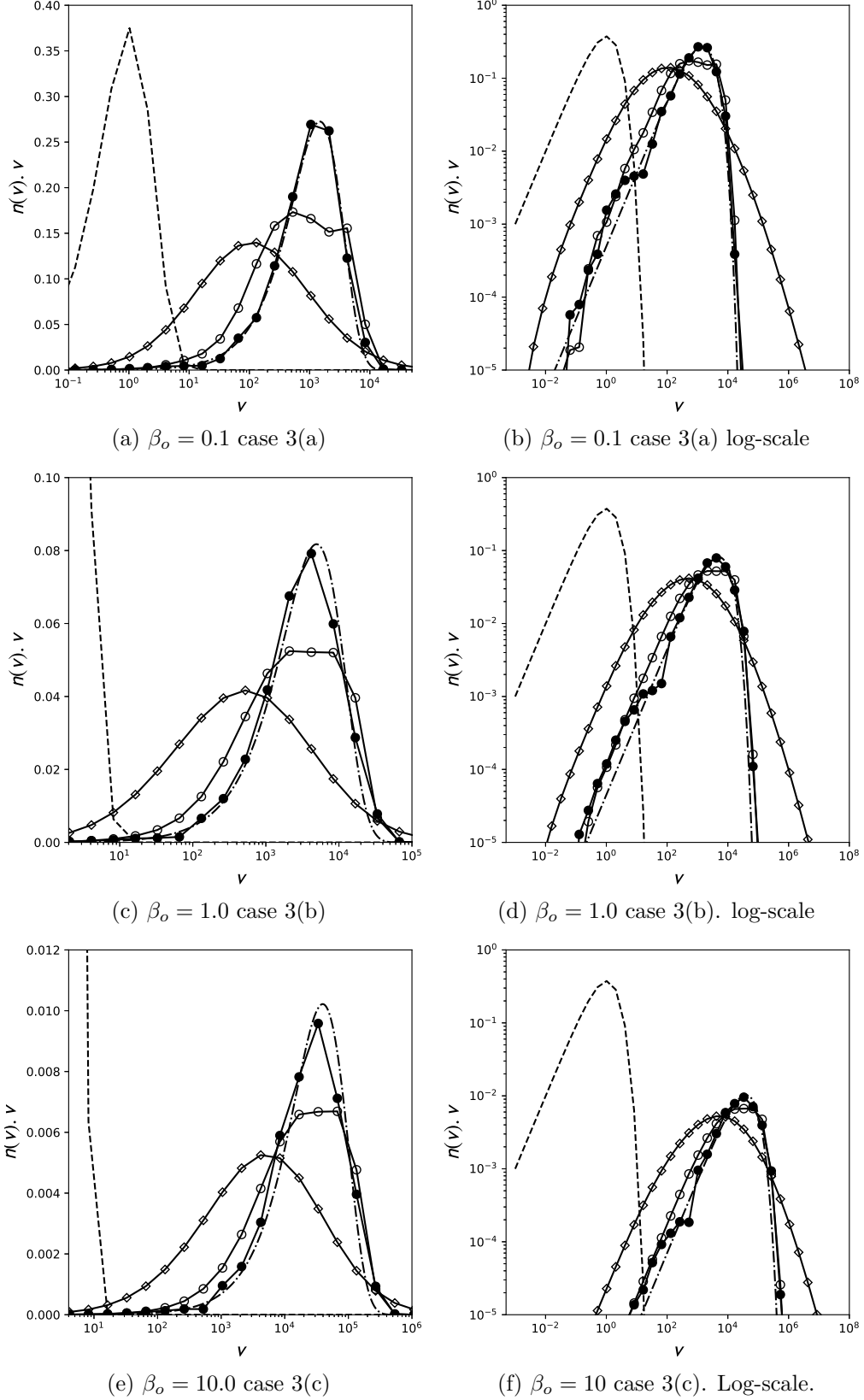


Figure 4.6: Size Distribution  $n(v; t) \cdot v$ . Surface growth ( $G(v) = v$ ) & agglomeration: case 3(a), 3(b), 3(c) of Table 4.3.  $\beta_o$ : size-independent collision kernel (Eq. (4.3.6)). Dashed line: initial distribution.  $t = 7$ , dashed dotted line: analytical solution. Line with empty diamonds: 2-point sectional method. Line with empty circles: 3-point sectional method. Line with full circles: hybrid method,  $N_P = 10^3$ .

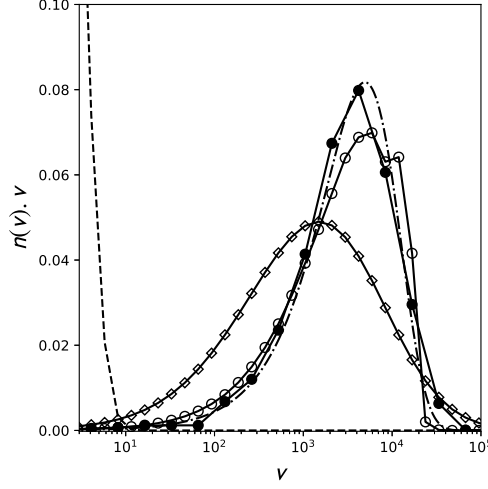


Figure 4.7: Size Distribution  $n(v; t) \cdot v$ . Growth & agglomeration: case 3(d) of Table 4.3. Dashed line: initial distribution. Dashed dotted line: analytical solution at  $t = 7$ . Line with empty diamonds: 2-point sectional method ( $M = 80$  sections). Line with empty circles: 3-point sectional method ( $M = 80$  sections). Line with full circles: hybrid method,  $N_P = 10^3$  ( $M = 40$  sections).

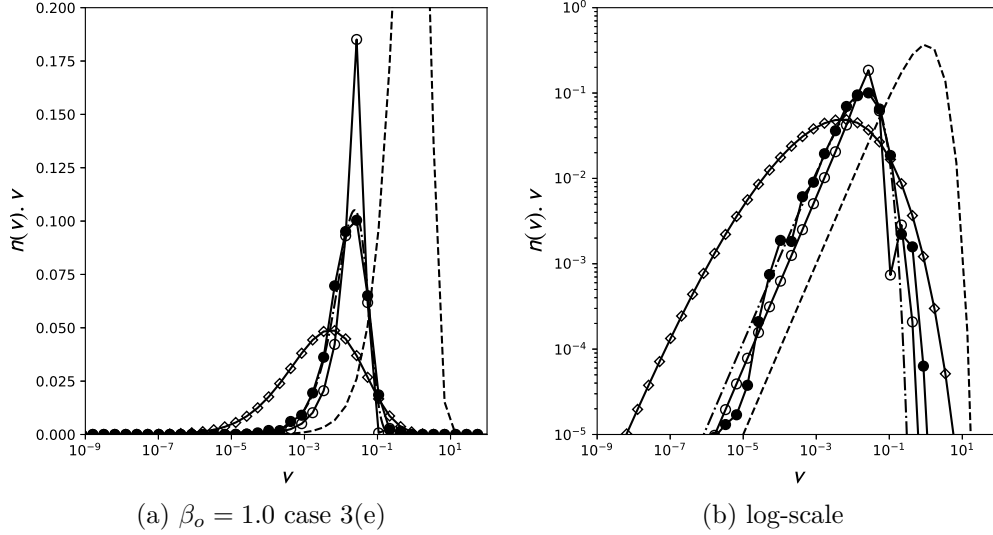


Figure 4.8: Size Distribution  $n(v; t) \cdot v$ . Surface loss ( $G(v) = -v$ ) & agglomeration: case 3(e) of Table 4.3.  $\beta_o$ : size-independent collision kernel (Eq. (4.3.6)). Dashed line: initial distribution.  $t = 5$ , dashed dotted line: analytical solution. Line with empty diamonds: 2-point sectional method. Line with empty circles: 3-point sectional method. Line with full circles: hybrid method,  $N_P = 10^3$ .

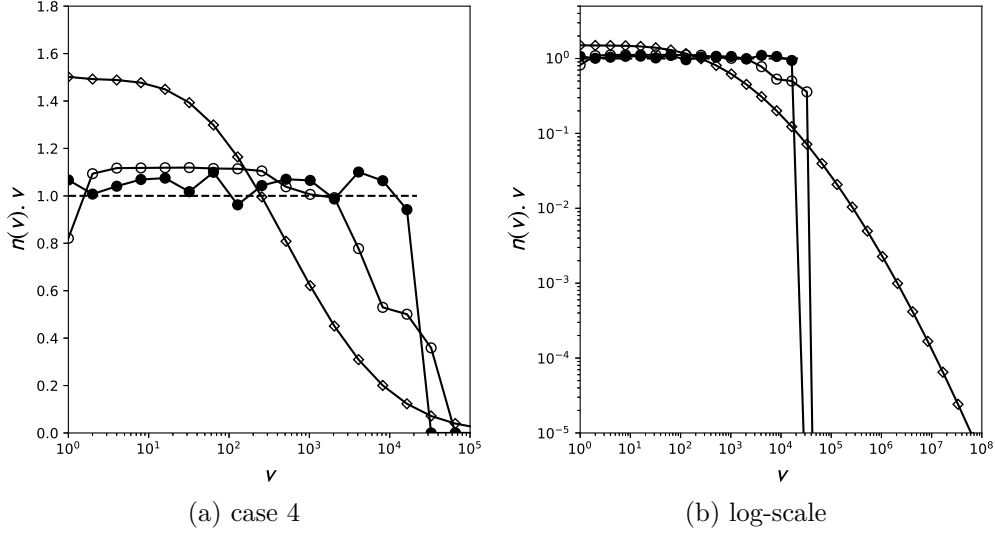


Figure 4.9: Size Distribution  $n(v; t) \cdot v$ . Nucleation and growth Case 4 of Table 4.4. Dash-dot line: analytical solution at  $t = 9.7$ . Line with empty diamonds: 2-point sectional method. Line with empty circles: 3-point sectional method. Line with full circles: hybrid method,  $N_P = 10^3$ .

equivalent to decreasing  $\mathcal{R}_\tau$ . This results in higher levels of  $\epsilon_{EMD}$  for both 2-point and 3-point fixed-sectional methods, while  $\epsilon_{EMD}$  remains relatively low and almost constant with the hybrid method (Table 4.5). Similarly, the error on the second moment  $\epsilon_{M_2}$  increases from case 3(c) to 3(a), especially using the 2-point fixed-sectional method.

Using the same sections discretization, the extra CPU cost of the hybrid method stays moderate (Table 4.5), between 8% and 42%, except for cases 3(a) and 3(b) featuring parameters requiring sub-stepping to solve growth because of the small  $\mathcal{R}_\tau$  ratios. Overall, the sectional method yields lower error as mesh is refined, but with a CPU cost rapidly growing. For instance, in the case 3(d), where the grid of the sectional method has been refined to reach the accuracy of the hybrid method, the sectional method costs about 8 times more than the novel hybrid approach.

## 4.5 Convergence and response to resolution parameters

The proposed hybrid method features two resolution parameters:  $N_P$  the total number of stochastic particles, and  $M$  the number of sections discretizing the particle size space. The effects of these parameters on accuracy and CPU cost are now assessed. The CPU cost is normalised by the computational cost of the 3-point sectional method for  $M = 30$ .

Test case 3(b) (growth and agglomeration) is chosen for this analysis with particle volume  $v$  ranging from  $6.66 \cdot 10^{-7}$  to  $7.3 \cdot 10^5$ . On the fixed-sectional part, geometric grids are used and  $M$  and  $F_s$  (Eq. (4.3.2)) are varied, keeping the size range constant.  $N_P$  is varied for the stochastic part.

Comparison of the obtained solutions through the hybrid method and the sectional 3-point method is performed at the normalised time  $t = 7$ . A measure of normalized  $L_1$  error of calculated distributions against analytical solutions is provided. To make error comparison more meaningful across solutions obtained with different values of  $M$ , for each solution, the  $M$  values of  $N_i/\Delta v_i$  obtained after calculation are linearly interpolated over  $M_R = 1000$  logarithmically spaced  $v_i$  points over the size range. Then, these  $M_R$  calculated  $N_i/\Delta v_i$  values are compared with the analytical

Table 4.5: Accuracy and CPU costs. Case 1: Pure growth. Case 2: Pure agglomeration, Case 3: Growth/Loss &amp; agglomeration. Case 4: Nucleation &amp; growth.

Case	Error	Method		
		Sectional 2pt	Sectional 3pt	Hybrid
1(a)	$\epsilon_{M_1}(\%)$	-0.13	-	-0.0078
	$\epsilon_{M_2}(\%)$	1.5	-	-0.012
	$\epsilon_{EMD}$	0.11	-	1.9e-17
	CPU time	1.0	-	1.1
1(b)	$\epsilon_{M_1}(\%)$	-2.9	-2.9	-2.7
	$\epsilon_{M_2}(\%)$	770 845	105	-5
	CPU time	1.0	1.0	1.4
2(a)	$\epsilon_{M_1}(\%)$	0.4	0.4	-0.1
	$\epsilon_{M_2}(\%)$	1.6	1.6	0.7
	$\epsilon_{EMD}$	0.006	0.006	0.013
	CPU time	1.0	1.0	1.3
2(b)	$\epsilon_{M_1}(\%)$	-1.1	-1.1	-2.2
	$\epsilon_{M_2}(\%)$	0.4	0.4	-1.4
	$\epsilon_{EMD}$	0.0008	0.0008	0.0048
	CPU time	1.0	1.0	1.2
3(a)	$\epsilon_{M_1}(\%)$	5.4	5.6	-0.5
	$\epsilon_{M_2}(\%)$	48 783	54	1.8
	$\epsilon_{EMD}$	0.62	0.19	0.06
	CPU time	1.0	1.1	1.7
3(b)	$\epsilon_{M_1}(\%)$	5.4	5.7	0.9
	$\epsilon_{M_2}(\%)$	22 141	49	16
	$\epsilon_{EMD}$	0.60	0.17	0.10
	CPU time	1.0	1.0	1.3
3(c)	$\epsilon_{M_1}(\%)$	5.7	5.5	0.4
	$\epsilon_{M_2}(\%)$	9 811	49	17
	$\epsilon_{EMD}$	0.57	0.16	0.13
	CPU time	1.0	1.0	1.1
3(d)	$\epsilon_{M_1}(\%)$	0.6	0.5	0.9
	$\epsilon_{M_2}(\%)$	776	-1.4	16
	$\epsilon_{EMD}$	0.44	0.08	0.10
	CPU time	1.0	1.1	0.1
3(e)	$\epsilon_{M_1}(\%)$	5.4	5.8	1.1
	$\epsilon_{M_2}(\%)$	760	33	32
	$\epsilon_{EMD}$	0.47	0.24	0.09
	CPU time	1.0	1.1	1.2
4	$\epsilon_{M_1}(\%)$	-3.4	-3.4	-3.4
	$\epsilon_{M_2}(\%)$	696 121	60	-9
	$\epsilon_{EMD}$	0.66	0.18	0.02
	CPU time	1.0	1.0	1.5

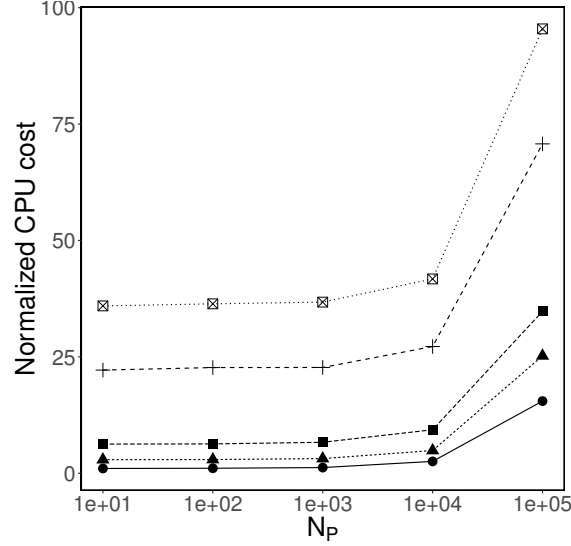


Figure 4.10: Normalized CPU cost vs  $N_P$  for different values of  $M$ . Hybrid method. Solid line with full circles:  $M = 30$ . Dotted line with triangles:  $M = 40$ . Dashed line with full squares:  $M = 50$ . Dashed line with plus symbols:  $M = 70$ . Dotted line with cross-square symbols:  $M = 80$ . Agglomeration and growth (Case 3, Table 4.3).

$n(v_i)$  values. The error metric is defined as:

$$L_{1_{error}} = \frac{\sum_{i=1}^{M_R} |N_i / \Delta v_i - n(v_i)| \cdot \Delta v_i}{\sum_{i=1}^{M_R} n(v_i) \cdot \Delta v_i}. \quad (4.5.1)$$

Let us first examine the evolution of the normalized CPU cost as a function of  $N_P$  and  $M$ . Figure 4.10 shows that from  $N_P = 10$  to  $N_P = 1000$ , CPU cost is nearly constant for a given value of  $M$ . A slight increase is observed from  $N_P = 1000$  to  $N_P = 10^4$  and then there is a sharp increase from  $N_P = 10^4$  to  $N_P = 10^5$ . This is because the calculation of agglomeration source terms is made at the level of the sections with a CPU cost scaling with  $M$ . On the other hand, stochastic particles need to be counted in each section and then reallocated over the sections according to the calculated agglomeration (and nucleation) source terms. The CPU cost of these operations depends on  $M$  and  $N_P$ . In this test case, the cost linked to stochastic particles count and reallocation stays low as compared with the one linked to agglomeration source terms calculation up to  $N_P = 1000$  and becomes significant for  $N_P = 10000$  and  $N_P = 10^5$ . Figure 4.11 confirms that CPU cost depends on  $M$  for all values of  $N_P$ . From  $N_P = 10$  to  $N_P = 1000$  the CPU overhead linked to the use of the hybrid method instead of the sectional method is relatively low as compared with the overcost caused by an increase of  $M$  (the lines are practically superposed at the plotted scale). The overcost stays moderate for  $N_P = 10000$  and turns very high for  $N_P = 10^5$ .

Now, the impact of  $M$  and  $N_P$  on accuracy is examined. Figure 4.12 shows that for  $N_P = 10$  and  $N_P = 100$  the hybrid method cannot perform well. After increasing  $N_P$  up to 1000, the error on the PSD significantly decreases. However, for the tested values of  $M$ , further increasing  $N_P$  only decreases  $L_{1_{error}}$  marginally. Once a sufficient value of  $N_P$  is reached,  $M$  becomes the main driver of  $L_{1_{error}}$ .

Figure 4.13a shows that the error decreases with  $M$  for both methods. Moreover, the hybrid method yields lower error than the 3-point sectional method for the whole range of  $M$  tested. Figure 4.13b confirms that the hybrid method constitutes an interesting tradeoff between accuracy and CPU cost as compared with the 3-point sectional methods. Figure 4.14 illustrates the convergence of both 3-point sectional and hybrid method versus  $M$ .

Finally, the degree of variability of the solution induced by the random character of particle allocation is examined. Figure 4.15 shows average values and standard deviation over 10 runs of

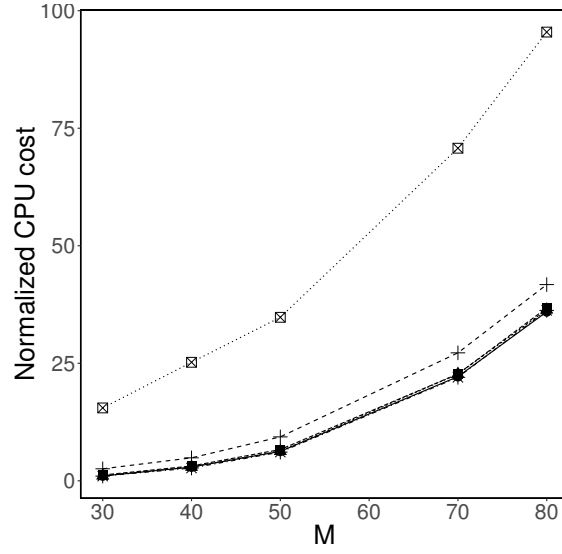


Figure 4.11: Normalized CPU cost vs  $M$  for different values of  $N_P$  (Hybrid method) and for the 3-point sectional method. Solid line with full circles:  $N_P = 10$ . Dotted line with triangles:  $N_P = 100$ . Dashed line with full squares:  $N_P = 1000$ . Dashed line with plus symbols:  $N_P = 10000$ . Dotted line with cross-square symbols:  $N_P = 10^5$ . Solid line with stars: 3-point sectional. (Case 3, Table 4.3.)

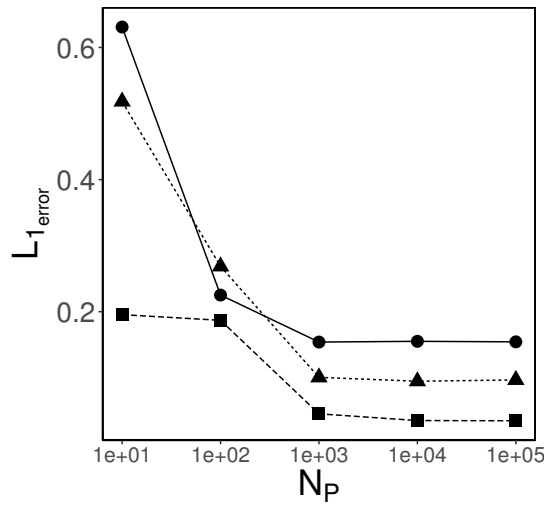


Figure 4.12:  $L_1$  error vs  $N_P$  for different values of  $M$  (Hybrid method). Solid line with full circles:  $M = 30$ . Dotted line with triangles:  $M = 40$ . Dashed line with full squares:  $M = 80$ . (Case 3, Table 4.3 at the normalised time  $t = 7$ .)

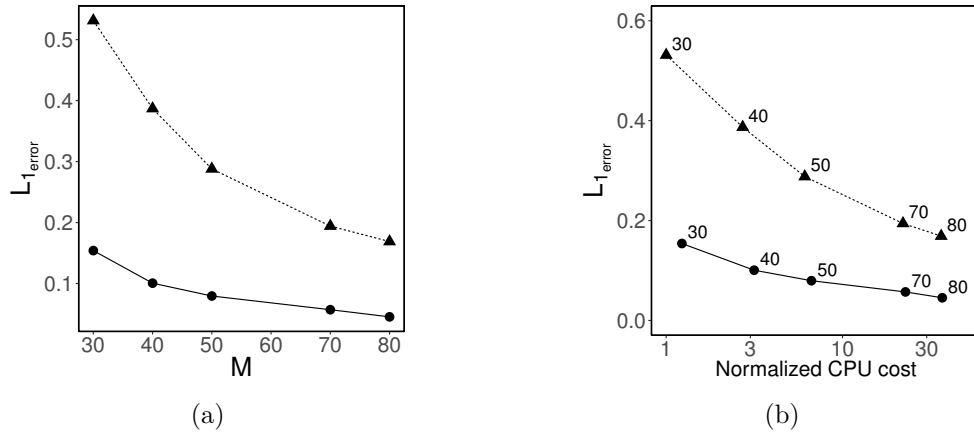


Figure 4.13: (a):  $L_{1_{error}}$  vs  $M$ . (b):  $L_{1_{error}}$  vs normalized CPU cost. Solid line with full circles: Hybrid method,  $N_P = 1000$ . Dotted line with triangles: 3-point sectional method. Text labels in (b):  $M$ . (Case 3, Table 4.3 at the normalised time  $t = 7$ .)

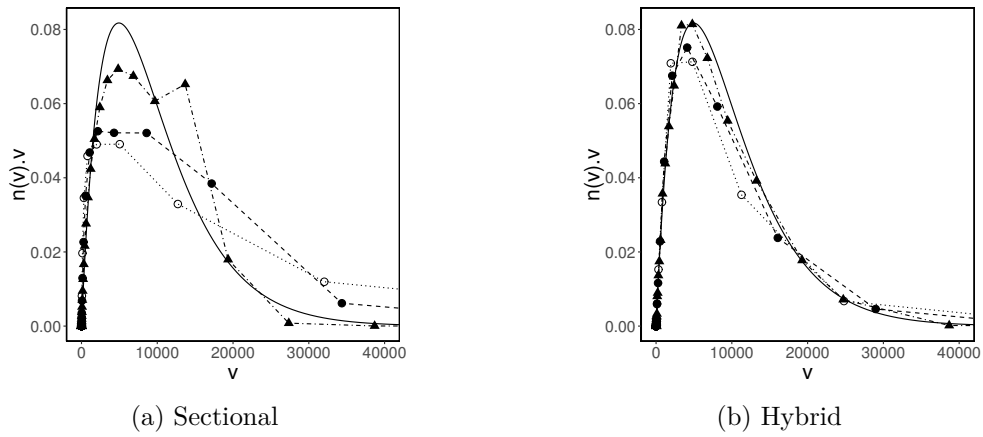


Figure 4.14: Size distribution  $n(v; t) \cdot v$  for different values of  $M$ . (a): 3-point sectional method. (b): Hybrid method,  $N_P = 1000$ . Solid line: analytical solution at  $t = 7$ . Dashed-dot line with triangles:  $M = 80$ . Dashed line with full circles:  $M = 40$ . Dotted line with empty circles:  $M = 30$ . (Case 3, Table 4.3).

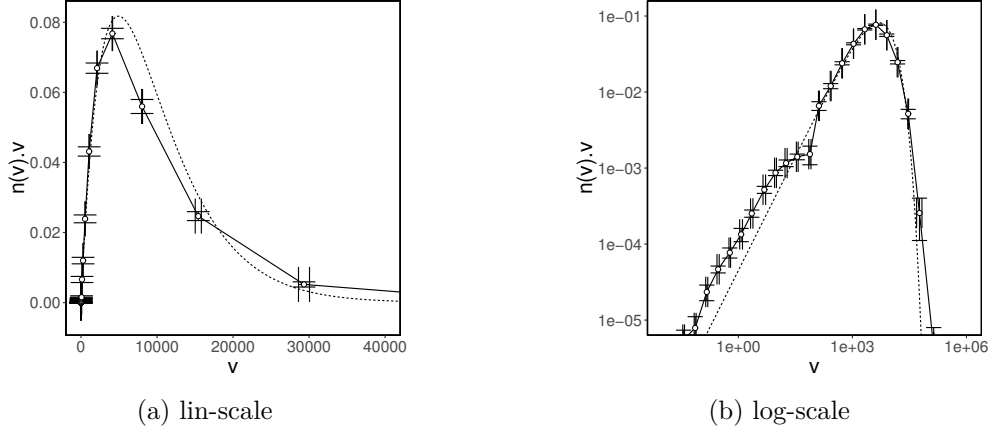


Figure 4.15: Average values and standard deviation over 10 runs. Dashed line: analytical solution at  $t = 7.0$ . Solid line with empty circles: hybrid method solution at  $t = 7.0$  with  $M = 40$  and  $N_P = 1000$ . Vertical error bars: standard deviation around average values of  $n(v) \cdot v$ . (Case 3, Table 4.3.) Horizontal error bars: standard deviation around average values of  $v_i^*$  (Eq. (4.2.25)).

$n(v) \cdot v$  and of  $v_i^*$  (Eq. (4.2.25)) for case 3(b), with  $M = 40$  and  $N_P = 1000$ . Non-negligible variance is observed, especially at the tails of the distribution where less stochastic particles are present. However, the distribution does not qualitatively vary from one run to the other. The observed standard deviation on  $L_{1_{error}}$  over these 10 runs is 0.007 which represents about 6.5% of average  $L_{1_{error}}$ . This enables us to be confident on the level of accuracy of the solution obtained after only one run, without averaging over several runs (at least for  $N_P \geq 1000$ ).

## 4.6 Chapter summary

A novel hybrid stochastic/sectional method for solving the population balance equation (PBE) has been presented. To design this numerical method, the particle size distribution (PSD) is decomposed into the total number density of particles times the particle size probability density function (PDF). The PDF is discretized into a fixed number of stochastic particles whose evolution is governed by a Monte Carlo procedure. The stochastic particles carry information on their size and the surface growth/loss is then solved in a direct manner, without resorting to any discretization of the size space. This represents a serious advantage compared with fixed-sectional methods, which require some specific treatment to control the non-linear convective term representative of growth/loss in size space. These numerical treatments usually go with artificial diffusion of the PSD in size space.

In this hybrid approach, the agglomeration and nucleation sources are however computed following a fixed-sectional discretization of sizes. These sources or sinks are then transformed into numbers of stochastic particles to be exchanged between sections following a Monte Carlo procedure. The transformation of these sources into integer numbers of particles leads to residuals, which are cumulated and transported through a usual 3-point fixed-sectional approach, thus allowing for securing accuracy, even with a moderate number of stochastic particles and then at a moderate CPU cost.

## Chapter 5

# Application to a laminar premixed flame

### Contents

<b>5.1</b>	<b>Modeling of nucleation, growth and agglomeration source terms . . . .</b>	<b>98</b>
<b>5.2</b>	<b>Simulation of a one-dimensional freely propagating laminar premixed flame . . . . .</b>	<b>100</b>
5.2.1	Flow configuration and model parameters . . . . .	100
5.2.2	Results . . . . .	101
<b>5.3</b>	<b>Parametric analysis of aggregate shape modeling . . . . .</b>	<b>104</b>
<b>5.4</b>	<b>Comparison between hybrid and sectional methods . . . . .</b>	<b>107</b>

In this chapter, the HYPE method is tested on a laminar premixed flame. First, the models used for the physical source terms of nucleation, growth and agglomeration are presented. Then, the experimental flame is briefly described as well as the simulation settings. Subsequently, the results in terms of gaseous species, integral soot quantities and Particle Size Distribution are presented. A discussion on aggregate shape modeling and a parametric analysis are carried out. Finally, the results of the hybrid (HYPE) and fixed-sectional method are compared.

## 5.1 Modeling of nucleation, growth and agglomeration source terms

Each stochastic particle is associated with a volume  $v^k$ . Soot particles are considered spherical (usual assumption in the range of sizes studied [Zhao et al. \(2003\)](#); [Aubagnac-Karkar et al. \(2015\)](#)), except for the results presented in section 5.3.

Well established nucleation modeling by the collision of two pyrene ( $\text{C}_{16}\text{H}_{10}$ ) is used ([Appel et al., 2000](#)),

$$\dot{H}(\underline{x}, t) = 0.5\beta_{\text{py}}N_{\text{py}}^2, \quad (5.1.1)$$

with

$$N_{\text{py}} = [\text{C}_{16}\text{H}_{10}]\mathcal{N}_A, \quad (5.1.2)$$

the volume number of pyrene molecules,  $\mathcal{N}_A$  is the Avogadro constant.

The surface growth rate  $G$  is controlled by (i) condensation of pyrene molecules on soot particles ( $G_{\text{Cond}}$ ), (ii)  $\text{C}_2\text{H}_2$  (acetylene) addition by the HACA mechanism and surface oxidation by  $\text{O}_2$  and  $\text{OH}$  ( $G_{\text{HACA, Oxi}}$ ) ([Appel et al., 2000](#)).  $G(v^k; \underline{x}, t) = G_{\text{Cond}}(v^k; \underline{x}, t) + G_{\text{HACA, Oxi}}(v^k; \underline{x}, t)$  is applied to each particle  $v^k$  through equation (4.2.11). The condensation source term is:

$$G_{\text{Cond}}(v^k; \underline{x}, t) = m_{\text{py}}\dot{H}_{\text{Cond}}(v^k; \underline{x}, t)/N_i(\underline{x}, t), \quad (5.1.3)$$

(for  $v^k \in I_{v_i}$ ), with  $m_{\text{py}}$  the mass of one pyrene molecule and

$$\dot{H}_{\text{Cond}}(v^k; \underline{x}, t) = \beta_{v^k, \text{py}} N_i(\underline{x}, t) N_{\text{py}}. \quad (5.1.4)$$

The surface reaction source term is

$$G_{\text{HACA}, \text{Oxi}}(v^k; \underline{x}, t) = (\dot{\omega}_{\text{C}_2\text{H}_2} + \dot{\omega}_{\text{O}_2} + \dot{\omega}_{\text{OH}}) / N_i(\underline{x}, t), \quad (5.1.5)$$

with the chemical sources,

$$\dot{\omega}_{\text{C}_2\text{H}_2} = 2W_{\text{C}} k_{\text{C}_2\text{H}_2} [R_{v^k}] [\text{C}_2\text{H}_2], \quad (5.1.6)$$

$$\dot{\omega}_{\text{O}_2} = -2W_{\text{C}} k_{\text{O}_2} [R_{v^k}] [\text{O}_2], \quad (5.1.7)$$

$$\dot{\omega}_{\text{OH}} = -W_{\text{C}} k_{\text{OH}} [S_{v^k}] [\text{OH}], \quad (5.1.8)$$

where  $W_{\text{C}}$  is the molar mass of Carbon, and  $k_{\text{C}_2\text{H}_2}$ ,  $k_{\text{O}_2}$ ,  $k_{\text{OH}}$  are calculated using the kinetic parameters given in Appel et al. (2000).  $[S_{v^k}]$  and  $[R_{v^k}]$ , are obtained as in Aubagnac-Karkar et al. (2015); Appel et al. (2000) through

$$[S_{v^k}] + [R_{v^k}] = s^k \chi \alpha_{\text{HACA}} N_i(\underline{x}, t) / \mathcal{N}_A, \quad (5.1.9)$$

$s^k$  is the particle surface and  $\chi$  is the number of sites per unit surface of soot.  $[S_{v^k}]$  is representative of stable sites at soot particles surface and  $[R_{v^k}]$  of radical sites.  $[R_{v^k}]$  is calculated assuming that radical sites are in quasi-steady state.  $\alpha_{\text{HACA}}(v^k)$  is adapted from Appel et al. (2000), calculating its value for each stochastic particle instead of using the first size moment to calculate a unique value of  $\alpha_{\text{HACA}}$ . In practice

$$\alpha_{\text{HACA}}(v^k) = \tanh \left( \frac{a}{\log(\rho_{\text{soot}} \times v^k / (W_{\text{C}} / \mathcal{N}_A))} + b \right), \quad (5.1.10)$$

where  $a = 12.65 - 0.00563T$  and  $b = -1.38 + 0.00068T$ . This dependence of  $\alpha_{\text{HACA}}(v^k)$  on particle size expresses the fact that mature particles feature a lower proportion of active sites per unit of surface.

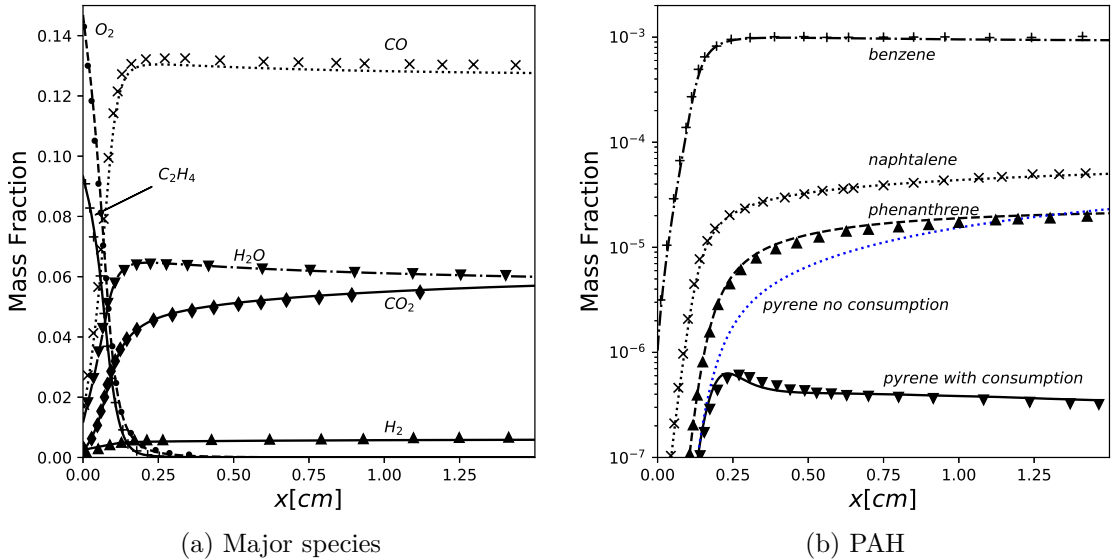


Figure 5.1: Species mass fractions. Lines: present simulation. Symbols: reference Zhao et al. (2003).

Agglomeration is described by the standard Smoluchowski equation. The collision rates entering the Smoluchowski equation expressing  $\dot{A}_i(\underline{x}, t)$ , are calculated depending on the Knudsen number

as in [Kazakov and Frenklach \(1998\)](#); [Blanquart and Pitsch \(2009b\)](#), with  $\beta_{v_i, v_j}^{f, m}$  in the free molecular regime and  $\beta_{v_i, v_j}^{cont}$  in the continuum regime. The harmonic mean of the asymptotic values is taken in the transition regime  $\beta_{v_i, v_j}^{f, m} \beta_{v_i, v_j}^{cont} / (\beta_{v_i, v_j}^{f, m} + \beta_{v_i, v_j}^{cont})$ . Collision frequencies are calculated in the same manner for collisions between pyrene molecules (nucleation) or between pyrene molecules and soot particles (condensation). The Smoluchowski equation is discretized following equation 3.5.1 to account for the source term  $\dot{A}_i(\underline{x}, t)$  in each  $I_{v_i}$  interval (or section).

## 5.2 Simulation of a one-dimensional freely propagating laminar premixed flame

### 5.2.1 Flow configuration and model parameters

A one-dimensional fuel-rich ( $\phi = 2.07$ ) laminar premixed ethylene-argon-oxygen flame [Zhao et al. \(2003\)](#) is simulated at ambient pressure. The velocity, temperature and mole fractions in the fresh gases are 8.26 cm/s, 300 K,  $X_{C_2H_4} = 0.133$ ,  $X_{O_2} = 0.193$  and  $X_{Ar} = 0.674$ , respectively. Soot particles whose mobility diameter is superior to 3 nm were detected through SMPS, to provide PSD at several heights above burner. Both measurements and simulations reported in [Zhao et al. \(2003\)](#) will serve as reference to evaluate the proposed soot modeling.

The gaseous one-dimensional flame is first computed with complex molecular transport and the detailed chemical scheme by Appel et al. [Appel et al. \(2000\)](#) (101 species and 544 elementary reactions) using CANTERA ([Goodwin et al., 2017](#)). To limit potential compensation of errors between heat transfer and chemistry, as in previous works ([Zhao et al., 2003](#)), the measured temperature profile is imposed.

The gas phase species mass fractions (Figures 5.1a and 5.1b) agree with previous calculations, in which soot chemistry was fully coupled. In our case, only pyrene consumption is considered when solving Eqs. (4.2.7)-(4.2.9) for soot, without much impact on most influential species. As in [Zhao et al. \(2003\)](#); [Balthasar and Kraft \(2003\)](#), soot dynamics are simulated in a moving reference frame, following the fluid particles from fresh to burnt gases. For the sake of comparison, as in [Zhao et al. \(2003\)](#), a shift by +0.25 cm of the computational distance above the burner is added, to account for the probe cooling effect.

To compare against experiments, soot number density is expressed as  $n(d) = dN(\log(d))/d\log(d)$  and total number density reads  $N = \int_{d_o}^{\infty} n(d)d\log(d)$  with  $d$  being the particle diameter in nm and  $d_o$  the lowest soot particle diameter considered. The particle characteristic size is defined from its volume or mass as one can be directly deduced from the other through  $m^k = \rho_{soot} \times v^k$ . Particle volume freely evolves according to Eq. (4.2.11) during growth and oxidation. According to the algorithm discussed above, for nucleation and agglomeration, intervals of sizes  $I_{v_i}$  must be defined. The nucleation mass  $m_o = 2m_{py}$ , corresponds to the mass of nascent soot particles from the collision of two pyrene molecules. The left boundary of  $I_{v_o}$  is  $v_o = m_o \times \rho_{soot}$ . This corresponds to a diameter of 0.88 nm. A geometric grid is used, following:

$$v_i^{inf} = v_o F_s^i, \quad (5.2.1)$$

Here the value of  $F_s = 1.5$  is used. The upper diameter of the grid is 51 nm. Another size range and other values of  $F_s$  are also tested in section 5.4. The stochastic particles are initialised at the lowest section and  $N_T(t = 0) = 1.0 \text{ cm}^{-3}$ . This initial distribution is only necessary to start the calculation but it is largely negligible as compared to  $N_T$  levels reached during the calculation (see Figure 5.2a). This approach has been validated elsewhere against analytical test cases featuring simultaneous nucleation and growth ([Bouaniche et al., 2019b](#)).

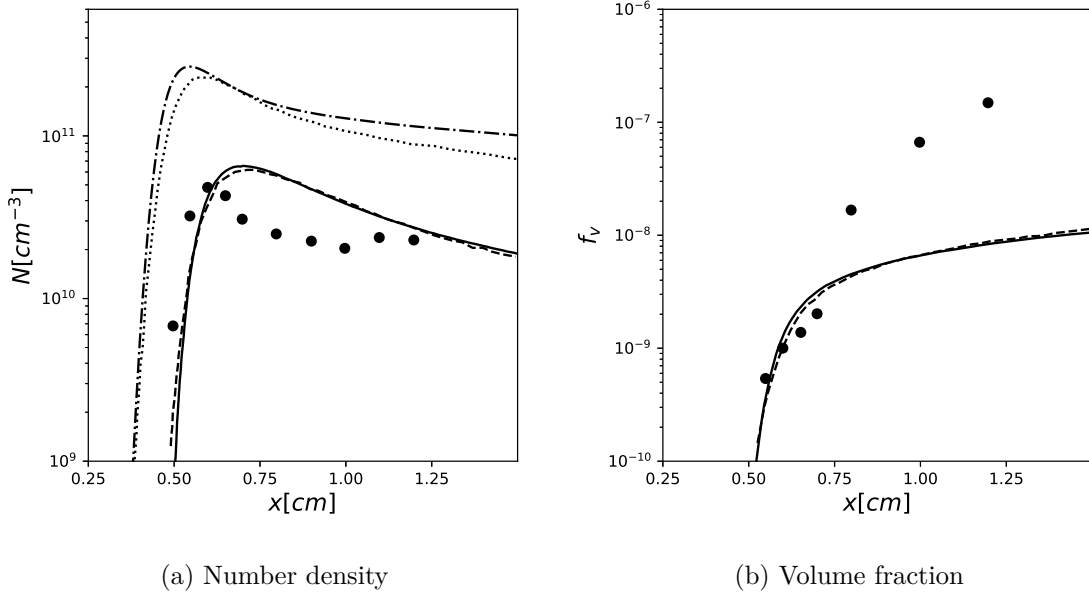


Figure 5.2: Soot number density and volume fraction *vs* height above burner. Symbols: experiments. (a) and (b) (diameters larger than 3 nm) Solid line: present simulation. Dashed line: reference simulation Zhao et al. (2003). (a) (for all diameters) Dash-dot line: present simulation. Dotted line: reference Zhao et al. (2003).

### 5.2.2 Results

Figure 5.2a shows that the simulation approximates well  $N_T$ , the total number density. The satisfactory prediction of pyrene mass fraction, aside from a small over-prediction for  $H > 1$  cm (Fig. 5.1b), brings confidence on the calculation of the nucleation term. Therefore, observing good results on total number density suggests that agglomeration is well resolved. The over-prediction of  $N_T$  against the reference calculation (Zhao et al., 2003) post-processing all diameters seen for higher values of  $H$ , the distance to the burner, may be explained by the stronger nucleation induced by the small over-prediction of pyrene.

Soot volume fraction also agrees with the previously published simulations (Fig. 5.2b). This was expected as the same physical models for the nucleation, agglomeration and surface growth source terms were used. However, compared to measurements, soot volume fraction is significantly underestimated in both simulations above  $H = 0.75$  cm, which may indicate an underestimation of surface growth. A possible cause of surface growth underestimation could be the soot formation and growth models. Another possible cause could be the models used for aggregate geometry through the calculated collision diameters and reactive surface. In the present study, new source terms models are out of scope. Only the  $\alpha$  parameter is varied and the influence of aggregate shape modelling on the Particle Size Distribution is looked at (section 5.3). Indeed, it is not obvious that soot particles can be modelled as perfect spheres in premixed ethylene flames as reported in Schenk et al. (2015). Figure 5.3 shows PSD and confirms the capability of the model to capture the soot size distribution. A unique nucleation mode is seen in both reference and present simulation for the lower streamwise position  $H$ . The transition to the bimodal distribution, with an additional accumulation mode, takes place approximately at the same height above burner. Finally, at  $H = 1.2$  cm both PSD feature similar shapes. The present calculation shows higher number densities for small particles, which is in line with the previous observation that nucleation and total number density are slightly enhanced in the current simulation for higher values of  $H$ .

In this first attempt, the numerical noise was minimized by performing the simulation with a set of  $N_P = 10^4$  stochastic particles. The crosses in Fig. 5.3 show results obtained with  $N_P = 1000$ ,

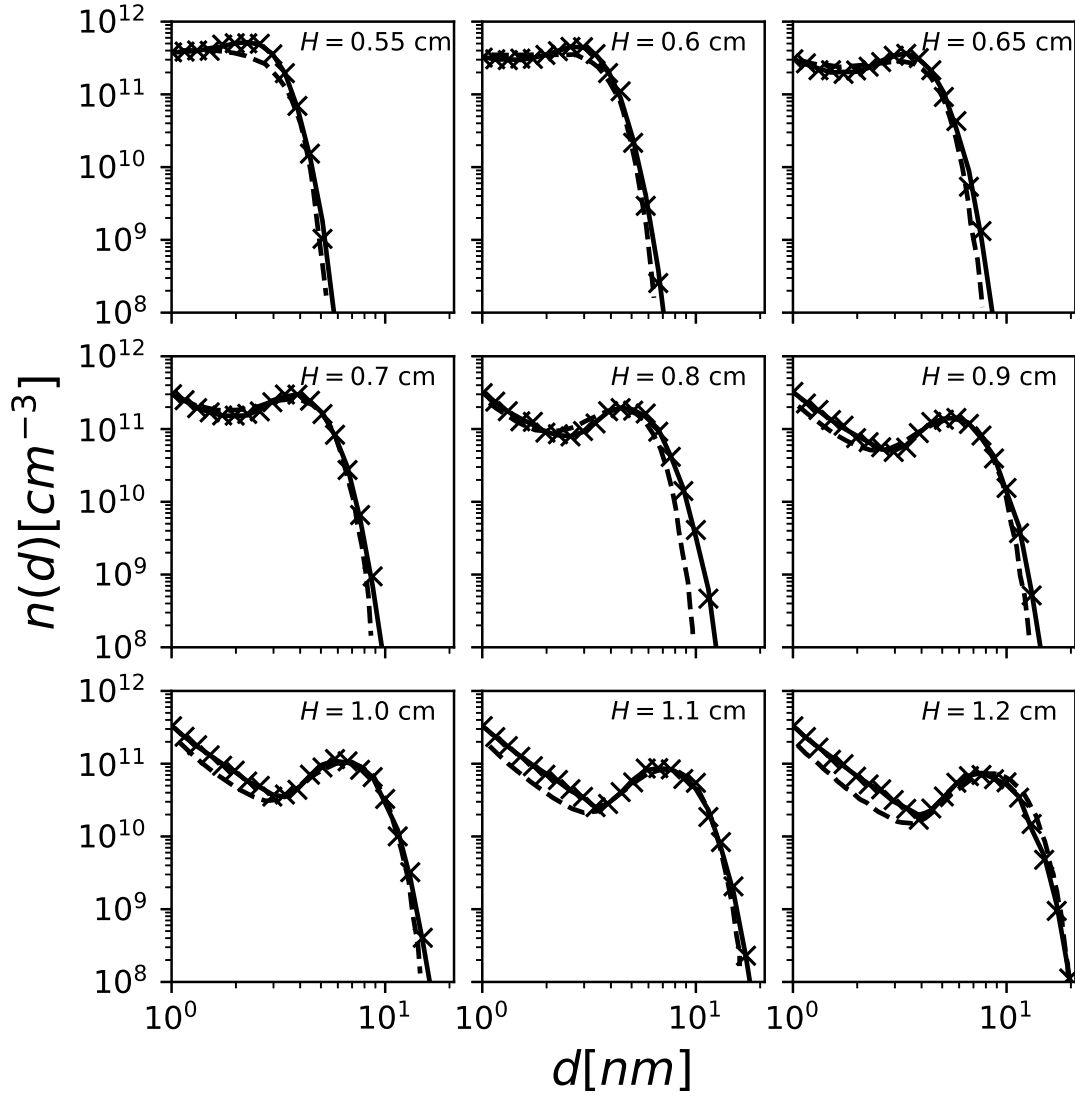


Figure 5.3: Particle Size Distribution for several heights above the burner. Solid line: present simulation with  $10^4$  stochastic particles. Cross: 1000 stochastic particles. Dashed line: reference simulation (Zhao et al., 2003) with  $2 \cdot 10^5$  stochastic particles.

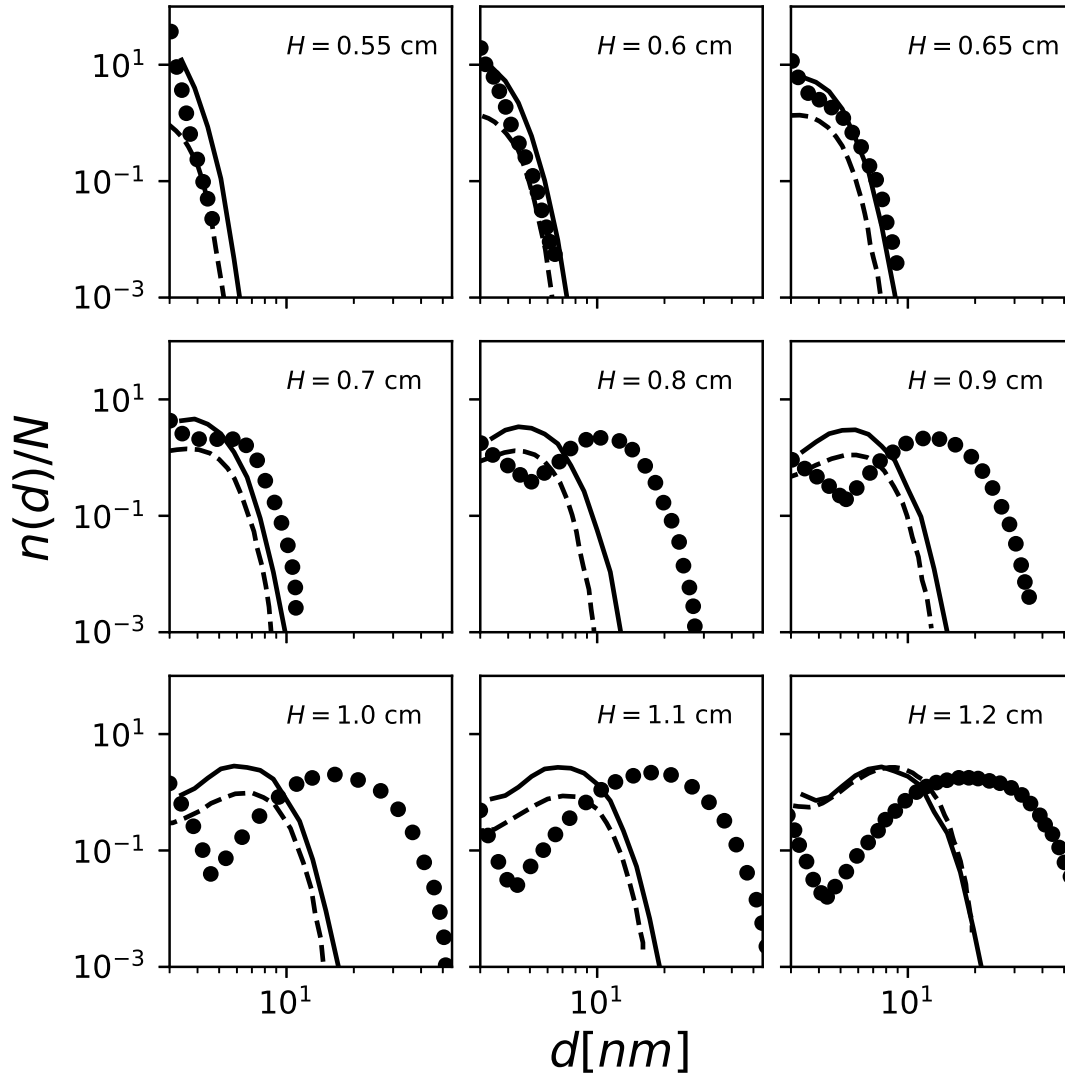


Figure 5.4: Normalized Particle Size Distribution for several heights above the burner. Solid line: present simulation. Dashed line: reference simulation [Zhao et al. \(2003\)](#). Symbols: experiments.

without much differences. This is to be compared with the reference simulation of ([Zhao et al., 2003](#)) where the number of stochastic particles was  $N_P = 2 \cdot 10^5$ . As further assessed in section 5.4, the moderate CPU cost of the proposed method allows to envision the use of the hybrid strategy in LES within either Eulerian or Lagrangian context for transporting the stochastic particles, defining  $N_P$ , the total number of stochastic particles, from those present within a mesh cell [Haworth \(2010\)](#).

Figure 5.4 presents PSD with number densities normalized by total number density. The computations (current and reference one) predict the right trend of the evolution, from a pure nucleation mode toward a bimodal distribution. The localization of the number density dip between both modes at about 4 nm compares well to experiment. Nevertheless, both computations fail to reproduce the number densities in the accumulation mode. Measured diameters are significantly larger than simulated ones, which goes with the underestimation of soot volume fraction in both simulations.

As discussed in [Zhao et al. \(2003\)](#), this underestimation could result from the disturbance by the probe, responsible of flow stagnation in front of the sampling orifice, increasing particles residence time and therefore their sizes. On the modeling side, the underestimation may come from

source terms modeling (in particular, surface growth). A second candidate for this difference is the mobility diameters measured by SMPS, which might not be directly comparable to diameters simulated assuming perfect spheres and constant density of the solid. A point which is now further examined.

### 5.3 Parametric analysis of aggregate shape modeling

The influence of particle shape modeling on computed PSD and on integral values, as soot volume fraction, is now explored. The measured mobility diameters, which were directly used for comparison in Fig. 5.4, are converted into equivalent sphere diameters assuming specific fractal shapes, thus enabling more meaningful comparisons between experiment and simulations. Then, the agglomeration modeling is improved with a particle shape based on the fractal law, to better estimate, in additional simulations, the collision diameters in the calculation of the  $\beta_{v_i, v_j}$ , the frequency of collision of the particles and the aggregate surfaces.

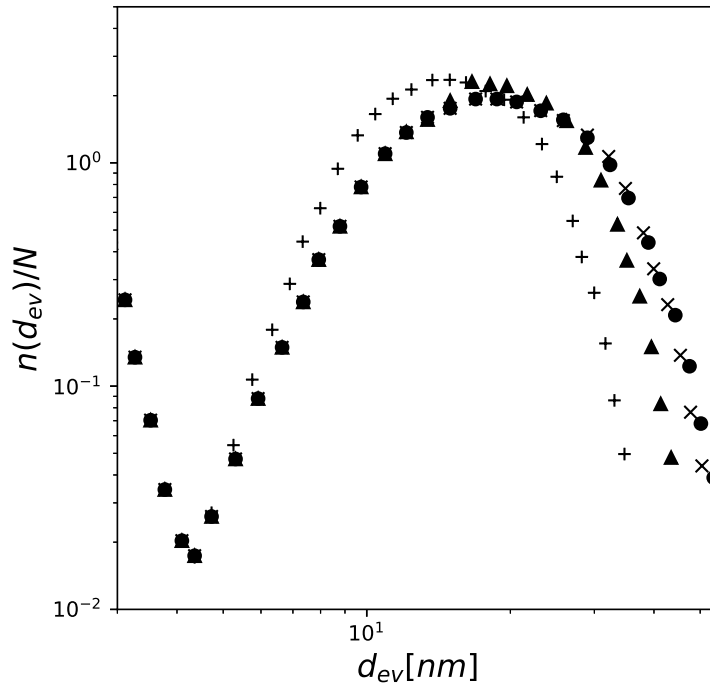


Figure 5.5: Normalized Number Density at  $H = 1.2$  cm *vs* the sphere equivalent diameter  $d_{ev}$ . Circles:  $d_m$  measured mobility diameters. Crosses:  $d_{ev}$  with  $d_p = 30$  nm. Triangles:  $d_{ev}$  with  $d_p = 15$  nm. Plus symbols:  $d_{ev}$  with  $d_p = 5$  nm.

Using the semi-empirical closure for the effective density measurements of the fractal aggregates proposed by Yon et al. [Yon et al. \(2015\)](#), an equivalent sphere diameters  $d_{ev}$  can be inferred from  $d_m$ , the measured mobility diameters. The calculation is made under the pressure and temperature conditions of the experiment, with a primary particle density  $\rho_{soot} = 1800 \text{ kg.m}^{-3}$  and a fractal dimension  $D_f = 1.73$ , i.e. corresponding to the soot properties determined in the conversion model used in the present study (Table 1 of [Yon et al. \(2015\)](#) for 'CAST' aggregates). Consequently, the corresponding parameters have been determined in a propane diffusion flame. Nevertheless, by keeping in mind the large experimental uncertainties related to the determination of these parameters, there is, up to now, no evidences of a possible variability of these parameters to the fuel and

the nature of the flame. For example, the authors of [Schenk et al. \(2015\)](#) measured  $D_f$  ranging from 1.2 to 1.8 in a series of premixed ethylene flames. Similar values have been used for simulating ethylene premixed flames, for example in [Saggese et al. \(2015\)](#) the authors used a constant value of  $D_f = 1.8$ . Concerning the density of the primary particles,  $\rho_{soot} = 1800 \text{ kg.m}^{-3}$  is the most encountered value related to black carbon and “mature soot”. The existence of a strong dependence of this parameter to the content of organic carbon has been recently shown ([Ouf et al., 2019](#)). This reference reports a density up to  $1834 \text{ kg.m}^{-3}$  for low OC content (below 5 percent) and smaller values for organic particles. Nevertheless, up to now, it is difficult to assess the amount of organic carbon of soot in flames. In consequence, the hypothesis of mature and inorganic soot is done. This hypothesis is done by experimentalists, for example, the value of  $1860 \text{ kg.m}^{-3}$  was used for the particle size determination based on LII models ([Bladh et al., 2015](#)). It is also a common value for numerical studies on ethylene premixed flames in the literature. Similarly, the values of  $1800 \text{ kg.m}^{-3}$  and  $1860 \text{ kg.m}^{-3}$  were used in [Eberle et al. \(2017b\)](#) and [Aubagnac-Karkar et al. \(2015\)](#) respectively. The number density distribution versus  $d_{ev}$ , calculated from the measurements of  $d_m$ , are shown in Fig. 5.5 for various  $d_p$ , the diameter of the primary particles. For the higher values of  $d_p$ , the particles are mostly spherical and  $d_{ev}$  does not significantly differ from the measured mobility diameter. The departure from the spherical shape becomes significant as the characteristic size  $d_p$  of the primary particles decreases, leading to aggregates composed of many primary particles.

Additional simulations are performed in which the mobility  $d_m$  and collision  $d_c$  diameters, which enter the calculation of the collision frequencies  $\beta_{v_i, v_j}$ , are estimated from  $d_g$ , the gyration diameter. The constant of proportionality is evaluated by considering the limit of a single sphere, as in [Kruis et al. \(1993\)](#); [Blanquart and Pitsch \(2009b\)](#); [Kazakov and Frenklach \(1998\)](#) (equation 2.3.5).  $d_g$  is estimated according to the fractal law

$$n_p = k_f (d_g/d_p)^{D_f}. \quad (5.3.1)$$

$n_p$  is the number of primary particles in the aggregates,  $D_f$  is the fractal dimension, and  $k_f$  is the fractal pre-factor.  $D_f = 1.73$  and  $k_f = 1.94$  are assumed constant for aggregates verifying  $n_p > 10$  ([Yon et al., 2015](#); [Lattuada et al., 2003](#)).  $n_p = v^k/(\pi d_p^3/6)$  can be inferred from  $v^k$ , the aggregate volume solved with the PDF of sizes. The only parameter left to determine  $d_g$  from (1.2.1) is then  $d_p$ . An attempt to estimate  $d_p$  is done by performing a preliminary simulation accounting only for nucleation and surface growth, thus without agglomeration, leading to  $d_p$  of the order of 5 nm at the streamwise position  $H = 1.2 \text{ cm}$ .

To analyze the sensitivity of the modeling to these various particle parameters, simulations including the fractal law are performed first fixing  $d_p = 5 \text{ nm}$  and varying  $\alpha_{HACA}$ , calibrating in the modeling the surface reactivity of the particles (Fig. 5.6). In a second series of simulations (Fig. 5.7),  $\alpha_{HACA} = 1$  and  $d_p$  is varied between 5 nm up to an upper value for which the fractal law provides results similar to those of spherical particles (denoted ‘spheres’, dotted line in Fig. 5.7). It is important to note that we considered the particles to be spherical when the corresponding volume is lower or equal to the one of a primary spherule i.e  $d_{ev} \leq d_p$ .

Experimental results are fairly well reproduced with  $\alpha_{HACA} = 1.0$  and  $d_p = 5 \text{ nm}$  (Figs. 5.6 and 5.7). For the lower values of  $d_p$ , the reactive surface available for  $C_2H_2$  addition is higher, which explains higher values of the volume fraction as observed in Figure 5.8. Moreover, for small values of  $d_p$ , aggregates are more open and  $d_c$ , the collision diameter, increases, which in turn increases collision rates (in particular in the free molecular regime) and the distribution is shifted towards larger particles (Fig. 5.7).

This exercise illustrates the strong impact of particle shape modeling when comparing against experiments. In particular, spherical particles might not always be the best choice. Also, bi-variate [Patterson and Kraft \(2007\)](#) or even tri-variate modeling [Blanquart and Pitsch \(2009b\)](#) could constitute an interesting alternative to calculate  $d_p$ .

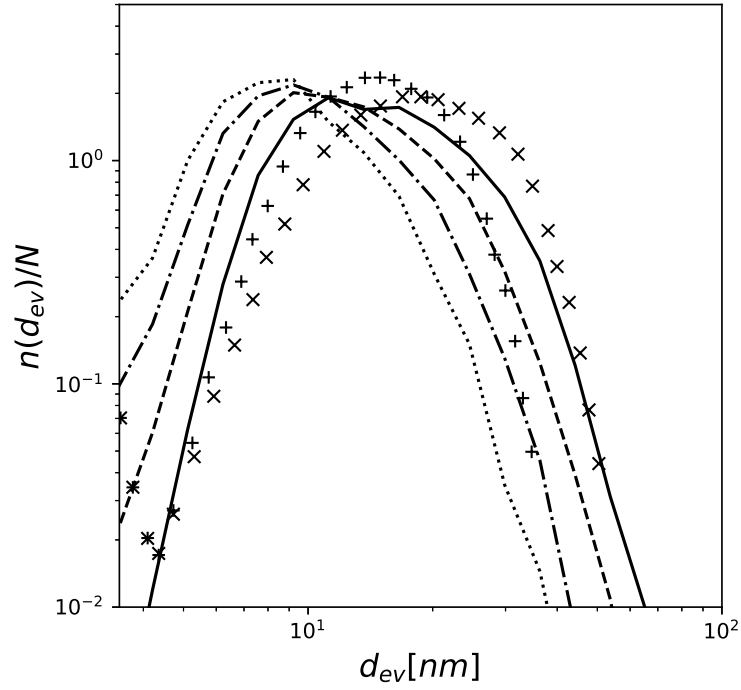


Figure 5.6: Normalized PSD at  $H = 1.2$  cm.  $d_p = 5$  nm. Solid line:  $\alpha_{\text{HACA}} = 1.0$ . Dashed line:  $\alpha_{\text{HACA}} = 0.9$ . Dash-dot line:  $\alpha_{\text{HACA}} = 0.8$ . Dotted line:  $\alpha_{\text{HACA}} = 0.7$ . Crosses: experiments  $d_{ev}$  with  $d_p = 30$  nm. Plus symbols: experiments  $d_{ev}$  with  $d_p = 5$  nm.

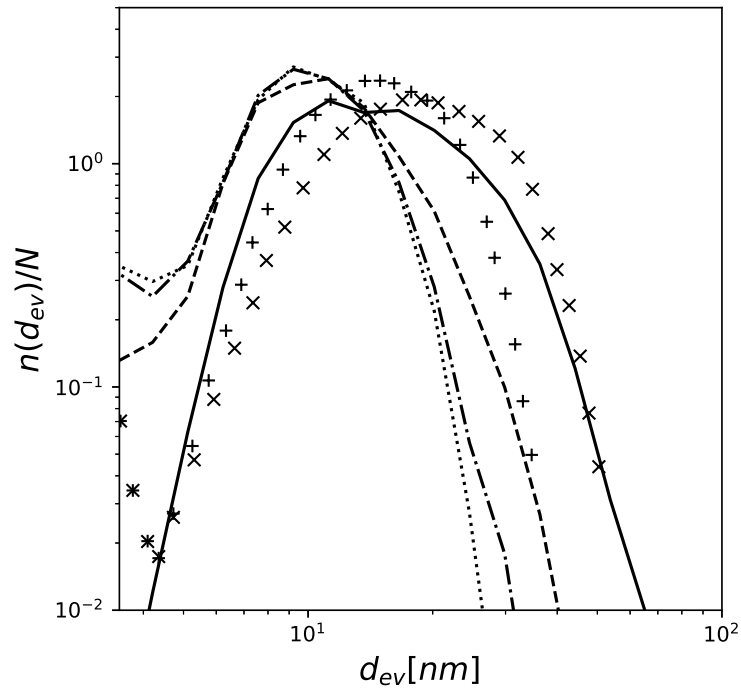


Figure 5.7: Normalized PSD at  $H = 1.2$  cm.  $\alpha_{\text{HACA}} = 1.0$ . Solid line:  $d_p = 5$  nm. Dashed line:  $d_p = 7$  nm. Dash-dot line:  $d_p = 10$  nm. Dotted line: sphere model. Crosses: experiments  $d_{ev}$  with  $d_p = 30$  nm. Plus symbols: experiments  $d_{ev}$  with  $d_p = 5$  nm.

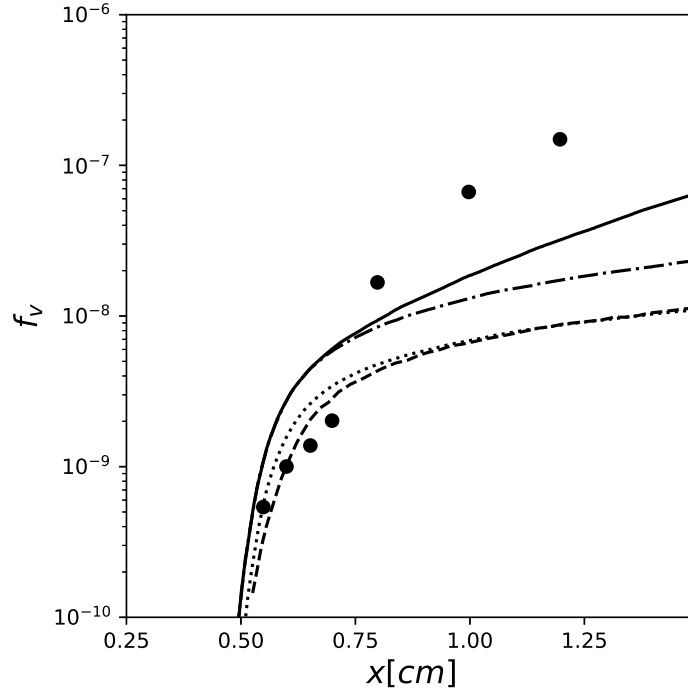


Figure 5.8: Soot volume fraction *vs* height above burner. Solid line:  $d_p = 5$  nm.  $\alpha_{\text{HACA}} = 1.0$ . Dash-dot line: spheres.  $\alpha_{\text{HACA}} = 1.0$ . Dotted line: spheres.  $\alpha_{\text{HACA}}$  from Appel et al. (2000) as in Zhao et al. (2003). Dashed line: reference Zhao et al. (2003). Symbols: experiment.

## 5.4 Comparison between hybrid and sectional methods

In this section, the present hybrid method is compared to a representative sectional method. The source terms for nucleation, growth and agglomeration are calculated in the same way for both methods. While growth is solved directly through stochastic particles in the hybrid method, a discretization scheme is used for the sectional method as in Park and Rogak (2004):

$$\frac{\partial N_i(\underline{x}, t)}{\partial t} = \frac{G(v_{i-1})N_{i-1}(\underline{x}, t)}{v_i - v_{i-1}} - \frac{G(v_i)N_i(\underline{x}, t)}{v_{i+1} - v_i}. \quad (5.4.1)$$

The impact of mesh resolution is studied hereafter. Again, a geometric grid is used as defined by equation (4.3.2). The centered section sizes range from 0.88 to 225 nm. This corresponds to a base case grid with  $F_s = 2$  and 25 sections which are typical values in the literature as for example in Eberle et al. (2017a). As the number of sections  $M$  is varied, the size range is kept constant and  $F_s$  is varied accordingly. The results for height above the burner of 1.2 cm can be seen in Figures 5.9 and 5.10 respectively in logarithmic and in linear scales. For the sake of clarity, the figures do not include the results for all grids for which calculations were run.

Considering the 200 sections simulation as a reference, the hybrid method yields better results than the sectional one using the same number of sections. For more quantitative comparison, the error against the 200 sections simulation can be calculated for each mesh. The Earth Mover's Distance (EMD) Rubner et al. (1998), also known as Wasserstein-1 distance, is used as metric of error. It is calculated using the 'emdist' package of the CRAN project Urbanek (2012). The EMD is then normalised by the standard deviation of the reference distribution. The evolution of this normalised EMD is given as a function of the number of sections in Figure 5.11. The hybrid method

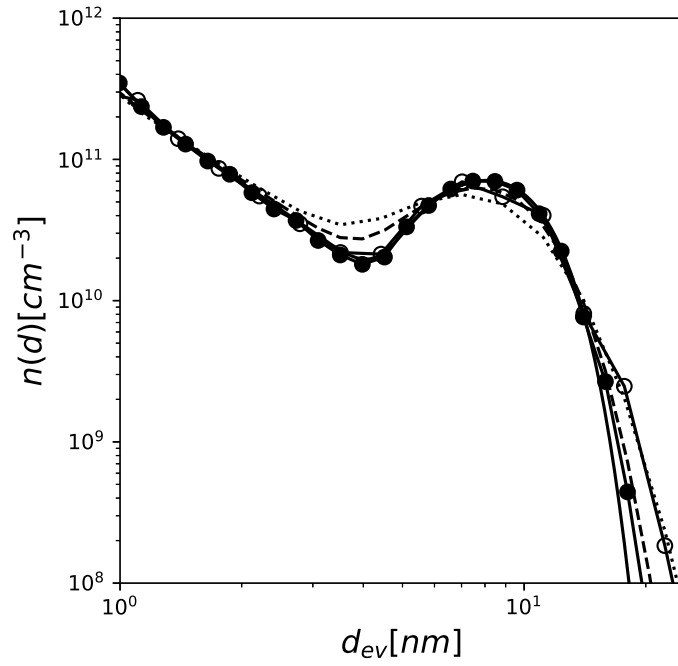


Figure 5.9: PSD at  $H = 1.2$  cm. Logarithmic scale. Dotted line: Sectional  $M = 25$ . Dashed line: Sectional  $M = 45$ . Solid line: Sectional  $M = 200$ . Line with empty circles: Hybrid  $M = 25$ . Line with full circles: Hybrid  $M = 45$ .

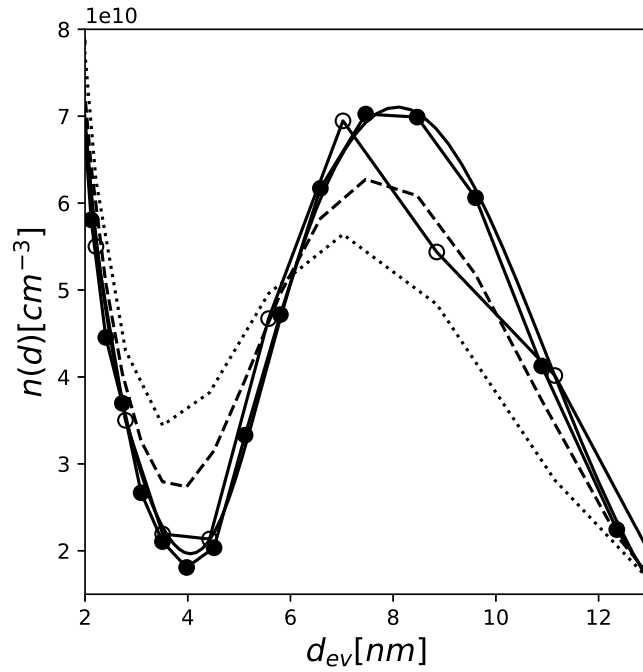


Figure 5.10: PSD at  $H = 1.2$  cm. Linear scale. Dotted line: Sectional  $M = 25$ . Dashed line: Sectional  $M = 45$ . Solid line: Sectional  $M = 200$ . Line with empty circles: Hybrid  $M = 25$ . Line with full circles: Hybrid  $M = 45$ .

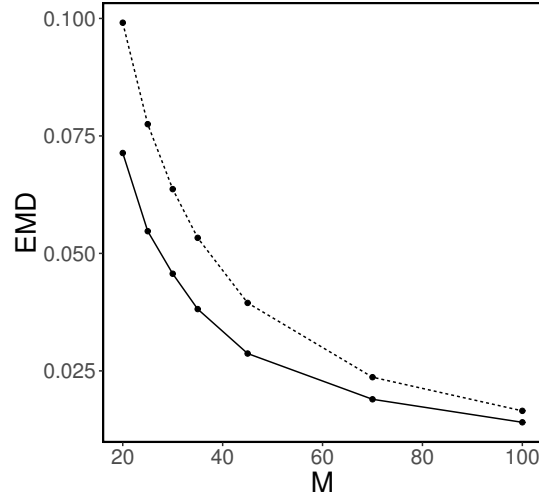


Figure 5.11: Normalised EMD as a function of the number of sections  $M$  (reference: 200 sections, solution at  $x = 1.2$  cm). Dashed line: Sectional method. Solid line: Hybrid method.

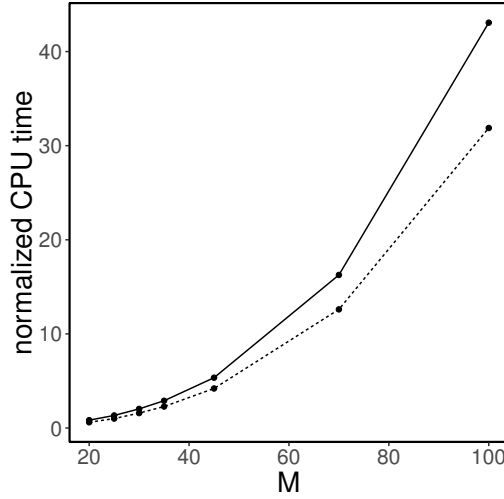


Figure 5.12: Normalised CPU cost as a function of the number of sections  $M$ . Dashed line: Sectional method. Solid line: Hybrid method.

yields lower error (with the same mesh refinement) for the whole range of tested grids. On the other hand, it presents a moderate CPU cost overhead as compared to the sectional method, as can be seen in Figure 5.12. The normalized CPU cost presented here is the CPU cost of the simulation divided by the CPU cost of the base case simulation (sectional, 25 sections). In order to assess the tradeoff between accuracy and cost the EMD error metric is plotted as a function of normalized CPU cost in Figure 5.13. For better readability, only the calculations up to 45 sections are shown on this last plot. Better accuracy is reached for lower CPU cost in the range of tested meshes. The hybrid method seems to offer an advantageous tradeoff in terms of CPU cost and accuracy, at least on this test case. Generalization of these conclusions will depend on the relative importance of agglomeration and growth source terms as the advantage of the present method over fixed sectional methods lays in accurate surface growth solving.

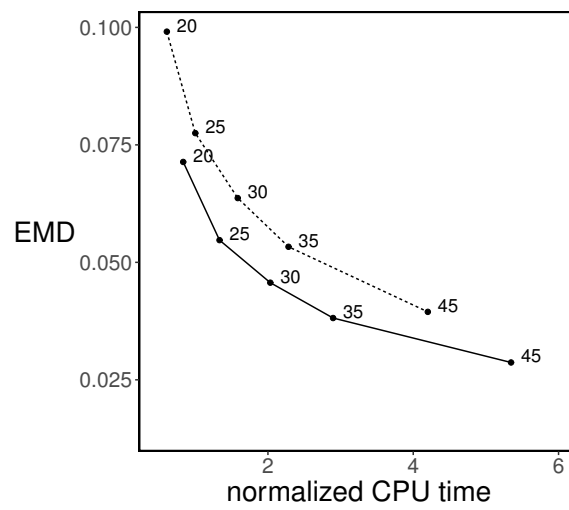


Figure 5.13: Normalised EMD as a function of normalised CPU cost. Dashed line: Sectional method. Solid line: Hybrid method. Labels: Number of sections

## Chapter 6

# Conclusions and perspectives

### Contents

<b>6.1 Conclusions</b>	<b>111</b>
<b>6.2 Perspectives</b>	<b>111</b>

## 6.1 Conclusions

The main achievements of this Ph.D. thesis can be summarized as follows:

- **A novel method (HYPE) has been proposed for the resolution of the Population Balance Equation.** This hybrid stochastic/sectional algorithm is aimed at offering an alternative to sectional methods such that surface growth/loss is resolved directly on a set of stochastic particles without numerical diffusion. On the other hand, the computational cost is maintained moderate as compared to standard Monte Carlo methods by avoiding to calculate agglomeration source terms through a sum on stochastic particles pairs. The space of particle size is discretized as for a sectional method for agglomeration source terms calculation, resulting in a similar computational cost. The calculation of these source terms drives the reallocation of the stochastic particles.
- **The HYPE method was implemented from zero during the Ph.D. thesis.**
- **Two fixed sectional methods were implemented from zero for comparison purpose.**
- **Analytical test cases were run. Accuracy and computational cost were measured and compared to fixed sectional methods. Comparison confirms the interest of the method, in accordance with the set objectives.**
- **The method was successfully applied to a 1-D premixed ethylene flame.**
- **Aggregate shape modelling was discussed and a parametric analysis was carried out.**

## 6.2 Perspectives

Full extension to spatially inhomogeneous cases still needs to be implemented. The stochastic particles would need to be transported also in physical space, for instance following well-established flow transport methods within the context of Monte Carlo solutions. This may be done either in Lagrangian ([Haworth, 2010](#)) or Eulerian ([Pope, 1981](#)) contexts. In the Lagrangian formulation,

aside from flow transport by a Langevin type equation, the time advancement of the PSD would be directly constructed from the set of stochastic particles present within a given mesh cell. In the Eulerian formulation, in addition to the local evolution of the stochastic particles simulating nucleation, surface growth/loss and agglomeration, the set of Monte Carlo particles fixed at every computational cell would exchange information with their neighboring nodes according to random processes simulating flow transport (Pope, 1981). Monte Carlo methods for the Population Balance Equation were previously successfully extended to spatially inhomogeneous flows (Zhao and Zheng, 2013).

A potential useful application of the HYPE method in the future is for validation or calibration of physical models for soot formation and evolution. Indeed, compensation of error must be minimized for the calibration of such models and the absence of numerical diffusion guarantees cleaner comparison of the models to experimental measurements. Direct calculation of estimated mobility diameters from equivalent sphere diameters (depending on some assumptions on aggregates shape) may also ease comparison between models and experiments.

Moreover, the HYPE code may be used for reduced model generation. Currently, it is being coupled to the ORCh code (Optimized Reduced Chemistry) (Jaouen et al., 2017). The objective is to run the HYPE method on a stochastic canonical case representative of turbulent combustion in an aeronautical burner. The generated database will then be fed into machine learning/deep learning models (similar to the ones used in Seltz et al. (2019)) to produce a reduced model derived for applications to aeronautical turbines. The purpose of this reduced model would be to solve only for some soot integral values and to deduce the PSD evolution.

## Chapter 7

# Appendix

### 7.1 Molecules structures

Molecule's structures and formulae are given here in alphabetic order. 2-D representations are from the [PubChem \(2019\)](#) website. Also, the paper [Bouaniche et al. \(2019a\)](#) has been added. Finally, a summary of the thesis written in french is available in this appendix.

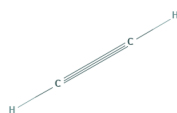


Figure 7.1: Acetylene  $C_2H_2$

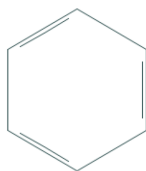


Figure 7.2: Benzene  $C_6H_6$

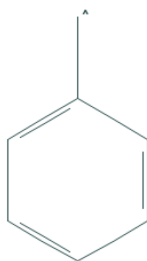
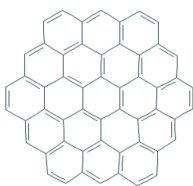
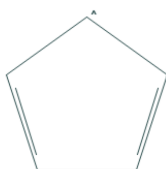
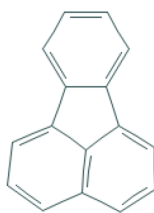
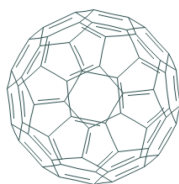
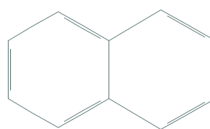
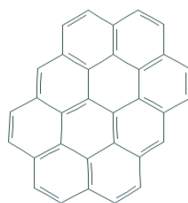
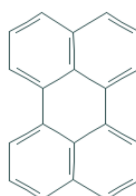
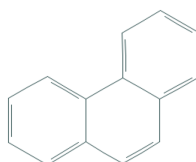
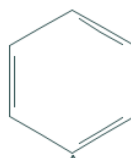
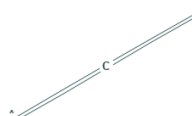


Figure 7.3: Benzyl radical  $C_7H_7$

Figure 7.4: Circumcoronene  $C_{54}H_{18}$ Figure 7.5: Coronene  $C_{24}H_{12}$ Figure 7.6: Cyclopentadienyl radical  $C_5H_5$ Figure 7.7: Ethylene  $C_2H_4$ Figure 7.8: Fluoranthene  $C_{16}H_{10}$ Figure 7.9: Fullerene  $C_{60}$

Figure 7.10: Naphthalene  $C_{10}H_8$ Figure 7.11: Ovalene  $C_{32}H_{14}$ Figure 7.12: Perylene  $C_{20}H_{12}$ Figure 7.13: Phenanthrene  $C_{14}H_{10}$ Figure 7.14: Phenyl radical  $C_6H_5$ Figure 7.15: Propargyl radical  $C_3H_3$

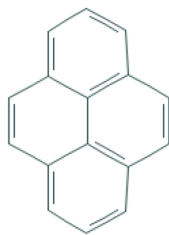



Figure 7.16: Pyrene  $C_{16}H_{10}$

## 7.2 Additional published paper

# Vitiated High Karlovitz n-decane/air Turbulent Flames: Scaling Laws and Micro-mixing Modeling Analysis

Alexandre Bouaniche<sup>1</sup> · Nicolas Jaouen<sup>1,2</sup> ·  
Pascale Domingo<sup>1</sup> · Luc Vervisch<sup>1</sup> 

Received: 1 March 2018 / Accepted: 4 June 2018  
© Springer Nature B.V. 2018

**Abstract** Turbulent flames with high Karlovitz numbers have deserved further attention in the most recent literature. For a fixed value of the Damköhler number (ratio between an integral mechanical time and a chemical time), the increase of the Karlovitz number (ratio between a chemical time and a micro-mixing time) by an order of magnitude implies the increase of the turbulent Reynolds number by two orders of magnitude (Bray, Symp. (Int.) Combust. **26**, 1–26 1996). In the practice of real burners featuring a limited range of variation of their turbulent Reynolds number, high Karlovitz combustion actually goes with a drastic reduction of the Damköhler number. Within this context, the relation between the dilution by burnt gases and the apparition of high Karlovitz flames is discussed. Basic scaling laws are reported which suggest that the overall decrease of the burning rate due to very fast mixing can indeed be compensated by the energy brought to the reaction zone by burnt gases. To estimate the validity of these scaling laws, in particular the response of the quenching Karlovitz versus the dilution level with a vitiated stream, the micro-mixing rate is varied in a multiple-inlet canonical turbulent and reactive micro-mixing problem. A reduced n-decane/air chemical kinetics is used, which has been derived from a more detailed scheme using a combination of a directed relation graphs analysis with a Genetic Algorithm. The multiple-inlet canonical micro-mixing problem includes liquid fuel injection and dilution by burnt gases, both calibrated from conditions representative of an aeronautical combustion chamber. The results confirm the possibility of reaching, with the help of a vitiated mixture, very high Karlovitz combustion before quenching occurs.

**Keywords** High Karlovitz combustion · Kerosene reduced chemistry · n-decane flame · Micro-mixing modeling · Large Eddy simulation · Spray flame

---

✉ Luc Vervisch  
vervisch@coria.fr

<sup>1</sup> CORIA - CNRS, Normandie Université, INSA de Rouen Normandie, Saint-Etienne-du-Rouvray, France

<sup>2</sup> Present address: Heat-Transfer & Reacting Flows, Royal Institute of Technology, Stockholm, Sweden

# 1 Introduction

In the quest for combustion systems with high fuel-efficiency, the strong increase of the turbulence intensity has recently seen a renewed interest [1–30]. Higher turbulence intensity is expected to favour enhanced micro-mixing of the reactants, followed by a higher volumetric burning rate. In his seminal works, Karlovitz [14] noted that flames can be ‘arrested by high velocity gradients and strong velocity fluctuations’. Such flame quenching by intense turbulence was examined under various conditions. One of the first experimental observation concluded that above a critical value of the number  $K = (\delta_L/S_L)(u'/\ell_T)$ , ratio between a chemical time and a mechanical time, of the order of a few tenth [31], combustion propagating in fresh gases cannot be sustained.  $u'$  denotes the rms turbulent velocity,  $\ell_T$  is the integral scale of turbulence,  $\delta_L$  the laminar flame thickness and  $S_L$  the laminar burning velocity. Results which immediately triggered further discussions on the exact definition of the characteristic scales chosen to measure  $K$  [32].

Along the same lines, the phenomenological analysis of the structure of turbulent flames initiated by Borghi [33], was followed by the development of combustion regime diagrams [34–36], built from Damköhler and Karlovitz numbers and additional ratios of times and length scales characteristic of the turbulence and the reaction zones. The Damköhler number is usually approximated as  $Da = \tau_T/\tau_c$ , where  $\tau_T$  is an integral mixing time and  $\tau_c$  a chemical time. The Karlovitz number relates to small-scale turbulent mixing,  $Ka = \tau_c/\tau_k$ , with  $\tau_k$  the small-scale (Kolmogorov) mixing time [37], leading to the relation [38]

$$Da \times Ka = \frac{\tau_T}{\tau_k} \approx Re_T^{1/2}, \quad (1)$$

where  $Re_T = u'\ell_T/\nu$  is the turbulent Reynolds number, with  $\nu$  the kinematic viscosity of the fluid. Therefore, for a fixed value of  $Da$  at which combustion occurs,  $Re_T \approx Ka^2$ , and increasing the Karlovitz number by, say a factor 10, would mean increasing the turbulent Reynolds number by a factor 100. Such large increase of the turbulent Reynolds number cannot always be achieved. In practice, when  $Ka$  goes up,  $Da$  does go down in order to fulfil the relation (1). In fact, this approximate relation (1) suggests that, at very high Reynolds numbers ( $Re_T \rightarrow \infty$ ), chemistry can still be fast ( $Da \rightarrow \infty$ ), as long as the chemical time scale is shorter (or of the order of) than the shortest flow time scale, i.e. the amplitude of  $Ka$  stays moderate. It is usually believed that this is the operating conditions of most practical combustion systems and it was the state of affair till around the year 2010. Over the last eight years however, studies have been published displaying an exponential growth of the Karlovitz number with years, see Fig. 1. As in the pioneer works reported above, the exact definition of  $Ka$  may differ from one study to the other, but the increase in  $Ka$  is large enough to be significant, whatever its exact definition. At the same time, the Damköhler number suffered from a drastic decrease of its amplitude (Fig. 2).

The flames at the highest  $Ka$  examined in the works of Fig. 1 were actually not ‘self-sustained’, but benefitted from a large reservoir of hot burnt gases, for instance a vitiated co-flow. These flames with very high values of the Karlovitz number (up to more than 1500), and thus very low values of the Damköhler numbers (down to 0.02), may eventually release less heat than they gain from burnt gases to maintain fuel oxidation. Nonetheless, all the fuel injected was burnt and thus high-Karlovitz combustion was achieved. This flame regime may be of interest locally in a combustion chamber, for instance to secure flame stabilisation in a highly turbulent flow zone. It is therefore legitimate to wonder by which mechanisms the dilution by burnt gases makes the flame more robust to high  $Ka$  (and low  $Da$ ) and how the response of the quenching Karlovitz number scales versus the level of dilution by burnt

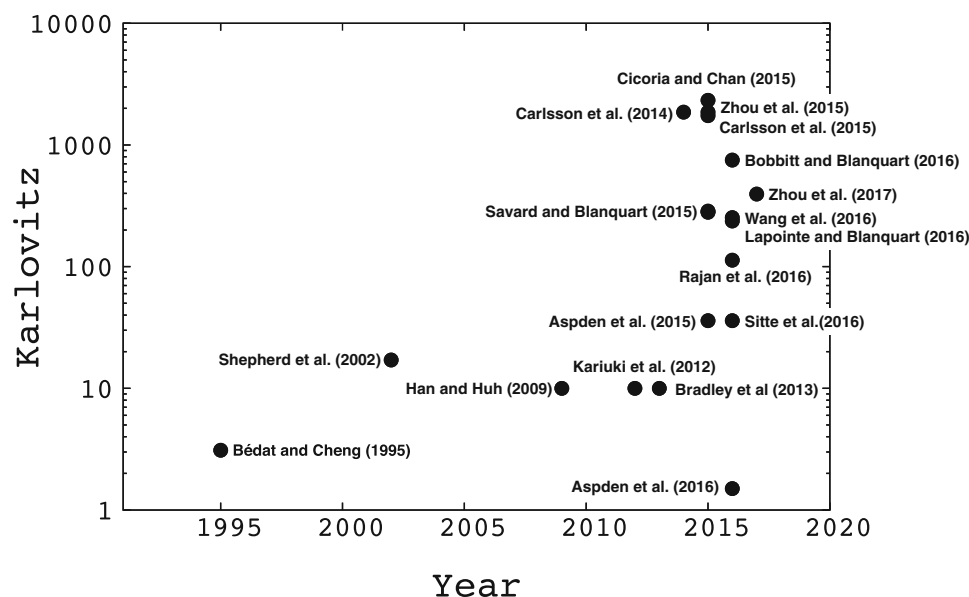


**Fig. 1** Karlovitz numbers considered in a sample of the literature over the past 25 years

gases. Among the numerous candidates, in the case of premixed combustion, an increase of the flame speed is a potential phenomenon and in the case of non-premixed systems, fast mixing with burnt gases may help local auto-ignition. At least three questions emerge from these preliminary remarks: (i) what is the basic scaling for flame speed including both dilution by burnt gases and Ka effect? (ii) In a non-premixed system, how much of recirculating burnt products must be included to secure high Ka combustion? (iii) What is the global scaling of Ka at quenching versus the dilution level of the fresh mixture with a vitiated stream.

In an attempt to answer these basic questions, simple scaling laws are proposed in this work combining premixed and non-premixed regimes. Simulations of micro-mixing/chemistry

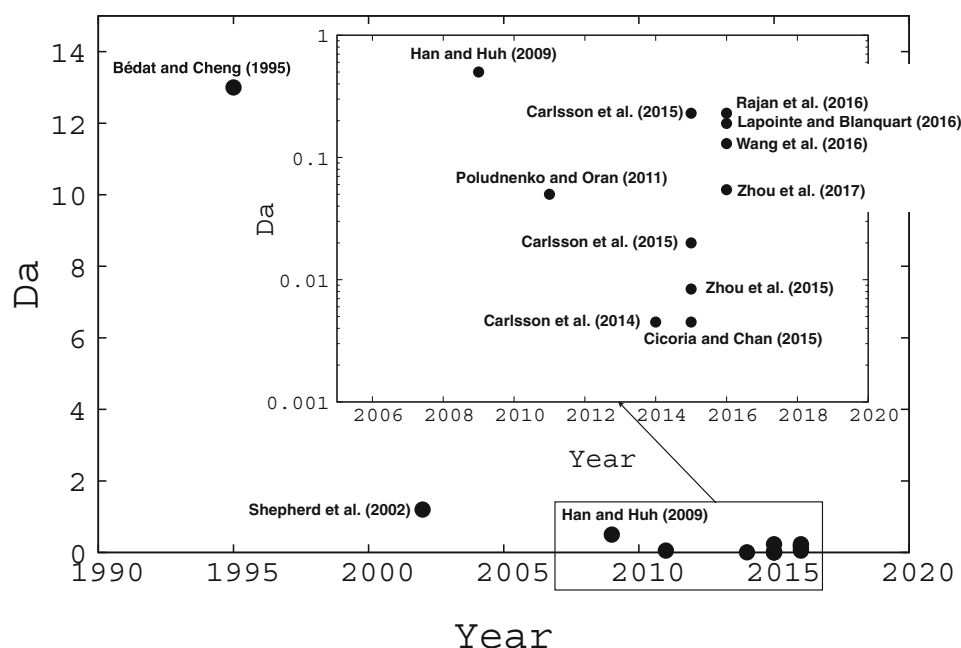


**Fig. 2** Damköhler numbers considered in a sample of the literature over the past 25 years, with a zoom over most recent years

interaction are then performed to verify the trends. If the effect of turbulence is oversimplified through a basic stochastic mixing closure, the impact of spray evaporation and of n-decane detailed chemistry is included. To do so, a set of reduced chemical schemes is first derived for n-decane/air combustion, as reported in the next section. The elementary scaling relations for high Ka flame in vitiated stream are discussed in the subsequent section, before examining the response of n-decane/air combustion at high Ka in the final section.

## 2 A Fuel-Spray Stochastic Micro-mixing Canonical Problem for High-Ka Analysis

Starting from a given set of initial conditions, representative of the streams feeding the reaction zones in an aeroengine, reference time evolutions of thermochemical quantities are constructed in a pseudo-reactor, combining the approaches discussed in [39, 40]. A set of  $N_p = 1000$  stochastic particles are distributed at initial time according to the chemical composition of three inlets, containing either liquid kerosene, air or burnt gases. This last inlet mimics recirculation of burnt gases, as it would be observed in a swirled fuel injection. After the initialisation, evaporation of the liquid fuel occurs and the gas phase evolves at about 10 bars according to a stochastic mixing model to which the chemical sources of kerosene/air chemistry are added. The thermochemical properties of the particles vary following a procedure explained below, to generate synthetic turbulent distributions, as the scatter plot of temperature versus mixture fraction seen in Fig. 3. Various distributions will be obtained varying both the initial amount of burnt gases and a Karlovitz number constructed from the control parameters of the canonical problem.

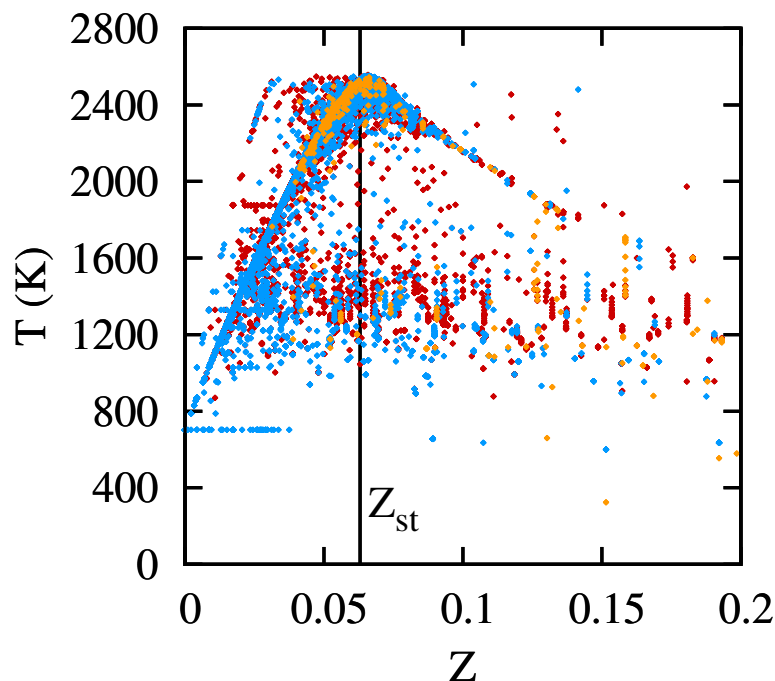


**Fig. 3** Scatter plot of stochastic particles temperature vs mixture fraction. Particles are coloured depending on their initial condition. Blue: air. Orange: kerosene. Red: burned gases.  $Z_{st}$  is the stoichiometric mixture fraction

The number of stochastic particles initially set at the concentration and temperature of the  $j$ -th inlet ( $j = 1, 2, 3$ ) is proportional to  $\dot{Q}_{m_j}$ , the mass flow rate injected by this inlet,

$$N_{P_j} = N_P \times \frac{\dot{Q}_{m_j}}{\dot{Q}_m}, \quad (2)$$

where  $\dot{Q}_m = \dot{Q}_{m_1} + \dot{Q}_{m_2} + \dot{Q}_{m_3}$  denotes the total mass flow rate. The liquid kerosene inlet at  $T = 450$  K represents 2.3% of  $\dot{Q}_m$  ( $\dot{Q}_{m_1} = 0.023\dot{Q}_m$ ). The mass flow rate of the air inlet at  $T = 703$  K is  $\dot{Q}_{m_2} = 0.644\dot{Q}_m$ . To mimic the injection of primary and secondary air, as done in some combustion chambers, 60% of the total mass of air is introduced at the initial time, the rest of air particles are then progressively released over 1 ms. The third and last inlet of burnt gases, taken at chemical equilibrium for the equivalence ratio of the full mixture at  $T = 1877$  K, brings  $\dot{Q}_{m_3} = 0.333\dot{Q}_m$ . These 33% were estimated from large eddy simulation of a representative aeronautical combustion chamber [41] and these burnt gases secure ignition in a first set of calculations.

As in Farcy et al. [39], the elementary mass flow rate  $\dot{q}_m = \dot{q}_{m_L}^p(t) + \dot{q}_{m_G}^p(t)$  carried by every  $p$ -th particle ( $p = 1, \dots, N_P$ ) is decomposed into liquid ( $\dot{q}_{m_L}^p(t)$ ) and gas ( $\dot{q}_{m_G}^p(t)$ ) phases. The evolution of the thermochemical property  $\phi^p$  carried by the  $p$ -th stochastic particles reads

$$\frac{d\phi^p(t)}{dt} = \text{MIX}^p(\tau) + \dot{\omega}_\phi^p + \dot{\omega}_{v\phi}^p, \quad (3)$$

where  $\dot{\omega}_\phi^p$  is the gaseous phase chemical source obtained from the chemical scheme,  $\dot{\omega}_{v\phi}^p$  relates to the liquid fuel (evaporation or heat), computed from the particle properties.  $\text{MIX}^p(\tau)$  denotes the Curl [42] micro-mixing closure, with  $\tau$  the characteristic micro-mixing time. Many other micro-mixing models exist in the literature, like modified Curl [43, 44], Euclidian Minimum Spanning Tree (EMST) [45], Multiple Mapping Conditioning (MMC), which allows for introducing flamelet-like correlations between species [46], or again the advanced hierarchical parcel-swapping representation of turbulent mixing [47]. However, for examining the global scaling laws considered in this work, the basic version of the Curl micro-mixing model was found sufficient.

To account for the evaporation of the liquid fuel, the simplified modeling used in [39] is adopted. The thermal condition is assumed above the liquid boiling point and the droplets diameter follows the so-called  $D^2$ -law [48–50],  $d_j^2(t) = d_j^2(t_0)(1 - (t/\tau_v))$ . The characteristic evaporation time is fixed at  $\tau_v = 0.491$  ms, which was estimated from the experimental results by Nomura et al. [51]. It was thus preferred to fix  $\tau_v$  from experiments, rather than introducing additional uncertainties in its dynamic calculation from approximate liquid and flow properties.

The rate of gaseous mass of the  $i$ -th component released by a single droplet reads

$$\dot{W}_i^p(t) = Y_{i,L}^p(t) \times \rho_L \frac{\pi}{6} \left[ \frac{d_j^3(t) - d_j^3(t + \Delta t)}{\Delta t} \right], \quad (4)$$

where  $Y_{i,L}^p$  denotes the mass fraction of the  $i$ -species in the liquid of the  $p$ -th particle. A single stochastic particle issued from the  $j$ -th inlet carries a number  $\dot{n}_j$  of droplets injected

per unit time. Then, the balance between liquid and gaseous mass flow rates carried by a given particle issued from the  $j$ -th inlet may be written

$$\dot{q}_{m_G}^p(t + \Delta t) = \dot{q}_{m_G}^p(t) + \sum_{i=1}^{N_s} \dot{n}_j \dot{W}_i^p(t) \Delta t, \quad (5)$$

$$\dot{q}_{m_L}^p(t + \Delta t) = \dot{q}_{m_L}^p(t) - \sum_{i=1}^{N_s} \dot{n}_j \dot{W}_i^p(t) \Delta t, \quad (6)$$

where  $N_s$  is the number of species considered. The net gaseous source of evaporation of the  $i$ -th chemical species in the  $p$ -th particle is

$$\dot{\omega}_{v_i}^p(t) = \frac{1}{\Delta t} \left[ \frac{\dot{q}_{m_G}^p(t) Y_{i,G}^p(t) + \dot{n}_j \dot{W}_i^p(t) \Delta t}{\dot{q}_{m_G}^p(t + \Delta t)} - Y_{i,G}^p(t) \right], \quad (7)$$

where  $Y_{i,G}^p$  is the gaseous mass fraction of the  $i$ -th species in the  $p$ -th particle. The source of the sensible enthalpy  $h_s$  is

$$\dot{\omega}_{h_s}^p(t) = \frac{1}{\Delta t} \left[ \frac{\dot{q}_{m_G}^p(t) h_s^p(t) + \sum_{i=1}^N \dot{n}_j \dot{W}_i^p(t) [h_i(T_B) - \mathcal{L}_{v_i}] \Delta t}{\dot{q}_{m_G}^p(t + \Delta t)} - h_s^p(t) \right], \quad (8)$$

in which  $T_B = 750$  K is the boiling temperature,  $h_i$  is the enthalpy of the  $i$ -th species and  $\mathcal{L}_{v_i} = 251\,000$  J/kg is the latent heat of evaporation. At injection, a single droplet diameter  $d = 12.8$   $\mu\text{m}$  is imposed, as it was estimated from the Sauter mean diameter of a representative aeronautical injector. This modeling leads to usual and generic scatter plot responses, as seen in Fig. 3.

### 3 Reduced n-decane Chemistry

The Luche et al. [52, 53] chemical kinetics accounts for 91 species and 991 reacting steps, and is derived from the more detailed kerosene-air mechanism by Dagaut [54]. This mechanism was selected because of its reasonable size, at least in comparison to other more detailed schemes for kerosene-air combustion. It is not attempted to provide in this work a reduced chemistry for kerosene that would benefit from the most recent findings in terms of real aeronautical fuels [55], which may include complex chemical properties distributions across the distillation curve and related complex phenomena. The sole objective is to compare the normalised response of a chemical scheme featuring multiple chemical time scales against the scaling laws discussed thereafter, and using the Luche et al. mechanism as a starting point is sufficient to address this point.

To further reduce the Luche et al. chemistry so that multiple calculations can be performed, the ORCh approach is followed [40], which combines the directed graph analysis with error propagation (DRGEP) [56, 57]. Species and reactions are progressively removed according to their relative importance measured along reference chemical evolutions ( $\phi^D(t)$  trajectories), with the automatic generation of an analytical part using quasi-steady state assumption (QSS) and a subsequent optimisation of the chemical rates with a Genetic Algorithm. All detail concerning this combination of reduction/optimisation methods to generate a series of reduced chemical kinetics can be found in [40, 58].

To compact the information and ease the analysis, two additional deterministic trajectories are solved, from the air and kerosene inlets, with the linear relaxation deterministic micro-mixing closure (IEM or LMSE) [34, 59]

$$\frac{d\phi^D(t)}{dt} = \frac{\langle\phi\rangle(t) - \phi^D(t)}{\tau} + \dot{\omega}_\phi^D. \quad (9)$$

The statistical mean entering this deterministic mixing model is computed at every instant in time from the full set of stochastic particles,

$$\langle\phi\rangle(t) = \frac{\sum_{p=1}^{N_P} \dot{q}_{m_G}^p(t) \phi^p(t)}{\sum_{p=1}^{N_P} \dot{q}_{m_G}^p(t)}. \quad (10)$$

These additional deterministic trajectories are easily coupled with a Genetic Algorithm, to optimise chemical rates after chemistry reduction [40]. Figure 4 shows typical  $\phi^D(t)$  distributions.

The kerosene in the initial mechanism by Luche et al. [52, 53] is a surrogate composed of n-decane (n-C<sub>10</sub>H<sub>22</sub>, 76.7388% in mass), propylbenzene (PHC<sub>3</sub>H<sub>7</sub>, 13.1402%) and propylcyclohexane (CYC<sub>9</sub>H<sub>18</sub>, 10.1210%). In the present reduction, the initial composition of the fuel is even more simplified to 100% n-decane. The species of the reduced mechanism are given in Table 1. This mechanism relies on the transport of 26 chemical species and on the solving of 24 quasi-steady state relations and contains 338 elementary reactions.

The associated trajectories (9) for operating conditions reported above are displayed in Figs. 4 and 5, in which the symbols denote the detailed scheme. The trajectories from fuel and air inlet differ till a residence time of 1 ms, before the species evolve toward the equilibrium condition. The thermal energy brought by the burnt gases first promote the formation of NO through their mixing with fresh air. At 0.5 ms, the temperature conditions are so that part of this NO is recombined into NO<sub>2</sub>, to then increase again after 1.25 ms through the mixing with the remaining air in a post-flame region. Aside from the unavoidable difference in n-decane (fuel surrogate in the detailed mechanism and only n-decane in the reduced one in Fig. 3), the response of the reduced scheme stays very close to the detailed one, specifically in terms of position of ignition and of the peak of CO (Fig. 3), which will be considered thereafter in the analysis increasing Ka and varying the amount of burnt gases.

The reduced mechanism has been obtained considering only the turbulent micro-mixing problem (3), which overall features similarities with non-premixed combustion. It is therefore of interest to verify that a perfectly premixed combustion regime is also reproduced. Figure 6 shows a comparison of the flame velocity, the equilibrium temperature and the equilibrium levels for CO and for NO obtained from perfectly premixed kerosene-air flame computations at a pressure of  $9.63 \cdot 10^5$  Pa with the Cantera solver [60]. Some departure is observed on the estimation of the flame speed  $S_L$  for equivalence ratios between unity and 2, but overall the description is acceptable considering the level of reduction. For comparison, are added the results obtained with a less reduced chemical mechanism (32 transported species, with 27 QSS relations and 419 elementary reactions), obtained keeping the original surrogate fuel composition. Both reduced mechanisms perfectly capture the equilibrium temperature and equilibrium CO level for every equivalence ratio. An over prediction of the NO levels is achieved using the most reduced mechanisms for conditions around the stoichiometric point. However, because NOx species will not be considered in the subsequent analysis, this most reduced mechanism based on n-decane (Table 1) is retained.

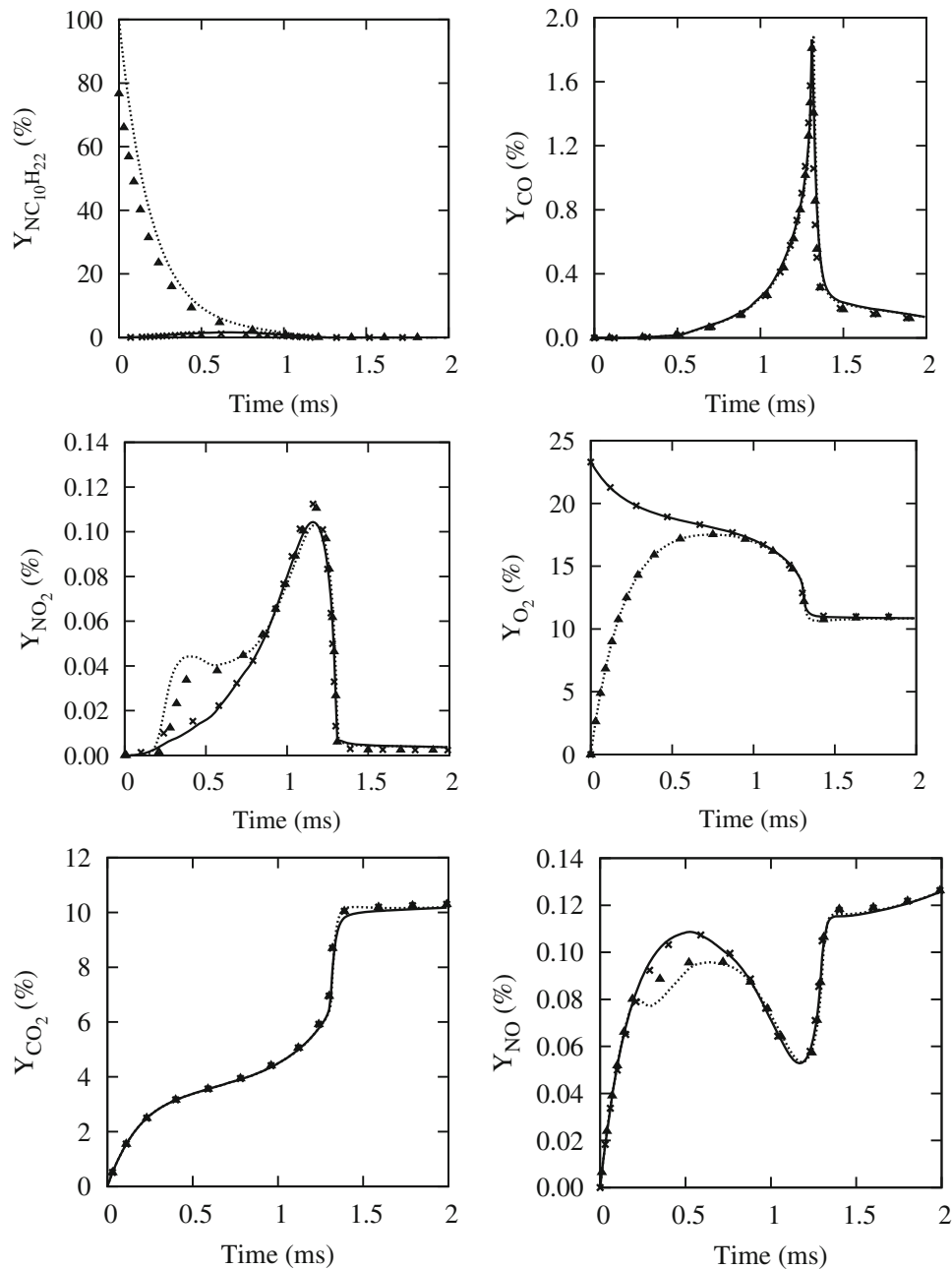


**Fig. 4** Representative species trajectories (9) for the kerosene surrogate and n-decane reduced mechanism.  $\tau = 0.2$  ms. Symbols: Reference chemistry [53]. Lines: Reduced n-decane mechanism (Table 1). Solid-line: Air inlet trajectory. Dotted-Line: Fuel inlet trajectory

**Table 1** Species of a n-decane ( $n\text{-C}_{10}\text{H}_{22}$ ) reduced mechanism composed of 26 transported species associated to 24 QSS relations and 338 reactions

Transported species	Analytically resolved species (QSS)
$\text{H}_2$ , $\text{O}_2$ , $\text{CO}$ , $\text{CO}_2$ , $\text{CH}_4$ , $\text{C}_2\text{H}_6$ , $\text{CH}_2\text{O}$ , $\text{C}_2\text{H}_2$ , $\text{C}_2\text{H}_4$ , $\text{C}_3\text{H}_6$ , $\text{C}_4\text{H}_6$ , $\text{NC}_{10}\text{H}_{22}$ , $\text{H}$ , $\text{O}$ , $\text{OH}$ , $\text{HO}_2$ , $\text{H}_2\text{O}$ , $\text{CH}_3$ , $\text{C}_3\text{H}_3$ , $\text{AC}_3\text{H}_5$ , $\text{BC}_6\text{H}_{13}$ , $\text{N}_2$ $\text{NO}$ , $\text{HCN}$ , $\text{N}_2\text{O}$ , $\text{NO}_2$	$\text{HCO}$ , $\text{CH}_3\text{OH}$ , $\text{C}_2\text{H}_5$ , $\text{CH}_3\text{O}$ , $\text{CH}_2\text{OH}$ , $\text{CH}_2\text{CO}$ , $\text{C}_2\text{H}_3$ , $\text{CH}_2\text{HCO}$ , $\text{HCCO}$ , $\text{NC}_3\text{H}_7$ , $\text{PC}_4\text{H}_9$ , $\text{AC}_6\text{H}_{13}$ , $\text{AC}_8\text{H}_{17}$ , $\text{C}_{10}\text{H}_{21}(\text{L})$ $\text{HNO}$ , $\text{HONO}$ , $\text{H}_2\text{CN}$ , $\text{NNH}$ , $\text{NH}_2$ , $\text{NH}$ , $\text{N}$ , $\text{CN}$ , $\text{NCO}$ , $\text{HNCO}$

**Fig. 5** Temperature trajectories (9).  $\tau_T = 0.2$  ms. Symbols: Reference chemistry [53]. Lines: Reduced n-decane mechanism (Table 1). Solid-line: Air inlet trajectory. Dotted-line: Fuel inlet trajectory

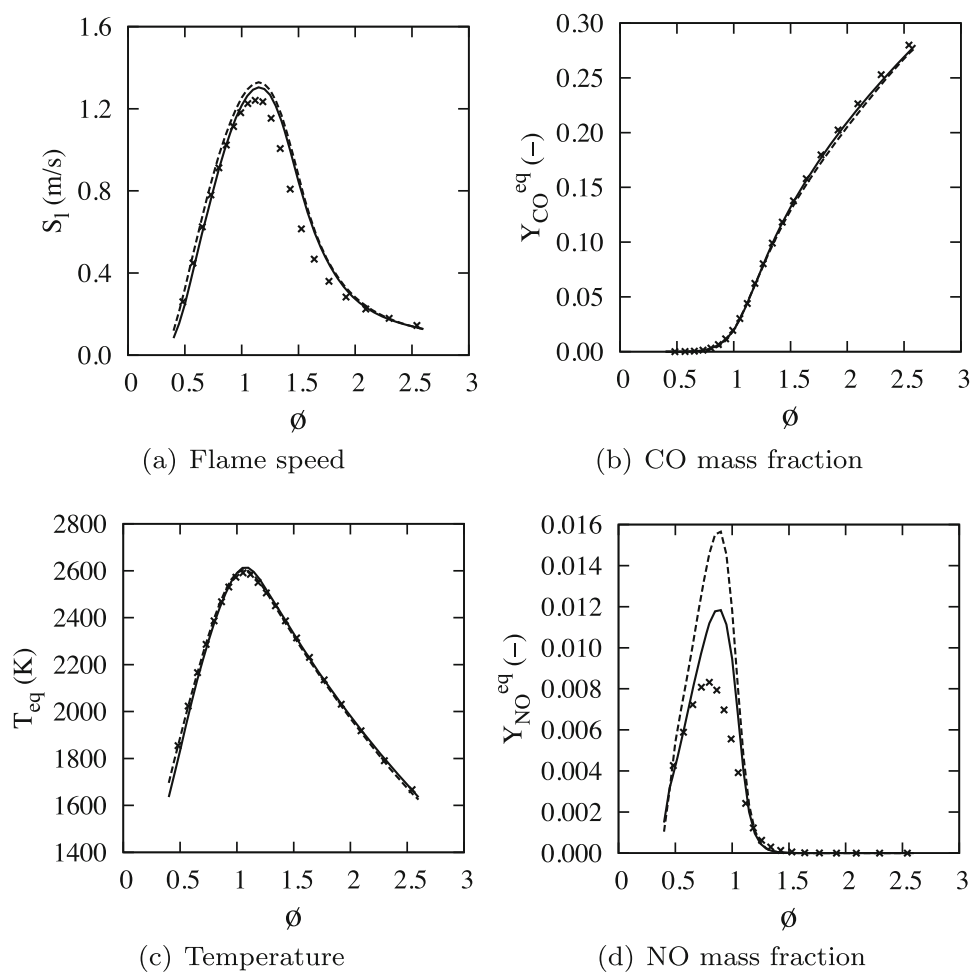
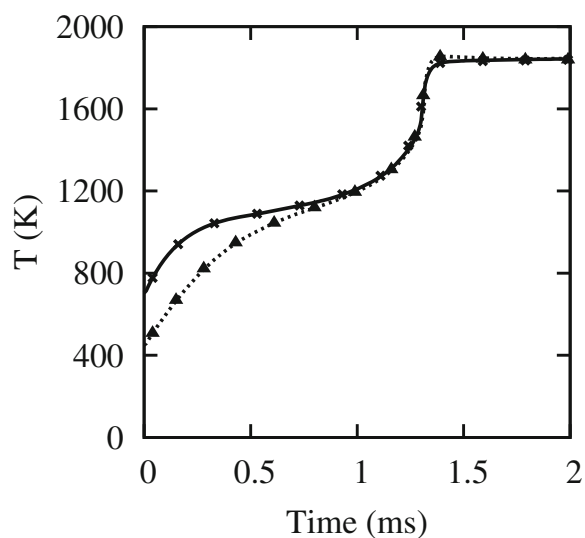


**Fig. 6** Freely propagating premixed flames. Response versus equivalence ratio, species and temperature taken in burnt gases. Symbols: Reference chemistry [53]. Solid-line: Reduced surrogate mechanism. Dashed-line: Reduced n-decane mechanism (Table 1)

## 4 Basic Scaling for High-Ka Flames in Vitiated Mixture

Oversimplified scaling relations for weakly vitiated flames are recalled in this section.

### 4.1 Vitiated steady premixed flamelet

Consider the steady premixed laminar flamelet equation

$$\rho u \frac{d\phi}{d\xi} = \frac{d}{d\xi} \left( \rho D_\phi \frac{d\phi}{d\xi} \right) + \dot{\omega}_\phi - \rho \dot{S}_{K_\phi}, \quad (11)$$

where  $\rho$  is the density,  $u$  is the velocity,  $D_\phi$  is the diffusion coefficient of the scalar  $\phi$  evolving through the flame front and  $\dot{\omega}_\phi$  its chemical source. The coordinate in the direction normal to the flame front is  $\xi$  and  $\dot{S}_{K_\phi}$  is a leakage term, representative of all fluxes occurring along the flame surface [61], as transverse convection and diffusion resulting from straining and curvature of the flamelet surface.

The fresh gases condition  $\phi_u$  is expressed from a reference fresh gases unburnt condition  $\phi_o$  and the dilution (or vitiating) factor  $f_b$  (the subscript ‘u’ and ‘b’ denote unburnt and burnt gases respectively)

$$\phi_u = \phi_o(1 - f_b) + f_b\phi_b. \quad (12)$$

$f_b = 0$  corresponds to fresh mixtures (fuel mixed with oxidiser) and burnt vitiating gases appears for  $0 < f_b \ll 1$ .

Integrating (11) through an unstrained one-dimensional flame ( $\dot{S}_{K_\phi} = 0$ ) and accounting for mass conservation, the unstrained flame speed reads

$$S_L(f_b, \dot{S}_{K_\phi} = 0) = u_u = \left( \frac{\rho_b}{\rho_u} \right) u_b = \frac{1}{\phi_b - \phi_u} \left[ \frac{1}{\rho_u} \int_{-\infty}^{+\infty} \rho \dot{\omega}_\phi d\xi \right]. \quad (13)$$

The peak reaction rate in the integral in Eq. 13 is toward the burnt gas side, also it is assumed that the density weighted integral of the source does not vary much with dilution by burnt gases, at least for weak levels of  $f_b$ . Combining this hypothesis with the relations (13) and (12) leads to

$$\begin{aligned} S_L(f_b, \dot{S}_{K_\phi} = 0) &= \frac{1}{1 - f_b} \times \frac{1}{\phi_b - \phi_o} \left[ \frac{1}{\rho_o} \int_{-\infty}^{+\infty} \rho \dot{\omega}_\phi d\xi \right], \\ &= \left( \frac{1}{1 - f_b} \right) S_L^o \end{aligned} \quad (14)$$

with  $S_L^o = S_L(f_b = 0, \dot{S}_{K_\phi} = 0)$ . Figure 7 shows the evaluation of this relation in the simulation of a freely propagating premixed flame with a single-step chemistry cast as in [62], for a Zeldovich number  $\beta = 15$ . The expected trend is recovered for  $0 < f_b \ll 1$ . In this single-step chemistry simulation, the addition of the vitiating gases is mimicked by preheating the fresh mixture, and the one-dimensional flame is computed with a fully compressible sixth-order flow solver using a PADE scheme [63]. This hyperbolic behaviour of flame speed versus dilution by burnt gases was also reported in the literature at various places, for instance simulating vitiating premixed flamelets with detailed chemistry (see Fig. 4a in [64]).<sup>1</sup>

<sup>1</sup>This scaling may also be retrieved from high-activation energy asymptotic developments after matching fluxes with vitiating fresh gases [65].

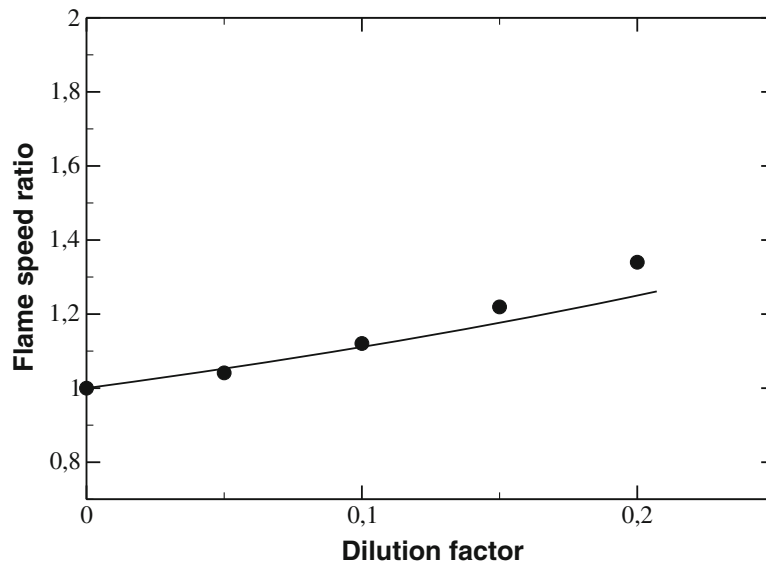


**Fig. 7** Flame speed  $S_L(f_b)$  versus the dilution factor  $f_b$  (12). Line: Eq. 14. Symbol: Simulation of 1D freely propagating premixed flame

Considering now a flamelet submitted to stretch without dilution and assuming that the integral of the source stays close to the unstretched flame burning velocity, Eq. 11 leads to

$$\begin{aligned} \rho_o S_L(f_b = 0, \dot{S}_{K_\phi}) &= \frac{1}{\phi_b - \phi_o} \left[ \int_{-\infty}^{+\infty} \rho \dot{\omega}_\phi d\xi - \int_{-\infty}^{+\infty} \rho \dot{S}_{K_\phi} d\xi \right], \\ &= \rho_o S_L^o \left( 1 - \frac{\int_{-\infty}^{+\infty} \rho \dot{S}_{K_\phi} d\xi}{(\phi_b - \phi_o) \rho_o S_L^o} \right). \end{aligned} \quad (15)$$

The usual linear response of the flame speed to small levels of stretch is found [66]

$$S_L(f_b = 0, \dot{S}_{K_\phi}) = S_L^o (1 - K), \quad (16)$$

with  $(\phi_b - \phi_o) \rho_o S_L^o \times K = \int_{-\infty}^{+\infty} \rho \dot{S}_{K_\phi} d\xi$ .

The linear reduction of flame speed by  $(1 - K)$  (16) and the increase of flame speed by  $(1 - f_b)^{-1}$  (14), suggest that the effect of flame speed reduction by tangential stretch applied to the flame surface can be compensated by the vitiation of the fresh gases.

## 4.2 Vitiating diffusion flamelet quenching

The relation (14) for the unstretched and diluted flame may also be combined with an estimation of the quenching condition in a diffusion flamelet.  $\tau_{mq}$  the mechanical time at quenching in a non-premixed system is known to relate to the stoichiometric and freely propagating flame speed as [35, 67]

$$\frac{1}{\tau_{mq}} = \frac{Z_{st}^2 (1 - Z_{st})^2}{a_T / S_L^2}, \quad (17)$$

where  $a_T$  is the thermal diffusivity and  $Z_{st}$  the stoichiometric value of the mixture fraction [35]. Assuming a fixed reference chemical time,  $Ka_q$ , the Karlovitz number at quenching varies as  $\tau_{mq}^{-1}$ . The introduction in Eq. 17 of the relation (14), giving the unstrained flame speed  $S_L = S_L(f_b, \dot{S}_K = 0)$  in the presence of dilution, provides a scaling relation for a non-premixed system weakly vitiated by burnt gases

$$Ka_q(f_b) \approx \left( \frac{1}{1 - f_b} \right)^2. \quad (18)$$

Hence, the value of the Karlovitz number at the quenching point should increase in the presence of dilution by burnt gases ( $f_b > 0$ ), making the reaction zones evolving in vitiated mixture more robust to intense turbulence. This scaling is now tested against calculations with the reduced kerosene chemistry.

## 5 Response of Ka at Quenching in a Vitiated Stream

The above dilution factor  $f_b$  calibrates the relative amount of burnt and fresh gases present in the unburnt mixture (12). In the canonical problem used for chemistry reduction (Eqs. 3 and 9), the relative amount of burnt gases introduced initially may be varied adjusting the mass flow rates of the three streams injected in the system ( $\dot{Q}_{m1}$ : fuel,  $\dot{Q}_{m2}$ : air and  $\dot{Q}_{m3}$ : burnt gases), thus varying  $\langle Y_i(t = 0) \rangle$ , the averaged mass fractions injected at  $t = 0$ , including liquid fuel.

To study the sensitivity of the pseudo-reactor to the amount of added recirculating burnt gases,  $f_b$  is defined as

$$f_b = \frac{\dot{Q}_{m3}}{\dot{Q}_m - \dot{Q}_{m3}}. \quad (19)$$

where  $\dot{Q}_m = \sum_j \dot{Q}_{mj}$  is the total mass flow rate injected. With this definition,  $f_b = 0$  in the case of no-dilution by burnt gases and  $f_b = 1$  in the asymptotic limit where mass flow rates of fresh ( $\dot{Q}_{m1} + \dot{Q}_{m2}$ ) and burnt gases ( $\dot{Q}_{m3}$ ) are equal.

The response of the turbulence/chemistry interaction to variations of  $\tau$ , the micro-mixing time, is characterized by three stages [62]. (i) very small micro-mixing times, and thus very fast micro-mixing, prevent combustion. (ii) intermediate values of  $\tau$  lead to ignition and burning with turbulence/chemistry interaction. (iii) above a given threshold, the too large micro-mixing times, associated with very small frequency of micro-mixing, do not allow for sufficient mixing of the fresh and burnt gases to secure ignition within the allowed residence time (here 2 ms). These three stages ((i) no-burning, (ii) burning and (iii) no-burning) are seen in Fig. 8, displaying  $\langle c \rangle$ , the average progress variable ( $c = 0$  in the fresh gases and  $c = 1$  in fully burnt products) plotted at  $t_{End} = 2$  ms for cases featuring a micro-mixing time  $\tau$  varying between 0.002 and 0.8 ms, and for the representative case  $f_b = 0.5$ . The average progress of reaction  $\langle c \rangle$  is here calculated from the normalised production of  $CO_2$  by combustion

$$\langle c \rangle(t) = \frac{\langle Y_{CO_2} \rangle(t) - \langle Y_{CO_2} \rangle(t = 0)}{Y_{CO_2}^{Eq*} - \langle Y_{CO_2} \rangle(t = 0)}, \quad (20)$$

with  $Y_{CO_2}^{Eq*}$  calculated from the full mixture at  $t = 0$ , including primary and secondary air.

A zoom in the high-Ka zone is given in Fig. 8b. The decrease of  $\tau$  down to  $\tau = 0.015$  ms (thus the increase of Ka) is followed by a rapid transition from burning to non-burning in

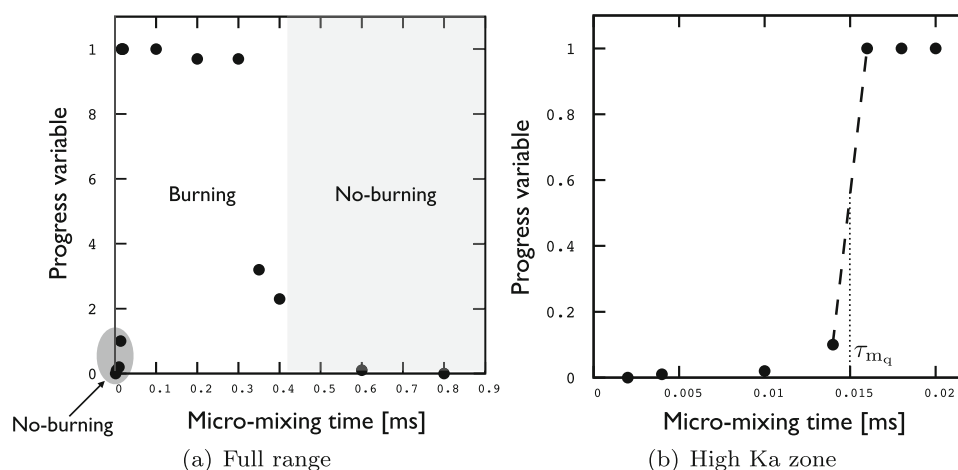


**Fig. 8** Response of the progress variable  $c^D(t_{\text{End}})$  versus mechanical mixing time.  $f_b = 0.5$  and  $t_{\text{End}} = 2$  ms

the progress variable response. The mid-point of a linear distribution constructed between the last fully burning point and the first very weakly burning condition is chosen to define,  $\tau_{mq}$ , the mechanical time at quenching. This determines the smallest micro-mixing time that does allow for ignition and burning in the combustion problem defined by Eq. 3. The corresponding quenching Karlovitz number can then be related to a limit value that would prevent ignition and thus flame stabilisation in burnt gases vitiated mixture.

The dilution factor  $f_b$  (19) is now varied between 0.25 and 1. For every case, a set of trajectories (9) are obtained for given values of  $\tau$ , to determine the response of  $\tau_{mq}$  versus  $f_b$ , according to the procedure shown in Fig. 8b. To define a Karlovitz number, a chemical time must be chosen. With complex chemistry, in the present case 48 species, many options exist. After considering the evolution of various species, the trajectories of carbon monoxide were found to provide a similar shape for the various dilution levels, it is also a species which is

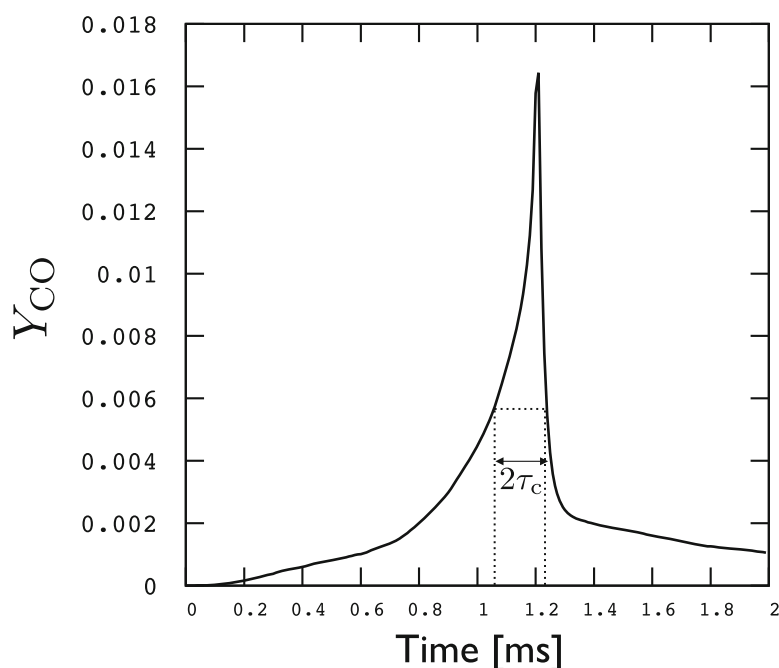


**Fig. 9** Illustration of the arbitrary definition of the chemical time from  $Y_{CO}^D(t)$ , the CO mass fraction deterministic trajectory (9). Representative case  $f_b = 0.5$

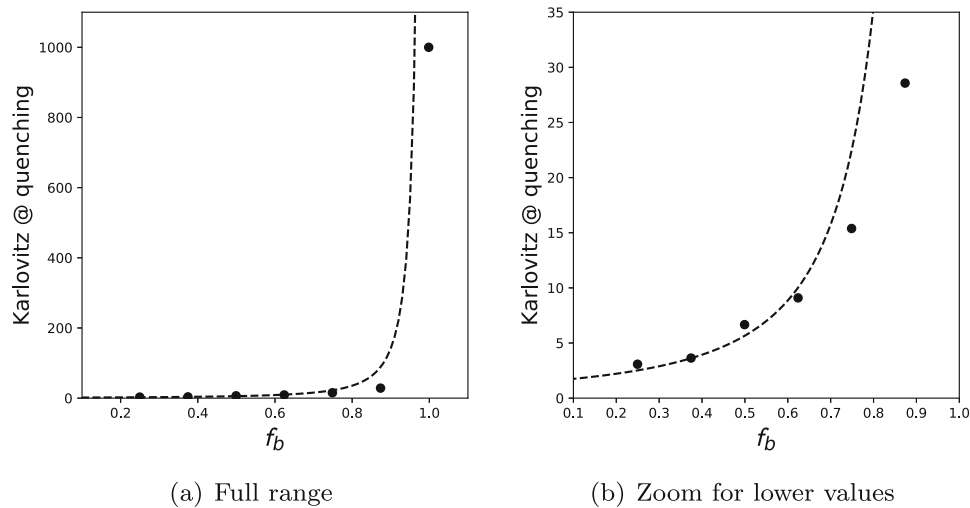


**Fig. 10** Response of  $Ka_q$  versus  $f_b$ . Circle: simulations (Eqs. 3 and 9). Dashed line: Eq. 18 (b): zoom in moderate  $Ka$  level

well captured by the reduced scheme (Fig. 3). The decay of the CO mass fraction after its peak value can be interpolated

$$Y_{CO}(t) = Y_{CO}^{\max} \exp(-(t - t_{\text{peak}})/t_0), \quad (21)$$

where  $Y_{CO}^{\max} = Y_{CO}(t_{\text{peak}})$  denotes the peak CO mass fraction (Fig. 9). The characteristic relaxation time  $t_0$  is measured from the observed CO distribution, so that  $Y_{CO}(t_{\text{peak}} + t_0) = Y_{CO}^{\max} \exp(-1)$ . Twice the chemical time,  $2\tau_c$ , is arbitrarily chosen as the time duration between the two observations of  $Y_{CO}^{\max} \exp(-1)$  in the CO distributions (Fig. 9). The value of the Karlovitz at quenching for various  $f_b$  is finally taken as the ratio

$$Ka_q(f_b) = \frac{\tau_c}{\tau_{mq}}. \quad (22)$$

Obviously, other formulations could be introduced, however this global measure is sufficient to compare against the basic scaling discussed above.

The response of  $Ka_q$  versus the dilution factor  $f_b$  is given in Fig. 10. The robustness of the n-decane combustion to intense mixing does increase with dilution by burnt gases. A rapid growth of the value of  $Ka_q$  at quenching is particularly observed after reaching  $f_b = 0.6$  (Fig. 10b). Interestingly, a zoom in the lower values of  $f_b$  shows that the response of  $Ka_q$  follows quite well the scaling given by Eq. 18. It is worthwhile to note that the relation (18), which was derived for  $0 < f_b \ll 1$  (thus without matching in the one-dimensional approximate analysis the  $f_b$  definition based on the mass flow rate (19)), seems here reasonably fit for approximating the flame response, even up to large values of  $f_b$ .

## 6 Discussion and Summary

A stochastic canonical problem has been constructed to explore turbulence chemistry/interaction with kerosene liquid fuel injection. The information obtained has been used at first to optimise a reduced chemical scheme, whose objective is to predict major species only. Then, the response of the quenching Karlovitz number to the amount of burnt gases mixed with the fresh mixture has been studied. It is found that basic scaling laws derived for burnt-gases vitiated premixed and non-premixed systems agree well with the results, with dilution promoting an inverse squared enhancement of the flame robustness to intense turbulence.

**Table 2** Characteristic length scales approximated from quasi-DNS of a swirl burner [68, 69]

$Re_T$	$Re_\lambda$	$\ell_T$	$\tau_T$	$\eta_k$	$\tau_k$
1480	149	7 mm	2 ms	29 mm	0.051 ms

Estimating characteristic length and time scales relevant for turbulent flames in real combustion systems, or in experiments representative of real injectors, is not an easy task [13]. Along these lines, well-resolved Large Eddy Simulation (LES) or quasi Direct Numerical Simulation (DNS) of real burners provide additional information. The Table 2 summarises length and time scales extracted from the quasi-DNS [68] of the aeronautical swirl burned studied experimentally by Meier et al. [69].

In Fig. 8 for  $f_b = 0.5$ , combustion is expected for micro-mixing times in the range  $0.015 \text{ ms} < \tau < 0.1 \text{ ms}$ . Interestingly,  $\tau_k$  in Table 2 lies within this range, close to the lower limit for this swirled flow injector, which was designed to operate with a quite strong precessing vortex core, featuring a characteristic frequency of about 540 Hz with a time scale of the order of 1.9 ms, thus with strong recirculation of burnt gases. Drawing further conclusions on the exact numbers would not be fair at this stage. However, above results open perspectives for advanced injector design, thus considering high Karlovitz combustion aside from toy problems. The opportunity of counterbalancing the negative impact of strong turbulence on the flame-base thanks to entrainment of burnt gases, appears actually stronger than expected from usual combustion regime analysis. At the same times, it confirms that high Karlovitz combustion can hardly be sustained without addition of burnt gases.

**Acknowledgements** The first author is supported by the European Union under the project SOPRANO, Horizon 2020 Grant Agreement No. 690724. The second author was funded by ANRT (Agence Nationale de la Recherche et de la Technology), SAFRAN-SNECMA and Air Liquide under the CIFRE No 1053/2013. Computing time has been provided by CRIANN (Centre Régional Informatique et d'Applications Numériques de Normandie).

### Compliance with Ethical Standards

**Conflict of interests** The authors declare that they have no conflict of interest.

**Publisher's Note** Springer Nature remains neutral with regard to jurisdictional claims in published maps and institutional affiliations.

## References

1. Aspden, A.J., Day, M.S., Bell, J.B.: Turbulence-chemistry interaction in lean premixed hydrogen combustion. *Proc. Combust. Inst.* **35**(2), 1321–1329 (2015)
2. Aspden, A.J., Day, M.S., Bell, J.B.: Three-dimensional direct numerical simulation of turbulent lean premixed methane combustion with detailed kinetics. *Combust. Flame* **166**, 266–283 (2016)
3. Bagdanavicius, A., Bowen, P.J., Bradley, D., Lawes, M., Mansour, M.S.: Stretch rate effects and flame surface densities in premixed turbulent combustion up to 1.25 MPa. *Combust. Flame* **162**(11), 4158–4166 (2015)
4. Bédard, B., Cheng, R.K.: Experimental study of premixed flames in intense isotropic turbulence. *Combust. Flame* **100**(3), 485–494 (1995)
5. Bobbitt, B., Blanquart, G.: Vorticity isotropy in high Karlovitz number premixed flames. *Phys. Fluids* **28**, 1070 (2016)
6. Bradley, D., Lawes, M., Liu, K., Mansour, M.S.: Measurements and correlations of turbulent burning velocities over wide ranges of fuels and elevated pressures. *Combust. Flame* **34**(1), 1519–1526 (2013)

7. Carlsson, H., Yu, R., Bai, X.S.: Direct numerical simulation of lean premixed CH<sub>4</sub>/air and H<sub>2</sub>/air flames at high Karlovitz numbers. *Int. J. Hydrog. Energy* **39**(35), 20,216–20,232 (2014)
8. Carlsson, H., Yu, R., Bai, X.S.: Flame structure analysis for categorization of lean premixed CH<sub>4</sub>/air and H<sub>2</sub>/air flames at high Karlovitz numbers: direct numerical simulation studies. *Proc. Combust. Inst.* **35**(2), 1425–1432 (2015)
9. Cicoria, D., Chan, C.K.: Large Eddy simulation of lean turbulent hydrogen-enriched methane-air premixed flames at high Karlovitz numbers. *Int. J. Hydrog. Energy* **41**(47), 22,479–22,496 (2016)
10. Haiou, W., Hawkes, R., Chen, J.H.: A direct numerical simulation study of flame structure and stabilisation of an experimental high Ka CH<sub>4</sub>/air premixed jet flame. *Combust. Flame* **180**, 110–123 (2017)
11. Han, I., Huh, K.Y.: Effects of the Karlovitz number on the evolution of the flame surface density in turbulent premixed flames. *Proc. Combust. Inst.* **32**(1), 1419–1425 (2009)
12. Huang, C.C., Shy, S.S., Liu, C.C., Yan, Y.Y.: A transition on minimum ignition energy for lean turbulent methane combustion in flamelet and distributed regimes. *Proc. Combust. Inst.* **31**(1), 1401–1409 (2007)
13. Kariuki, J., Dawson, J.R., Mastorakos, E.: Measurements in turbulent premixed bluff body flames close to blow-off. *Combust. Flame* **159**(8), 2589–2607 (2012)
14. Karlovitz, B.: Open turbulent flames. *Symp. (Int.) Combust.* **4**(1), 60–67 (1953)
15. Lapointe, S., Blanquart, G.: Fuel and chemistry effects in high Karlovitz premixed turbulent flames. *Combust. Flame* **167**, 294–307 (2016)
16. Lapointe, S., Savard, B., Blanquart, G.: Differential diffusion effects, distributed burning, and local extinctions in high Karlovitz premixed flames. *Combust. Flame* **162**(9), 3341–3355 (2015)
17. Poludnenko, A.Y., Oran, E.S.: The interaction fo high-speed turbulence with flames: turbulent flame speed. *Combust. Flame* **158**(2), 301–326 (2011)
18. Ranjan, R., Muralidharan, B., Nagaoka, Y., Menon, S.: Subgrid-scale modeling of reaction-diffusion and scalar transport in turbulent premixed flames. *Combust. Sci. Technol.* **188**(9), 1496–1537 (2016)
19. Savard, B., Blanquart, G.: Broken reaction zone and differential diffusion effects in high Karlovitz n-C<sub>7</sub>H<sub>16</sub> premixed turbulent flames. *Combust. Flame* **162**(5), 2020–2033 (2015)
20. Savard, B., Bobbitt, B., Blanquart, G.: Structure of a high Karlovitz n-C<sub>7</sub>H<sub>16</sub> premixed turbulent flame. *Proc. Combust. Inst.* **35**(2), 1377–1384 (2015)
21. Shepherd, I.G., Cheng, R.K., Plessing, T., Kortschik, C., Peters, N.: Premixed flame front structure in intense turbulence. *Proc. Combust. Inst.* **29**(2), 1833–1840 (2002)
22. Shy, S.S., Liu, C.C., Lin, J.Y., Chen, L.L., Lipatnikov, A.N., Yang, S.I.: Correlations of high-pressure lean methane and syngas turbulent burning velocities: effects of turbulent Reynolds, Damköhler, and Karlovitz numbers. *Proc. Combust. Inst.* **35**(2), 1509–1516 (2015)
23. Sitte, M.P., Bach, E., Kariuki, J., Bauer, H.J., Mastorakos, E.: Simulations and experiments on the ignition probability in turbulent premixed bluff-body flames. *Combust. Theor. Model.* **20**(3), 548–565 (2016)
24. Sjöholm, J., Rosell, J., Li, B., Richter, M., Li, Z., Bai, X.S., Aldén, M.: Simultaneous visualization of OH, CH, CH<sub>2</sub>O and toluene PLIF in a methane jet flame with varying degrees of turbulence. *Proc. Combust. Inst.* **34**(1), 1475–1482 (2013)
25. Wang, H., Hawkes, E.R., Chen, J.H.: Turbulence-flame interactions in DNS of a laboratory high Karlovitz premixed turbulent jet flame. *Phys. Fluids* **28**, 095,107 (2016)
26. Yang, S.I., Shy, S.S.: Global quenching of premixed CH<sub>4</sub>/air flames: effects of turbulent straining, equivalence ratio, and radiative heat loss. *Proc. Combust. Inst.* **29**(2), 1841–1847 (2002)
27. Yuen, F.T.C., Gülder, Ö.L.: Turbulent premixed flame front dynamics and implications for limits of flamelet hypothesis. *Proc. Combust. Inst.* **34**(1), 1393–1400 (2013)
28. Zhou, B., Brackmann, C., Li, Q., Wang, Z., Petersson, P., Li, Z., Aldén, M., Bai, X.S.: Distributed reactions in highly turbulent premixed methane/air flames: Part I. Flame structure characterization. *Combust. Flame* **162**(7), 2937–2953 (2015)
29. Zhou, B., Brackmann, C., Li, Z., Aldén, M., Bai, X.S.: Simultaneous multi-species and temperature visualization of premixed flames in the distributed reaction zone regime. *Proc. Combust. Inst.* **35**(2), 1409–1416 (2015)
30. Zhou, B., Brackmann, C., Wang, Z., Li, Z., Richter, M., Aldén, M., Bai, X.S.: Thin reaction zone and distributed reaction zone regimes in turbulent premixed methane/air flames: scalar distributions and correlations. *Combust. Flame* **175**, 220–236 (2017)
31. Chomiak, J., Jarosinski, J.: Flame quenching by turbulence. *Combust. Flame* **48**, 241–249 (1982)
32. Karlovitz, B., Lewis, B.: Comment on the paper “Flame quenching by turbulence”. *Combust. Flame* **54**(1–3), 229 (1983)
33. Borghi, R.: Mise au point sur la structure des flammes turbulentes. *J. Chim. Phys.* **81**(6), 361–370 (1984)

34. Borghi, R.: Turbulent combustion modelling. *Prog. Energy Combust. Sci.* **14**, 245–292 (1988)
35. Peters, N.: *Turbulent Combustion*. Cambridge University Press, Cambridge (2000)
36. Peters, N.: Multiscale combustion and turbulence. *Proc. Combust. Inst.* **32**(1), 1–25 (2009)
37. Libby, P.A.: *Introduction to Turbulence. Combustion*. Taylor & Francis, New York (1996)
38. Bray, K.N.C.: The challenge of turbulent combustion. *Symp. (Int.) Combust.* **26**, 1–26 (1996)
39. Farcy, B., Vervisch, L., Domingo, P., Perret, N.: Reduced-order modeling for the control of selective non-catalytic reduction (SNCR). *AIChE J.* **62**(3), 928–938 (2016)
40. Jaouen, N., Vervisch, L., Domingo, P., Ribert, G.: Automatic reduction and optimisation of chemistry for turbulent combustion modeling: impact of the canonical problem. *Combust. Flame* **175**, 60–79 (2017)
41. Jaouen, N.: *An Automated Approach to Derive and Optimise Reduced Chemical Mechanisms for Turbulent Combustion*. Ph.D. thesis, Normandy University, INSA Rouen Normandie (2016)
42. Curl, R.I.: Dispersed phase mixing. Theory and effects in simple reactors. *AIChE* **9**(2), 175–181 (1963)
43. Dopazo, C.: Relaxation of initial probability density functions in the turbulent convection of scalar fields. *Phys. Fluids* **22**(1), 20–30 (1979)
44. Janicka, J., Kolbe, W., Kollmann, W.: Closure of the transport equation for the probability density function of turbulent scalar fields. *J. Non-Equilib. Thermodyn.* **4**, 47–66 (1979)
45. Xu, J., Pope, S.: Pdf calculations of turbulent nonpremixed flames with local extinction. *Combust. Flame* **123**, 281–307 (2000)
46. Sundaram, B., Klimenko, A.Y., Cleary, M.J., Maas, U.: Prediction of NO<sub>x</sub> in premixed high-pressure lean methane flames with an MMC-partially stirred reactor. *Proc. Combust. Inst.* **35**(2), 1517–1525 (2015)
47. Kerstein, A.R.: Hierarchical parcel-swapping representation of turbulent mixing. Part 2. Application to channel flow. *J. Fluid Mech.* **750**, 421–463 (2014)
48. Sirignano, W.A.: Fuel droplet vaporization and spray combustion theory. *Prog. Energy Combust. Sci.* **8**, 291–322 (1983)
49. Sirignano, W.A.: Advances in droplet array combustion theory and modeling. *Prog. Energy Combust. Sci.* **42**, 54–86 (2014)
50. Spalding, D.B.: The combustion of liquid fuels. *Symp. (Int.) Combust.* **4**, 847–864 (1953)
51. Nomura, H., Murakoshi, T., Suganuma, Y., Ujiie, Y., Hashimoto, N., Nishida, H.: Microgravity experiments of fuel droplet evaporation in sub- and supercritical environments. *Proc. Combust. Inst.* **36**(2), 2425–2432 (2017)
52. Luche, J.: *Elaboration of Reduced Kinetic Models of Combustion. Application to the a Kerosene Mechanism*. Ph.D. thesis, Orléans University (2003)
53. Luche, J., Reuillon, M., Boettner, J.C., Cathonnet, M.: Reduction of large detailed kinetic mechanisms: application to kerosene/air combustion. *Combust. Sci. Technol.* **176**(11), 1935–1963 (2004)
54. Dagaut, P.: On the kinetics of hydrocarbons oxidation from natural gas to kerosene and diesel fuel. *Phys. Chem. Chem. Phys.* **4**(11), 2079–2094 (2002)
55. Wang, H., Xu, R., Wang, K., Bowman, C.T., Hanson, R.K., Davidson, D.F., Brezinsky, K., Egolfopoulos, F.N.: A physics-based approach to modeling real-fuel combustion chemistry - I: evidence from experiments, and thermodynamic, chemical kinetic and statistical considerations. *Combust. Flame.* <https://doi.org/10.1016/j.combustflame.2018.03.019> (2018)
56. Lu, T., Law, C.K.: A directed relation graph method for mechanism reduction. *Proc. Combust. Inst.* **30**(1), 1333–1341 (2005)
57. Pepiot, P., Pitsch, H.: An efficient error propagation based reduction method for large chemical kinetic mechanisms. *Combust. Flame* **154**(1–2), 67–81 (2008)
58. Jaouen, N., Vervisch, L., Domingo, P.: Auto-thermal reforming (ATR) of natural gas: an automated derivation of optimised reduced chemical schemes. *Proc. Combust. Inst.* **36**(3), 3321–3330 (2017)
59. Dopazo, C., O'Brien, E.: Functional formulation of nonisothermal turbulent reactive flows. *Phys. Fluids* **17**, 1968–1975 (1974)
60. Goodwin, D.: Cantera: an object-oriented software toolkit for chemical kinetics, thermodynamics, and transport processes. <http://code.google.com/p/cantera> (2009)
61. de Goey, L., Boonkcamp, J.T.T.: A flamelet description of premixed laminar flames and the relation with flame stretch. *Combust. Flame* **119**, 253–271 (1999)
62. Liñán, A., Williams, F.A.: *Fundamental Aspects of Combustion*. Oxford University Press, Oxford (1993)
63. Lele, S.K.: Compact finite difference schemes with spectral like resolution. *J. Comput. Phys.* **103**, 16–42 (1992)
64. Wang, K., Ribert, G., Domingo, P., Vervisch, L.: Self-similar behavior and chemistry tabulation of burnt-gases diluted premixed flamelets including heat-loss. *Combust. Theor. Model.* **4**(14), 541–570 (2010)

65. Boulanger, J.: Asymptotic Analysis and Direct Numerical Simulation of Partially Premixed Combustion. Ph.D. thesis, INSA de Rouen Normandie (2002)
66. Clavin, P.: Premixed combustion and gasdynamics. *Annu. Rev. Fluid Mech.* **26**, 321–52 (1994)
67. Peters, N.: Length scales in laminar and turbulent flames. In: Oran, E.S., Boris, J.A. (eds.) *Numerical Approaches to Combustion Modeling*, Prog. Astronautics and Aeronautics, vol. 135, pp. 155–182. AIAA, Washington (1991)
68. Moureau, V., Domingo, P., Vervisch, L.: From Large-Eddy simulation to direct numerical simulation of a lean premixed swirl flame: filtered laminar flame-pdf modeling. *Combust. Flame* **158**(7), 1340–1357 (2011)
69. Meier, W., Weigand, P., Duan, X., Giezendanner-Thoben, R.: Detailed characterization of the dynamics of thermoacoustic pulsations in a lean premixed swirl flame. *Combust. Flame* **150**(1/2), 2–26 (2007)

## 7.3 Summary in french / Résumé en français

Dans cette section, le contenu de cette thèse est résumé en français.

### Contexte

Les particules de suie sont générées par la combustion dans différents contextes comme les feux domestiques ou brûleurs industriels, fourneaux, moteur à combustion interne ou turbines aéronautiques. Généralement produites lors d'une combustion riche, les particules de suie sont habituellement considérées comme des sous-produits indésirables mais peuvent parfois être synthétisées de manière volontaire dans certaines applications. Un bref aperçu de l'impact des particules de suie sur l'environnement et l'industrie est donné ci-après.

### Impacts sur la santé

Les particules de suie peuvent causer des maladies cardio-vasculaires, des cancers ou des maladies respiratoires ([Niranjan and Thakur, 2017](#)). En général, le terme *Black Carbon* (BC) est utilisé dans les études médicales ou environnementales pour désigner les particules de suie. Une mesure plus générale de concentration en particules ou d'émissions est le niveau de *Particulate Matter* (PM). Toutes les particules, indépendamment de leur composition, sont mesurées en fonction de leur taille. PM2.5 correspond à des particules dont le diamètre est inférieur à 2,5 microns, tandis que PM10 correspond à des particules dont le diamètre est inférieur à 10 microns. Le terme *ultra-fine particles* se réfère quant à lui aux particules dont le diamètre est inférieur à 100 nanomètres. Il est estimé que l'exposition long terme aux PM2.5 a causé environ 467 000 décès prématurés en Europe en 2013 ([Guerreiro et al., 2016](#)).

Différents groupes d'experts ont rassemblé les conclusions de nombreuses études afin d'apporter les informations pertinentes aux preneurs de décision et aux agences de régulation. Par exemple, l'Organisation Mondiale de la Santé a remis un rapport sur les preuves des impacts de la pollution de l'air sur la santé (rapport REVIHAAP) dans lequel les effets sur la santé des PM, y compris *Black Carbon* ont été quantifiés ([WHO, 2013](#)). Plus récemment, l'ANSES (Agence Nationale de Sécurité sanitaire de l'alimentation, de l'Environnement et du travail) a compilé des contributions scientifiques nouvelles et quantifié l'impact des particules de suie (et d'autres particules) issues de différents secteurs et, en particulier, du secteur du transport routier ([ANSES, 2019](#)). Les conclusions principales sont les suivantes:

- Parmi les *Particulate Matter* (différents types de particules) le plus haut niveau de preuve de nocivité est atteint pour les particules de suie, le carbone organique, et les particules ultra-fines (moins de 100 nanomètres).
- Le niveau de preuve de nocivité des particules émises par le secteur du transport routier est considéré comme 'fort'.
- La nocivité de la combustion du charbon, de produits pétroliers et de biomasse a été confirmée.
- Pour les réglementations futures, l'agence recommande de cibler prioritairement des indicateurs de niveaux de particules de suie, de carbone organique, de particules ultra-fines en plus des indicateurs sur les particules plus grosses PM2.5 et PM10.

C'est pourquoi il est essentiel de développer des méthodes de mesure précises et des modèles numériques pour les particules ultra-fines, en particulier pour les particules de suie.

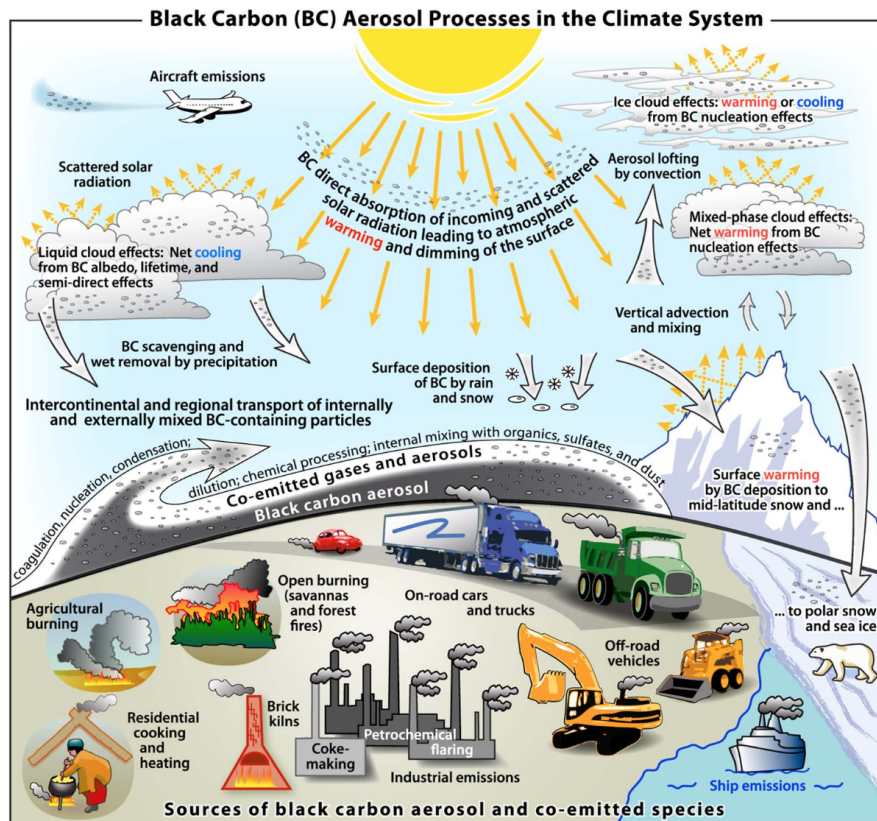


Figure 7.17: Schema des sources d'émission de *Black Carbon* primaire et des procédés par lesquels le *Black Carbon* induit un forçage climatique. Source: Bond et al. (2013)

## Impacts sur le climat

Les émissions de *Black Carbon* induisent un forçage climatique significatif. In Bond et al. (2013), une évaluation complète du forçage climatique par tous les procédés liés aux sources riches en *black carbon* a été effectuée. Les niveaux d'incertitude sont élevés mais une des principale conclusions est qu'il y a une très haute probabilité que les émissions de *black carbon* (seul, sans considérer les espèces co-émises) contribuent à un forçage positif et donc au réchauffement. En revanche, si les espèces co-émises sont considérées, le forçage net pourrait être légèrement négatif. Une représentation schématique des procédés par lesquels le *Black Carbon* induit un forçage climatique est disponible sur la figure 7.17. Les distributions géographiques des émissions de *Black Carbon*, de leur concentration, du forçage climatique et de la réponse en température sont illustrées sur la Figure 7.18.

## Régulation et évolution des émissions en Europe

Des normes européennes d'émissions ont été implémentées afin de définir les limites acceptables d'émissions à l'échappement des véhicules neufs vendus au sein de l'Union Européenne. Les dernières normes EURO 6 définissent des limites en masse et en nombre: pour les niveaux de PM (*Particulate Matter* en g/km) et PN (*Particulate Number* en particules/km). Pour les véhicules diesel et essence. Les normes PM successives ont été de plus en plus contraignantes (Figure 7.19), tandis que les normes PN ont été introduites avec EURO 5b pour les véhicules diesel et EURO 6b pour les véhicules à essence. Dans les deux cas, la limite est de  $6 \cdot 10^{11} [\text{particle}/\text{km}]$ .

Ces normes ont entraîné une réduction significative des émissions de PM et BC par le secteur automobile en Europe comme cela peut être observé sur la Figure 7.20. D'autres secteurs contribuent aux émissions de BC, en particulier les ménages, commerces et institutions (cette catégorie inclut

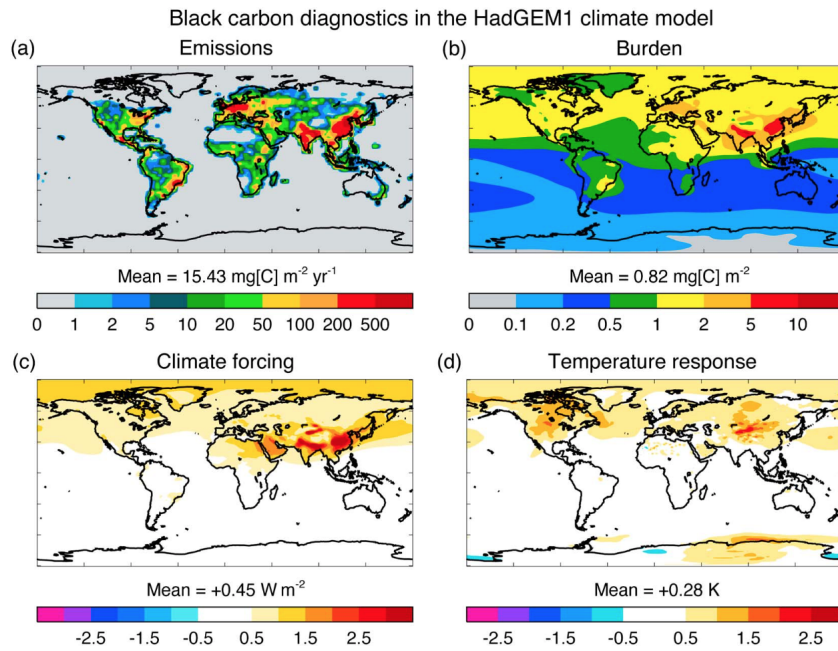


Figure 7.18: Données issues du modèle HadGEM. Source: [Bond et al. \(2013\)](#). (a) Emissions de particules de BC [ $\text{mg.m}^{-2}.\text{yr}^{-1}$ ], (b) Concentration en BC [ $\text{mg.m}^{-2}$ ], (c) forçage radiatif direct dû aux particules de BC [ $\text{W.m}^{-2}$ ], et (d) Variation de température de surface [ $\text{K}$ ] en réponse au forçage radiatif direct dû aux particules de BC.

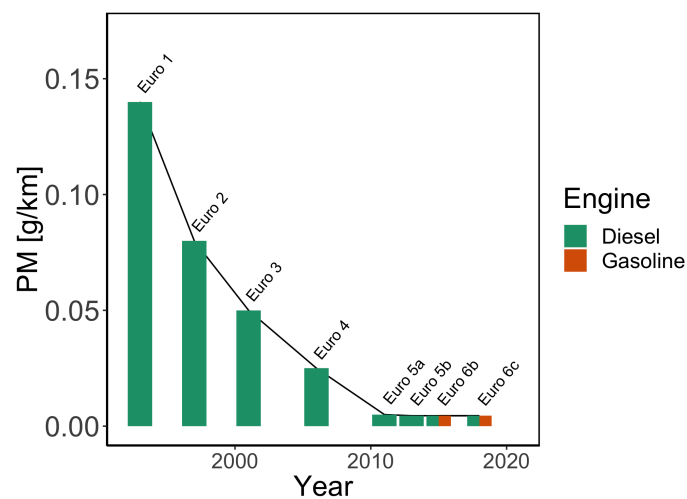


Figure 7.19: Evolution des normes européennes pour les émissions de PM.

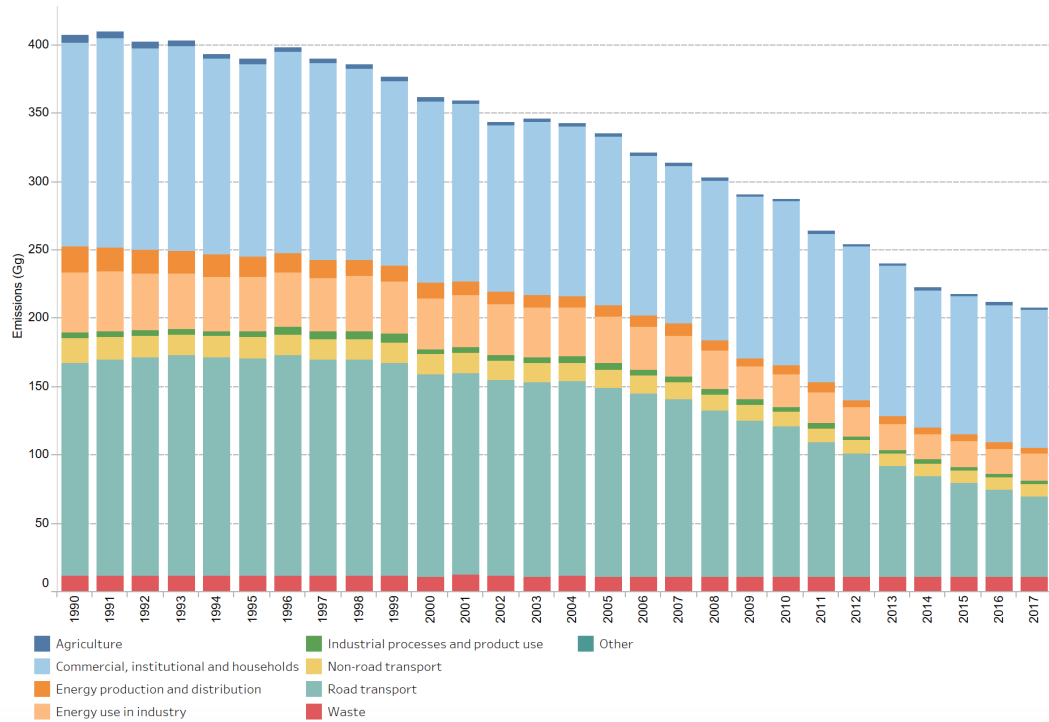


Figure 7.20: Evolution des émissions de BC par secteur en Europe. Source: European Environment Agency (EEA).

la combustion domestique de biomasse comme les feux de cheminée). De plus, les émissions liées aux moyens de transport non-routiers sont non-négligeables. Dans le contexte aéronautique, il n'existe pas encore de normes sur les émissions de PM. Cependant, des programmes de recherche incluant des industriels et des laboratoires académiques visent à une meilleure compréhension de la formation des particules de suie dans les turbines aéronautiques. Par exemple, le projet SOPRANO, coordonné par SAFRAN Tech et financé par le programme de la commission européenne H2020, a financé cette thèse. L'objectif principal du projet est d'améliorer les approches numériques et expérimentales liées à la caractérisation et la prédiction des émissions de particules de suie dans un environnement de brûleur bas-NO<sub>x</sub>. En particulier, des modèles numériques doivent être disponibles pour prédire précisément la distribution de tailles de particules (Particle Size Distribution, PSD) afin de permettre une conception optimisée des futurs moteurs. Dans ce contexte, cette thèse vise à amener un modèle numérique précis pour l'évolution de la PSD.

## Synthèse de matériaux

Dans certaines applications, les particules de suie peuvent être utilisées pour de la synthèse de matériaux. L'objectif est alors de garantir une génération reproductible de particules avec une taille, cristallinité et morphologie bien définies. Les agrégats de suie sont intéressants pour les électrocéramiques (utilisation finale: capteurs, batteries) car ils facilitent le transport d'électrons en minimisant la résistance de contact (Strobel and Pratsinis, 2007). Une autre utilisation des agrégats de suie est dans les catalyseurs et fibres optiques car ils facilitent le transport de réactifs et des produits gazeux dans les lits catalytiques (Keesidis et al., 2017). La synthèse par combustion permet de hauts degrés de pureté ce qui n'est pas toujours le cas des procédés conventionnels en phase liquide ou solide. Par conséquent, une connaissance approfondie de la formation des particules de suie et de l'évolution de la PSD ainsi que de la morphologie des agrégats sont intéressants afin de pouvoir assurer la reproductibilité de la fabrication de produits à haute valeur ajoutée comme des nanotubes de carbone.

## Particules de suie: Définition et description

### Définition

Les particules de suie sont produites durant la combustion incomplète d'hydrocarbures. Principalement composées d'atomes de carbone, elles contiennent également une quantité non-négligeable d'atomes d'hydrogène.

La terminologie et les définitions varient en fonction du domaine scientifique. En science atmosphérique, le terme Black Carbon (BC) est utilisé pour les particules exclusivement formées pendant une combustion incomplète d'hydrocarbures. Une combinaison de propriétés distingue le BC d'autres matériaux absorbant comme les composés de carbone organique ([Bond et al., 2013](#)):

- Une importante absorption de la lumière visible à 550 nm.
- Une résistance à la décomposition à la chaleur. La température de vaporisation est autour de 4000K.
- La morphologie en aggrégat.
- L'insolubilité dans l'eau.

En science de la combustion, le terme de particule de suie n'est pas seulement utilisé pour les aggrégats mais également pour les particules naissantes et les agglomérats. Les particules naissantes sont formées par nucléation à partir des hydrocarbures aromatiques polycycliques (PAH) ([McEnally et al., 2006](#)). Les particules naissantes présentent un ratio des éléments carbone-hydrogène (C/H) compris entre 1.4 et 2.5 ([Russo et al., 2015](#)). Leur taille est comprise entre 1 et 6 nm ([Wang, 2011a](#)). Ces particules naissantes grossissent par coalescence (en fusionnant entre elles lorsqu'elles entrent en collision) et par réaction de surface. Elles forment de plus grosses particules primaires avec des diamètres compris entre 10 et 50 nm ([Wang, 2011a](#)). Tandis que les particules grossissent, elles sont soumises à des réactions de déshydrogénation et se solidifient progressivement et forment alors des aggrégats plutôt que des sphères. L'aggrégation, en opposition à la coalescence, signifie que les particules primaires (ou sphérules) adhèrent l'une à l'autre par un point de contact au lieu de fusionner lorsqu'elles entrent en collision. Les agglomérats se transforment alors en aggrégats graphitiques via la croissance surfacique. Tandis que les particules de suie réagissent et deviennent 'matures', le rapport C/H augmente ([Russo et al., 2015](#)). Un schéma de [Michelsen \(2017\)](#) est reproduit ici (Fig. 7.21). Il représente la formation de particules de suie et leur évolution dans une flamme. Différents termes sont illustrés: particules naissantes (*incipient particles*), agglomérats (*agglomerates*), aggrégats graphitiques (*graphitic aggregates*).

Les propriétés d'absorption sont également utilisées pour caractériser les particules naissantes dans le domaine de la combustion. En fonction de leur faculté à absorber des radiations de l'ultra-violet (UV) à l'infra-rouge (IR) (qui augmente avec la maturité des particules) et de la taille des particules, deux définitions des particules naissantes coexistent dans la communauté de la combustion ([Betrancourt, 2017](#)):

- D'après la première définition, deux classes de particules naissantes existent en fonction de leurs propriétés d'absorption ([D'Anna, 2009](#); [Michelsen, 2017](#)):
  - Les particules naissantes désordonnées qui sont transparentes au visible et IR et ont un diamètre moyen d'environ 3 nm.
  - Les particules naissantes dites empilées, dont le diamètre est supérieur à 3 nm et qui absorbent dans le visible et IR.

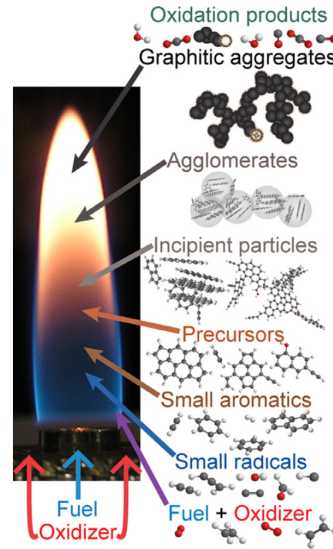


Figure 7.21: Schema de la formation des particules de suie dans une flamme. Les espèces moléculaires et particules ne sont pas représentées à l'échelle. Source: [Michelsen \(2017\)](#)

- D'après la seconde définition, les particules de suie peuvent absorber depuis les UV jusqu'aux IR et peuvent avoir un diamètre minimal de 1 nm. Elles sont définies comme des particules capables d'émettre des radiations de corps noir naturellement à température de flamme ou de manière induite par laser (*laser induced incandescence*, LII) ([Desgroux et al., \(2017\)](#)).

## Morphologie

Les particules de suie sont généralement considérées, soit sphériques (particules naissantes), soit comme des agrégats constitués de plusieurs particules primaires sphériques (sphérules). La figure 7.22 montre une représentation d'un agrégat fractal et les dimensions caractéristiques correspondantes, définies ci-après.

$d_p$  est le diamètre d'une sphérule primaire avec  $R_p$  le rayon correspondant.  $n_p$  est le nombre de sphérules primaires composant l'agrégat.  $d_c$  est le diamètre de la sphère circonscrite à l'agrégat. Cette dimension est également utilisée comme diamètre de collision. Le rayon correspondant est noté  $R_c$ .  $d_g$  est le diamètre de gyration avec le rayon correspondant  $R_g$ .  $d_g$  est caractéristique de la distribution de masse de l'agrégat (lié au moment d'inertie).

Il est admis que les particules de suie, dans certains intervalles de taille, ont une structure fractale, c'est-à-dire une relation entre  $n_p$  et  $d_g$ . Cette relation est décrite par la loi fractale:

$$n_p = k_f (d_g/d_p)^{D_f} . \quad (7.3.1)$$

$D_f$  est la dimension fractale,  $k_f$  est le pre-facteur fractal. Ces constantes peuvent être déterminées expérimentalement. La figure 7.23 (de [Yon et al. \(2011\)](#)) montre un exemple d'accord entre des mesures et une loi fractale théorique avec différentes valeurs de  $D_f$  et  $k_f$  en fonction du carburant.

La morphologie des particules de suie dépend de plusieurs paramètres et peut être difficile à prédire. Elle peut varier en fonction du carburant mais également en fonction des conditions de fonctionnement. Par exemple, dans [Liati et al. \(2014\)](#), des images d'échantillons de particules de suie issue de la même turbine à gas ont été observées par microscope électronique en transmission. Ces images ont été comparées à différents niveaux de puissance du moteur. Les niveaux de puissance à 100%, 65% and 7% sont notés respectivement P100, P65 et P7. Ces niveaux de puissance correspondent approximativement au décollage, vitesse de croisière et à la circulation au sol respectivement. Des images représentatives des agrégats pour chaque niveau de puissance sont montrées

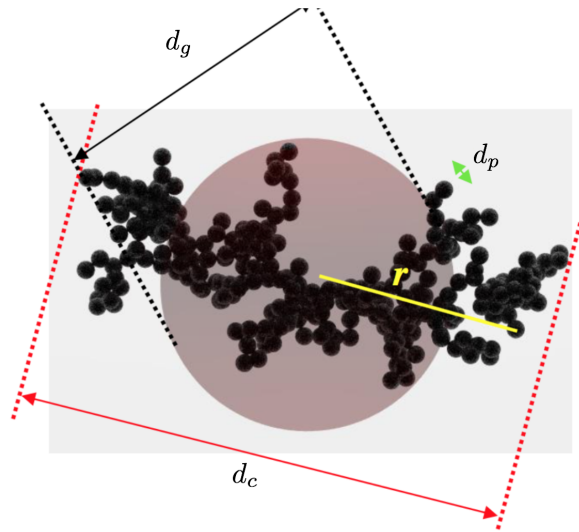


Figure 7.22: Représentation d'un agrégat de suie et de ses dimensions caractéristiques.

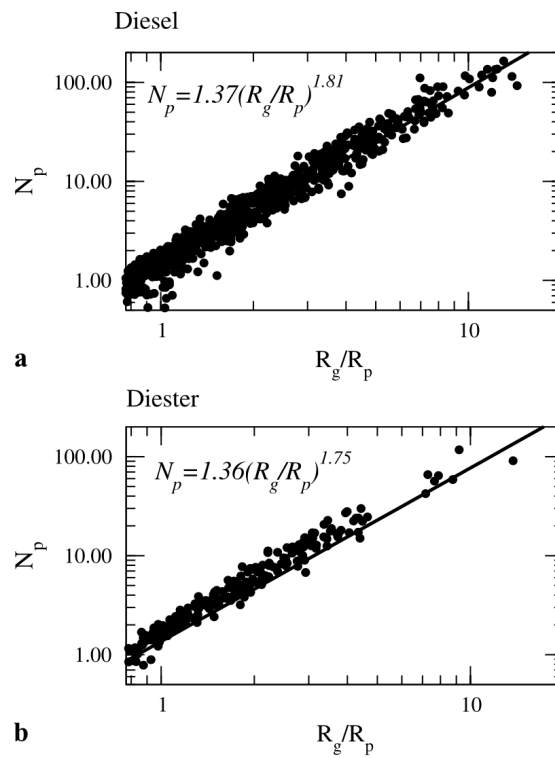


Figure 7.23: Loi fractale pour des particules de suie issue de (a) diesel et (b) diester. Points: Mesures. Lignes: Loi fractale paramétrée. Source: [Yon et al. \(2011\)](#)

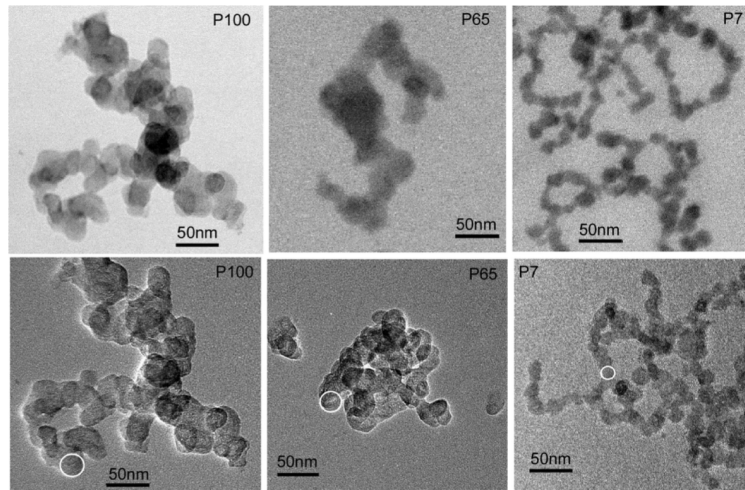


Figure 7.24: Image BF-STEM (ligne supérieure) et images TEM (ligne inférieure) d'aggrégat de suie issus de différent niveaux de puissance moteur. Sur la ligne inférieure, des exemples de sphérules primaires ont été entourés. Source: [Liati et al. \(2014\)](#)

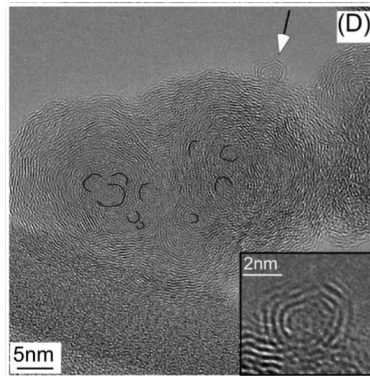


Figure 7.25: Images HRTEM de particules primaires de suie (de l'échantillon P100) présentant plusieurs 'coeurs'. Celles-ci sont entourées de lamelles de graphène. Source: [Liati et al. \(2014\)](#).

sur la figure 7.24. Les auteurs de l'étude observent que la taille de sphérules primaires diminue tandis que la puissance de fonctionnement diminue. Les sphérules qui composent un aggrégat de l'échantillon P100 peuvent être observés sur la figure 1.9.

## Objectifs

La simulation des flammes produisant des particules de suie est complexe à différents niveaux.

- D'abord, des phénomènes chimiques et physiques complexes comme la nucléation entrent en jeu dans la formation des particules de suie. Il est difficile de produire des modèles généralisables et quantitatifs et les plus précis d'entre eux incluent des schemas cinétiques lourds.
- De plus, une fois que les termes sources physiques sont estimés, l'évolution de la distribution de tailles de particules (PSD) à travers la nucléation, l'agglomération et les réactions de croissance/oxydation de surface doit être résolue. Ceci est fait par la résolution de l'équation de bilan de population (PBE). Différentes techniques ont été développées dans ce but. Elles peuvent être classifiées entre les principales classes de méthodes suivantes: hypothèse monodisperse, méthodes des moments (MOM), méthodes sectionnelle et méthodes de Monte Carlo. Chaque

classe présente des avantages et inconvénients spécifiques et le choix parmi ces différentes alternatives peut varier selon l'application.

- Enfin, les phénomènes de radiation et d'interaction chimie-turbulence peuvent jouer un rôle important selon les applications.

Dans cette thèse, nous nous focaliserons sur le second point. Le principal objectif est de **développer une méthode précise et efficace pour la résolution de l'équation de bilan de population**. Les phénomènes de radiation et d'interaction chimie-turbulence sont au-delà du cadre de cette étude. Des concepts généraux et de récents progrès sur la compréhension de la physique et de la chimie des suies (premier point) seront présentés. Cependant, la partie innovante de cette thèse est le développement et la validation d'une nouvelle méthode numérique.

La méthode proposée, appelée HYPE (pour *HYbrid Population balance Equation*) consiste en une formulation hybride avec des particules stochastiques définissant une fonction de densité de probabilité (PDF) et d'une discrétisation sectionnelle fixe pour le calcul des termes sources d'agglomération. Les objectifs de cette méthode sont de:

- Résoudre précisément l'évolution de la distribution de tailles de particules. Une attention particulière doit être apportée au terme source de croissance/réduction.
- Maintenir un coût de calcul relativement modéré comparé à celui d'autres méthodes numériques hautement précises.

La Figure 7.26 illustre les principales étapes de la simulation d'une flamme et des particules de suie associées ainsi que le rôle de la méthode numérique proposée (HYPE).

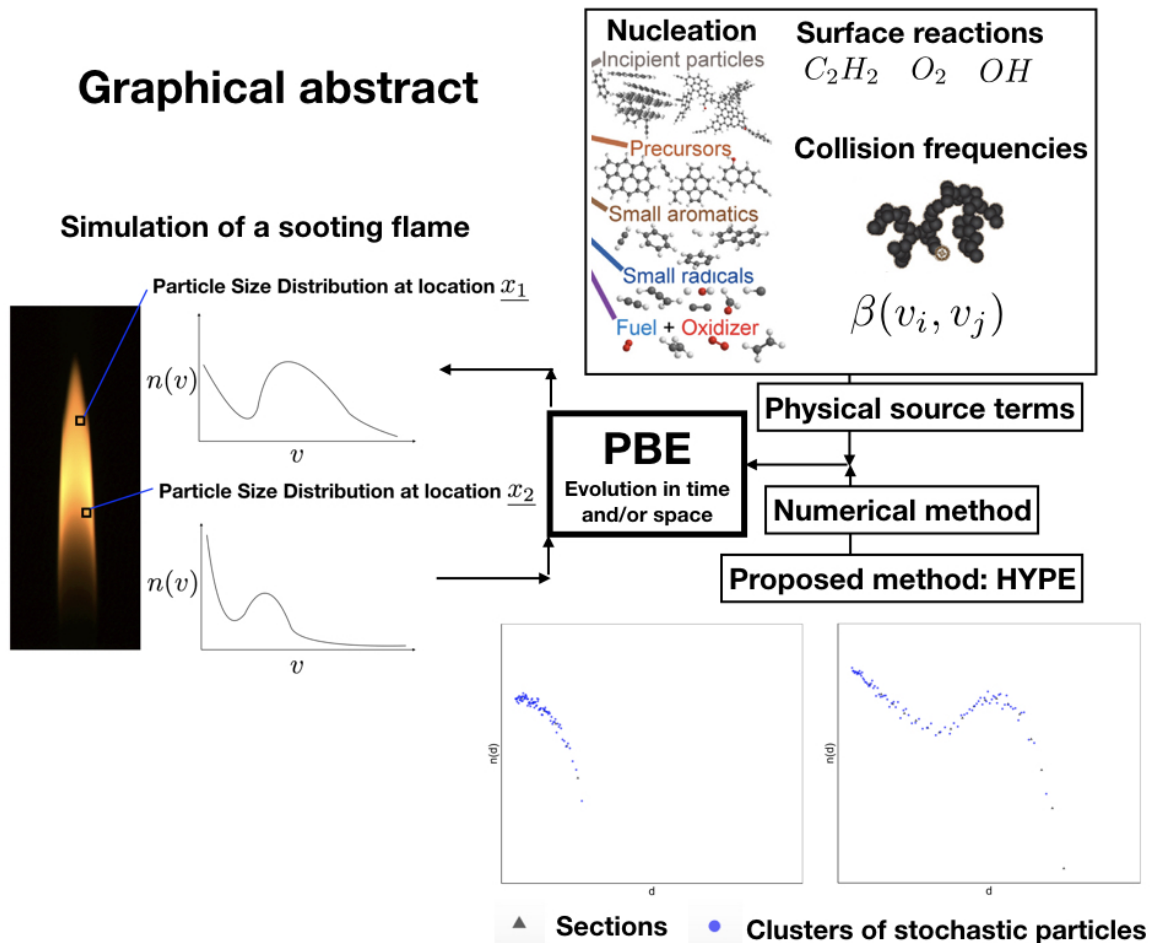


Figure 7.26: Graphical abstract

## Une nouvelle méthode hybride stochastique/sectionnelle: la méthode HYPE

Dans cette partie, une formulation détaillée de la méthode HYPE est d'abord effectuée. Ensuite, l'algorithme pratique est présenté. Des cas tests analytiques sont calculés. Finalement, la précision et le coût de calcul sont mesurés et comparés à des méthodes sectionnelles de référence.

### Formulation du problème

La méthode est décrite ici comme dans [Bouaniche et al. \(2019b\)](#). Comme expliqué précédemment, la distribution de tailles de particules (PSD)  $n(v; \underline{x}, t)$ , nombre de particules à la taille caractéristique  $v$  (en termes de volume ou masse,  $v$  est une variable continue indépendante), par unité de volume de fluide et par unité de taille caractéristique de l'aérosol soumis aux phénomènes simultanés de nucléation, réactions de surface, et agglomération, est régie par l'équation de bilan de population (PBE) ([Ramkrishna, 2000](#); [Solsvik and Jakobsen, 2015](#)):

$$\begin{aligned} \frac{\partial n(v; \underline{x}, t)}{\partial t} + \mathbf{u} \cdot \nabla n(v; \underline{x}, t) + \frac{\partial}{\partial v} [G(v)n(v; \underline{x}, t)] = \dot{h}(v_o; \underline{x}, t) \\ + \frac{1}{2} \int_0^v \beta(v - \bar{v}, \bar{v}) n(v - \bar{v}; \underline{x}, t) n(\bar{v}; \underline{x}, t) d\bar{v} - n(v; \underline{x}, t) \int_0^\infty \beta(v, \bar{v}) n(\bar{v}; \underline{x}, t) d\bar{v}, \end{aligned} \quad (7.3.2)$$

avec les notations usuelles utilisées.  $G(v) > 0$  est le taux de croissance de surface ou  $G(v) < 0$  de décroissance de surface.  $\dot{h}(v_o) > 0$  est le taux de nucléation ou  $\dot{h}(v_o) < 0$  le taux de 'disparition' vu à la plus petite taille  $v_o$ . Le terme source intégral du membre de droite de l'équation prend en compte l'agglomération selon la version continue de l'équation de Smoluchowski ([Smoluchowski, 1917](#)), avec  $\beta(v, \bar{v})$  la fréquence de collision pour deux particules de volumes  $v$  et  $\bar{v}$ . L'évolution de la PSD est donc pilotée par une équation intégro-différentielle-partielle de type hyperbolique.

Le taux de variation surfacique  $G(v)$  correspond à un terme convectif dans l'espace des tailles de particules. La résolution de  $G(v)$  est complexe, de manière similaire au terme convectif non-linéaire dans l'espace physique ([Ferziger and Perić, 1996](#)), ce qui justifie la proposition d'une méthode dans cette étude.

D'autres quantités liées à la PSD sont introduites.  $N_i(\underline{x}, t)$  est défini comme le nombre de particules à la taille caractéristique  $v_i$  par unité de volume de fluide.

$$N_i(\underline{x}, t) = \int_{I_{v_i}} n(v; \underline{x}, t) dv, \quad (7.3.3)$$

où l'intervalle  $I_{v_i} \equiv [v_i^{inf}, v_i^{sup}]$  définit la  $i$ -ème section fixe de taille. La densité de nombre totale par unité de volume de fluide est la somme sur toutes les tailles ou sur les  $M$  sections considérées.

$$N_T(\underline{x}, t) = \int_{v_o}^\infty n(v; \underline{x}, t) dv = \sum_{i=0}^{M-1} N_i(\underline{x}, t). \quad (7.3.4)$$

De même, le terme source de nucléation par unité de volume de fluide est

$$\dot{H}_o(\underline{x}, t) = \int_{I_{v_o}} \dot{h}(v; \underline{x}, t) dv. \quad (7.3.5)$$

Le terme source d'agglomération de Smoluchowski (Eq. (7.3.2)),

$$\begin{aligned} & \dot{a}(v; \underline{x}, t) \\ &= \frac{1}{2} \int_0^v \beta(v - \bar{v}, \bar{v}) n(v - \bar{v}; \underline{x}, t) n(\bar{v}; \underline{x}, t) d\bar{v} - n(v; \underline{x}, t) \int_0^\infty \beta(v, \bar{v}) n(\bar{v}; \underline{x}, t) d\bar{v}, \end{aligned} \quad (7.3.6)$$

conduit à la définition du terme source d'agglomération pour la  $i$ -ème section

$$\dot{A}_i(\underline{x}, t) = \int_{I_{v_i}} \dot{a}(v; \underline{x}, t) dv, \quad (7.3.7)$$

et  $A_T$  est le terme source (négatif) total dû à l'agglomération sur toutes les particules, donc la somme des  $A_i(\underline{x}, t)$  sur toutes les sections

$$\dot{A}_T(\underline{x}, t) = \int_{v_o}^\infty \dot{a}(v; \underline{x}, t) dv = \sum_{i=0}^{M-1} \dot{A}_i(\underline{x}, t). \quad (7.3.8)$$

Toutes ces quantités permettent de combiner la PBE avec l'évolution de la PDF des tailles caractéristiques de particule.

## Méthode hybride stochastique/sectionnelle

**Paramètres de contrôle et description statistique** Afin de bénéficier d'une description dans laquelle la croissance de surface (ou décroissance) est calculée sous la forme d'un terme linéaire, au lieu de résoudre directement la PBE discrétisée, il est proposé de considérer  $N_T(\underline{x}, t)$ , le nombre total de particules par unité de volume et  $\bar{P}(v^*; \underline{x}, t)$ , la fonction de densité de probabilité (PDF) des tailles caractéristiques de particules, où  $v^* \in [v_o, \infty]$  correspond à l'espace d'échantillonnage associé à la variable  $v$ , vue comme une variable aléatoire.

La relation entre  $n(v; \underline{x}, t)$ , la densité de nombre de particules par unité de taille,  $N_i(\underline{x}, t)$ , la densité de nombre de particules dont la taille est dans la section  $I_{v_i}$  ( $v \in I_{v_i}$ ) à la localisation dans l'espace physique  $\underline{x}$  au temps  $t$  (Eq. (7.3.3)), et  $\bar{P}(v^*; \underline{x}, t)$ , la PDF des tailles de particules s'exprime:

$$\int_{I_{v_i}} n(v^*; \underline{x}, t) dv^* = N_i(\underline{x}, t) = N_T(\underline{x}, t) \int_{I_{v_i}} \bar{P}(v^*; \underline{x}, t) dv^*, \quad (7.3.9)$$

où

$$\int_{I_{v_i}} \bar{P}(v^*; \underline{x}, t) dv^* \quad (7.3.10)$$

est la probabilité de trouver des particules de taille  $v \in I_{v_i}$ . Puisque (7.3.9) devrait être valide quel que soit  $I_{v_i}$ ,

$$n(v^*; \underline{x}, t) = N_T(\underline{x}, t) \bar{P}(v^*; \underline{x}, t). \quad (7.3.11)$$

La fonction

$$\delta(v - v^*) = \lim_{dv \rightarrow 0} 1/dv \text{ if } v \in [v^* - dv/2, v^* + dv/2] \quad (7.3.12)$$

$$= 0 \text{ otherwise,} \quad (7.3.13)$$

est introduite et  $\bar{P}(v^*; \underline{x}, t) = \overline{\delta(v(\underline{x}, t) - v^*)}$ , où  $\bar{\cdot}$  correspond à la moyenne statistique (Lundgren, 1967; Dopazo, 1979; Kollmann, 1990; Dopazo et al., 1997).

Le terme de nucléation dans la PBE (Eq. (7.3.2)) peut être écrit  $\dot{h}(v_o; \underline{x}, t) = \dot{H}_o(\underline{x}, t)\delta(v_o - v^*)$ , avec  $\dot{H}_o(\underline{x}, t)$  défini par (7.3.5) dans la limite où la taille de l'intervalle  $I_o$  tend vers zéro. De même, le terme d'agglomération peut être écrit  $\dot{a}(v^*; \underline{x}, t) = \dot{A}_i(\underline{x}, t)\delta(v_i - v^*)$ , avec  $\dot{A}_i(\underline{x}, t)$  défini par (7.3.7) dans la limite où  $I_{v_i}$  tend vers zéro. La PBE devient alors

$$\begin{aligned} \frac{\partial n(v^*; \underline{x}, t)}{\partial t} + \mathbf{u} \cdot \nabla n(v^*; \underline{x}, t) &+ \frac{\partial}{\partial v^*} [G(v^*)n(v^*; \underline{x}, t)] \\ &= \dot{H}_o(\underline{x}, t)\delta(v_o - v^*) + \dot{A}_i(\underline{x}, t)\delta(v_i - v^*). \end{aligned} \quad (7.3.14)$$

La densité de nombre totale  $N_T$  évolue selon

$$\frac{\partial N_T(\underline{x}, t)}{\partial t} + \mathbf{u}(\underline{x}, t) \cdot \nabla N_T(\underline{x}, t) = \dot{H}(\underline{x}, t) + \dot{A}_T(\underline{x}, t), \quad (7.3.15)$$

avec  $\dot{A}_T(\underline{x}, t)$  donné par (7.3.8). D'après (7.3.11) la PDF évolue selon

$$\frac{\partial \bar{P}(v^*; \underline{x}, t)}{\partial t} = \left[ \frac{1}{n(v^*; \underline{x}, t)} \frac{\partial n(v^*; \underline{x}, t)}{\partial t} - \frac{1}{N_T(\underline{x}, t)} \frac{\partial N_T(\underline{x}, t)}{\partial t} \right] \bar{P}(v^*; \underline{x}, t). \quad (7.3.16)$$

En introduisant (7.3.14) et (7.3.15) dans cette expression, l'équation d'évolution de la PDF est obtenue

$$\begin{aligned} \frac{\partial \bar{P}(v^*; \underline{x}, t)}{\partial t} + \mathbf{u}(\underline{x}, t) \cdot \nabla \bar{P}(v^*; \underline{x}, t) &= \overbrace{-\frac{\partial}{\partial v^*} [G(v^*)\bar{P}(v^*; \underline{x}, t)]}^{(i)} \\ &+ \underbrace{\frac{\dot{H}_o(\underline{x}, t)}{N_T(\underline{x}, t)} (\delta(v_o - v^*) - \bar{P}(v^*; \underline{x}, t))}_{(ii)} \\ &+ \underbrace{\frac{1}{N_T(\underline{x}, t)} (\dot{A}_i(\underline{x}, t)\delta(v_i - v^*) - \dot{A}_T(\underline{x}, t)\bar{P}(v^*; \underline{x}, t))}_{(iii)}. \end{aligned} \quad (7.3.17)$$

Dans cette équation de bilan, comme dans la PBE, l'évolution de la taille des particules au taux de croissance  $G(v_i)$  est un terme convectif dans l'espace des tailles (terme (i)). Le terme (ii) du membre de droite est la nucléation, qui se décompose en deux parties préservant la normalisation de la PDF. La première, proportionnelle à  $\delta(v_o - v^*)$ , augmente la probabilité de trouver les plus petites particules, en accord avec le taux de nucléation  $\dot{H}_o(\underline{x}, t)/N_T(\underline{x}, t)$ , tandis que le second diminue, au même taux, la probabilité pour toutes les tailles. Une formulation similaire est utilisée pour l'agglomération (terme (iii)), avec la probabilité évoluant au taux positif ou négatif  $\dot{A}_i(\underline{x}, t)/N_T(\underline{x}, t)$ , associé à la correction proportionnelle à  $-\dot{A}_T(\underline{x}, t)/N_T(\underline{x}, t) > 0$ , tel que la normalisation de la PDF est préservée. En effet, lorsque deux particules de tailles caractéristiques  $v_i$  et  $v_j$  s'agglomèrent, la probabilité de leurs tailles initiales respectives diminue ( $\dot{A}_i(\underline{x}, t) < 0$  and  $\dot{A}_j(\underline{x}, t) < 0$ ), tandis que la probabilité de la nouvelle taille formée  $v_k$  augmente ( $\dot{A}_k(\underline{x}, t) > 0$ ). Cependant, étant donné que la densité de nombre totale en particules physiques diminue au cours du phénomène d'agglomération, la probabilité de toutes les tailles augmente proportionnellement à  $-\dot{A}_T$ , le terme source (négatif) global.

Les solutions des équations (7.3.15) et (7.3.17) fournissent toutes les informations nécessaires pour simuler la nucléation et la croissance d'un ensemble de particules transportées dans un fluide. La distribution de tailles de particules  $N_i(\underline{x}, t)$  peut alors être déduite de (7.3.9).

Puisque l'objectif de la présente étude est de proposer un outil pour la résolution numérique des termes contrôlant l'évolution de la PSD, un réacteur homogène est considéré ( $\mathbf{u} = 0$ ).

**Solution hybride stochastique/sectionnelle-fixe** La fonction de densité de probabilité  $\bar{P}(v^*; t)$  peut être discrétisée sur un ensemble de  $N_P$  particules stochastiques, chacune comportant une information de taille de particule (par exemple le volume), c'est-à-dire  $v = v^k$  pour  $k = 1, \dots, N_P$  et  $\bar{P}(v^*; t) = (1/N_P) \sum_{k=1}^{N_P} \delta(v^k(t) - v^*)$ . Le nombre total de particules stochastiques  $N_P$  est constant.

L'espace de  $v$  est également discrétisé en  $M$  sections fixes, afin de définir un maillage fournissant la distribution de  $\Delta v_i = v_i^{sup} - v_i^{inf}$ , pour  $i = 0, \dots, M-1$ . Des maillages uniformes, géométriques et exponentiels sont testés dans les paragraphes suivants. La taille caractéristique  $v^k$  d'une particule stochastique peut prendre n'importe quelle valeur entre les limites  $[v_o, v_M]$ , indépendamment du maillage fixé.

Parmi cet ensemble de  $N_P$  particules, un nombre entier  $n_{P_i}(t)$  de particules stochastiques comprend des tailles telles que  $v^k \in I_{v_i} \equiv [v_i^{inf}, v_i^{sup}]$ . Ce nombre de particules stochastiques est lié à la PDF et à  $N_i(t)$ , la densité de nombre de particules physiques (Eq. (4.2.1)), selon:

$$\int_{I_{v_i}} \bar{P}(v^*; t) dv^* = \frac{n_{P_i}(t)}{N_P} = \frac{N_i(t)}{N_T(t)}. \quad (7.3.18)$$

Afin de simuler l'évolution dans le temps de la PDF à travers  $v^k(t)$ , l'évolution temporelle des particules stochastiques, une méthode de pas de temps fractionnaire est employée. En commençant à l'instant  $t^n$ , la croissance/diminution de surface est d'abord appliquée pour avancer la solution à l'instant  $t^{n+\frac{1}{2}}$ . Ceci est appliqué de manière déterministe à chaque  $k$ -ème particule, comme un simple procédé linéaire proportionnel à  $G(v^k(t))$ , ce qui est l'avantage majeur de la méthode proposée. Ensuite, à partir de l'instant  $t^{n+\frac{1}{2}}$ , la solution est avancée à  $t^{n+1}$  en appliquant les effets de la nucléation et de l'agglomération qui sont simulés en déplaçant les particules stochastiques entre les sections. Le nombre de particules stochastiques sélectionnées de manière aléatoire pour être retirées d'une section et allouées à une autre est calculé selon les taux de nucléation et d'agglomération qui pilotent l'évolution de la PDF (Eq. (7.3.17)). A chaque instant  $t^n$ ,  $\delta t$  est calculé tel que la stabilité est garantie. Différentes valeurs de  $\delta t$  peuvent être nécessaires en pratique afin d'avancer de  $t^n$  à  $t^{n+\frac{1}{2}}$  (croissance/diminution) et de  $t^{n+\frac{1}{2}}$  à  $t^{n+1}$  (nucléation et agglomération).

**Croissance/perte de surface** Pendant la phase de croissance ou de perte de surface, la taille de la  $k$ -ème particule stochastique évolue selon

$$\frac{dv^k(t)}{dt} = G(v^k(t)), \quad k = 1, \dots, N_P. \quad (7.3.19)$$

A chaque particule stochastique correspond une taille mise à jour  $v^k(t^{n+\frac{1}{2}})$ . La densité de nombre totale reste constante pendant l'étape de croissance ( $dN_T(t)/dt = 0$ ). Une fois que l'équation (7.3.19) est résolue pour chaque particule, une distribution mise à jour de particules stochastiques est disponible et la PDF  $\bar{P}(v^*; t^{n+\frac{1}{2}})$  est connue ainsi que  $n_{P_i}(t^{n+\frac{1}{2}})$  le nombre de particules stochastiques dans chaque section.

**Nucléation et agglomération** La nucléation et l'agglomération sont appliqués successivement, ce qui impacte le nombre de densité total  $N_T(t)$  et la PDF via le changement de  $n_{P_i}(t^{n+\frac{1}{2}})$  pour chaque intervalle  $I_{v_i}$ . En commençant à  $N_T(t^n) = N_T(t^{n+\frac{1}{2}})$ , la densité de nombre évolue de  $t^{n+\frac{1}{2}}$  à  $t^{n+1}$  avec

$$\frac{dN_T(t)}{dt} = \dot{H}_o(t) + \dot{A}_T(t). \quad (7.3.20)$$

Une fois que  $N_T(\underline{x}, t^{n+1})$  est connu (7.3.20), l'équation de la PDF (7.3.17) est avancée dans le temps avec la nucléation et l'agglomération:

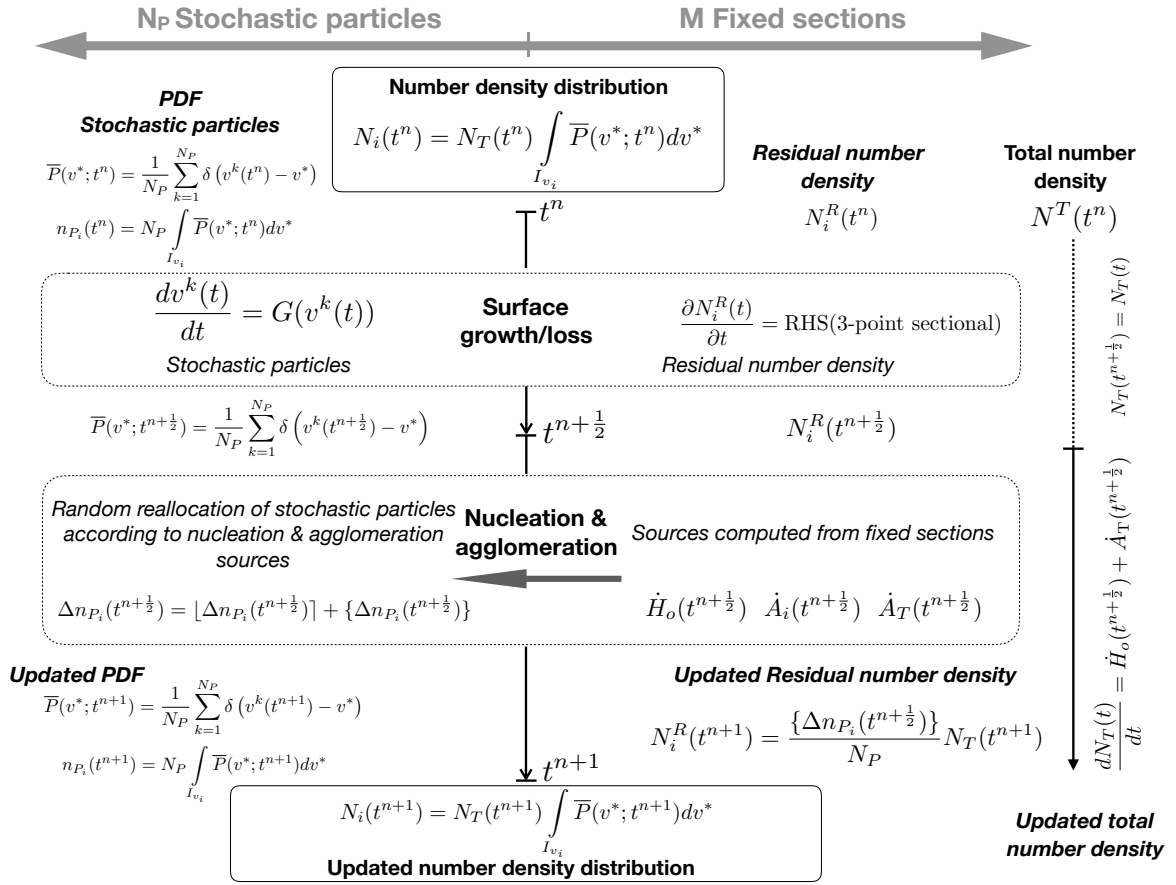


Figure 7.27: Organigramme de la méthode hybride stochastique/sectionnelle-fixe

$$\begin{aligned}\bar{P}(v^*; t^{n+1}) &= \alpha_{H_o} \delta(v_o - v^*) + \alpha_{A_i} \delta(v_i - v^*) \\ &+ (1 - \alpha_{H_o} - \alpha_{A_T}) \bar{P}(v^*; t^{n+\frac{1}{2}}),\end{aligned}\quad (7.3.21)$$

avec  $\alpha_{H_o}$  l'augmentation relative de  $\bar{P}(v_o; t^{n+\frac{1}{2}})$  par nucléation (et la diminution de  $\bar{P}(v^*; t^{n+\frac{1}{2}})$  pour  $v^* \neq v_o$ ),  $\alpha_{A_i}$  l'augmentation/diminution relative due à l'agglomération et  $\alpha_{A_T}$  la source (négative) totale d'agglomération définie par Eq. (7.3.17):

$$\alpha_{H_o} = \frac{\dot{H}_o(t^{n+\frac{1}{2}})}{N_T(t^{n+1})} \cdot \delta t, \quad (7.3.22)$$

$$\alpha_{A_i} = \frac{\dot{A}_i(t^{n+\frac{1}{2}})}{N_T(t^{n+1})} \cdot \delta t, \quad (7.3.23)$$

$$\alpha_{A_T} = \frac{\dot{A}_T(t^{n+\frac{1}{2}})}{N_T(t^{n+1})} \cdot \delta t. \quad (7.3.24)$$

D'après Eq. (7.3.18), en intégrant sur  $I_{v_i}$  et en multipliant par  $N_P$ , l'évolution de la PDF donnée par la relation (4.2.13) conduit à l'évolution du nombre de particules stochastiques par section. Cette évolution temporelle discrétisée est organisée selon:

$$n_{P_i}(t^{n+1}) = n_{P_i}(t^{n+\frac{1}{2}}) + \Delta n_{P_i}(t^{n+\frac{1}{2}}), \quad (7.3.25)$$

avec des incrémentations  $\Delta n_{P_i}(t^{n+\frac{1}{2}})$  sous la forme de nombres réels, qui devront être transformés par la suite en nombres entiers de particules dans l'algorithme de Monte Carlo. D'après (7.3.21),

$$\begin{aligned}\Delta n_{P_o}(t^{n+\frac{1}{2}}) &= (\alpha_{H_o} + \alpha_{A_o}) N_P - (\alpha_{H_o} + \alpha_{A_T}) n_{P_o}(t^{n+\frac{1}{2}}) \\ &+ \alpha_{R_o} N_P,\end{aligned}\quad (7.3.26)$$

$$\begin{aligned}\Delta n_{P_i}(t^{n+\frac{1}{2}}) &= \alpha_{A_i} N_P - (\alpha_{H_o} + \alpha_{A_T}) n_{P_i}(t^{n+\frac{1}{2}}) \\ &+ \alpha_{R_i} N_P \text{ for } i \neq o.\end{aligned}\quad (7.3.27)$$

Les termes proportionnels à  $\alpha_{R_i}$  sont l'accumulation de l'erreur d'arrondi, qui tend vers zéro pour  $N_P \rightarrow \infty$ . Après accumulation sur plusieurs itérations, cela impacte les particules lorsque  $\alpha_{R_i} \geq 1/N_P$ . A chaque itération,  $\Delta n_{P_i}(t^{n+\frac{1}{2}})$  est ainsi décomposé en une partie entière et une partie fractionnaire (décimale). La partie décimale  $\{\Delta n_{P_i}(t^{n+\frac{1}{2}})\}$  est définie en fonction de la partie entière qui est le plus proche entier  $\lfloor \Delta n_{P_i}(t^{n+\frac{1}{2}}) \rfloor$ ,

$$\{\Delta n_{P_i}(t^{n+\frac{1}{2}})\} = \Delta n_{P_i}(t^{n+\frac{1}{2}}) - \lfloor \Delta n_{P_i}(t^{n+\frac{1}{2}}) \rfloor. \quad (7.3.28)$$

La partie entière  $\lfloor \Delta n_{P_i}(t^{n+\frac{1}{2}}) \rfloor$  définit la variation du nombre de particules stochastiques au sein d'une section pendant l'étape de réallocation correspondant à la nucléation et à l'agglomération. L'algorithme de Monte Carlo suivant est appliqué:

- Si  $\lfloor \Delta n_{P_i}(t^{n+\frac{1}{2}}) \rfloor$  est négatif, un nombre aléatoire  $-\lfloor \Delta n_{P_i}(t^{n+\frac{1}{2}}) \rfloor$  de particules stochastiques est sélectionné parmi les  $n_{P_i}(t^{n+\frac{1}{2}})$  particules présentes dans  $I_{v_i}$ .
- Toutes les particules sélectionnées de tous les intervalles  $I_{v_i}$  ( $i = 0, \dots, M-1$ ) constituent un ensemble  $\mathcal{P}(t^{n+\frac{1}{2}})$  de particules dont les caractéristiques doivent changer.

Table 7.1: Growth parameters

Cas	1(a)	1(b)
Distrib. initiale	1 for $0.2 \leq v$ ; 0 else	$\delta(1)$
Taux de croissance	0.05	$v$
Freq. Agglo.	0	0
Nombre de sections	20	40
Type de maillage	unif. $\Delta v = 0.2$	geo. $F_s = 2$
Intervalle de taille	0 – 4	$0.7 - 7.3 \cdot 10^{11}$

- Si  $\lfloor \Delta n_{P_i}(t^{n+\frac{1}{2}}) \rfloor$  est positif,  $\lfloor \Delta n_{P_i}(t^{n+\frac{1}{2}}) \rfloor$  particules sont prises de  $\mathcal{P}(t^{n+\frac{1}{2}})$  et allouées à  $I_{v_i}$  à la taille représentative  $v_i^*(t^{n+\frac{1}{2}})$ , définie pour conserver la mass, comme expliqué dans le paragraphe suivant.

Plus le nombre total de particules stochastiques  $N_P$  est grand, plus la contribution relative de la partie décimale  $\{\Delta n_{P_i}(t^{n+\frac{1}{2}})\}$  à  $\Delta n_{P_i}(t^{n+\frac{1}{2}})$  est petite. Cette partie résiduelle décimale définit  $N_i^R(t^n)$ , une densité de nombre résiduelle de particules physiques dans la section  $v_i$ , qui est calculée au temps  $t^n$  suivant (7.3.18)

$$N_i^R(t^n) = \frac{\{\Delta n_{P_i}(t^{n-\frac{1}{2}})\}}{N_P} N_T(t^n), \quad (7.3.29)$$

où  $\Delta n_{P_i}(t^{n-\frac{1}{2}})$  correspond à  $\Delta n_{P_i}$  de l'itération précédente dans le temps. La croissance/réduction des particules physiques représentées par cette densité de nombre résiduelle  $N_i^R(t^n)$  n'est pas incluse dans les particules stochastiques et nécessite une résolution spécifique, entre  $t^n$  et  $t^{n+\frac{1}{2}}$  (c'est-à-dire en même temps que la croissance/réduction pour les particules stochastiques Eq. (7.3.19)). Cela est fait via une méthode sectionnelle basée sur la discrétisation à 3 points pour la croissance/réduction des particules (Park and Rogak, 2004) (Eq. 3.5.18). Ensuite,  $N_i^R(t^{n+\frac{1}{2}})$  est connu et  $\alpha_{R_i}$  est obtenu à partir de

$$\alpha_{R_i} = \frac{N_i^R(t^{n+\frac{1}{2}})}{N_T(t^{n+1})}, \quad (7.3.30)$$

et appliqué aux équations (7.3.26) et (7.3.27) pour calculer  $\Delta n_{P_i}(t^{n+\frac{1}{2}})$ . Pour des valeurs suffisamment grandes de  $N_P$ , typiquement  $10^5$  comme montré ci-après, le nombre de densité résiduel est négligeable et ne va pas perturber considérablement la précision de la méthode. Dans ce cas,  $\alpha_R(v_i)$  peut être fixé à zéro dans les expressions (7.3.26) et (7.3.27). Cependant, comme montré ci-dessous, considérer la contribution de la partie résiduelle permet de réduire  $N_P$  (jusqu'à  $10^3$  ou moins) et par conséquent, le coût de calcul.

De manière optionnelle, un seuil peut également être paramétré tel que lorsque le nombre de particules stochastiques présentes dans une section donnée devient trop petit, la croissance/réduction de surface est entièrement résolue via l'évolution de  $N_i^R(t)$ . En pratique, un seuil de 5 particules par section est utilisé et a été considéré suffisant pour éviter un éventuel bruit en queue de distribution.

Un organigramme résumant la méthode est représenté Figure 7.27

**Termes sources d'agglomération** La méthode proposée dans Kumar and Ramkrishna (1996a) est retenue pour calculer les termes sources d'agglomération  $\dot{A}_i(t)$  de l'équation (7.3.23). Pour deux particules quelconques entrant en collision, de volume  $v$  dans la section  $i$  et  $\bar{v}$  dans la section  $j$ , la fréquence de collision  $\beta(v, \bar{v})$  est supposée constante, égale à  $\beta(v_i, v_j) = \beta_{i,j}$ . Les particules formées par agglomération sont distribuées dans les sections d'une manière qui conserve les moments d'ordre 0 et 1 de la PSD, c'est-à-dire le nombre et la masse. Cette méthode évite l'évaluation d'une double intégrale des fréquences de collision et est par conséquent peu coûteuse (voir Kumar and Ramkrishna (1996a) pour plus de détails). la source d'agglomération utilisée dans (7.3.23) s'exprime:

$$\begin{aligned}
\dot{A}_i(t) &= \sum_{\substack{j,k \\ v_{i-1} \leq v_j + v_k \leq v_{i+1}}}^{k \leq j \leq i} \left(1 - \frac{\delta_{j,k}}{2}\right) \eta \beta_{j,k} N_j(t) N_k(t) \\
&- N_i(t) \sum_{k=0}^{M-1} \beta_{i,k} N_k(t),
\end{aligned} \tag{7.3.31}$$

avec

$$\eta = \begin{cases} \frac{v_{i+1}^* - (v_j^* + v_k^*)}{v_{i+1}^* - v_i^*} & \text{if } v_i^* \leq v_j^* + v_k^* \leq v_{i+1}^*, \\ \frac{v_{i-1}^* - (v_j^* + v_k^*)}{v_{i-1}^* - v_i^*} & \text{if } v_{i-1}^* \leq v_j^* + v_k^* \leq v_i^*, \end{cases} \tag{7.3.32}$$

Dans l'approche hybride stochastique/sectionnelle-fixe, le volume caractéristique  $v_i^*$  doit être représentatif de la masse moyenne des particules contenue dans la  $i$ -ème section.  $v_i^*$  est calculé de manière dynamique, en fonction des volumes des particules stochastiques contenues dans la section et en fonction des termes résiduels résultants de l'opération d'arrondi,

$$v_i^*(t^{n+\frac{1}{2}}) = \frac{(N_T(t^n)/N_P) \sum_{k=1}^{n_{P_i}(t)} v_i^k(t^{n+\frac{1}{2}}) + N_i^R(t^{n+\frac{1}{2}}) v_i^*(t^n)}{(N_T(t^n)/N_P) n_{P_i}(t^{n+\frac{1}{2}}) + N_i^R(t^{n+\frac{1}{2}})}, \tag{7.3.33}$$

où  $v_i^k = v^k$  si  $v^k \in I_{v_i}$  et  $v_i^k = 0$  sinon,  $n_{P_i}(t^{n+\frac{1}{2}})$  est le nombre de particules stochastiques dans la  $i$ -ème section (Eq. (7.3.18)) et  $N_i^R(t^{n+\frac{1}{2}})$  est la densité de nombre résiduelle dans la section après application de la croissance surfacique.  $v_i^*$  doit être mis à jour de nouveau après la réallocation des particules due à l'agglomération, pour en déduire  $v_i^*(t^{n+1})$  de l'équation (7.3.33) avec  $N_T(t^{n+1})$ ,  $v_i^k(t^{n+1})$ ,  $N_i^R(t^{n+1})$ ,  $v_i^*(t^{n+\frac{1}{2}})$ ,  $n_{P_i}(t^{n+1})$ .

Une fois que  $v_i^*$  est déterminé, les particules assignées à la  $i$ -ème section sont distribuées dans la section suivant deux étapes:

- D'abord, les  $\lfloor \Delta n_{P_i}(t^{n+\frac{1}{2}}) \rfloor$  particules sont allouées aléatoirement dans chaque section aux tailles  $v^k(t^{n+\frac{3}{4}})$ , qui sont des tirages d'une variable aléatoire  $v$  suivant une distribution linéaire par parties définie par la PDF.

$$p(v \mid v_i^{inf}, v_i^{sup}, w_i, w_{i+1}) = 2 \frac{w_i(v_i^{sup} - v) + w_{i+1}(v - v_i^{inf})}{(w_i + w_{i+1}) \Delta v_i^2}. \tag{7.3.34}$$

Dans cette distribution, les poids  $w_i$  sont calculés comme les variations des densités de nombre à  $v_i^*$ ,

$$\begin{aligned}
w_i &= \Delta n_i(t^{n+\frac{1}{2}}) + \frac{\Delta n_i(t^{n+\frac{1}{2}}) - \Delta n_{i-1}(t^{n+\frac{1}{2}})}{v_i^* - v_{i-1}^*} (v_i^{inf} - v_{i-1}^*), \\
w_{i+1} &= \Delta n_{i+1}(t^{n+\frac{1}{2}}) + \frac{\Delta n_{i+1}(t^{n+\frac{1}{2}}) - \Delta n_i(t^{n+\frac{1}{2}})}{v_{i+1}^* - v_i^*} (v_i^{sup} - v_i^*),
\end{aligned}$$

avec  $\Delta n_i(t) = \Delta n_{P_i}(t) N_T(t) / (N_P \Delta v_i)$  (Eq. (7.3.18)). Une telle distribution garantit une allocation relativement continue des particules stochastiques. Cependant, elle ne garantit pas strictement la conservation de la masse/volume de particules.

Table 7.2: Agglomeration parameters

Case	2(a)	2(b)
Initial	$e^{-v}$	$e^{-v}$
Agglo. kernel	1	$v_i + v_j$
Number of sections	40	40
Grid type: Exponential, $\alpha$	1.17	1.25
Size range	$6.7 \cdot 10^{-2} - 209$	$6.7 \cdot 10^{-2} - 2006$

- La conservation de la masse est obtenue dans un second temps en appliquant un facteur de correction  $K_i$

$$K_i = \frac{v_i^*(t^{n+\frac{1}{2}})}{(1/n_{P_i}(t^{n+\frac{3}{4}})) \sum_{k=1}^{n_{P_i}(t^{n+1})} v_i^k(t^{n+\frac{3}{4}})} , \quad (7.3.35)$$

Ensuite,

$$v_i^k(t^{n+1}) = K_i v_i^k(t^{n+\frac{3}{4}}) , \quad (7.3.36)$$

et la masse est conservée au cours de l'étape de réallocation.

La taille de nucléation est fixée à la limite inférieure de la plus petite section  $v_o$ . Comme les étapes numériques correspondant aux phénomènes de nucléation/agglomération et de croissance sont séquentielles dans le modèle, il est nécessaire de prendre en compte la dispersion des tailles de nucléation effectives dues à la croissance des particules pendant un pas de temps de nucléation/agglomération. Pour  $\lfloor \Delta n_{P_o}(t^{n+\frac{1}{2}}) \rfloor > 0$ , les  $\lfloor \Delta n_{P_o}(t^{n+\frac{1}{2}}) \rfloor$  particules sont par conséquent allouées aléatoirement suivant une distribution uniforme entre  $v_o$  et  $v_o + G(v_o)\delta t$ .

**Pas de temps** Comme indiqué précédemment, une méthode de pas de temps fractionnaire est adoptée. La notation  $\delta t$  utilisée plus haut était schématique pour expliquer la structure de l'algorithme. Le pas de temps caractéristique du premier sous pas de temps de croissance (Fig. 7.27) est calculé en suivant une condition usuelle de Courant Friedrichs Lewy (CFL) (Ferziger and Perić, 1996), basée sur le taux de croissance  $G(v)$  et la discrétisation des sections

$$\delta t_G = C \min [\Delta v_0/|G(v_0)|, \dots, \Delta v_{M-1}/|G(v_{M-1})|] . \quad (7.3.37)$$

Les calculs ont été réalisés avec  $C = 0.01$  afin de garantir la stabilité des parties sectionnelles et stochastiques.

Le temps caractéristique de nucléation-agglomération de l'algorithme est déterminé dans le but de limiter le changement relatif de la distribution

$$\delta t_A = (\gamma + \sigma) \frac{N_T}{\left| \dot{H}_o + \dot{A}_T \right| + \sum_{i=0}^{M-1} \left| \dot{A}_i \right|} , \quad (7.3.38)$$

avec  $\sigma = 0.02$  dans les simulations présentées ci-après. Si la nucléation domine, comme par exemple au début d'un calcul avec une distribution initiale négligeable et présente en majorité dans la plus petite section, de plus larges pas de temps peuvent être autorisés afin de permettre à  $N_T$  de s'accroître plus rapidement jusqu'à ce que l'échange de particules entre les sections deviennent significatif. Dans ce cas,  $\gamma = 1$  est utilisé dans l'équation (7.3.38). Ce régime spécifique 'nucléation-dominant' est considéré comme atteint à un certain instant si:

$$\left| \dot{H}_o(t) + \dot{A}_T(t) \right| > 100 \cdot \sum_{i=0}^{M-1} \left| \dot{A}_i(t) \right| , \quad (7.3.39)$$

$$N_0(t)/N_T(t) > 0.99 . \quad (7.3.40)$$

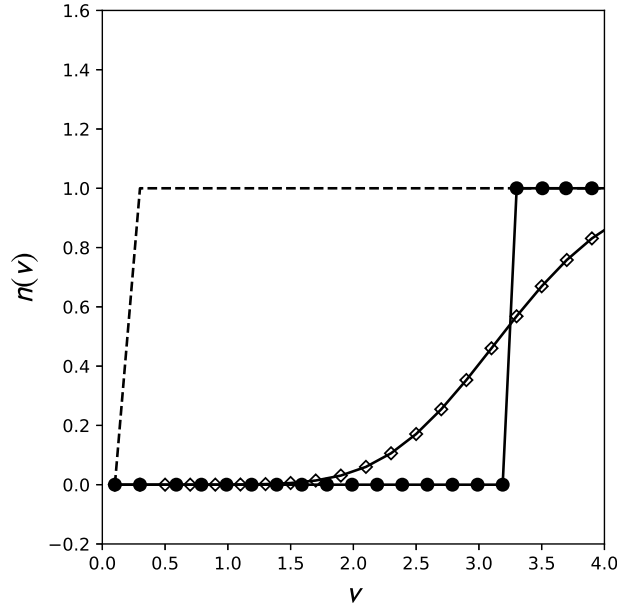


Figure 7.28: PSD  $n(v; t)$ . Croissance: cas 1(a) du tableau 7.1. Pointillés: Distribution initiale (la discontinuité est entre les abscisses centrées des sections). Temps normalisé:  $t = 60$ . Ligne avec diamants vides: méthode sectionnelle 2-points. Ligne avec cercles pleins: méthode hybride,  $N_P = 10^3$  (les valeurs sont données à  $v_i^*$  (Eq. (7.3.33))).

Sinon,  $\gamma = 0$  est imposé dans (7.3.38) afin de résoudre les régimes plus généraux de l'évolution de la PSD.

Pour les cas tests considérés dans cette étude,  $\delta t_G \leq \delta t_A$  et une ou plusieurs sous-itérations de croissance peuvent être appliquées entre deux sous-itérations d'agglomération/nucléation.  $\delta t_G$  est ensuite ajusté afin que  $\delta t_A$  soit un de ses multiples, tout en vérifiant la condition de stabilité.

## Cas tests analytiques

Des cas tests analytiques pour lesquels les termes sources ont des formes simplifiées, permettant de connaître la solution analytique ont été simulés. Cela permet d'évaluer de manière détaillée la précision de la méthode numérique. Les conditions initiales et termes sources sont disponibles dans la thèse complète (en anglais). Seules les figures illustrant les principaux résultats sont reportées dans ce résumé en français.

Table 7.3: Précision et coût CPU. Cas 1: Pure croissance, Cas 2: Pure agglomération, Cas 3: Croissance/perte & agglomération. Cas 4: Nucléation & croissance.

Cas	Erreur	Methode		
		Sectionnelle 2pt	Sectionnelle 3pt	Hybride
1(a)	$\epsilon_{M_1}(\%)$	-0.13	-	-0.0078
	$\epsilon_{M_2}(\%)$	1.5	-	-0.012
	$\epsilon_{EMD}$	0.11	-	1.9e-17
	Temps CPU	1.0	-	1.1
1(b)	$\epsilon_{M_1}(\%)$	-2.9	-2.9	-2.7
	$\epsilon_{M_2}(\%)$	770 845	105	-5
	Temps CPU	1.0	1.0	1.4
2(a)	$\epsilon_{M_1}(\%)$	0.4	0.4	-0.1
	$\epsilon_{M_2}(\%)$	1.6	1.6	0.7
	$\epsilon_{EMD}$	0.006	0.006	0.013
	Temps CPU	1.0	1.0	1.3
2(b)	$\epsilon_{M_1}(\%)$	-1.1	-1.1	-2.2
	$\epsilon_{M_2}(\%)$	0.4	0.4	-1.4
	$\epsilon_{EMD}$	0.0008	0.0008	0.0048
	Temps CPU	1.0	1.0	1.2
3(a)	$\epsilon_{M_1}(\%)$	5.4	5.6	-0.5
	$\epsilon_{M_2}(\%)$	48 783	54	1.8
	$\epsilon_{EMD}$	0.62	0.19	0.06
	Temps CPU	1.0	1.1	1.7
3(b)	$\epsilon_{M_1}(\%)$	5.4	5.7	0.9
	$\epsilon_{M_2}(\%)$	22 141	49	16
	$\epsilon_{EMD}$	0.60	0.17	0.10
	Temps CPU	1.0	1.0	1.3
3(c)	$\epsilon_{M_1}(\%)$	5.7	5.5	0.4
	$\epsilon_{M_2}(\%)$	9 811	49	17
	$\epsilon_{EMD}$	0.57	0.16	0.13
	Temps CPU	1.0	1.0	1.1
3(d)	$\epsilon_{M_1}(\%)$	0.6	0.5	0.9
	$\epsilon_{M_2}(\%)$	776	-1.4	16
	$\epsilon_{EMD}$	0.44	0.08	0.10
	Temps CPU	1.0	1.1	0.1
3(e)	$\epsilon_{M_1}(\%)$	5.4	5.8	1.1
	$\epsilon_{M_2}(\%)$	760	33	32
	$\epsilon_{EMD}$	0.47	0.24	0.09
	CPU time	1.0	1.1	1.2
4	$\epsilon_{M_1}(\%)$	-3.4	-3.4	-3.4
	$\epsilon_{M_2}(\%)$	696 121	60	-9
	$\epsilon_{EMD}$	0.66	0.18	0.02
	Temps CPU	1.0	1.0	1.5

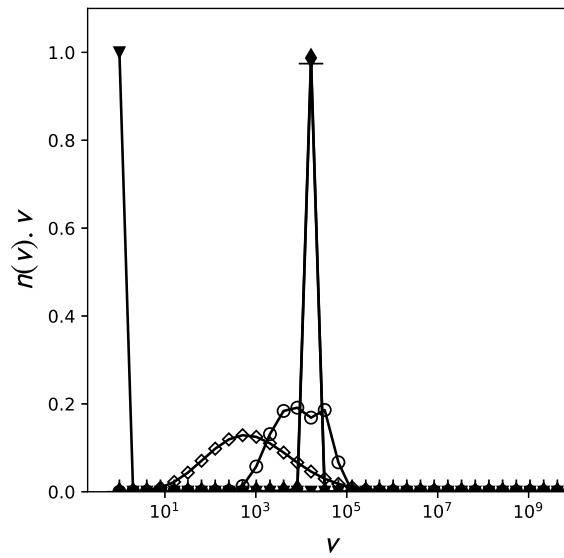


Figure 7.29: Distribution de tailles  $n(v; t) \cdot v$ . Croissance: cas 1(b) du Tableau 4.1. Triangles: distribution initiale. Symboles plus: solution analytique. Ligne avec des diamants vides: méthode sectionnelle 2-points. Ligne avec des cercles: méthode sectionnelle 3-points (Park and Rogak, 2004). Diamants pleins: méthode hybride sans terme résiduel,  $\alpha_R = 0$ ,  $N_P = 10^3$ .

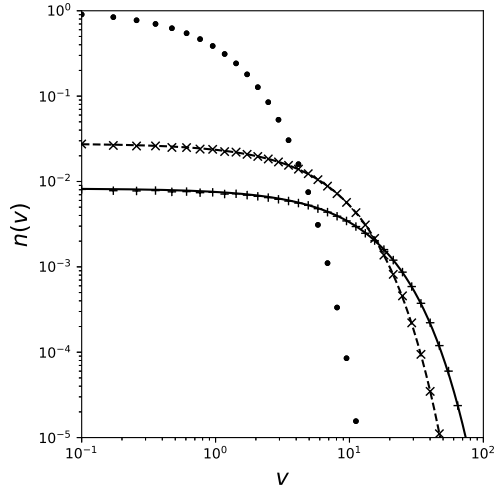
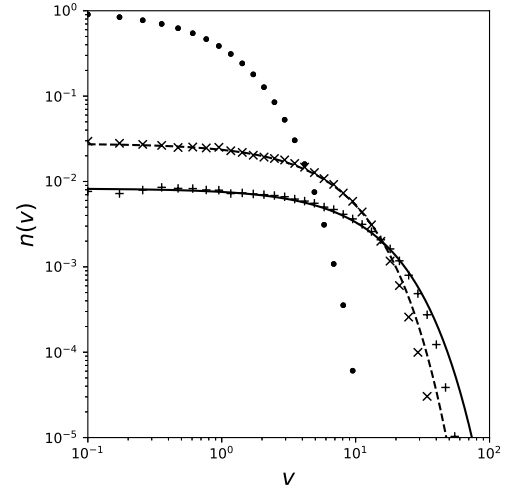
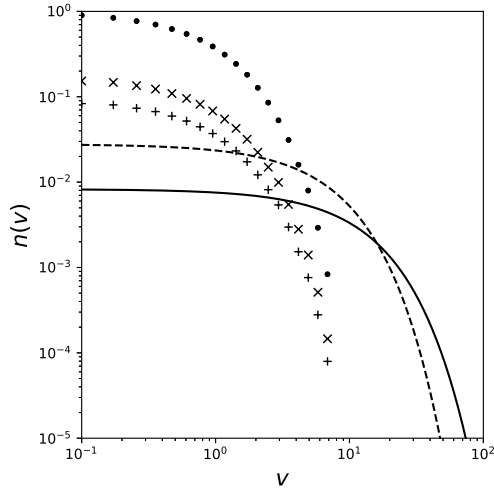
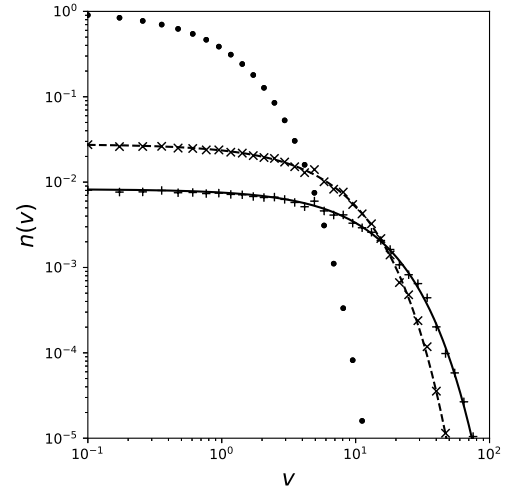
(a)  $N_P = 10^5, \alpha_R = 0$ (b)  $N_P = 10^4, \alpha_R = 0$ (c)  $N_P = 10^3, \alpha_R = 0$ (d)  $N_P = 10^3, \alpha_R$  by (4.2.22).

Figure 7.30: PSD  $n(v; t)$ . Agglomération à fréquence de collision constante: cas 2(a) du Tableau 4.2. Points: distribution initiale.  $t = 10$ , pointillés: solution analytique, croix: méthode hybride.  $t = 20$ , ligne pleine: solution analytique, plus: méthode hybride. (a)-(c): sans terme résiduel,  $\alpha_R = 0$ . (d): avec terme résiduel (Eq. (7.3.30)).

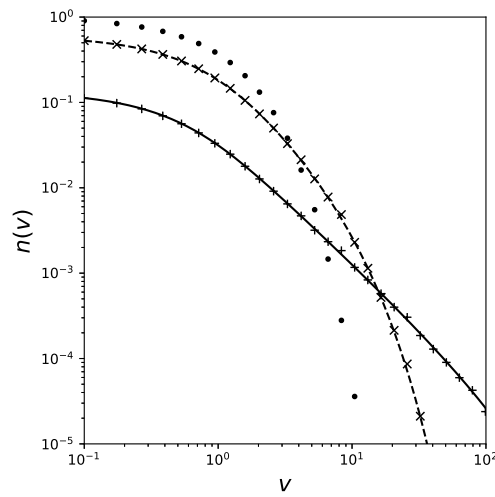


Figure 7.31: PSD  $n(v; t)$ . Agglomération à fréquence de collision dépendante de la taille: cas 2(b) du tableau 7.2. Points: distribution initiale.  $t = 0.5$ , pointillés: solution analytique, croix: méthode hybride.  $t = 2$ , ligne pleine: solution analytique, plus: méthode hybride,  $N_P = 10^4$ .

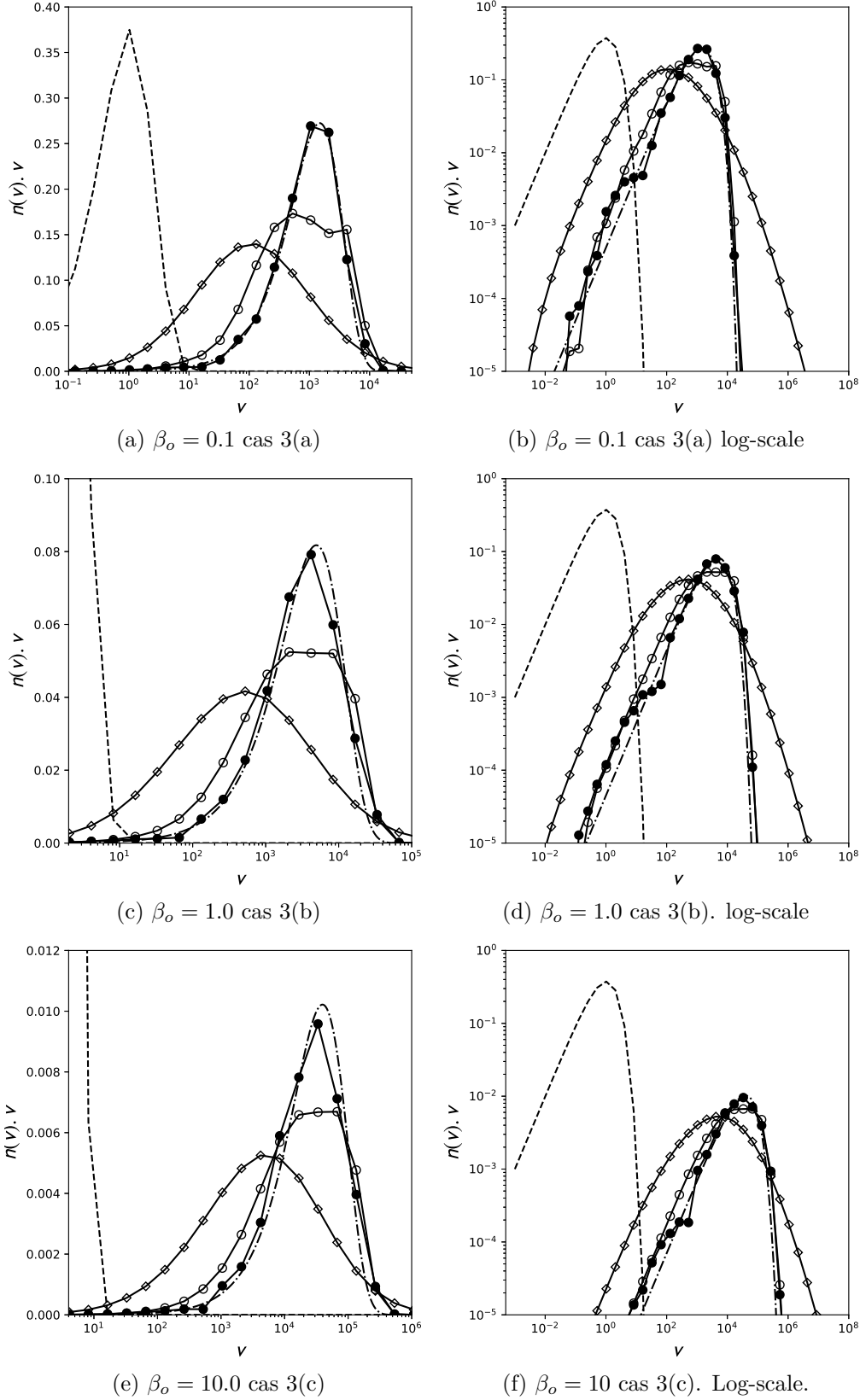


Figure 7.32: Distribution de tailles  $n(v; t) \cdot v$ . Croissance de surface ( $G(v) = v$ ) & agglomération: cas 3(a), 3(b), 3(c) du Tableau 4.3.  $\beta_o$ : fréquence de collision constante (Eq. (4.3.6)). Pointillés: distribution initiale.  $t = 7$ , lignes à pointillés-points: solution analytique. Ligne avec diamants vides: méthode sectionnelle 2-points. Ligne avec cercles vides: méthode sectionnelle 3-points. Ligne avec cercles pleins: méthode hybride,  $N_P = 10^3$ .

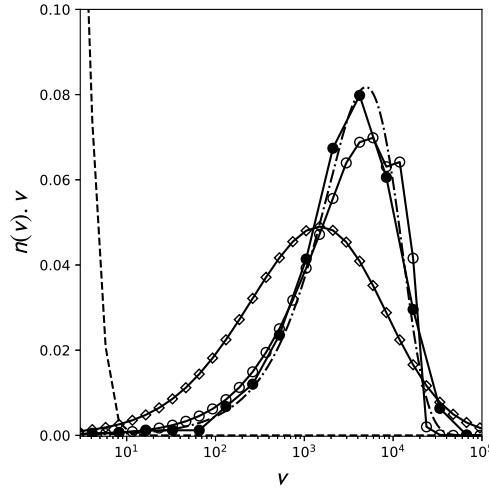


Figure 7.33: Distribution de tailles  $n(v; t) \cdot v$ . Croissance et agglomération: cas 3(d) du tableau 4.3. Pointillés: distribution initiale. Pointillés et points: solution analytique à  $t = 7$ . Ligne avec diamants vides: méthode sectionnelle 2-points ( $M = 80$  sections). Ligne avec cercles vides: méthode sectionnelle 3-points ( $M = 80$  sections). Ligne avec cercles pleins: méthode hybride,  $N_P = 10^3$  ( $M = 40$  sections).

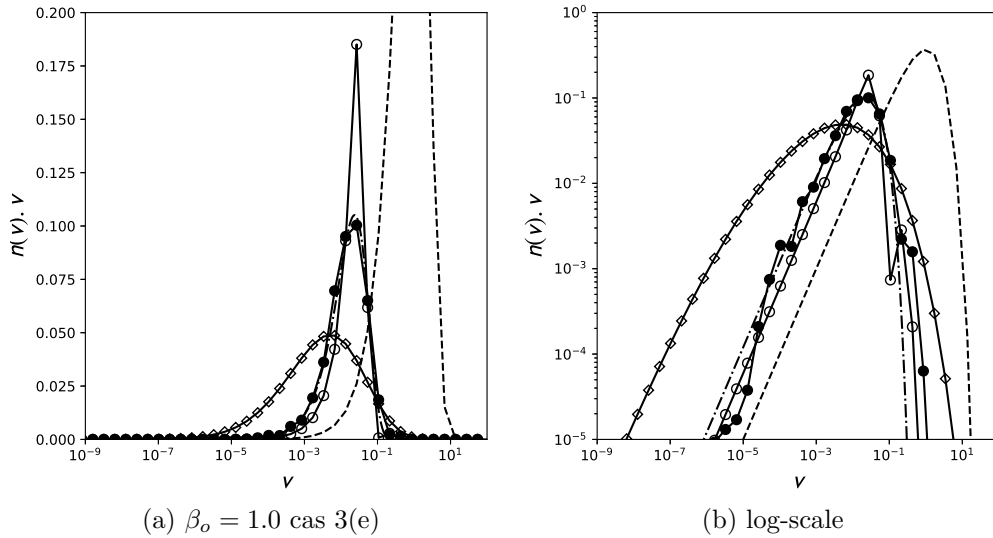


Figure 7.34: Distribution de tailles  $n(v; t) \cdot v$ . Perte de surface ( $G(v) = -v$ ) & agglomération: cas 3(e) du tableau 4.3.  $\beta_o$ : fréquence de collision constante (Eq. (4.3.6)). Pointillés: distribution initiale.  $t = 5$ , pointillés-points: solution analytique. Ligne avec diamants vides: méthode sectionnelle 2-points. Ligne avec cercles vides: méthode sectionnelle 3-points. Ligne avec cercles pleins: méthode hybride,  $N_P = 10^3$ .

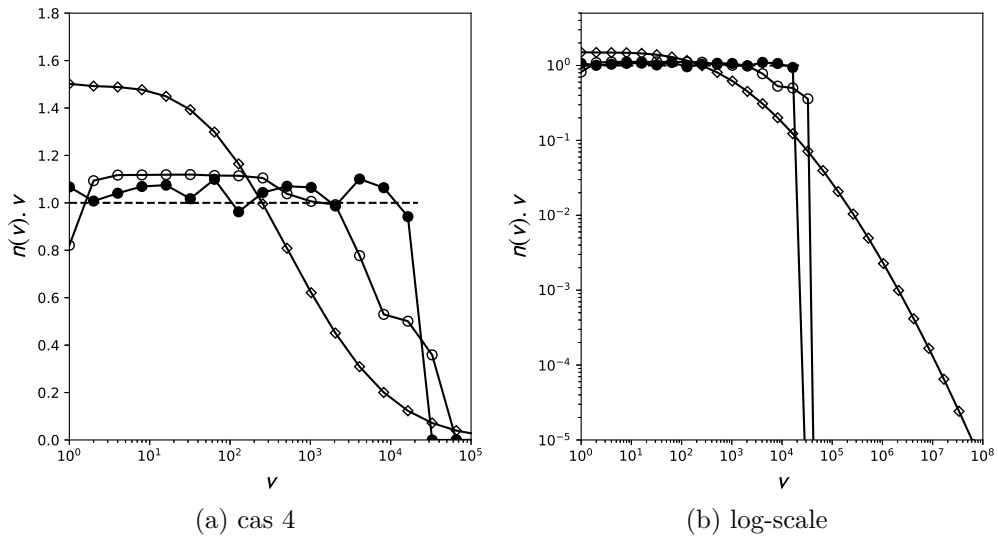


Figure 7.35: Distribution de tailles  $n(v; t) \cdot v$ . Nucléation et croissance cas 4 du tableau 4.4. Pointillés: solution analytique à  $t = 9.7$ . Ligne avec diamants vides: méthode sectionnelle 2-points. Ligne avec cercles vides: méthode sectionnelle 3-points. Ligne avec cercles pleins: méthode hybride,  $N_P = 10^3$ .

# Bibliography

- Aamir D. Abid, Nicholas Heinz, Erik D. Tolmachoff, Denis J. Phares, Charles S. Campbell, and Hai Wang. On evolution of particle size distribution functions of incipient soot in premixed ethylene–oxygen–argon flames. *Combustion and Flame*, 154(4):775 – 788, 2008. ISSN 0010-2180. doi: <https://doi.org/10.1016/j.combustflame.2008.06.009>. URL <http://www.sciencedirect.com/science/article/pii/S0010218008001971>.
- B. D. Adamson, S. A. Skeen, M. Ahmed, and N. Hansen. Detection of aliphatically bridged multi-core polycyclic aromatic hydrocarbons in sooting flames with atmospheric-sampling high-resolution tandem mass spectrometry. *The Journal of Physical Chemistry A*, 122(48):9338–9349, 2018. doi: 10.1021/acs.jpca.8b08947. URL <https://doi.org/10.1021/acs.jpca.8b08947>. PMID: 30415549.
- ANSES. Avis et rapport de l’anses relatif à l’état des connaissances sur les particules de l’air ambiant (effets sanitaires associés à la composition chimique, émissions du trafic routier). Technical report, ANSES, 2019. URL <https://www.anses.fr/fr/system/files/AIR2014SA0156Ra.pdf>.
- Jörg Appel, Henning Bockhorn, and Michael Frenklach. Kinetic modeling of soot formation with detailed chemistry and physics: laminar premixed flames of c2 hydrocarbons. *Combustion and Flame*, 121(1):122 – 136, 2000. ISSN 0010-2180. doi: [https://doi.org/10.1016/S0010-2180\(99\)00135-2](https://doi.org/10.1016/S0010-2180(99)00135-2). URL <http://www.sciencedirect.com/science/article/pii/S0010218099001352>.
- D. Aubagnac-Karkar. *Sectional soot modeling for Diesel RANS simulations*. PhD thesis, Centrale Supélec, 2014. URL <https://tel.archives-ouvertes.fr/tel-01132323>.
- Damien Aubagnac-Karkar, Jean-Baptiste Michel, Olivier Colin, Pauline E. Vervisch-Kljakic, and Nasser Darabiha. Sectional soot model coupled to tabulated chemistry for diesel rans simulations. *Combustion and Flame*, 162(8):3081 – 3099, 2015. ISSN 0010-2180. doi: <https://doi.org/10.1016/j.combustflame.2015.03.005>. URL <http://www.sciencedirect.com/science/article/pii/S0010218015000802>.
- Damien Aubagnac-Karkar, Abderrahman El Bakali, and Pascale Desgroux. Soot particles inception and pah condensation modelling applied in a soot model utilizing a sectional method. *Combustion and Flame*, 189:190 – 206, 2018. ISSN 0010-2180. doi: <https://doi.org/10.1016/j.combustflame.2017.10.027>. URL <http://www.sciencedirect.com/science/article/pii/S0010218017304248>.
- H. Babovsky. On a monte carlo scheme for smoluchowski’s coagulation equation. *MCMA*, 5:1–18, 1999.
- A. El Bakali, X. Mercier, M. Wartel, F. Acevedo, I. Burns, L. Gasnot, J.-F. Pauwels, and P. Desgroux. Modeling of pahs in low pressure sooting premixed methane flame. *Energy*, 43(1):73 – 84, 2012. ISSN 0360-5442. doi: <https://doi.org/10.1016/j.energy.2011.12.026>. URL <http://www.sciencedirect.com/science/article/pii/S0360544211008516>. 2nd International Meeting on Cleaner Combustion (CM0901-Detailed Chemical Models for Cleaner Combustion).
- M Balthasar and M Kraft. A stochastic approach to calculate the particle size distribution function of soot particles in laminar premixed flames. *Combustion and Flame*, 133(3):289 – 298, 2003. ISSN 0010-2180. doi: [https://doi.org/10.1016/S0010-2180\(03\)00003-8](https://doi.org/10.1016/S0010-2180(03)00003-8). URL <http://www.sciencedirect.com/science/article/pii/S0010218003000038>.
- C. Betrancourt. *Experimental study of soot formation in laminar premixed flames of fuels of interest for automobile and aeronautics : a focus on the soot nucleation process*. PhD thesis, Université de Lille 1, 2017. URL <https://ori-nuxeo.univ-lille1.fr/nuxeo/site/esupversions/b1d72ba0-dd59-4d2e-8308-18f012c3beb7>.
- J.S. Bhatt and R.P. Lindstedt. Analysis of the impact of agglomeration and surface chemistry models on soot formation and oxidation. *Proceedings of the Combustion Institute*, 32(1):713 – 720, 2009. ISSN 1540-7489. doi: <https://doi.org/10.1016/j.proci.2008.06.201>. URL <http://www.sciencedirect.com/science/article/pii/S1540748908003738>.
- G.A. Bird. *Molecular Gas Dynamics*. Clarendon Press, 1976. ISBN .

- Fabrizio Bisetti, Guillaume Blanquart, Michael E. Mueller, and Heinz Pitsch. On the formation and early evolution of soot in turbulent nonpremixed flames. *Combustion and Flame*, 159(1):317 – 335, 2012. ISSN 0010-2180. doi: <https://doi.org/10.1016/j.combustflame.2011.05.021>. URL <http://www.sciencedirect.com/science/article/pii/S0010218011001672>.
- Henrik Bladh, Nils-Erik Olofsson, Thomas Mouton, Johan Simonsson, Xavier Mercier, Alessandro Faccinetto, Per-Erik Bengtsson, and Pascale Desgroux. Probing the smallest soot particles in low-sooting premixed flames using laser-induced incandescence. *Proceedings of the Combustion Institute*, 35(2):1843 – 1850, 2015. ISSN 1540-7489. doi: <https://doi.org/10.1016/j.proci.2014.06.001>. URL <http://www.sciencedirect.com/science/article/pii/S154074891400159X>.
- G. Blanquart and H. Pitsch. Analyzing the effects of temperature on soot formation with a joint volume-surface-hydrogen model. *Combustion and Flame*, 156(8):1614 – 1626, 2009a. ISSN 0010-2180. doi: <https://doi.org/10.1016/j.combustflame.2009.04.010>. URL <http://www.sciencedirect.com/science/article/pii/S0010218009001205>.
- G. Blanquart, P. Pepiot-Desjardins, and H. Pitsch. Chemical mechanism for high temperature combustion of engine relevant fuels with emphasis on soot precursors. *Combustion and Flame*, 156(3):588 – 607, 2009. ISSN 0010-2180. doi: <https://doi.org/10.1016/j.combustflame.2008.12.007>. URL <http://www.sciencedirect.com/science/article/pii/S0010218008003957>.
- Guillaume Blanquart and H. Pitsch. A joint volume-surface-hydrogen multi-variate model for soot formation. In H. Bockhorn, A. D’Anna, A. F. Sarofim, and H. Wang, editors, *Combustion Generated Fine Carbonaceous Particles*, pages 437–463. KIT Scientific Publisher, Karlsruhe, 01 2009b.
- Rainer Bleck. A fast, approximative method for integrating the stochastic coalescence equation. *Journal of Geophysical Research (1896-1977)*, 75(27):5165–5171, 1970. doi: 10.1029/JC075i027p05165. URL <https://agupubs.onlinelibrary.wiley.com/doi/abs/10.1029/JC075i027p05165>.
- Linda G. Blevins, Robert A. Fletcher, Bruce A. Benner, Eric B. Steel, and George W. Mulholland. The existence of young soot in the exhaust of inverse diffusion flames. *Proceedings of the Combustion Institute*, 29(2):2325 – 2333, 2002. ISSN 1540-7489. doi: [https://doi.org/10.1016/S1540-7489\(02\)80283-8](https://doi.org/10.1016/S1540-7489(02)80283-8). URL <http://www.sciencedirect.com/science/article/pii/S1540748902802838>.
- Michele Bolla, Daniele Farrace, Yuri M. Wright, and Konstantinos Boulouchos. Modelling of soot formation in a heavy-duty diesel engine with conditional moment closure. *Fuel*, 117:309 – 325, 2014. ISSN 0016-2361. doi: <https://doi.org/10.1016/j.fuel.2013.09.041>. URL <http://www.sciencedirect.com/science/article/pii/S0016236113008843>.
- T. C. Bond, S. J. Doherty, D. W. Fahey, P. M. Forster, T. Berntsen, B. J. DeAngelo, M. G. Flanner, S. Ghan, B. Kärcher, D. Koch, S. Kinne, Y. Kondo, P. K. Quinn, M. C. Sarofim, M. G. Schultz, M. Schulz, C. Venkataraman, H. Zhang, S. Zhang, N. Bellouin, S. K. Guttikunda, P. K. Hopke, M. Z. Jacobson, J. W. Kaiser, Z. Klimont, U. Lohmann, J. P. Schwarz, D. Shindell, T. Storelvmo, S. G. Warren, and C. S. Zender. Bounding the role of black carbon in the climate system: A scientific assessment. *Journal of Geophysical Research: Atmospheres*, 118(11): 5380–5552, 2013. doi: 10.1002/jgrd.50171. URL <https://agupubs.onlinelibrary.wiley.com/doi/abs/10.1002/jgrd.50171>.
- Alexandre Bouaniche, Nicolas Jaouen, Pascale Domingo, and Luc Vervisch. Vitiated high karlovitz n-decane/air turbulent flames: Scaling laws and micro-mixing modeling analysis. *Flow, Turbulence and Combustion*, 102:235–252, 2019a. ISSN 1386-6184. doi: <https://doi.org/10.1007/s10494-018-9946-y>. URL <https://link.springer.com/article/10.1007%2Fs10494-018-9946-y>.
- Alexandre Bouaniche, Luc Vervisch, and Pascale Domingo. A hybrid stochastic/fixed-sectional method for solving the population balance equation. *Chemical Engineering Science*, 209:115198, 2019b. ISSN 0009-2509. doi: <https://doi.org/10.1016/j.ces.2019.115198>. URL <http://www.sciencedirect.com/science/article/pii/S0009250919306906>.
- A. Bruno, C. de Lisio, P. Minutolo, and A. D’Alessio. Evidence of fluorescent carbon nanoparticles produced in premixed flames by time-resolved fluorescence polarization anisotropy. *Combustion and Flame*, 151(3):472 – 481, 2007. ISSN 0010-2180. doi: <https://doi.org/10.1016/j.combustflame.2007.06.014>. URL <http://www.sciencedirect.com/science/article/pii/S0010218007001708>.
- Jeremy Cain, Alexander Laskin, Mohammad Reza Kholghy, Murray J. Thomson, and Hai Wang. Molecular characterization of organic content of soot along the centerline of a coflow diffusion flame. *Phys. Chem. Chem. Phys.*, 16: 25862–25875, 2014. doi: 10.1039/C4CP03330B. URL <http://dx.doi.org/10.1039/C4CP03330B>.

- Francesco Carbone, Kevin Gleason, and Alessandro Gomez. Probing gas-to-particle transition in a moderately sooting atmospheric pressure ethylene/air laminar premixed flame. part i: gas phase and soot ensemble characterization. *Combustion and Flame*, 181:315 – 328, 2017. ISSN 0010-2180. doi: <https://doi.org/10.1016/j.combustflame.2017.01.029>. URL <http://www.sciencedirect.com/science/article/pii/S0010218017300421>.
- H.X. Chen and R.A. Dobbins. Crystallogenesis of particles formed in hydrocarbon combustion. *Combustion Science and Technology*, 159(1):109–128, 2000. doi: 10.1080/00102200008935779. URL <https://doi.org/10.1080/00102200008935779>.
- Seung-Hyun Chung. *Computational modeling of soot nucleation*. PhD thesis, University of Michigan, 2011.
- Anna Ciajolo, Rosalba Barbella, Antonio Tregrossi, and Loretta Bonfanti. Spectroscopic and compositional signatures of pah-loaded mixtures in the soot inception region of a premixed ethylene flame. *Symposium (International) on Combustion*, 27(1):1481 – 1487, 1998. ISSN 0082-0784. doi: [https://doi.org/10.1016/S0082-0784\(98\)80555-9](https://doi.org/10.1016/S0082-0784(98)80555-9). URL <http://www.sciencedirect.com/science/article/pii/S0082078498805559>. Twenty-Seventh Symposium (International) on Combustion Volume One.
- Mario Commodo, Gianluigi De Falco, Annalisa Bruno, Carmela Borriello, Patrizia Minutolo, and Andrea D’Anna. Physicochemical evolution of nascent soot particles in a laminar premixed flame: from nucleation to early growth. *Combustion and Flame*, 162(10):3854 – 3863, 2015a. ISSN 0010-2180. doi: <https://doi.org/10.1016/j.combustflame.2015.07.022>. URL <http://www.sciencedirect.com/science/article/pii/S0010218015002230>.
- Mario Commodo, Gabriella Tessitore, Gianluigi De Falco, Annalisa Bruno, Patrizia Minutolo, and Andrea D’Anna. Further details on particle inception and growth in premixed flames. *Proceedings of the Combustion Institute*, 35(2):1795 – 1802, 2015b. ISSN 1540-7489. doi: <https://doi.org/10.1016/j.proci.2014.06.004>. URL <http://www.sciencedirect.com/science/article/pii/S154074891400162X>.
- Pascale Desgroux, Alessandro Faccinetto, Xavier Mercier, Thomas Mouton, Damien Aubagnac Karkar, and Abderrahman El Bakali. Comparative study of the soot formation process in a “nucleation” and a “sooting” low pressure premixed methane flame. *Combustion and Flame*, 184:153 – 166, 2017. ISSN 0010-2180. doi: <https://doi.org/10.1016/j.combustflame.2017.05.034>. URL <http://www.sciencedirect.com/science/article/pii/S0010218017302109>.
- R.A. Dobbins, R.A. Fletcher, and W. Lu. Laser microprobe analysis of soot precursor particles and carbonaceous soot. *Combustion and Flame*, 100(1):301 – 309, 1995. ISSN 0010-2180. doi: [https://doi.org/10.1016/0010-2180\(94\)00047-V](https://doi.org/10.1016/0010-2180(94)00047-V). URL <http://www.sciencedirect.com/science/article/pii/S001021809400047V>.
- R.A. Dobbins, R.A. Fletcher, and H.-C. Chang. The evolution of soot precursor particles in a diffusion flame. *Combustion and Flame*, 115(3):285 – 298, 1998. ISSN 0010-2180. doi: [https://doi.org/10.1016/S0010-2180\(98\)00010-8](https://doi.org/10.1016/S0010-2180(98)00010-8). URL <http://www.sciencedirect.com/science/article/pii/S0010218098000108>.
- C. Dopazo. Relaxation of initial probability density functions in the turbulent convection of scalar fields. *Phys. Fluids*, 22(1):20–30, 1979.
- C. Dopazo, L. Valino, and F. Fuego. Statistical description of the turbulent mixing of scalar fields. *International Journal of Modern Physics B*, 11(25), 1997.
- Seth B. Dworkin, Qingan Zhang, Murray J. Thomson, Nadezhda A. Slavinskaya, and Uwe Riedel. Application of an enhanced pah growth model to soot formation in a laminar coflow ethylene/air diffusion flame. *Combustion and Flame*, 158(9):1682 – 1695, 2011. ISSN 0010-2180. doi: <https://doi.org/10.1016/j.combustflame.2011.01.013>. URL <http://www.sciencedirect.com/science/article/pii/S0010218011000289>.
- A. D’Anna, A. Rolando, C. Allouis, P. Minutolo, and A. D’Alessio. Nano-organic carbon and soot particle measurements in a laminar ethylene diffusion flame. *Proceedings of the Combustion Institute*, 30(1):1449 – 1456, 2005. ISSN 1540-7489. doi: <https://doi.org/10.1016/j.proci.2004.08.276>. URL <http://www.sciencedirect.com/science/article/pii/S0082078404002693>.
- Andrea D’Anna. Combustion-formed nanoparticles. *Proceedings of the Combustion Institute*, 32(1):593 – 613, 2009. ISSN 1540-7489. doi: <https://doi.org/10.1016/j.proci.2008.09.005>. URL <http://www.sciencedirect.com/science/article/pii/S1540748908003787>.
- N.A. Eaves, S.B. Dworkin, and M.J. Thomson. The importance of reversibility in modeling soot nucleation and condensation processes. *Proceedings of the Combustion Institute*, 35(2):1787 – 1794, 2015. ISSN 1540-7489. doi: <https://doi.org/10.1016/j.proci.2014.05.036>. URL <http://www.sciencedirect.com/science/article/pii/S154074891400039X>.

- C. Eberle, P. Gerlinger, and M. Aigner. A sectional pah model with reversible pah chemistry for cfd soot simulations. *Combustion and Flame*, 179:63 – 73, 2017a. ISSN 0010-2180. doi: <https://doi.org/10.1016/j.combustflame.2017.01.019>. URL <http://www.sciencedirect.com/science/article/pii/S0010218017300196>.
- Christian Eberle, Peter M. Gerlinger, and Manfred Aigner. *Large Eddy Simulations of a Sooting Lifted Turbulent Jet-Flame*, chapter ., page . AIAA, 2017b. doi: 10.2514/6.2017-1785. URL <https://arc.aiaa.org/doi/abs/10.2514/6.2017-1785>.
- Christian Eberle, Peter M. Gerlinger, and Manfred Aigner. *Large Eddy Simulations of a Sooting Lifted Turbulent Jet-Flame*, chapter ., page . Aerospace Research Central, 2017c. doi: 10.2514/6.2017-1785. URL <https://arc.aiaa.org/doi/abs/10.2514/6.2017-1785>.
- A. Eibeck and W. Wagner. An efficient stochastic algorithm for studying coagulation dynamics and gelation phenomena. *SIAM Journal on Scientific Computing*, 22(3):802–821, 2000. doi: 10.1137/S1064827599353488. URL <https://doi.org/10.1137/S1064827599353488>.
- Ali Ergut, Silvia Granata, Jude Jordan, Joel Carlson, Jack B. Howard, Henning Richter, and Yiannis A. Levendis. Pah formation in one-dimensional premixed fuel-rich atmospheric pressure ethylbenzene and ethyl alcohol flames. *Combustion and Flame*, 144(4):757 – 772, 2006. ISSN 0010-2180. doi: <https://doi.org/10.1016/j.combustflame.2005.07.019>. URL <http://www.sciencedirect.com/science/article/pii/S0010218005002695>.
- Anne Felden, Eleonore Riber, and Benedicte Cuenot. Impact of direct integration of analytically reduced chemistry in les of a sooting swirled non-premixed combustor. *Combustion and Flame*, 191:270 – 286, 2018. ISSN 0010-2180. doi: <https://doi.org/10.1016/j.combustflame.2018.01.005>. URL <http://www.sciencedirect.com/science/article/pii/S0010218018300099>.
- J. H. Ferziger and M. Perić. *Computational Methods for Fluid Dynamics*. Springer, 1996. ISBN 3-540-59434-5.
- F. Filbet and P. Laurençot. Numerical simulation of the smoluchowski coagulation equation. *SIAM Journal on Scientific Computing*, 25(6):2004–2028, 2004. doi: 10.1137/S1064827503429132. URL <https://doi.org/10.1137/S1064827503429132>.
- B. Franzelli, A. Vié, and N. Darabiha. A three-equation model for the prediction of soot emissions in les of gas turbines. *Proceedings of the Combustion Institute*, 37(4):5411 – 5419, 2019. ISSN 1540-7489. doi: <https://doi.org/10.1016/j.proci.2018.05.061>. URL <http://www.sciencedirect.com/science/article/pii/S1540748918300622>.
- Eveline Fredrick, Pieter Walstra, and Koen Dewettinck. Factors governing partial coalescence in oil-in-water emulsions. *Advances in Colloid and Interface Science*, 153(1):30 – 42, 2010. ISSN 0001-8686. doi: <https://doi.org/10.1016/j.cis.2009.10.003>. URL <http://www.sciencedirect.com/science/article/pii/S0001868609000943>.
- Michael Frenklach. Method of moments with interpolative closure. *Chemical Engineering Science*, 57(12):2229 – 2239, 2002. ISSN 0009-2509. doi: [https://doi.org/10.1016/S0009-2509\(02\)00113-6](https://doi.org/10.1016/S0009-2509(02)00113-6). URL <http://www.sciencedirect.com/science/article/pii/S0009250902001136>. Population balance modelling of particulate systems.
- Michael Frenklach and Stephen J. Harris. Aerosol dynamics modeling using the method of moments. *Journal of Colloid and Interface Science*, 118(1):252 – 261, 1987. ISSN 0021-9797. doi: [https://doi.org/10.1016/0021-9797\(87\)90454-1](https://doi.org/10.1016/0021-9797(87)90454-1). URL <http://www.sciencedirect.com/science/article/pii/0021979787904541>.
- Michael Frenklach and Hai Wang. Detailed modeling of soot particle nucleation and growth. *Symposium (International) on Combustion*, 23(1):1559 – 1566, 1991. ISSN 0082-0784. doi: [https://doi.org/10.1016/S0082-0784\(06\)80426-1](https://doi.org/10.1016/S0082-0784(06)80426-1). URL <http://www.sciencedirect.com/science/article/pii/S0082078406804261>. Twenty-Third Symposium (International) on Combustion.
- Fuchs. *Mechanics of Aerosols*. Pergamon, 1964. ISBN .
- Lucien Gallen, Anne Felden, Eleonore Riber, and Bénédicte Cuenot. Lagrangian tracking of soot particles in les of gas turbines. *Proceedings of the Combustion Institute*, 37(4):5429 – 5436, 2019. ISSN 1540-7489. doi: <https://doi.org/10.1016/j.proci.2018.06.013>. URL <http://www.sciencedirect.com/science/article/pii/S1540748918301962>.
- Alejandro L. Garcia, Christian van den Broeck, Marc Aertsens, and Roger Serneels. A monte carlo simulation of coagulation. *Physica A: Statistical Mechanics and its Applications*, 143(3):535 – 546, 1987. ISSN 0378-4371. doi: [https://doi.org/10.1016/0378-4371\(87\)90164-6](https://doi.org/10.1016/0378-4371(87)90164-6). URL <http://www.sciencedirect.com/science/article/pii/0378437187901646>.
- Fred Gelbard and John H. Seinfeld. Numerical solution of the dynamic equation for particulate systems. *Journal of Computational Physics*, 28(3):357 – 375, 1978. ISSN 0021-9991. doi: [https://doi.org/10.1016/0021-9991\(78\)90058-X](https://doi.org/10.1016/0021-9991(78)90058-X). URL <http://www.sciencedirect.com/science/article/pii/002199917890058X>.

- Fred Gelbard and John H. Seinfeld. Sectional representations for simulating aerosol dynamics. *Journal of Colloid and Interface Science*, 76(2):541 – 556, 1980. ISSN 0021-9797. doi: [https://doi.org/10.1016/0021-9797\(80\)90394-X](https://doi.org/10.1016/0021-9797(80)90394-X). URL <http://www.sciencedirect.com/science/article/pii/002197978090394X>.
- Michael Goodson and Markus Kraft. An efficient stochastic algorithm for simulating nano-particle dynamics. *Journal of Computational Physics*, 183(1):210 – 232, 2002. ISSN 0021-9991. doi: <https://doi.org/10.1006/jcph.2002.7192>. URL <http://www.sciencedirect.com/science/article/pii/S0021999102971925>.
- D. G. Goodwin, H. K. Moffat, and R. L. Speth. Cantera: An object-oriented software toolkit for chemical kinetics, thermodynamics, and transport processes, 2017. Version 2.3.0.
- Roy G. Gordon. Error bounds in equilibrium statistical mechanics. *Journal of Mathematical Physics*, 9(5):655–663, 1968. doi: 10.1063/1.1664624. URL <https://doi.org/10.1063/1.1664624>.
- Horst-Henning Grotheer, Kai Hoffmann, Katrin Wolf, Santosh Kanjarkar, Claus Wahl, and Manfred Aigner. Study of carbonaceous nanoparticles in premixed c2h4–air flames and behind a spark ignition engine. *Combustion and Flame*, 156(4):791 – 800, 2009. ISSN 0010-2180. doi: <https://doi.org/10.1016/j.combustflame.2009.01.022>. URL <http://www.sciencedirect.com/science/article/pii/S0010218009000406>.
- C. Guerreiro, A. Gonzalez Ortiz, F. de Leeuw, M. Viana, and J. Horalek. Air quality in europe. Technical report, European Environment Agency, 2016.
- Hongsheng Guo, Zhongzhu Gu, Kevin A. Thomson, Gregory J. Smallwood, and Fazil F. Baksh. Soot formation in a laminar ethylene/air diffusion flame at pressures from 1 to 8atm. *Proceedings of the Combustion Institute*, 34(1):1795 – 1802, 2013. ISSN 1540-7489. doi: <https://doi.org/10.1016/j.proci.2012.07.006>. URL <http://www.sciencedirect.com/science/article/pii/S1540748912002970>.
- W. Hackbusch. On the efficient evaluation of coalescence integrals in population balance models. *Computing*, 78(2): 145–159, 2006. ISSN 0010-485X. doi: <https://doi.org/10.1007/s00607-006-0174-2>. URL <https://link.springer.com/article/10.1007/s00607-006-0174-2>.
- Zhao Haibo, Zheng Chuguang, and Xu Minghou. Multi-monte carlo approach for general dynamic equation considering simultaneous particle coagulation and breakage. *Powder Technology*, 154(2):164 – 178, 2005. ISSN 0032-5910. doi: <https://doi.org/10.1016/j.powtec.2005.04.042>. URL <http://www.sciencedirect.com/science/article/pii/S0032591005001944>.
- S.J. Harris and IAN M. Kennedy. The coagulation of soot particles with van der waals forces. *Combustion Science and Technology*, 59(4-6):443–454, 1988. doi: 10.1080/00102208808947110. URL <https://doi.org/10.1080/00102208808947110>.
- D. C. Haworth. Progress in probability density function methods for turbulent reacting flows. *Prog. Energy Combust. Sci.*, 36(2):168–259, 2010.
- Jennifer D. Herdman and J. Houston Miller. Intermolecular potential calculations for polynuclear aromatic hydrocarbon clusters. *The Journal of Physical Chemistry A*, 112(28):6249–6256, 2008. doi: 10.1021/jp800483h. URL <https://doi.org/10.1021/jp800483h>. PMID: 18572902.
- Klaus-Heinrich Homann. Fullerenes and soot formation— new pathways to large particles in flames. *Angewandte Chemie International Edition*, 37(18):2434–2451, 1998. doi: 10.1002/(SICI)1521-3773(19981002)37:18<2434::AID-ANIE2434>3.0.CO;2-L. URL <https://onlinelibrary.wiley.com/doi/abs/10.1002/%28SICI%291521-3773%2819981002%2937%3A18%3C2434%3A%3AAID-ANIE2434%3E3.0.CO%3B2-L>.
- M. J. Hounslow, R. L. Ryall, and V. R. Marshall. A discretized population balance for nucleation, growth, and aggregation. *AIChE Journal*, 34(11):1821–1832, 1988. doi: 10.1002/aic.690341108. URL <https://aiche.onlinelibrary.wiley.com/doi/abs/10.1002/aic.690341108>.
- M. Hu, X. Jiang, and M. Absar. Equivalence testing of complex particle size distribution profiles based on earth mover’s distance. *AAPS J*, 20(62), 2018. ISSN 1550-7416.
- Nicolas Jaouen, Luc Vervisch, Pascale Domingo, and Guillaume Ribert. Automatic reduction and optimisation of chemistry for turbulent combustion modelling: Impact of the canonical problem. *Combustion and Flame*, 175: 60 – 79, 2017. ISSN 0010-2180. doi: <https://doi.org/10.1016/j.combustflame.2016.08.030>. URL <http://www.sciencedirect.com/science/article/pii/S0010218016302541>. Special Issue in Honor of Norbert Peters.
- K. O. Johansson, M. P. Head-Gordon, P. E. Schrader, K. R. Wilson, and H. A. Michelsen. Resonance-stabilized hydrocarbon-radical chain reactions may explain soot inception and growth. *Science*, 361(6406):997–1000, 2018. ISSN 0036-8075. doi: 10.1126/science.aat3417. URL <https://science.sciencemag.org/content/361/6406/997>.

- K.O. Johansson, J.Y.W. Lai, S.A. Skeen, D.M. Popolan-Vaida, K.R. Wilson, N. Hansen, A. Violi, and H.A. Michelsen. Soot precursor formation and limitations of the stabilomer grid. *Proceedings of the Combustion Institute*, 35(2):1819 – 1826, 2015. ISSN 1540-7489. doi: <https://doi.org/10.1016/j.proci.2014.05.033>. URL <http://www.sciencedirect.com/science/article/pii/S1540748914000364>.
- Andrei Kazakov and Michael Frenklach. Dynamic modeling of soot particle coagulation and aggregation: Implementation with the method of moments and application to high-pressure laminar premixed flames. *Combust. Flame*, 114(3):484 – 501, 1998. ISSN 0010-2180.
- Georgios A. Kelesidis, Eirini Goudeli, and Sotiris E. Pratsinis. Flame synthesis of functional nanostructured materials and devices: Surface growth and aggregation. *Proceedings of the Combustion Institute*, 36(1):29 – 50, 2017. ISSN 1540-7489. doi: <https://doi.org/10.1016/j.proci.2016.08.078>. URL <http://www.sciencedirect.com/science/article/pii/S1540748916304679>.
- Ian M. Kennedy, Wolfgang Kollmann, and J.-Y. Chen. A model for soot formation in a laminar diffusion flame. *Combustion and Flame*, 81(1):73 – 85, 1990. ISSN 0010-2180. doi: [https://doi.org/10.1016/0010-2180\(90\)90071-X](https://doi.org/10.1016/0010-2180(90)90071-X). URL <http://www.sciencedirect.com/science/article/pii/001021809090071X>.
- M. R. Kholghy, G. A. Kelesidis, and S. E. Pratsinis. Reactive polycyclic aromatic hydrocarbon dimerization drives soot nucleation. *Phys. Chem. Chem. Phys.*, 20:10926–10938, 2018. doi: 10.1039/C7CP07803J. URL <http://dx.doi.org/10.1039/C7CP07803J>.
- Mohammad Reza Kholghy, Armin Veshkini, and Murray John Thomson. The core-shell internal nanostructure of soot – a criterion to model soot maturity. *Carbon*, 100:508 – 536, 2016. ISSN 0008-6223. doi: <https://doi.org/10.1016/j.carbon.2016.01.022>. URL <http://www.sciencedirect.com/science/article/pii/S0008622316300227>.
- Mohammadreza Kholghy, Meghdad Saffaripour, Christopher Yip, and Murray John Thomson. The evolution of soot morphology in a laminar coflow diffusion flame of a surrogate for jet a-1. *Combustion and Flame*, 160(10):2119 – 2130, 2013. ISSN 0010-2180. doi: <https://doi.org/10.1016/j.combustflame.2013.04.008>. URL <http://www.sciencedirect.com/science/article/pii/S0010218013001521>.
- Uemit Koeylu, Yangchuan Xing, and Daniel E. Rosner. Fractal morphology analysis of combustion-generated aggregates using angular light scattering and electron microscope images. *Langmuir*, 11(12):4848–4854, 1995. doi: 10.1021/la00012a043. URL <https://doi.org/10.1021/la00012a043>.
- W. Kollmann. The pdf approach to turbulent flow. *Theoretical and Computational Fluid Dynamics*, 1:349–285, 1990.
- B. Koren and C.B. Vreugdenhil. *Numerical Methods for Advection-Diffusion Problems*. Vieweg, 1993. ISBN 978-3-528-07645-0.
- F. Einar Kruis, Karl A. Kusters, Sotiris E. Pratsinis, and Brian Scarlett. A simple model for the evolution of the characteristics of aggregate particles undergoing coagulation and sintering. *Aerosol Sci. Tech.*, 19(4):514–526, 1993.
- F.E. Kruis, A. Maisels, and H. Fissan. Direct simulation monte carlo method for particle coagulation and aggregation. *AIChE Journal*, 46(9):1735–1742, 2000. doi: 10.1002/aic.690460905. URL <https://aiche.onlinelibrary.wiley.com/doi/abs/10.1002/aic.690460905>.
- Sanjeev Kumar and D. Ramkrishna. On the solution of population balance equations by discretization—i. a fixed pivot technique. *Chemical Engineering Science*, 51(8):1311 – 1332, 1996a. ISSN 0009-2509. doi: [https://doi.org/10.1016/0009-2509\(96\)88489-2](https://doi.org/10.1016/0009-2509(96)88489-2). URL <http://www.sciencedirect.com/science/article/pii/0009250996884892>.
- Sanjeev Kumar and D. Ramkrishna. On the solution of population balance equations by discretization—ii. a moving pivot technique. *Chemical Engineering Science*, 51(8):1333 – 1342, 1996b. ISSN 0009-2509. doi: [https://doi.org/10.1016/0009-2509\(95\)00355-X](https://doi.org/10.1016/0009-2509(95)00355-X). URL <http://www.sciencedirect.com/science/article/pii/000925099500355X>.
- Sanjeev Kumar and D. Ramkrishna. On the solution of population balance equations by discretization—iii. nucleation, growth and aggregation of particles. *Chemical Engineering Science*, 52(24):4659 – 4679, 1997. ISSN 0009-2509. doi: [https://doi.org/10.1016/S0009-2509\(97\)00307-2](https://doi.org/10.1016/S0009-2509(97)00307-2). URL <http://www.sciencedirect.com/science/article/pii/S0009250997003072>. Festschrift for Professor M. M. Sharma.
- Marco Lattuada, Hua Wu, and Massimo Morbidelli. A simple model for the structure of fractal aggregates. *Journal of Colloid and Interface Science*, 268(1):106 – 120, 2003.
- K.M. Leung, R.P. Lindstedt, and W.P. Jones. A simplified reaction mechanism for soot formation in nonpremixed flames. *Combustion and Flame*, 87(3):289 – 305, 1991. ISSN 0010-2180. doi: [https://doi.org/10.1016/0010-2180\(91\)90114-Q](https://doi.org/10.1016/0010-2180(91)90114-Q). URL <http://www.sciencedirect.com/science/article/pii/001021809190114Q>.

- Randall J. LeVeque. Wave propagation algorithms for multidimensional hyperbolic systems. *Journal of Computational Physics*, 131(2):327 – 353, 1997. ISSN 0021-9991. doi: <https://doi.org/10.1006/jcph.1996.5603>. URL <http://www.sciencedirect.com/science/article/pii/S002199919695603X>.
- R.J. Leveque. *Numerical Methods for Conservation Laws*. Birkhauser Verlag, 1992.
- Anthi Liati, Benjamin T. Brem, Lukas Durdina, Melanie Vögtli, Yadira Arroyo Rojas Dasilva, Panayotis Dimopoulos Eggenschwiler, and Jing Wang. Electron microscopic study of soot particulate matter emissions from aircraft turbine engines. *Environmental Science & Technology*, 48(18):10975–10983, 2014. doi: 10.1021/es501809b. URL <https://doi.org/10.1021/es501809b>. PMID: 25180674.
- Kurt Liffman. A direct simulation monte-carlo method for cluster coagulation. *Journal of Computational Physics*, 100(1):116 – 127, 1992. ISSN 0021-9991. doi: [https://doi.org/10.1016/0021-9991\(92\)90314-O](https://doi.org/10.1016/0021-9991(92)90314-O). URL <http://www.sciencedirect.com/science/article/pii/0021999192903140>.
- Yulan Lin, Kangtaek Lee, and Themis Matsoukas. Solution of the population balance equation using constant-number monte carlo. *Chemical Engineering Science*, 57(12):2241 – 2252, 2002. ISSN 0009-2509. doi: [https://doi.org/10.1016/S0009-2509\(02\)00114-8](https://doi.org/10.1016/S0009-2509(02)00114-8). URL <http://www.sciencedirect.com/science/article/pii/S0009250902001148>. Population balance modelling of particulate systems.
- Anxiong Liu and Stelios Rigopoulos. A conservative method for numerical solution of the population balance equation, and application to soot formation. *Combustion and Flame*, 205:506 – 521, 2019. ISSN 0010-2180. doi: <https://doi.org/10.1016/j.combustflame.2019.04.019>. URL <http://www.sciencedirect.com/science/article/pii/S0010218019301646>.
- T. S. Lundgren. Distribution function in the statistical theory of turbulence. *Physics Fluids*, 10(5):969–975, 1967.
- D.L. Ma, D.K. Tafti, and R.D. Braatz. High-resolution simulation of multidimensional crystal growth. *Industrial and Engineering Chemistry Research*, 41(25):6217–6223, 2002. doi: 10.1021/ie010680u. URL <https://doi.org/10.1021/ie010680u>.
- Arkadi Maisels, F. Einar Kruis, and Heinz Fissan. Direct simulation monte carlo for simultaneous nucleation, coagulation, and surface growth in dispersed systems. *Chemical Engineering Science*, 59(11):2231 – 2239, 2004. ISSN 0009-2509. doi: <https://doi.org/10.1016/j.ces.2004.02.015>. URL <http://www.sciencedirect.com/science/article/pii/S0009250904001368>.
- Qian Mao, Adri C.T. van Duin, and K.H. Luo. Formation of incipient soot particles from polycyclic aromatic hydrocarbons: A reaxff molecular dynamics study. *Carbon*, 121:380 – 388, 2017. ISSN 0008-6223. doi: <https://doi.org/10.1016/j.carbon.2017.06.009>. URL <http://www.sciencedirect.com/science/article/pii/S0008622317305766>.
- Daniele L. Marchisio and Rodney O. Fox. Solution of population balance equations using the direct quadrature method of moments. *Journal of Aerosol Science*, 36(1):43 – 73, 2005. ISSN 0021-8502. doi: <https://doi.org/10.1016/j.jaerosci.2004.07.009>. URL <http://www.sciencedirect.com/science/article/pii/S0021850204003052>.
- Daniele L. Marchisio, Jesse T. Pikturka, Rodney O. Fox, R. Dennis Vigil, and Antonello A. Barresi. Quadrature method of moments for population-balance equations. *AIChE Journal*, 49(5):1266–1276, 2003. doi: 10.1002/aic.690490517. URL <https://aiche.onlinelibrary.wiley.com/doi/abs/10.1002/aic.690490517>.
- Nick M Marinov, William J Pitz, Charles K Westbrook, Antonio M Vincitore, Marco J Castaldi, Selim M Senkan, and Carl F Melius. Aromatic and polycyclic aromatic hydrocarbon formation in a laminar premixed n-butane flame. *Combustion and Flame*, 114(1):192 – 213, 1998. ISSN 0010-2180. doi: [https://doi.org/10.1016/S0010-2180\(97\)00275-7](https://doi.org/10.1016/S0010-2180(97)00275-7). URL <http://www.sciencedirect.com/science/article/pii/S0010218097002757>.
- Fabian Mauss, Thomas Schäfer, and Henning Bockhorn. Inception and growth of soot particles in dependence on the surrounding gas phase. *Combustion and Flame*, 99(3):697 – 705, 1994. ISSN 0010-2180. doi: [https://doi.org/10.1016/0010-2180\(94\)90064-7](https://doi.org/10.1016/0010-2180(94)90064-7). URL <http://www.sciencedirect.com/science/article/pii/0010218094900647>. 25th Symposium (International) on Combustion Papers.
- Charles S. McEnally, Lisa D. Pfefferle, Burak Atakan, and Katharina Kohse-Höinghaus. Studies of aromatic hydrocarbon formation mechanisms in flames: Progress towards closing the fuel gap. *Progress in Energy and Combustion Science*, 32(3):247 – 294, 2006. ISSN 0360-1285. doi: <https://doi.org/10.1016/j.pecs.2005.11.003>. URL <http://www.sciencedirect.com/science/article/pii/S0360128505000602>.
- Robert McGraw. Description of aerosol dynamics by the quadrature method of moments. *Aerosol Science and Technology*, 27(2):255–265, 1997. doi: 10.1080/02786829708965471. URL <https://doi.org/10.1080/02786829708965471>.

- J. Thomas Mckinnon, Eleanor Meyer, and Jack B Howard. Infrared analysis of flame-generated pah samples. *Combustion and Flame*, 105(1):161 – 166, 1996. ISSN 0010-2180. doi: [https://doi.org/10.1016/0010-2180\(95\)00185-9](https://doi.org/10.1016/0010-2180(95)00185-9). URL <http://www.sciencedirect.com/science/article/pii/S0010218095001859>.
- Alexander M. Mebel, Yuri Georgievskii, Ahren W. Jasper, and Stephen J. Klippenstein. Temperature- and pressure-dependent rate coefficients for the haca pathways from benzene to naphthalene. *Proceedings of the Combustion Institute*, 36(1):919 – 926, 2017. ISSN 1540-7489. doi: <https://doi.org/10.1016/j.proci.2016.07.013>. URL <http://www.sciencedirect.com/science/article/pii/S1540748916302693>.
- C.M. Megaridis and R.A. Dobbins. A bimodal integral solution of the dynamic equation for an aerosol undergoing simultaneous particle inception and coagulation. *Aerosol Science and Technology*, 12(2):240–255, 1990. doi: 10.1080/02786829008959343. URL <https://doi.org/10.1080/02786829008959343>.
- Tyler R. Melton, Antonio M. Vincitore, and Selim M. Senkan. The effects of equivalence ratio on the formation of polycyclic aromatic hydrocarbons and soot in premixed methane flames. *Symposium (International) on Combustion*, 27(2):1631 – 1637, 1998. ISSN 0082-0784. doi: [https://doi.org/10.1016/S0082-0784\(98\)80001-5](https://doi.org/10.1016/S0082-0784(98)80001-5). URL <http://www.sciencedirect.com/science/article/pii/S0082078498800015>.
- Tyler R Melton, Fikret Inal, and Selim M Senkan. The effects of equivalence ratio on the formation of polycyclic aromatic hydrocarbons and soot in premixed ethane flames. *Combustion and Flame*, 121(4):671 – 678, 2000. ISSN 0010-2180. doi: [https://doi.org/10.1016/S0010-2180\(99\)00180-7](https://doi.org/10.1016/S0010-2180(99)00180-7). URL <http://www.sciencedirect.com/science/article/pii/S0010218099001807>.
- X. Mercier, O. Carrivain, C. Irimiea, A. Faccinetto, and E. Therssen. Dimers of polycyclic aromatic hydrocarbons: the missing pieces in the soot formation process. *Phys. Chem. Chem. Phys.*, 21:8282–8294, 2019. doi: 10.1039/C9CP00394K. URL <http://dx.doi.org/10.1039/C9CP00394K>.
- H.A. Michelsen. Probing soot formation, chemical and physical evolution, and oxidation: A review of in situ diagnostic techniques and needs. *Proceedings of the Combustion Institute*, 36(1):717 – 735, 2017. ISSN 1540-7489. doi: <https://doi.org/10.1016/j.proci.2016.08.027>. URL <http://www.sciencedirect.com/science/article/pii/S1540748916304163>.
- James A. Miller and Stephen J. Klippenstein. The recombination of propargyl radicals: Solving the master equation. *The Journal of Physical Chemistry A*, 105(30):7254–7266, 2001. doi: 10.1021/jp0102973. URL <https://doi.org/10.1021/jp0102973>.
- James A. Miller and Carl F. Melius. Kinetic and thermodynamic issues in the formation of aromatic compounds in flames of aliphatic fuels. *Combustion and Flame*, 91(1):21 – 39, 1992. ISSN 0010-2180. doi: [https://doi.org/10.1016/0010-2180\(92\)90124-8](https://doi.org/10.1016/0010-2180(92)90124-8). URL <http://www.sciencedirect.com/science/article/pii/S0010218092901248>.
- P. Minutolo, G. Gambi, and A. D’Alessio. The optical band gap model in the interpretation of the uv-visible absorption spectra of rich premixed flames. *Symposium (International) on Combustion*, 26(1):951 – 957, 1996. ISSN 0082-0784. doi: [https://doi.org/10.1016/S0082-0784\(96\)80307-9](https://doi.org/10.1016/S0082-0784(96)80307-9). URL <http://www.sciencedirect.com/science/article/pii/S0082078496803079>.
- Kai Moshhammer, Lars Seidel, Yu Wang, Hatem Selim, S. Mani Sarathy, Fabian Mauss, and Nils Hansen. Aromatic ring formation in opposed-flow diffusive 1,3-butadiene flames. *Proceedings of the Combustion Institute*, 36(1):947 – 955, 2017. ISSN 1540-7489. doi: <https://doi.org/10.1016/j.proci.2016.09.010>. URL <http://www.sciencedirect.com/science/article/pii/S1540748916304862>.
- K. Narayanaswamy, G. Blanquart, and H. Pitsch. A consistent chemical mechanism for oxidation of substituted aromatic species. *Combustion and Flame*, 157(10):1879 – 1898, 2010. ISSN 0010-2180. doi: <https://doi.org/10.1016/j.combustflame.2010.07.009>. URL <http://www.sciencedirect.com/science/article/pii/S0010218010001975>.
- Karl Netzell, Harry Lehtiniemi, and Fabian Mauss. Calculating the soot particle size distribution function in turbulent diffusion flames using a sectional method. *Proceedings of the Combustion Institute*, 31(1):667 – 674, 2007. ISSN 1540-7489. doi: <https://doi.org/10.1016/j.proci.2006.08.081>. URL <http://www.sciencedirect.com/science/article/pii/S1540748906003440>.
- M. Nicmanis and M.J. Hounslow. A finite element analysis of the steady state population balance equation for particulate systems: Aggregation and growth. *Computers and Chemical Engineering*, 20:S261 – S266, 1996. ISSN 0098-1354. doi: [https://doi.org/10.1016/0098-1354\(96\)00054-3](https://doi.org/10.1016/0098-1354(96)00054-3). URL <http://www.sciencedirect.com/science/article/pii/S0098135496000543>. European Symposium on Computer Aided Process Engineering-6.
- Rituraj Niranjana and Ashwani Kumar Thakur. The toxicological mechanisms of environmental soot (black carbon) and carbon black: Focus on oxidative stress and inflammatory pathways. *Frontiers in Immunology*, 8:763, 2017. doi: 10.3389/fimmu.2017.00763. URL <https://www.ncbi.nlm.nih.gov/pmc/articles/PMC5492873/>.

- Berk Oktem, Michael P. Tolocka, Bin Zhao, Hai Wang, and Murray V. Johnston. Chemical species associated with the early stage of soot growth in a laminar premixed ethylene-oxygen-argon flame. *Combustion and Flame*, 142(4):364 – 373, 2005. ISSN 0010-2180. doi: <https://doi.org/10.1016/j.combustflame.2005.03.016>. URL <http://www.sciencedirect.com/science/article/pii/S0010218005001033>.
- F.-X. Ouf, S. Bourrous, S. Fauvel, A. Kort, L. Lintis, J. Nuvoli, and J. Yon. True density of combustion emitted particles: A comparison of results highlighting the influence of the organic contents. *Journal of Aerosol Science*, 134:1 – 13, 2019. ISSN 0021-8502. doi: <https://doi.org/10.1016/j.jaerosci.2019.04.007>. URL <http://www.sciencedirect.com/science/article/pii/S0021850219300114>.
- S.H. Park and S.N. Rogak. A novel fixed-sectional model for the formation and growth of aerosol agglomerates. *Journal of Aerosol Science*, 35(11):1385 – 1404, 2004. ISSN 0021-8502. doi: <https://doi.org/10.1016/j.jaerosci.2004.05.010>. URL <http://www.sciencedirect.com/science/article/pii/S0021850204000941>.
- Sungwoo Park, Yu Wang, Suk Ho Chung, and S. Mani Sarathy. Compositional effects on pah and soot formation in counterflow diffusion flames of gasoline surrogate fuels. *Combustion and Flame*, 178:46 – 60, 2017. ISSN 0010-2180. doi: <https://doi.org/10.1016/j.combustflame.2017.01.001>. URL <http://www.sciencedirect.com/science/article/pii/S0010218017300019>.
- R. Patterson. *Numerical Modelling of Soot Formation*. PhD thesis, Trinity College, 2007.
- Robert I.A. Patterson and Markus Kraft. Models for the aggregate structure of soot particles. *Combustion and Flame*, 151(1):160 – 172, 2007. ISSN 0010-2180. doi: <https://doi.org/10.1016/j.combustflame.2007.04.012>. URL <http://www.sciencedirect.com/science/article/pii/S0010218007001162>.
- Robert I.A. Patterson, Jasdeep Singh, Michael Balthasar, Markus Kraft, and Wolfgang Wagner. Extending stochastic soot simulation to higher pressures. *Combustion and Flame*, 145(3):638 – 642, 2006. ISSN 0010-2180. doi: <https://doi.org/10.1016/j.combustflame.2006.02.005>. URL <http://www.sciencedirect.com/science/article/pii/S0010218006000678>.
- Robert I.A. Patterson, Wolfgang Wagner, and Markus Kraft. Stochastic weighted particle methods for population balance equations. *Journal of Computational Physics*, 230(19):7456 – 7472, 2011. ISSN 0021-9991. doi: <https://doi.org/10.1016/j.jcp.2011.06.011>. URL <http://www.sciencedirect.com/science/article/pii/S0021999111003603>.
- Warumporn Pejpichestakul, Eliseo Ranzi, Matteo Pelucchi, Alessio Frassoldati, Alberto Cuoci, Alessandro Parente, and Tiziano Faravelli. Examination of a soot model in premixed laminar flames at fuel-rich conditions. *Proceedings of the Combustion Institute*, 37(1):1013 – 1021, 2019. ISSN 1540-7489. doi: <https://doi.org/10.1016/j.proci.2018.06.104>. URL <http://www.sciencedirect.com/science/article/pii/S1540748918302876>.
- Matteo Pelucchi, Mattia Bissoli, Carlo Cavallotti, Alberto Cuoci, Tiziano Faravelli, Alessio Frassoldati, Eliseo Ranzi, and Alessandro Stagni. Improved kinetic model of the low-temperature oxidation of n-heptane. *Energy & Fuels*, 28(11):7178–7193, 2014. doi: 10.1021/ef501483f. URL <https://doi.org/10.1021/ef501483f>.
- I. Pesmazoglou, A.M. Kempf, and S. Navarro-Martinez. Stochastic modelling of particle aggregation. *International Journal of Multiphase Flow*, 80:118 – 130, 2016. ISSN 0301-9322. doi: <https://doi.org/10.1016/j.ijmultiphaseflow.2015.12.004>. URL <http://www.sciencedirect.com/science/article/pii/S0301932215002748>.
- C.J. Pope and J.B. Howard. Simultaneous particle and molecule modeling (spamm): An approach for combining sectional aerosol equations and elementary gas-phase reactions. *Aerosol Science and Technology*, 27(1):73–94, 1997. doi: 10.1080/02786829708965459. URL <https://doi.org/10.1080/02786829708965459>.
- S. Pope. Monte Carlo method for the PDF equations of turbulent reacting flow. *Combust. Sci. Tech.*, 25:159–174, 1981.
- PubChem. Pubchem, 2019. URL <https://pubchem.ncbi.nlm.nih.gov>.
- S. Qamar, M.P. Elsner, I.A. Angelov, G. Warnecke, and A. Seidel-Morgenstern. A comparative study of high resolution schemes for solving population balances in crystallization. *Computers & Chemical Engineering*, 30(6):1119 – 1131, 2006. ISSN 0098-1354. doi: <https://doi.org/10.1016/j.compchemeng.2006.02.012>. URL <http://www.sciencedirect.com/science/article/pii/S0098135406000445>.
- S. Qamar, A. Ashfaq, G. Warnecke, I. Angelov, M.P. Elsner, and A. Seidel-Morgenstern. Adaptive high-resolution schemes for multidimensional population balances in crystallization processes. *Computers & Chemical Engineering*, 31(10):1296 – 1311, 2007. ISSN 0098-1354. doi: <https://doi.org/10.1016/j.compchemeng.2006.10.014>. URL <http://www.sciencedirect.com/science/article/pii/S0098135406002882>.

- Shamsul Qamar and Gerald Warnecke. Solving population balance equations for two-component aggregation by a finite volume scheme. *Chemical Engineering Science*, 62(3):679 – 693, 2007. ISSN 0009-2509. doi: <https://doi.org/10.1016/j.ces.2006.10.001>. URL <http://www.sciencedirect.com/science/article/pii/S0009250906006336>.
- T. E. Ramabhadran, T. W. Peterson, and J. H. Seinfeld. Dynamics of aerosol coagulation and condensation. *AIChE Journal*, 22(5):840–851, 1976.
- D. Ramkrishna. *Population balances. Theory and applications to particulate systems in engineering*. Academic Press San Diego, 2000. ISBN 0-12-576970-9.
- H Richter and J.B Howard. Formation of polycyclic aromatic hydrocarbons and their growth to soot—a review of chemical reaction pathways. *Progress in Energy and Combustion Science*, 26(4):565 – 608, 2000. ISSN 0360-1285. doi: [https://doi.org/10.1016/S0360-1285\(00\)00009-5](https://doi.org/10.1016/S0360-1285(00)00009-5). URL <http://www.sciencedirect.com/science/article/pii/S0360128500000095>.
- Henning Richter, Silvia Granata, William H. Green, and Jack B. Howard. Detailed modeling of pah and soot formation in a laminar premixed benzene/oxygen/argon low-pressure flame. *Proceedings of the Combustion Institute*, 30(1):1397 – 1405, 2005. ISSN 1540-7489. doi: <https://doi.org/10.1016/j.proci.2004.08.088>. URL <http://www.sciencedirect.com/science/article/pii/S0082078404001419>.
- S. Rigopoulos. Population balance modelling of polydispersed particles in reactive flows. *Progress in Energy and Combustion Science*, 36(4):412 – 443, 2010. ISSN 0360-1285. doi: <https://doi.org/10.1016/j.pecs.2009.12.001>. URL <http://www.sciencedirect.com/science/article/pii/S0360128509000690>.
- Stelios Rigopoulos and Alan G. Jones. Finite-element scheme for solution of the dynamic population balance equation. *AIChE Journal*, 49(5):1127–1139, 2003. doi: 10.1002/aic.690490507. URL <https://aiche.onlinelibrary.wiley.com/doi/abs/10.1002/aic.690490507>.
- P. Rodrigues. *Modelisation multiphysique de flammes turbulentes suitees avec la prise en compte des transferts radiatifs et des transferts de chaleur parietaux*. PhD thesis, Centrale Supélec, 2018.
- Pedro Rodrigues, Benedetta Franzelli, Ronan Vicquelin, Olivier Gicquel, and Nasser Darabiha. Coupling an les approach and a soot sectional model for the study of sooting turbulent non-premixed flames. *Combustion and Flame*, 190:477 – 499, 2018. ISSN 0010-2180. doi: <https://doi.org/10.1016/j.combustflame.2017.12.009>. URL <http://www.sciencedirect.com/science/article/pii/S0010218017304765>.
- A.I. Roussos, A.H. Alexopoulos, and C. Kiparissides. Part iii: Dynamic evolution of the particle size distribution in batch and continuous particulate processes: A galerkin on finite elements approach. *Chemical Engineering Science*, 60(24):6998 – 7010, 2005. ISSN 0009-2509. doi: <https://doi.org/10.1016/j.ces.2005.06.021>. URL <http://www.sciencedirect.com/science/article/pii/S0009250905005622>.
- Y. Rubner, C. Tomasi, and L. J. Guibas. A metric for distributions with applications to image databases. In *Sixth International Conference on Computer Vision (IEEE Cat. No.98CH36271)*, pages 59–66, Jan 1998.
- C. Russo, A. Tregrossi, and A. Ciajolo. Dehydrogenation and growth of soot in premixed flames. *Proceedings of the Combustion Institute*, 35(2):1803 – 1809, 2015. ISSN 1540-7489. doi: <https://doi.org/10.1016/j.proci.2014.05.024>. URL <http://www.sciencedirect.com/science/article/pii/S1540748914000273>.
- Meghdad Saffaripour, Armin Veshkini, Mohammadreza Kholghy, and Murray J. Thomson. Experimental investigation and detailed modeling of soot aggregate formation and size distribution in laminar coflow diffusion flames of jet a-1, a synthetic kerosene, and n-decane. *Combustion and Flame*, 161(3):848 – 863, 2014. ISSN 0010-2180. doi: <https://doi.org/10.1016/j.combustflame.2013.10.016>. URL <http://www.sciencedirect.com/science/article/pii/S0010218013003908>. Special Issue on Alternative Fuels.
- Chiara Saggese, Alessio Frassoldati, Alberto Cuoci, Tiziano Faravelli, and Eliseo Ranzi. A wide range kinetic modeling study of pyrolysis and oxidation of benzene. *Combustion and Flame*, 160(7):1168 – 1190, 2013. ISSN 0010-2180. doi: <https://doi.org/10.1016/j.combustflame.2013.02.013>. URL <http://www.sciencedirect.com/science/article/pii/S0010218013000631>.
- Chiara Saggese, Sara Ferrario, Joaquin Camacho, Alberto Cuoci, Alessio Frassoldati, Eliseo Ranzi, Hai Wang, and Tiziano Faravelli. Kinetic modeling of particle size distribution of soot in a premixed burner-stabilized stagnation ethylene flame. *Combustion and Flame*, 162(9):3356 – 3369, 2015. ISSN 0010-2180. doi: <https://doi.org/10.1016/j.combustflame.2015.06.002>. URL <http://www.sciencedirect.com/science/article/pii/S0010218015001807>.
- S. Salenbauch. *Modeling of soot formation and oxidation in reacting flows*. PhD thesis, TU Darmstadt, 2018.

- Steffen Salenbauch, Alberto Cuoci, Alessio Frassoldati, Chiara Saggese, Tiziano Faravelli, and Christian Hasse. Modeling soot formation in premixed flames using an extended conditional quadrature method of moments. *Combustion and Flame*, 162(6):2529 – 2543, 2015. ISSN 0010-2180. doi: <https://doi.org/10.1016/j.combustflame.2015.03.002>. URL <http://www.sciencedirect.com/science/article/pii/S0010218015000772>.
- Marina Schenk, Sydney Lieb, Henning Vieker, André Beyer, Armin Götzhäuser, Hai Wang, and Katharina Kohse-Höinghaus. Morphology of nascent soot in ethylene flames. *Proceedings of the Combustion Institute*, 35(2):1879 – 1886, 2015. ISSN 1540-7489. doi: <https://doi.org/10.1016/j.proci.2014.05.009>. URL <http://www.sciencedirect.com/science/article/pii/S1540748914000121>.
- M.A. Schiener and R.P. Lindstedt. Transported probability density function based modelling of soot particle size distributions in non-premixed turbulent jet flames. *Proceedings of the Combustion Institute*, 37(1):1049 – 1056, 2019. ISSN 1540-7489. doi: <https://doi.org/10.1016/j.proci.2018.06.088>. URL <http://www.sciencedirect.com/science/article/pii/S1540748918302712>.
- Charles A. Schuetz and Michael Frenklach. Nucleation of soot: Molecular dynamics simulations of pyrene dimerization. *Proceedings of the Combustion Institute*, 29(2):2307 – 2314, 2002. ISSN 1540-7489. doi: [https://doi.org/10.1016/S1540-7489\(02\)80281-4](https://doi.org/10.1016/S1540-7489(02)80281-4). URL <http://www.sciencedirect.com/science/article/pii/S1540748902802814>.
- Fabian Schulz, Mario Commodo, Katharina Kaiser, Gianluigi De Falco, Patrizia Minutolo, Gerhard Meyer, Andrea D’Anna, and Leo Gross. Insights into incipient soot formation by atomic force microscopy. *Proceedings of the Combustion Institute*, 37(1):885 – 892, 2019. ISSN 1540-7489. doi: <https://doi.org/10.1016/j.proci.2018.06.100>. URL <http://www.sciencedirect.com/science/article/pii/S1540748918302839>.
- William T. Scott. Analytic studies of cloud droplet coalescence I. *Journal of the Atmospheric Sciences*, 25(1):54–65, 1968.
- Andrea Seltz, Pascale Domingo, Luc Vervisch, and Zacharias M. Nikolaou. Direct mapping from les resolved scales to filtered-flame generated manifolds using convolutional neural networks. *Combustion and Flame*, 210:71 – 82, 2019. ISSN 0010-2180. doi: <https://doi.org/10.1016/j.combustflame.2019.08.014>. URL <http://www.sciencedirect.com/science/article/pii/S0010218019303773>.
- Fabian Sewerin and Stelios Rigopoulos. An explicit adaptive grid approach for the numerical solution of the population balance equation. *Chemical Engineering Science*, 168:250 – 270, 2017. ISSN 0009-2509. doi: <https://doi.org/10.1016/j.ces.2017.01.054>. URL <http://www.sciencedirect.com/science/article/pii/S0009250917300854>.
- L.A. Sgro, G. Basile, A.C. Barone, A. D’Anna, P. Minutolo, A. Borghese, and A. D’Alessio. Detection of combustion formed nanoparticles. *Chemosphere*, 51(10):1079 – 1090, 2003. ISSN 0045-6535. doi: [https://doi.org/10.1016/S0045-6535\(02\)00718-X](https://doi.org/10.1016/S0045-6535(02)00718-X). URL <http://www.sciencedirect.com/science/article/pii/S004565350200718X>. PIC7.
- B.H. Shah, Doraiswami Ramkrishna, and J. D. Borwanker. Simulation of particulate systems using the concept of the interval of quiescence. *AIChE Journal*, 23(6):897–904, 1977. doi: 10.1002/aic.690230617. URL <https://aiche.onlinelibrary.wiley.com/doi/abs/10.1002/aic.690230617>.
- Bikau Shukla and Mitsuo Koshi. Comparative study on the growth mechanisms of pahs. *Combustion and Flame*, 158(2):369 – 375, 2011. ISSN 0010-2180. doi: <https://doi.org/10.1016/j.combustflame.2010.09.012>. URL <http://www.sciencedirect.com/science/article/pii/S0010218010002634>.
- Jasdeep Singh, Robert I.A. Patterson, Markus Kraft, and Hai Wang. Numerical simulation and sensitivity analysis of detailed soot particle size distribution in laminar premixed ethylene flames. *Combustion and Flame*, 145(1): 117 – 127, 2006. ISSN 0010-2180. doi: <https://doi.org/10.1016/j.combustflame.2005.11.003>. URL <http://www.sciencedirect.com/science/article/pii/S0010218005003469>.
- Sourab Sinha, Ramees K. Rahman, and Abhijeet Raj. On the role of resonantly stabilized radicals in polycyclic aromatic hydrocarbon (pah) formation: pyrene and fluoranthene formation from benzyl–indenyl addition. *Phys. Chem. Chem. Phys.*, 19:19262–19278, 2017. doi: 10.1039/C7CP02539D. URL <http://dx.doi.org/10.1039/C7CP02539D>.
- Mariano Sirignano, Angelo Collina, Mario Commodo, Patrizia Minutolo, and Andrea D’Anna. Detection of aromatic hydrocarbons and incipient particles in an opposed-flow flame of ethylene by spectral and time-resolved laser induced emission spectroscopy. *Combustion and Flame*, 159(4):1663 – 1669, 2012. ISSN 0010-2180. doi: <https://doi.org/10.1016/j.combustflame.2011.11.005>. URL <http://www.sciencedirect.com/science/article/pii/S001021801100352X>.

- Mariano Sirignano, Daniel Bartos, Marielena Conturso, Matthew Dunn, Andrea D'Anna, and Assaad R. Masri. Detection of nanostructures and soot in laminar premixed flames. *Combustion and Flame*, 176:299 – 308, 2017. ISSN 0010-2180. doi: <https://doi.org/10.1016/j.combustflame.2016.10.009>. URL <http://www.sciencedirect.com/science/article/pii/S001021801630308X>.
- N.A. Slavinskaya and P. Frank. A modelling study of aromatic soot precursors formation in laminar methane and ethene flames. *Combustion and Flame*, 156(9):1705 – 1722, 2009. ISSN 0010-2180. doi: <https://doi.org/10.1016/j.combustflame.2009.04.013>. URL <http://www.sciencedirect.com/science/article/pii/S0010218009001242>.
- Nadezhda A. Slavinskaya, Uwe Riedel, Seth B. Dworkin, and Murray J. Thomson. Detailed numerical modeling of pah formation and growth in non-premixed ethylene and ethane flames. *Combustion and Flame*, 159(3):979 – 995, 2012. ISSN 0010-2180. doi: <https://doi.org/10.1016/j.combustflame.2011.10.005>. URL <http://www.sciencedirect.com/science/article/pii/S0010218011003105>.
- Matthew Smith and Themis Matsoukas. Constant-number monte carlo simulation of population balances. *Chemical Engineering Science*, 53(9):1777 – 1786, 1998. ISSN 0009-2509. doi: [https://doi.org/10.1016/S0009-2509\(98\)00045-1](https://doi.org/10.1016/S0009-2509(98)00045-1). URL <http://www.sciencedirect.com/science/article/pii/S0009250998000451>.
- M. Smoluchowski. Mathematical theory of the kinetics of the coagulation of colloidal solutions. *Zeitschrift für Physikalische Chemie*, 19:129–135, 1917.
- M.D. Smooke, M.B. Long, B.C. Connelly, M.B. Colket, and R.J. Hall. Soot formation in laminar diffusion flames. *Combustion and Flame*, 143(4):613 – 628, 2005. ISSN 0010-2180. doi: <https://doi.org/10.1016/j.combustflame.2005.08.028>. URL <http://www.sciencedirect.com/science/article/pii/S0010218005002488>. Special Issue to Honor Professor Robert W. Bilger on the Occasion of His Seventieth Birthday.
- J. Solsvik and H. A. Jakobsen. The foundation of the population balance equation: A review. *Journal of Dispersion Science and Technology*, 36(4):510–520, 2015.
- Stephen E. Stein and A. Fahr. High-temperature stabilities of hydrocarbons. *The Journal of Physical Chemistry*, 89(17):3714–3725, 1985. doi: [10.1021/j100263a027](https://doi.org/10.1021/j100263a027). URL <https://doi.org/10.1021/j100263a027>.
- Reto Strobel and Sotiris E. Pratsinis. Flame aerosol synthesis of smart nanostructured materials. *J. Mater. Chem.*, 17:4743–4756, 2007. doi: [10.1039/B711652G](https://doi.org/10.1039/B711652G). URL <http://dx.doi.org/10.1039/B711652G>.
- H. Tang and T. Tang. Adaptive mesh methods for one- and two-dimensional hyperbolic conservation laws. *SIAM Journal on Numerical Analysis*, 41(2):487–515, 2003. doi: [10.1137/S003614290138437X](https://doi.org/10.1137/S003614290138437X). URL <https://doi.org/10.1137/S003614290138437X>.
- P.A. Tesner, T.D. Smegiriova, and V.G. Knorre. Kinetics of dispersed carbon formation. *Combustion and Flame*, 17(2):253 – 260, 1971. ISSN 0010-2180. doi: [https://doi.org/10.1016/S0010-2180\(71\)80168-2](https://doi.org/10.1016/S0010-2180(71)80168-2). URL <http://www.sciencedirect.com/science/article/pii/S0010218071801682>.
- S. Urbanek. Package emdist, 2012. URL <https://cran.r-project.org/web/packages/emdist/emdist.pdf>.
- John R. van Peborgh-Gooch and Michael J. Hounslow. Monte carlo simulation of size-enlargement mechanisms in crystallization. *AIChE Journal*, 42(7):1864–1874, 1996. doi: [10.1002/aic.690420708](https://doi.org/10.1002/aic.690420708). URL <https://aiche.onlinelibrary.wiley.com/doi/abs/10.1002/aic.690420708>.
- Armin Veshkini, Nick A. Eaves, Seth B. Dworkin, and Murray J. Thomson. Application of pah-condensation reversibility in modeling soot growth in laminar premixed and nonpremixed flames. *Combustion and Flame*, 167:335 – 352, 2016. ISSN 0010-2180. doi: <https://doi.org/10.1016/j.combustflame.2016.02.024>. URL <http://www.sciencedirect.com/science/article/pii/S0010218016300013>.
- Angela Violi, Adel F. Sarofim, and Gregory A. Voth. Kinetic monte carlo–molecular dynamics approach to model soot inception. *Combustion Science and Technology*, 176(5-6):991–1005, 2004. doi: [10.1080/00102200490428594](https://doi.org/10.1080/00102200490428594). URL <https://doi.org/10.1080/00102200490428594>.
- H. Wang, D.X. Du, C.J. Sung, and C.K. Law. Experiments and numerical simulation on soot formation in opposed-jet ethylene diffusion flames. *Symposium (International) on Combustion*, 26(2):2359 – 2368, 1996. ISSN 0082-0784. doi: [https://doi.org/10.1016/S0082-0784\(96\)80065-8](https://doi.org/10.1016/S0082-0784(96)80065-8). URL <http://www.sciencedirect.com/science/article/pii/S0082078496800658>.
- Hai Wang. Formation of nascent soot and other condensed-phase materials in flames. *Proceedings of the Combustion Institute*, 33(1):41 – 67, 2011a. ISSN 1540-7489. doi: <https://doi.org/10.1016/j.proci.2010.09.009>. URL <http://www.sciencedirect.com/science/article/pii/S1540748910003937>.

- Hai Wang. Formation of nascent soot and other condensed-phase materials in flames. *Proceedings of the Combustion Institute*, 33(1):41 – 67, 2011b. ISSN 1540-7489. doi: <https://doi.org/10.1016/j.proci.2010.09.009>. URL <http://www.sciencedirect.com/science/article/pii/S1540748910003937>.
- Hai Wang and Michael Frenklach. A detailed kinetic modeling study of aromatics formation in laminar premixed acetylene and ethylene flames. *Combustion and Flame*, 110(1):173 – 221, 1997. ISSN 0010-2180. doi: [https://doi.org/10.1016/S0010-2180\(97\)00068-0](https://doi.org/10.1016/S0010-2180(97)00068-0). URL <http://www.sciencedirect.com/science/article/pii/S0010218097000680>.
- Yu Wang, Abhijeet Raj, and Suk Ho Chung. A pah growth mechanism and synergistic effect on pah formation in counterflow diffusion flames. *Combustion and Flame*, 160(9):1667 – 1676, 2013. ISSN 0010-2180. doi: <https://doi.org/10.1016/j.combustflame.2013.03.013>. URL <http://www.sciencedirect.com/science/article/pii/S0010218013001016>.
- Curt M. White. Prediction of the boiling point, heat of vaporization, and vapor pressure at various temperatures for polycyclic aromatic hydrocarbons. *Journal of Chemical & Engineering Data*, 31(2):198–203, 1986. doi: 10.1021/je00044a020. URL <https://doi.org/10.1021/je00044a020>.
- Europe WHO. Review of evidence on health aspects of air pollution – revihaap project: final technical report. Technical report, World Health Organization/Europe, 2013. URL <http://www.euro.who.int/en/health-topics/environment-and-health/air-quality/publications/2013/review-of-evidence-on-health-aspects-of-air-pollution-revihaap-project-final-technical-report>.
- Achim Wick, Tan-Trung Nguyen, Frédérique Laurent, Rodney O. Fox, and Heinz Pitsch. Modeling soot oxidation with the extended quadrature method of moments. *Proceedings of the Combustion Institute*, 36(1):789 – 797, 2017. ISSN 1540-7489. doi: <https://doi.org/10.1016/j.proci.2016.08.004>. URL <http://www.sciencedirect.com/science/article/pii/S1540748916303935>.
- Jiuzhong Yang, Long Zhao, Wenhao Yuan, Fei Qi, and Yuyang Li. Experimental and kinetic modeling investigation on laminar premixed benzene flames with various equivalence ratios. *Proceedings of the Combustion Institute*, 35(1):855 – 862, 2015. ISSN 1540-7489. doi: <https://doi.org/10.1016/j.proci.2014.05.085>. URL <http://www.sciencedirect.com/science/article/pii/S1540748914000881>.
- J. Yon, R. Lemaire, E. Therssen, P. Desgroux, A. Coppalle, and K.F. Ren. Examination of wavelength dependent soot optical properties of diesel and diesel/rapeseed methyl ester mixture by extinction spectra analysis and lii measurements. *Appl. Phys. B*, 104:253–271, 2011. ISSN 1432-0649. doi: <https://doi.org/10.1007/s00340-011-4416-4>. URL <https://link.springer.com/article/10.1007/s00340-011-4416-4>.
- J. Yon, A. Bescond, and F.-X. Ouf. A simple semi-empirical model for effective density measurements of fractal aggregates. *Journal of Aerosol Science*, 87:28 – 37, 2015. ISSN 0021-8502.
- Jérôme Yon, François-Xavier Ouf, Damien Hebert, James Brian Mitchell, Nadine Teuscher, Jean-Luc Le Garrec, Alexandre Bescond, Werner Baumann, Djoudi Ourdani, Thomas Bizien, and Javier Perez. Investigation of soot oxidation by coupling lii, saxs and scattering measurements. *Combustion and Flame*, 190:441 – 453, 2018. ISSN 0010-2180. doi: <https://doi.org/10.1016/j.combustflame.2017.12.014>. URL <http://www.sciencedirect.com/science/article/pii/S0010218017304819>.
- Mingzhou Yu, Jianzhong Lin, and Tatleung Chan. A new moment method for solving the coagulation equation for particles in brownian motion. *Aerosol Science and Technology*, 42(9):705–713, 2008. doi: 10.1080/02786820802232972. URL <https://doi.org/10.1080/02786820802232972>.
- C. Yuan and R.O. Fox. Conditional quadrature method of moments for kinetic equations. *Journal of Computational Physics*, 230(22):8216 – 8246, 2011. ISSN 0021-9991. doi: <https://doi.org/10.1016/j.jcp.2011.07.020>. URL <http://www.sciencedirect.com/science/article/pii/S0021999111004396>.
- C. Yuan, F. Laurent, and R.O. Fox. An extended quadrature method of moments for population balance equations. *Journal of Aerosol Science*, 51:1 – 23, 2012. ISSN 0021-8502. doi: <https://doi.org/10.1016/j.jaerosci.2012.04.003>. URL <http://www.sciencedirect.com/science/article/pii/S0021850212000699>.
- Wenhao Yuan, Yuyang Li, Philippe Dagaut, Jiuzhong Yang, and Fei Qi. Experimental and kinetic modeling study of styrene combustion. *Combustion and Flame*, 162(5):1868 – 1883, 2015. ISSN 0010-2180. doi: <https://doi.org/10.1016/j.combustflame.2014.12.008>. URL <http://www.sciencedirect.com/science/article/pii/S0010218014004027>.
- Bin Zhao, Zhiwei Yang, Murray V. Johnston, Hai Wang, Anthony S. Wexler, Michael Balthasar, and Markus Kraft. Measurement and numerical simulation of soot particle size distribution functions in a laminar premixed ethylene-oxygen-argon flame. *Combust. Flame*, 133(1):173 – 188, 2003.

- H. Zhao, A. Maisels, T. Matsoukas, and C. Zheng. Analysis of four monte carlo methods for the solution of population balances in dispersed systems. *Powder Technology*, 173(1):38 – 50, 2007. ISSN 0032-5910. doi: <https://doi.org/10.1016/j.powtec.2006.12.010>. URL <http://www.sciencedirect.com/science/article/pii/S0032591006005481>.
- H. Zhao, F.E. Kruis, and C. Zheng. Reducing statistical noise and extending the size spectrum by applying weighted simulation particles in monte carlo simulation of coagulation. *Aerosol Science and Technology*, 43(8):781–793, 2009. doi: 10.1080/02786820902939708. URL <https://doi.org/10.1080/02786820902939708>.
- Haibo Zhao and Chuguang Zheng. A population balance-monte carlo method for particle coagulation in spatially inhomogeneous systems. *Computers & Fluids*, 71:196 – 207, 2013. ISSN 0045-7930. doi: <https://doi.org/10.1016/j.compfluid.2012.09.025>. URL <http://www.sciencedirect.com/science/article/pii/S0045793012004069>.